**LAL 05-162**
November 2005

Laboratoire
de l'Accélérateur
Linéaire

# Technical Performance of the NEMO 3 detector “Advantages and Limitations”

**Corinne Augier**
**for the NEMO Collaboration**

U.M.R
de
l'Université Paris-Sud

Institut National de
Physique Nucléaire et de
Physique des Particules du CNRS

LAL ~ Bât. 200 ~ B.P. 34 ~ 91898 Orsay Cedex ~ France

**LAL 05-162**
November 2005

# Technical performance of the NEMO 3 detector “Advantages and Limitations”

R. Arnold[e], **C. Augier**[h], J. Baker[d], A. Barabash[f], G. Broudin[a], V. Brudanin[g], A.J. Caffrey[d], V. Egorov[g], K. Errahmane[h], A.I. Etienvre[h], J.L. Guyonnet[e], F. Hubert[a], Ph. Hubert[a], C. Jollet[e], S. Jullian[h], O. Kochetov[g], V. Kovalenko[g], S. Konovalov[f], D. Lalanne[h], K. Lang[m], F. Leccia[a], C. Longuemare[i], G. Lutter[a], Ch. Marquet[a], F. Mauger[i], H. Ohsumi[l], F. Piquemal[a], J.L. Reyss[j], R. Saakyan[n], X. Sarazin[h], L. Simard[h], Yu. Shitov[g], A. Smolnikov[g], I. Štekl[c], C.S. Sutton[k], G. Szklarz[h], J. Thomas[n], V. Timkin[g], V. Tretyak[g], V. Umatov[f], L. Vála[c], I. Vanushin[f], V. Vasilyev[f], V. Vorobel[b], Ts. Vylov[g]

[a]CENBG, IN2P3-CNRS and Univ. Bordeaux I, 33170 Gradignan, France
[b]Charles University, Prague, Czech Republic
[c]IEAP, Czech Tech. Univ., Prague, Czech Republic
[d]INL, Idaho Falls, ID 83415, U.S.A.
[e]IReS, IN2P3-CNRS and Univ. Louis Pasteur, 67037 Strasbourg, France
[f]ITEP, 117259 Moscow, Russia
[g]JINR, 141980 Dubna, Russia
[h]LAL, IN2P3-CNRS and Univ. Paris-Sud 11, 91405 Orsay, France
[i]LPC, IN2P3-CNRS and Univ. Caen, 14032 Caen, France
[j]LSCE, CNRS, 91190 Gif-sur-Yvette, France
[k]MHC, South Hadley, Massachusetts 01075, U.S.A.
[l]Saga University, Saga 840-8502, Japan
[m]Texas University, Austin, TX 78712-1081, U.S.A.
[n]UCL, London WC1E 6BT, United Kingdom

## Abstract

The development of the NEMO 3 detector, which is now running in the Fréjus Underground Laboratory (L.S.M. Laboratoire Souterrain de Modane), was begun more than ten years ago. The NEMO 3 detector uses a tracking-calorimeter technique in order to investigate double beta decay processes for several isotopes. The technical description of the detector is followed by the presentation of its performance, including the methods used by the collaboration to address the radon problem.

# Contents

# Chapter 1

# General introduction

## 1.1 Objective of the experiment

The primary objective of the NEMO 3 experiment is to search for neutrinoless double beta decay for several isotopes. This research is one of the most pressing topics in neutrino physics, adressing the fundamental problem of whether neutrinos are Dirac or Majorana particles. An observation of the neutrinoless double beta decay ($\beta\beta0\nu$), which is forbidden by the Standard Model due to lepton number violation by two units

$$((A, Z) \;\rightarrow\; (A, Z+2) \;+\; 2e^{-}$$

would prove Majorana nature of neutrinos, particle which is its own antiparticle. Experimental signature of such a process is the observation of the two electrons, for which the total kinetic energy sum is exactly the transition energy, and physical observable is the half-life of this process.

### 1.1.1 Neutrino species, neutrino nature and mixing

The three active neutrino species can be expressed either as the flavor-eigenstates $\nu_{\ell l}$ ($\ell = e,\ \mu,\ \tau$) or the mass-eigenstates $\nu_{il}$ ($i = 1,\ 2,\ 3$). These two bases are related through a $(3 \times 3)$ unitary mixing matrix, $U$, called the Maki-Nakagawa-Sakata-Pontecorvo (MNSP) matrix [1]:

$$\nu_{\ell l} = \sum_{i=1}^{3} U_{\ell i} \nu_{il} \tag{1.1}$$

In the weak-basis where the charged lepton mass-matrix and the charged current coupling-matrix are diagonal, the neutrino mass matrix $m_\nu^{\alpha\beta}$ can be written:

$$m_\nu^{\alpha\beta} = \sum_{i=1}^{3} (U^*)_{\alpha i} m_i (U^\dagger)_{i\beta} \tag{1.2}$$

where $m_i$ are the neutrino mass-eigenvalues, which can be taken real and positive.
The general parametrization of $m_\nu$ is given by the matrix in Eq. 1.3:

$$m_\nu = \begin{pmatrix} m_{11} & m_{12} & m_{13} \\ m_{12} & m_{22} & m_{23} \\ m_{13} & m_{23} & m_{33} \end{pmatrix} \tag{1.3}$$

If neutrinos are Dirac-particles (with 4 states $\nu_L$, $\nu_R$, $\bar{\nu}_L$, $\bar{\nu}_R$, and conservation of lepton number), the $U$ matrix is analog to the Cabbibo-Kobayashi-Maskawa (CKM) mixing matrix of the quark sector and is parametrized with three angles and one CP-phase ($0 \leq \delta \leq 2\pi$) in the case of neutrino oscillations. Here, the $U$ matrix is given by the product of three rotation matrix in the respective planes (23) (atmospheric sector, K2K, $\theta_{23} \sim 45^o$), (13) (CHOOZ sector, with $\theta_{13} \lesssim 13^o$, or accelerators (JPARC)), and (12) (solar sector, reactors, $\theta_{12} \sim 30^o$), as shown in Eq. 1.4 [2]:

$$U = \begin{pmatrix} 1 & 0 & 0 \\ 0 & c_{23} & s_{23} \\ 0 & -s_{23} & c_{23} \end{pmatrix} \begin{pmatrix} c_{13} & 0 & s_{13}e^{-i\delta} \\ 0 & 1 & 0 \\ -s_{13}e^{i\delta} & 0 & c_{13} \end{pmatrix} \begin{pmatrix} c_{12} & s_{12} & 0 \\ -s_{12} & c_{12} & 0 \\ 0 & 0 & 1 \end{pmatrix} \tag{1.4}$$

If neutrinos are Majorana-particles (only 2 states $\nu_L$ and $\nu_R$, with non-conservation of lepton number), two phases $\phi_1$ and $\phi_2$ are added[1]. These phases appear only in processes which violate lepton number, as in $\beta\beta0\nu$ amplitude.

One usual parametrization for the MNSP mixing matrix $U$ in the Majorana case is presented in Eq. 1.5 [2]:

$$U = \begin{pmatrix} c_{12}\ c_{13} & s_{12}\ c_{13} & s_{13}e^{-i\delta} \\ -s_{12}\ c_{23} - c_{12}\ s_{23}\ s_{13}e^{i\delta} & c_{12}\ c_{23} - s_{12}\ s_{23}\ s_{13}e^{i\delta} & s_{23}\ c_{13} \\ s_{12}\ s_{23} - c_{12}\ c_{23}\ s_{13}e^{i\delta} & -c_{12}\ s_{23} - s_{12}\ c_{23}\ s_{13}e^{i\delta} & c_{23}\ c_{13} \end{pmatrix} \mathrm{Diag}\left\{1, e^{i\phi_1}, e^{i\phi_2}\right\} \tag{1.5}$$

where $\phi_{1,2}$ are Majorana phases and the left matrix is exactly the three matrix product from Eq. 1.4.

Thus, in general, the mixing matrix of three neutrinos is parametrized by three angles, $\theta_{12} = \theta_{\odot}$, $\theta_{13}$ and $\theta_{23} = \theta_{\text{atm}}$, one Dirac CP-violation phase $\delta$ and two Majorana CP-violation phases $\phi_1$ and $\phi_2$. The three neutrino masses $m_i$ should be added to this parameter set that describes the MNSP $U$ matrix (Eq. 1.5), representing therefore nine unknown parameters altogether.

Neutrino oscillation experiments have already provided measurements for the neutrino mass-squared differences, as well as the mixing angles. The allowed values for the $\theta_{ij}$ as well as the $\Delta m^2$'s are summarized in Fig 1.1. Connections between neutrino oscillation results, mass hierarchies and double beta decay will be explained in Section 1.1.2.

In most of supersymmetric or great unification models light and heavy Majorana neutrinos arise. A see-saw mechanism allows one to justify the small value of light neutrino masses (heavy neutrinos have mass of the order of great unification scale). The consequence of the Majorana neutrino is the non-conservation of the lepton number, which is a necessary condition for neutrinos with CP-violation to explain matter creation through leptogenesis by heavy Majorana neutrino decays.

### 1.1.2 Double beta decay

The neutrinoless double beta decay may arise if $\beta$-transition towards intermediate daughter nucleus $(A, Z+1)$ is forbidden or strongly suppressed. A $\beta\beta0\nu$ mode involves transition of two

---

[1] For $n$ families and Majorana case, the mixing matrix depends on $n(n+1)/2$ phases and only $n$ phases are absorbed by charged lepton redefinition. Thus $n(n-1)/2$ CP-phases stay for Majorana case, when only $(n-1)(n-2)/2$ CP-phases stay for Dirac-case.

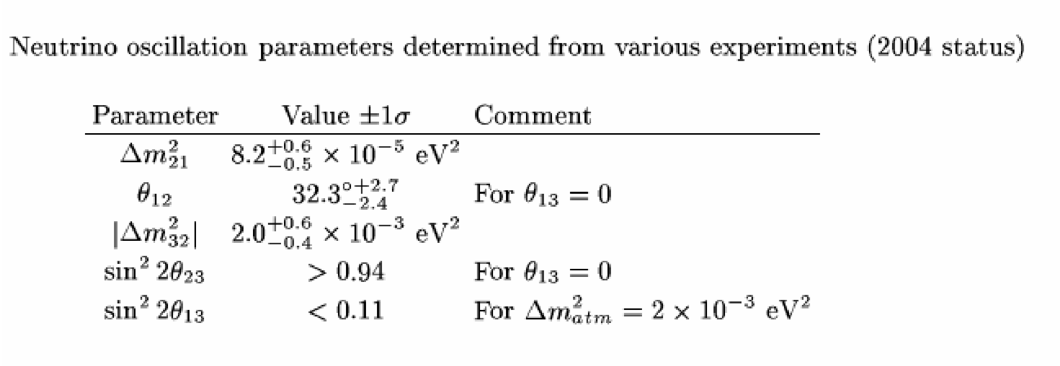

Neutrino oscillation parameters determined from various experiments (2004 status)

| Parameter | Value $\pm 1\sigma$ | Comment |
|---|---|---|
| $\Delta m^2_{21}$ | $8.2^{+0.6}_{-0.5} \times 10^{-5}$ eV$^2$ | |
| $\theta_{12}$ | $32.3^{\circ}{}^{+2.7}_{-2.4}$ | For $\theta_{13} = 0$ |
| $\lvert\Delta m^2_{32}\rvert$ | $2.0^{+0.6}_{-0.4} \times 10^{-3}$ eV$^2$ | |
| $\sin^2 2\theta_{23}$ | $> 0.94$ | For $\theta_{13} = 0$ |
| $\sin^2 2\theta_{13}$ | $< 0.11$ | For $\Delta m^2_{atm} = 2 \times 10^{-3}$ eV$^2$ |

Figure 1.1: This table summarizes the present status of knowledge of the oscillation parameters (assuming three mass eigenstates, i.e. disregarding the possible existence of sterile neutrino) [3].

neutrons into two protons with the emission of two electrons and nothing else. One can visualize it by assuming that the process involves the exchange of various virtual particles. Nevertheless, no matter what the vertex is, the $\beta\beta0\nu$ decay can proceed only when neutrinos are massive Majorana particles [4].

#### 1.1.2.1 Exchange of light Majorana neutrinos

Of primary interest is the process which was proposed years ago [5] and mediated by the **exchange of light Majorana neutrinos** interacting through the left-handed $V-A$ weak currents, for which right antineutrino emitted at first vertex is absorbed as left neutrino at the second one (see Fig. 1.2). This change in helicity is possible only if the exchanged Majorana neutrino is massive.

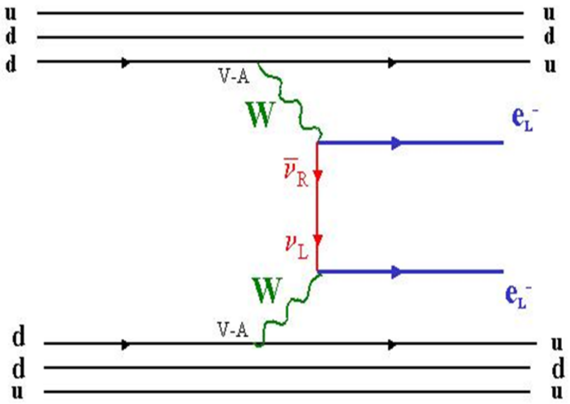

Figure 1.2: Neutrinoless double beta decay scheme mediated by the exchange of light Majorana neutrino interacting through the left-handed $V - A$ weak currents.

A half-life of the $\beta\beta0\nu$ decay process is connected to the effective neutrino mass by the relation:

$$(T^{0\nu}_{1/2})^{-1} = |\langle m_\nu\rangle|^2 \times |M_{0\nu}|^2 \times G^{0\nu}(Z, Q_{\beta\beta}) \tag{1.6}$$

where $G^{0\nu}$ is the phase-space factor that is analytically calculated, depending on $Z$ and proportional in first approximation to the transition energy to the fifth power, $Q^5_{\beta\beta}$ (see $G^{0\nu}$ values in Table 1.1). $M_{0\nu}$ is the nuclear matrix element (NME) of the relevant isotope for which calculations have large theoretical uncertainties[2]. It can be written as:

$$|M_{0\nu}| = |M^{GT}_{0\nu} - \frac{g_V^2}{g_A^2} M^F_{0\nu}| \tag{1.7}$$

where $M^{GT}_{0\nu}$ and $M^F_{0\nu}$ are respectively Gamow-Teller and Fermi nuclear matrix elements, and $g_V$ and $g_A$ are vector and axial coupling constants of weak interactions, with $g_V/g_A \sim 0.8$.

The effective neutrino mass $\langle m_\nu\rangle$, also called $m_{ee}$, is the (1,1) element of the matrix from Eq. 1.3 and is given by Eq. 1.8:

$$m_{ee} = m_{11} \equiv \langle m_\nu\rangle = \sum_i m_i U^2_{ei} \tag{1.8}$$

where $U_{ei}$ are coefficients of the MNSP mixing matrix from Eq. 1.5.
This effective mass is very important due to its dependence on mass eigenvalues $m_i$ and its relation to the oscillation parameters, which can give informations on a particular combination of neutrino masses, mixing angles and phases.
Thus, the effective mass is sensitive to the absolute scale of neutrino masses, solar mixing angle $\theta_{12}$ and the angle $\theta_{13}$. Moreover, it is the only experimentally practical quantity where the Majorana CP-phases of leptonic violation $\phi_{1,2}$ may appear. It is given by the relation [2]:

$$|\langle m_\nu\rangle| = |\cos^2\theta_{13}(|m_1|\cos^2\theta_{12} + |m_2|e^{2i\phi_1}\sin^2\theta_{12}) + |m_3|e^{2i(\phi_2-\delta)}\sin^2\theta_{13}| \tag{1.9}$$

Thus, measurements of the effective neutrino mass should help to conclude on the scheme of neutrino mass scale, which is unknown due to its dependence on the still not yet measured value of the $\Delta m_{23}$ sign from neutrino oscillation measurements.
Using values of Fig. 1.1 [3] and express $\langle m_\nu\rangle$ in terms of the three unknown quantities (the mass scale, represented by the mass of the lightest neutrino $m_{\nu_{min}}$, and the two Majorana phases), it is useful to distinguish three mass patterns (see Fig. 1.3). With $\nu_\mu \to \nu_\tau$ oscillations, $\Delta m^2_{23} \sim 2\times10^{-3}$ eV$^2$ and from $\nu_e \to \nu_\mu$ oscillations, $\Delta m^2_{12} \sim 8\times10^{-5}$ eV$^2$. Relation between $|\langle m_\nu\rangle|$ and $m_{\nu_{min}}$ depends on the mass hierarchy:

- Quasi-degenerate masses (QD): $m_1 \approx m_2 \approx m_3 \approx m_{\nu_{min}}$ where $m_i^2 \gg \sqrt{|\Delta m^2_{32}|}$ and typically $m_{\nu_{min}} \gtrsim 0.1$ eV. Using a conservative value of the cosmological limit $\Sigma m_i = m_1 + m_2 + m_3 \sim 3m_{\nu_{min}} \sim 2.1$ eV, it also results $m_{\nu_{min}} \lesssim 0.7$ eV ; in this case, $0.1 \lesssim |\langle m_\nu\rangle| \gtrsim 0.7$ eV

- Inverse hierarchy (IH): $m_3 \ll m_1 \lesssim m_2$ with $m_{1,2} \approx \sqrt{\Delta m^2_{32}} \sim 0.045$ eV ; it corresponds to $0.01 \lesssim |\langle m_\nu\rangle| \lesssim 0.1$ eV

- Normal hierarchy (NH): $m_1 \ll m_2 \ll m_3$, with $m_2 \approx \sqrt{\Delta m^2_{12}} \sim 0.009$ eV, $m_3 \approx \sqrt{\Delta m^2_{23}} \sim 0.045$ eV and $m_{\nu_{min}} = m_1$ ; typically it corresponds to $|\langle m_\nu\rangle| \lesssim 0.020$ eV.

These cases are summarized in Fig. 1.4 [3], which shows the plot of $\langle m_\nu\rangle$ as a function of the lightest neutrino mass, using the oscillation parameters in Fig. 1.1 with $\theta_{13} = 0$, and allowing

---

[2] Two methods are used for NME calculations, which are shell model and different types of calculations based on "Quasi Random Phase Approximation" (QRPA).

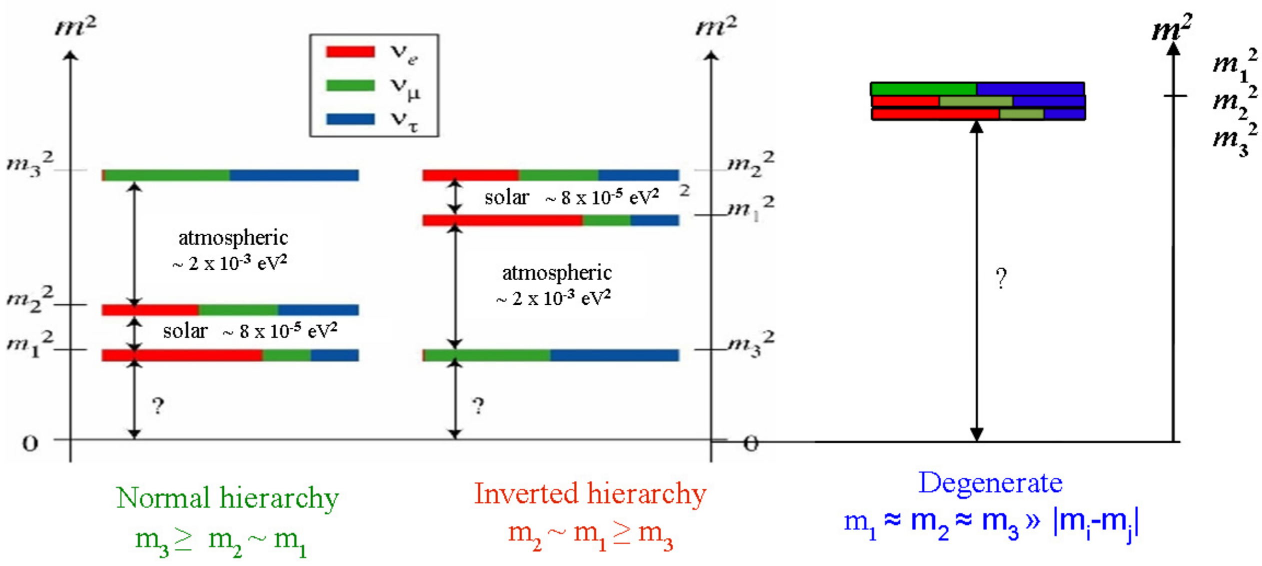

Figure 1.3: Neutrino mass and mixing for normal hierarchy, inverted hierarchy and degenerate neutrino case, as indicated by the current data [6].

for the maximum value of $\theta_{13}$ and one $\sigma$ variations of them. One can clearly see three regions (NH, IH and QD). Thus, determination of the $\langle m_\nu \rangle$ value would allow to distinguish between the different patterns and to determine a range of $m_{\nu_{min}}$.

#### 1.1.2.2 The other possibilities for particle exchange

There are other possibilities for the virtual particle exchange in neutrinoless double beta decay process:

**Right-handed $V + A$ weak current interaction mediated by the $W_R$ boson** (see Fig. 1.5). Inverse of the period can be written as:

$$\begin{aligned}(T^{0\nu}_{1/2})^{-1}(0^+ \to 0^+) &= C_1 \frac{|\langle m_\nu \rangle|^2}{m_e^2} + C_2 \,|\langle \lambda \rangle|\, \frac{|\langle m_\nu \rangle|}{m_e} \cos\psi_1 + C_3 \,|\langle \eta \rangle|\, \frac{|\langle m_\nu \rangle|}{m_e} \cos\psi_2 \\ &+ C_4 \,|\langle \lambda \rangle|^2 + C_5 \,|\langle \eta \rangle|^2 + C_6 \,|\langle \lambda \rangle|\, |\langle \eta \rangle| \,\cos(\psi_1 - \psi_2) \qquad (1.10)\end{aligned}$$

where $\lambda \sim \left(\frac{M_{WL}}{M_{WR}}\right)^2$ is the coupling constant between right-handed leptons and right-handed quarks. In the Eq. 1.10, $\eta$ is the coupling constant between right-handed leptons and left-handed quarks, depending on the mixing angle between $W_L$ and $W_R$; $\psi_1$ and $\psi_2$ are phases between $m_\nu$ and respectively $\lambda$ and $\eta$; $C_i$ are functions which contain nuclear matrix elements and phase space factors; finally $m_e$ is the electron mass.

**Right-handed weak current interaction between the fundamental states of parent nucleus and daughter nucleus**, which can not be distinguished from the exchange of a light neutrino except by the two-electron angular distribution. It is also possible to investigate $\beta\beta0\nu$

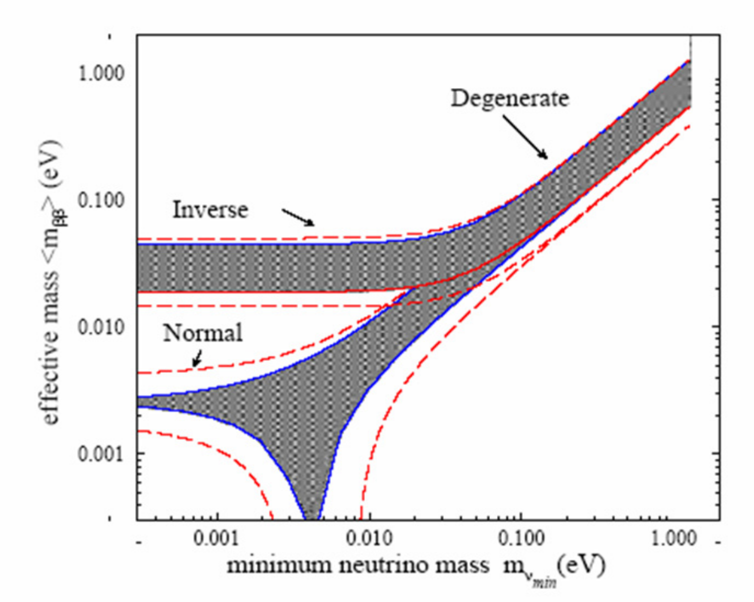

Figure 1.4: Effective neutrino mass from $\beta\beta0\nu$ decay measurements as a function of the lightest neutrino mass using the oscillation results, with indications on the different pattern mass. Depending on the $|\langle m_\nu\rangle|$ value, it should be possible to determine the neutrino mass scale and the right spectrum, corresponding to quasi-degenerate, inverse or normal hierarchies. The shaded region corresponds to the best values of oscillation parameters and $\theta_{13}=0$. The dashed lines indicate the expanded range corresponding to the $1\sigma$ errors of the oscillation parameters and the maximum allowed $\theta_{13}$. Note that the uppermost line is unchanged (within this scale) in this case.

transitions to the $2^+$ excited state, which involves a Majorana mass term through the $V+A$ interaction, with a right-handed current interaction at the second vertex.

Another mechanism which may contribute to the $\beta\beta0\nu$ process is the **emission of a Majoron** $J$ (see Fig. 1.6), the Goldstone boson associated with spontaneous symmetry breaking of lepton number (Majoron appears in theory after B-L global symmetry breaking). Depending on theoretical models one or several Majorons can be emitted during the double beta decay process. Thus, the search for the $\beta\beta J$ process involves a three (or more) body decay spectrum with the Majoron(s) avoiding detection, which imposes additional constraints on the design of a detector. In case of only one Majoron emission the inverse of the period can be written as

$$(T_{1/2}^{0\nu J})^{-1} = |\langle g_M\rangle|^2 \times |M_{0\nu J}|^2 \times G^{0\nu J} \tag{1.11}$$

where $G^{0\nu J}$ is the phase-space factor proportional in first approximation to the transition energy to the fifth power, $Q^5_{\beta\beta}$, and also function of $Z$; $M_{0\nu J}$ is the nuclear matrix element and $g_M$ is the coupling constant between neutrinos and Majoron.

Finally, the exchange can be mediated **through R-parity violation in supersymmetric models**. R-parity is associated with the $R_p=(-1)^{3B+L+2S}$ quantum number where $B$, $L$ and $S$ are respectively baryon, lepton and spin numbers. In case of lepton number $L$ violation, neutrinoless double beta decay $\beta\beta0\nu$ may occur by exchange of supersymmetric particles as gluinos or neutralinos (see Fig. 1.7). Double beta decay is sensitive to SUSY coupling constants ($\lambda'_{111}$, $\lambda'_{113}\lambda'_{131}$, ...).

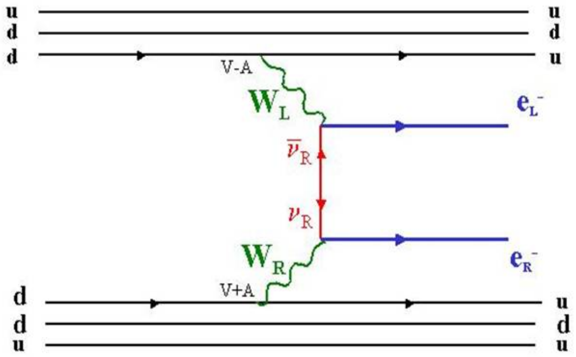

Figure 1.5 : Neutrinoless double beta decay process involving the exchange of right-handed $V+A$ weak current interaction mediated by the $W_R$ boson.

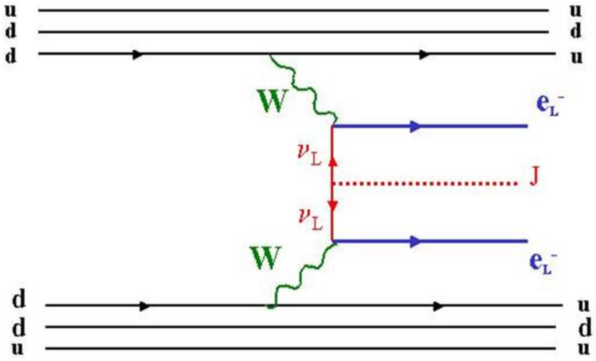

Figure 1.6 : Neutrinoless double beta decay process involving the exchange of Majoron particle $J$.

The objective of the NEMO 3 experiment is to investigate all these (hypothetical) decay modes to further understanding of the double beta decay. The NEMO 3 experiment aims to search for the effective Majorana neutrino mass down to a $|\langle m_\nu \rangle|$ level of a few 100 meV. If no such events are observed only a limit is reached on the $\beta\beta 0\nu$ half-life and an upper limit on $\langle m_\nu \rangle$ can be inferred from the relation given in Eq. 1.6.
Given the uncertainty in $|M_{0\nu}|$, a mass limit of 100 meV corresponds to a neutrinoless double beta decay with a half-life limit of the order of $10^{25}$ years for $^{100}$Mo. To improve the sensitivity of a double beta decay experiment it is preferable to study an isotope with a large $Q_{\beta\beta}$, not only to get a larger $G_{0\nu}$, but also to reduce the background in the search for a $\beta\beta 0\nu$ signal.
From the experimental point of view, for an experiment which observes $N_s$ signal events from a mass $M$ (in kg), during a time of exposure $t$ (in years), the period of the $\beta\beta 0\nu$ process (in years)

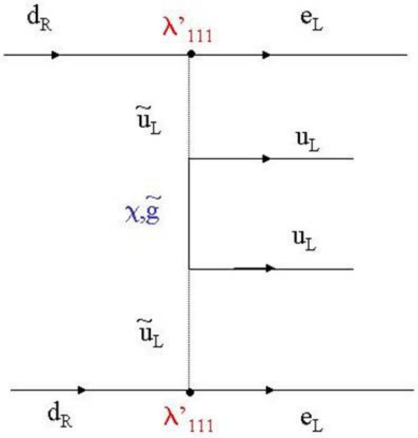

Figure 1.7: Neutrinoless double beta decay process involving the exchange of such supersymmetric particles as gluinos or neutralinos and being sensitive to $\lambda'_{111}$ coupling constant.

is given by the relation 1.12:

$$T_{1/2}^{0\nu} = \frac{\ln 2 \mathcal{N}}{A} \frac{M \, \varepsilon \, t}{N_s} \tag{1.12}$$

where $\varepsilon$ is the detection efficiency of the $\beta\beta 0\nu$ process, and $A$ is the atomic mass of the isotope and $\mathcal{N}$ is Avogadro number.
The sensitivity of the experiment can be calculated in case of observation of no signal events, that means if the number of observed events is equal to the number of expected background events. Thus it is possible to give a lower limit on the period of the $\beta\beta 0\nu$ process in years (see Eq. 1.13) assuming gaussian background:

$$T_{1/2}^{0\nu} \, (90\% \; C.L.) \; > \; \frac{\ln 2 \mathcal{N} \, \varepsilon}{1.64 \times A} \sqrt{\frac{M \times t}{R \times N_{bkg}}} \tag{1.13}$$

where $R$ is the detector energy resolution (FWHM) in keV and $N_{bkg}$ is the expected number of background events in counts.keV$^{-1}$.kg$^{-1}$.yr$^{-1}$.

In two-neutrino double beta decays ($\beta\beta 2\nu$), which are the second order weak interactions, nuclei decay by emitting two electrons accompanied by two undetected neutrinos (see Fig. 1.8).

$$(A, Z) \rightarrow (A, Z + 2) + 2e^- + 2\bar{\nu}_e$$

The $\beta\beta 2\nu$ process has already been observed for 10 isotopes: $^{48}$Ca, $^{76}$Ge, $^{82}$Se, $^{96}$Zr, $^{100}$Mo, $^{116}$Cd, $^{128}$Te, $^{130}$Te, $^{150}$Nd and $^{238}$U (see [7] for a review article). Fig. 1.9 shows as an example of the $\beta\beta 2\nu$ decay scheme for $^{100}$Mo nucleus.

The period of $\beta\beta 2\nu$ process, as shown in Eq. 1.14, is related to the phase-space factor $G^{2\nu}$ (see Table 1.1), which is also analytically calculated and, in first approximation, proportional to the transition energy to the eleventh power, $Q_{\beta\beta}^{11}$, and to the associated nuclear matrix element (NME) $|M_{2\nu}|$ of the relevant isotope for which calculations have also theoretical uncertainties.

$$(T_{1/2}^{2\nu})^{-1} = |M_{2\nu}|^2 \times G^{2\nu}(Z, Q_{\beta\beta}) \tag{1.14}$$

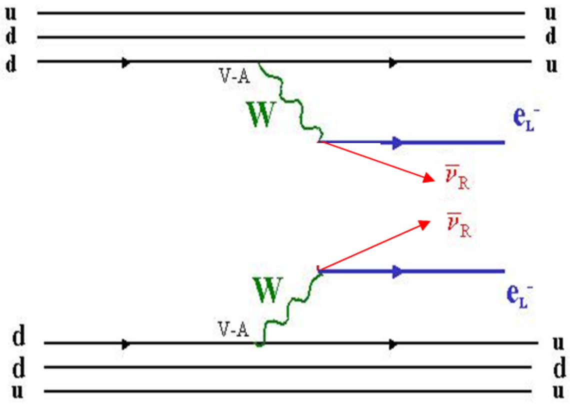

Figure 1.8: Two-neutrino double beta decay process $\beta\beta2\nu$.

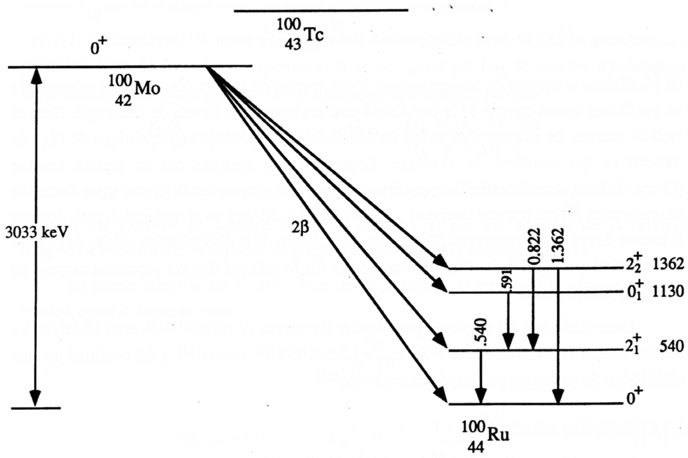

Figure 1.9: $^{100}$Mo → $^{100}$Ru double beta decay scheme.

Here the Fermi matrix element in NME definition is negligibly small because it does not connect states with different isospin. Although the isospin in nuclei is not conserved exactly, the admixtures of states with "wrong" isospin to the ground state are known to be very small. Thus in the following, $M_{2\nu}^{F}$ will be neglected when considering the $\beta\beta2\nu$ decay and $M_{2\nu} = M_{2\nu}^{GT}$ will be used. Measurements of $\beta\beta2\nu$ periods (greater than a few $10^{18}$ years) are very useful to obtain experimental values of $M_{2\nu}$, in order to find the best theoretical calculation techniques for two-neutrinos NME. It is also important because zero-neutrino NME calculations could maybe use these experimental two-neutrinos NME values as an input.

Experimental signature of the different $\beta\beta$ modes is the total energy of the two emitted electrons (see Fig. 1.10). $\beta\beta0\nu$ decay signal should produce a line spectrum at energy $Q_{\beta\beta}$ where as the $\beta\beta2\nu$ process (yellow in this figure) presents the continuous spectrum with energies between 0 and $Q_{\beta\beta}$. Processes with Majoron particles also present continuous spectrum but with different shapes than $\beta\beta2\nu$ decay one.

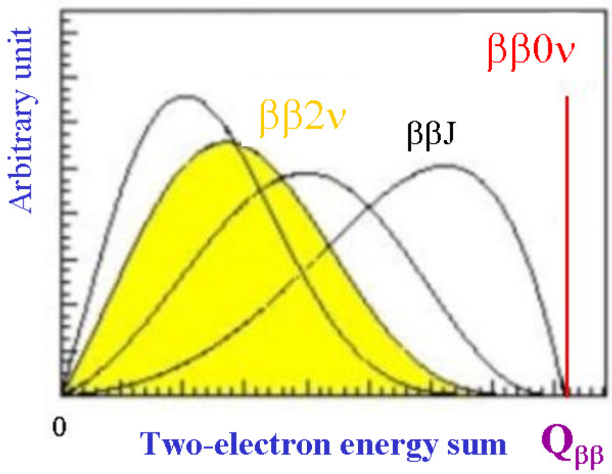

Figure 1.10 : Total energy sum of the two emitted electron divided by the energy transition $Q_{\beta\beta}$. For $\beta\beta0\nu$ decay in red line is the sum corresponding to a Dirac peak with $Q_{\beta\beta}$ energy; in the case of $\beta\beta2\nu$ decay process, there is a continuous spectrum. Black curves correspond to different hypothesis for Majoron emission.

Table 1.1 presents all double beta decay isotopes ($\beta^-\beta^-$ process), with their $Q_{\beta\beta}$ values [8] and their natural isotopic abundance $\eta$. Also are given in this table $\beta\beta0\nu$ and $\beta\beta2\nu$ phase space factors [9], which are called $G^{0\nu}$ and $G^{2\nu}$ as defined in Eq. 1.6 and Eq. 1.14 respectively.

Measurements of a half-life as long as $10^{25}$ years for $\beta\beta0\nu$ is a challenging proposition. It requires a solid understanding of natural and cosmogenic radioactive backgrounds in the materials from which the detector is made and backgrounds induced by the radioactivity from the walls and atmosphere in the underground laboratory. The NEMO (Neutrino Ettore Majorana Observatory) collaboration started a R&D program in 1988. Two prototypes, NEMO 1 [10] and NEMO 2 [11], were constructed and run to demonstrate the feasibility of the experimental technique. The development of NEMO 3 was begun more than ten years ago [12]. It reflects a more than a 10-fold improvement in the NEMO 2 sensitivity in order to measure double beta decay half-life limits of around $10^{25}$ yr for the $\beta\beta0\nu$ process, $10^{23}$ yr for the $\beta\beta J$ process, and $10^{22}$ yr for the $\beta\beta2\nu$ process.

NEMO 1 was a tracking detector consisting of 64 drift cells operating in Geiger mode. It has been used to study electron tracking down to 100 keV. NEMO 2 has been used to test the calorimeter part and to study backgrounds. It was a tracko-calo detector, with plastic scintillators coupled to low activity photomultiplier tubes (PMTs). Analysis of data and simulated events with electrons, $\gamma$-rays and delayed $\alpha$-particles have been used to measure internal contamination of the source foil in radio-impurities, to study radon deposit on $\beta\beta$ source foil and to measure external neutrons and $\gamma$-ray fluxes. Period and angular distributions of $\beta\beta2\nu$ processes were obtained for $^{100}$Mo [13], $^{116}$Cd [14], $^{82}$Se [15] and $^{96}$Zr [16]. The experience with the NEMO 2 technical choices were used to design and build the NEMO 3 detector.

## 1.2 General description of the NEMO 3 detector

The philosophy behind NEMO 3 is the direct detection of the two electrons from $\beta\beta$ decay by a tracking device and a calorimeter. The NEMO 3 detector, for which the general layout is shown in Fig. 1.11, is similar in function to the earlier prototype detector, NEMO 2, but has lower radioactivity and is able to accommodate up to 10 kg of double beta decay isotopes.

The NEMO 3 detector is now installed and running in the Fréjus Underground Laboratory (LSM[3]) in France. It is cylindrical in design and divided into 20 equal sectors, as shown in Fig. 1.12 and Fig. 1.13. The segmentation permits easy access to source foils of the different isotopes. The source foils are $30-60$ mg/cm$^2$ thick and 2.5 m in height and are fixed vertically with a radius of 1.55 m between two concentric cylindrical tracking volumes composed of 6180 open octagonal drift cells. The drift cells are 270 cm long, operating in Geiger mode at 7 mbar above atmospheric pressure, with a partial pressure of 40 mbar of ethyl alcohol in a gas mixture of helium, argon and water[4]. The cells run vertically and three-dimensional tracking is accomplished with the arrival time of the signals on the anode wires and the plasma propagation times to the ends of the drift cells.

The energy and time-of-flight of particles are measured by plastic scintillators surrounding the tracking volume. To further enhance the acceptance, the end-caps (the top and bottom of the detector) are also equipped with scintillators in the spaces between the drift cell layers. This calorimeter is made of 1940 large blocks of scintillators coupled to very low radioactivity 3" or 5" PMTs. The 10 cm thick blocks of scintillator yield a high photon detection efficiency. Fig. 1.14 shows a picture of one sector of the NEMO 3 detector.

A solenoid surrounding the detector produces a 25 Gauss magnetic field parallel to the foil axis, in order to identify the particle charge. Pairs ($e^+e^-$) are produced in the source foils in the 1 to 10 MeV region by high-energy $\gamma$-rays from neutron capture. The curvature measurements also permit an efficient rejection of crossing electron events.

Finally, an external shield, in the form of 20 cm of low radioactivity iron, covers the detector to reduce $\gamma$-rays and thermal neutrons. Outside of this iron there is a borated water shield to thermalize fast neutrons and capture thermal neutrons.

In the NEMO 3 detector, electrons, positrons, photons and $\alpha$-particles can be identified. Thus, the detector is able to detect multi-particle events in the low energy domain of natural radioactivity.

## 1.3 Sources of background

The most significant concern in this double beta decay experiment is the background. The calorimeter measures the energy of the two electrons emitted from a common vertex in the source foil. The energy region of interest for the $\beta\beta0\nu$ signal is around 3 MeV ($Q_{\beta\beta}(^{100}\text{Mo}) =$ 3.034 MeV and $Q_{\beta\beta}(^{82}\text{Se}) = 2.995$ MeV [8]). This energy region is shared by some energetic natural radioactivity, which can produce two electrons in the source which mimic $\beta\beta0\nu$ decays. The key to the success of the experiment is to be able to positively identify these background events with high efficiency.

---

[3] Laboratoire Souterrain de Modane

[4] Proportion of 1% of argon and 1500 ppm of water in the mixture was added in December 2002

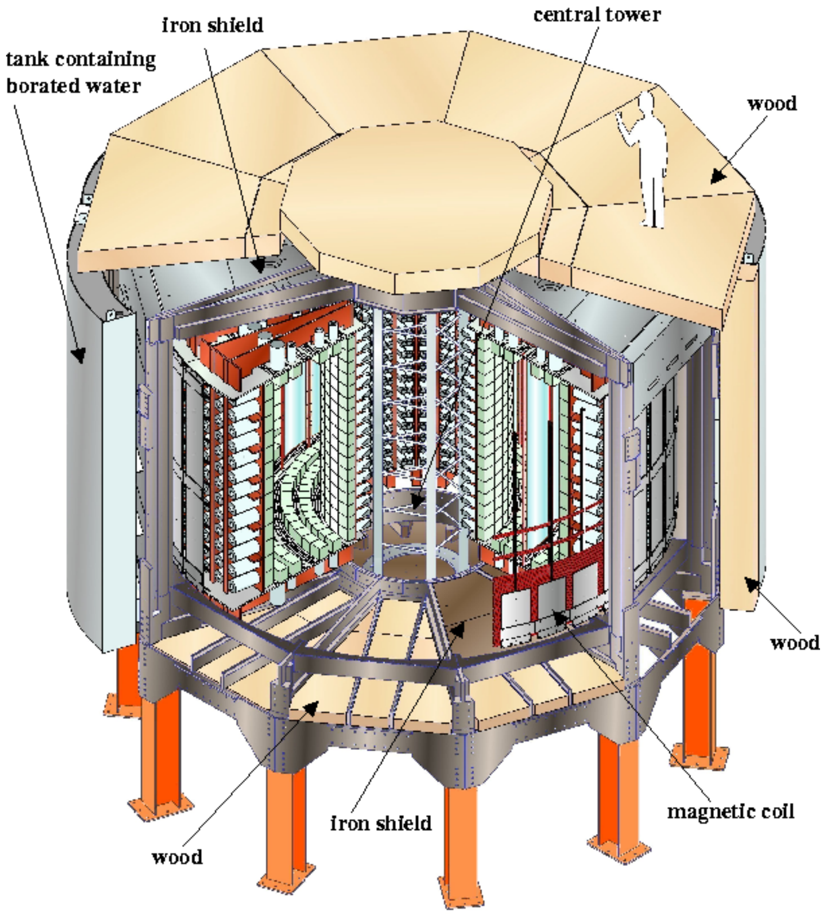

Figure 1.11 : An exploded view of the NEMO 3 detector. Note the coil, iron $\gamma$-ray shield, and the two different types of neutron shields, composed of water tanks and wood. The paraffin shield under the central tower is not shown on the picture.

#### 1.3.0.3 Natural decay chains and other radioactive isotopes

In general, natural radioactivity comes from very long half-life isotopes such as potassium (K), uranium (U) and thorium (Th) and needs to be carefully monitored. The natural decay chain for $^{235}$U (actinium series, see Fig. 1.15) is not taken into account, because even though the half-life is $7.04 \times 10^8$ yr its natural isotopic abundance is only 0.7%. Thus its decay chain daughter nuclei do not generate enough energy to mimic the $\beta\beta0\nu$ signal. The energy range of $^{40}$K decays is again not a background concern for the $\beta\beta0\nu$'s signal.

From the natural decay chains of uranium $^{238}$U and thorium $^{232}$Th series (see Fig. 1.15), only $^{214}$Bi and $^{208}$Tl are $\beta$-decay isotopes with $Q_\beta$ greater than 3 MeV (with respective $Q_\beta$ values of 3.270 and 4.992 MeV, and respective half-lives of 19.9 and 3.05 minutes [17]). $^{214}$Bi and $^{208}$Tl produce $\gamma$-rays and electrons that are energetic enough to simulate $\beta\beta0\nu$ events at 3 MeV (energies and intensities of most important $\gamma$-rays from different radioisotopes can be found in Table 1.2). The most energetic $\gamma$-rays are from $^{208}$Tl (2.615 MeV) for which the branching ratio is 35.6%.

In the Bi-Po process, $^{214}$Bi has $^{214}$Po as its daughter isotope which emits $\alpha$-particles with a 164 $\mu$s half-life ($Q_\alpha = 7833$ keV, with a branching ratio of 100%). Electronics designed to see delayed tracks for up to 710 $\mu$s, that means more than four periods of 164 $\mu$s, tag these $\alpha$-particles in order to measure and reject the $^{214}$Bi and $^{222}$Rn backgrounds (see Sections 2.5.2 and 4).

Radon ($^{222}$Rn, $T_{1/2} = 3.8235$ days) and thoron ($^{220}$Rn, $T_{1/2} = 55.6$ s), the decay products of $^{226}$Ra and $^{228}$Ra respectively, are $\alpha$-decay isotopes. Coming mainly from the rocks and present in varying concentrations in all buildings as well as in free air, the $^{222}$Rn and $^{220}$Rn are very diffusive rare gases which can enter the detector. Subsequent $\alpha$-decays of these gases give respectively $^{218}$Po ($E_\alpha(^{222}\text{Rn}) = 5489.5$ keV with $I_\alpha = 99.92\%$), which has $^{214}$Bi as a daughter, with a half-life of 30 minutes, and $^{216}$Po ($E_\alpha(^{220}\text{Rn}) = 6288.1$ keV with $I_\alpha = 99.87\%$) which has $^{208}$Tl as a daughter. Both can contaminate the interior of the detector, as explained in Section 4.

### 1.3.1 External and internal backgrounds

When describing the background, it is convenient to distinguish between the "internal" and "external" origins. The internal backgrounds come from radioactive contaminants inside the $\beta\beta$ source foil, while external backgrounds come from radioactive contaminants outside the $\beta\beta$ source foils.

The internal background for the $\beta\beta0\nu$ signal in the 3 MeV region has two origins. The first is the tail of the $\beta\beta2\nu$ decay distribution of the source, which cannot be separated from the $\beta\beta0\nu$ signal and the level of overlap depends on the energy resolution of the detector. Thus, this ultimately defines the half-life limits to which $\beta\beta0\nu$ can be searched for. The second background comes from the $\beta$-decays of $^{214}$Bi and $^{208}$Tl, which are present in the source at some level. They can mimic $\beta\beta$ events by three mechanisms. These are $\beta$-decay accompanied by an electron conversion process, Möller scattering of $\beta$-decay electrons in the source foil and $\beta$-decay emission to an excited state followed by a Compton scattered $\gamma$-ray. The last mechanism can be detected as two electron events if the $\gamma$-ray is not detected (see Fig. 1.18). Thus, the experiment requires ultra-pure source foils. The maximum levels of impurities in the source have been calculated so as to produce fewer events than the tail of the $\beta\beta2\nu$ decay gives in the region of interest for $\beta\beta0\nu$.

The external background is defined as events produced by $\gamma$-ray sources located outside the source foils and interacting with them. The interaction of $\gamma$-rays in the foils can lead to two electron-like events by $e^+e^-$ pair creation, double Compton scattering or Compton followed by Möller scattering (see Fig. 1.19). One of the main sources of this external radioactivity comes from the PMTs, but there are other sources too, such as cosmic rays, radon and neutrons. To decrease the background, the NEMO 3 detector was placed at a depth of 4800 m water equivalent, where cosmic ray fluxes have been found to be negligible. In the LSM, the flux of residual cosmic muons is $5\times10^{-5}$ m$^{-2}\times$s$^{-1}$ and the flux of fast, epithermal and thermal neutrons is few $10^{-6}$ neutrons.cm$^{-2}\times$s$^{-1}$ (for neutrons with energy greater than 1 MeV, the measured flux is $1.6\times10^{-6}$ cm$^{-2}\times$s$^{-1}$). Two shields and a magnetic field suppress the backgrounds from $\gamma$-rays and neutrons. The vigorous air ventilation system in the laboratory provides radon levels of $\sim 15-20$ Bq/m$^3$. All the materials used in the detector have been selected for their radiopurity properties and in particular, a substantial effort has been made to reduce the contamination of the PMTs with $^{40}$K, $^{214}$Bi and $^{208}$Tl (see Section 2.3.3 and Section 2.9).

Consequently, in the construction of the NEMO 3 experiment every attempt was made to minimize internal and external backgrounds by purification of the enriched isotopes and by carefully selecting all the detector materials, as described in Section 2.9. As it was shown with the NEMO 2 prototype, the NEMO 3 detector is also able to characterize and measure its own background.

| Transition | $Q_{\beta\beta}$ (keV) | $\eta$ (%) | $G^{2\nu}$ (yr$^{-1}$) | $G^{0\nu}$ (yr$^{-1}$) |
|---|---|---|---|---|
| $^{46}Ca \rightarrow ^{46} Ti$ | $987 \pm 4$ | 0.0035 | $1.148\ 10^{-22}$ | $1.397\ 10^{-27}$ |
| $^{48}Ca \rightarrow ^{48} Ti$ | $4271 \pm 4$ | 0.187 | $3.968\ 10^{-17}$ | $2.439\ 10^{-25}$ |
| $^{70}Zn \rightarrow ^{70} Ge$ | $1001 \pm 3$ | 0.62 | $3.155\ 10^{-22}$ | $2.342\ 10^{-27}$ |
| $^{76}Ge \rightarrow ^{76} Se$ | $2039.6 \pm 0.9$ | 7.8 | $1.305\ 10^{-19}$ | $2.445\ 10^{-26}$ |
| $^{80}Se \rightarrow ^{80} Kr$ | $130 \pm 9$ | 49.8 | $1.220\ 10^{-28}$ | $4.274\ 10^{-29}$ |
| $^{82}Se \rightarrow ^{82} Kr$ | $2995 \pm 6$ | 9.2 | $4.348\ 10^{-18}$ | $1.079\ 10^{-25}$ |
| $^{86}Kr \rightarrow ^{86} Sr$ | $1256 \pm 5$ | 17.3 | $3.333\ 10^{-21}$ | $6.369\ 10^{-27}$ |
| $^{94}Zr \rightarrow ^{94} Mo$ | $1145.3 \pm 2.5$ | 17.4 | $2.304\ 10^{-21}$ | $6.369\ 10^{-27}$ |
| $^{96}Zr \rightarrow ^{96} Mo$ | $3350 \pm 3$ | 2.8 | $1.927\ 10^{-17}$ | $2.242\ 10^{-25}$ |
| $^{98}Mo \rightarrow ^{98} Ru$ | $112 \pm 7$ | 24.1 | $9.709\ 10^{-29}$ | $6.711\ 10^{-29}$ |
| $^{100}Mo \rightarrow ^{100} Ru$ | $3034 \pm 6$ | 9.6 | $9.434\ 10^{-18}$ | $1.754\ 10^{-25}$ |
| $^{104}Ru \rightarrow ^{104} Pd$ | $1299 \pm 4$ | 18.7 | $9.174\ 10^{-21}$ | $1.202\ 10^{-26}$ |
| $^{110}Pd \rightarrow ^{110} Cd$ | $2013 \pm 19$ | 11.8 | $3.984\ 10^{-19}$ | $5.376\ 10^{-26}$ |
| $^{114}Cd \rightarrow ^{114} Sn$ | $534 \pm 4$ | 28.7 | $1.443\ 10^{-23}$ | $1.639\ 10^{-27}$ |
| $^{116}Cd \rightarrow ^{116} Sn$ | $2802 \pm 4$ | 7.5 | $8.000\ 10^{-18}$ | $1.894\ 10^{-25}$ |
| $^{122}Sn \rightarrow ^{122} Te$ | $364 \pm 4$ | 4.56 | $1.047\ 10^{-24}$ | $8.621\ 10^{-28}$ |
| $^{124}Sn \rightarrow ^{124} Te$ | $2288.1 \pm 1.6$ | 5.64 | $1.686\ 10^{-18}$ | $1.055\ 10^{-25}$ |
| $^{128}Te \rightarrow ^{128} Xe$ | $868 \pm 4$ | 31.7 | $8.475\ 10^{-22}$ | $6.993\ 10^{-27}$ |
| $^{130}Te \rightarrow ^{130} Xe$ | $2528.8 \pm 4$ | 33.8 | $4.808\ 10^{-18}$ | $1.698\ 10^{-25}$ |
| $^{134}Xe \rightarrow ^{134} Ba$ | $847 \pm 10$ | 10.4 | $8.621\ 10^{-22}$ | $7.692\ 10^{-27}$ |
| $^{136}Xe \rightarrow ^{136} Ba$ | $2479 \pm 8$ | 8.9 | $4.831\ 10^{-18}$ | $1.812\ 10^{-25}$ |
| $^{142}Ce \rightarrow ^{142} Nd$ | $1417.6 \pm 2.5$ | 11.1 | $7.246\ 10^{-20}$ | $1.812\ 10^{-26}$ |
| $^{146}Nd \rightarrow ^{146} Sm$ | $56 \pm 5$ | 17.2 | $4.854\ 10^{-30}$ | $1.418\ 10^{-28}$ |
| $^{148}Nd \rightarrow ^{148} Sm$ | $1928.3 \pm 1.9$ | 5.7 | $1.070\ 10^{-18}$ | $1.276\ 10^{-25}$ |
| $^{150}Nd \rightarrow ^{150} Sm$ | $3367.1 \pm 2.2$ | 5.6 | $1.189\ 10^{-16}$ | $8.000\ 10^{-25}$ |
| $^{154}Sm \rightarrow ^{104} Gd$ | $1251.9 \pm 1.5$ | 22.6 | $4.098\ 10^{-20}$ | $4.202\ 10^{-26}$ |
| $^{160}Gd \rightarrow ^{160} Dy$ | $1729.5 \pm 1.4$ | 21.8 | $6.623\ 10^{-19}$ | $1.252\ 10^{-25}$ |
| $^{170}Gr \rightarrow ^{170} Yd$ | $653.9 \pm 1.6$ | 14.9 | $5.495\ 10^{-22}$ | $1.445\ 10^{-26}$ |
| $^{176}Yb \rightarrow ^{176} Hf$ | $1078.8 \pm 2.7$ | 12.6 | $3.067\ 10^{-20}$ | $5.714\ 10^{-26}$ |
| $^{186}W \rightarrow ^{186} Os$ | $490.3 \pm 2.2$ | 28.6 | $1.302\ 10^{-22}$ | $1.439\ 10^{-26}$ |
| $^{192}Os \rightarrow ^{192} Pj$ | $417 \pm 4$ | 41.0 | $5.051\ 10^{-23}$ | $1.299\ 10^{-26}$ |
| $^{198}Pt \rightarrow ^{198} Hg$ | $1048 \pm 4$ | 7.2 | $6.135\ 10^{-20}$ | $1.144\ 10^{-25}$ |
| $^{204}Hg \rightarrow ^{204} Pb$ | $416.5 \pm 1.9$ | 6.9 | $8.130\ 10^{-23}$ | $1.976\ 10^{-26}$ |
| $^{232}Th \rightarrow ^{232} U$ | $858 \pm 6$ | 100 | $5.952\ 10^{-20}$ | $2.519\ 10^{-25}$ |
| $^{238}U \rightarrow ^{238} Pu$ | $1145.8 \pm 1.7$ | 99.275 | $6.803\ 10^{-19}$ | $5.952\ 10^{-25}$ |

Table 1.1: Table of double beta decay isotopes, with $Q_{\beta\beta}$ values, natural isotopic abundance $\eta$ and phase space factors for $\beta\beta 2\nu$ ($G^{2\nu}$) and $\beta\beta 0\nu$ ($G^{0\nu}$) process respectively.

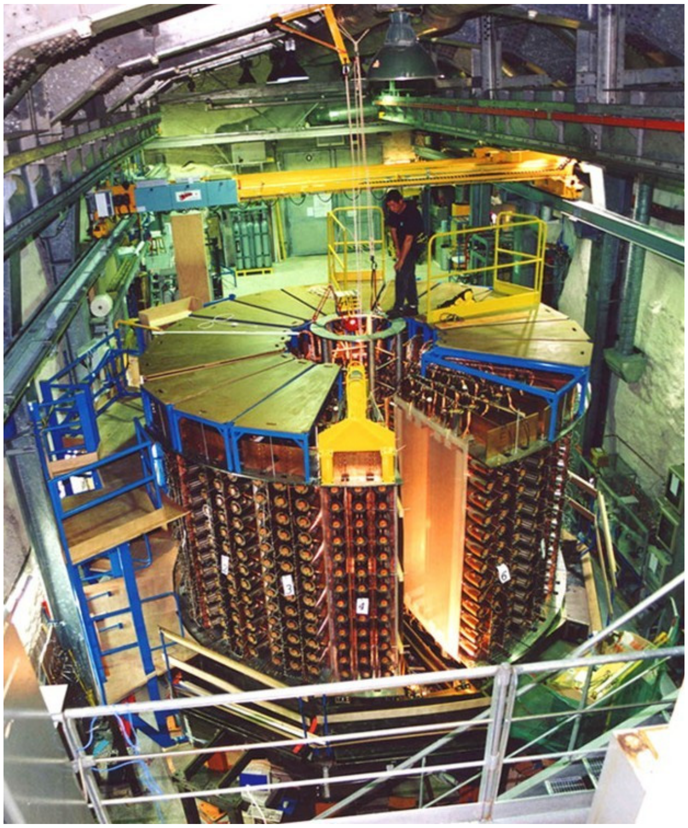

Figure 1.12: View of the NEMO 3 detector in the LSM before the installation of the last sector.

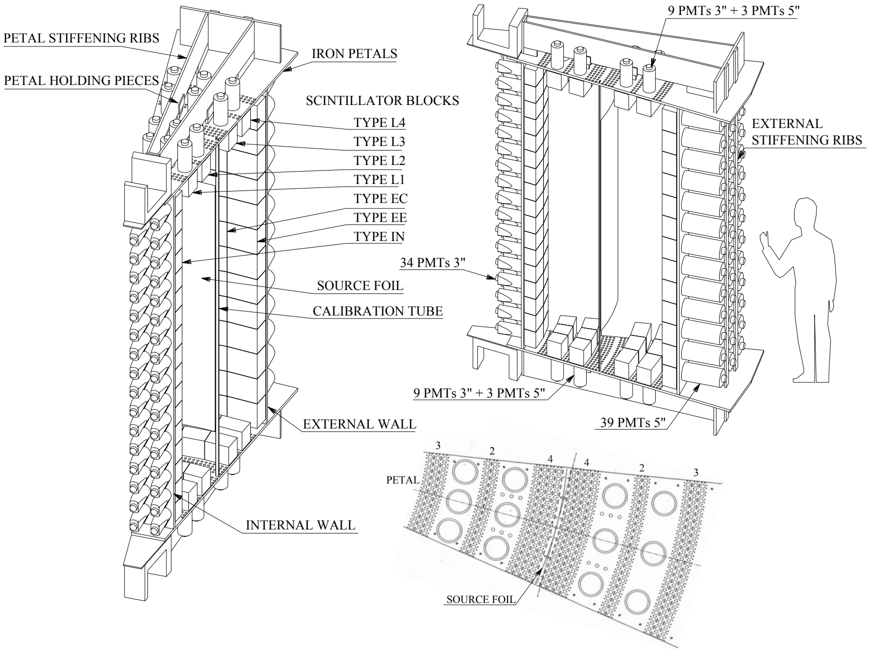

Figure 1.13: One sector of NEMO 3 with details on the source foil, scintillator blocks and photomultipliers. The Geiger cells are located between the internal and external walls. L4, L3,... IN identify different shapes of scintillator blocks. A petal (end-cap) is also shown with the "4-2-3" layer configuration for the Geiger cells.

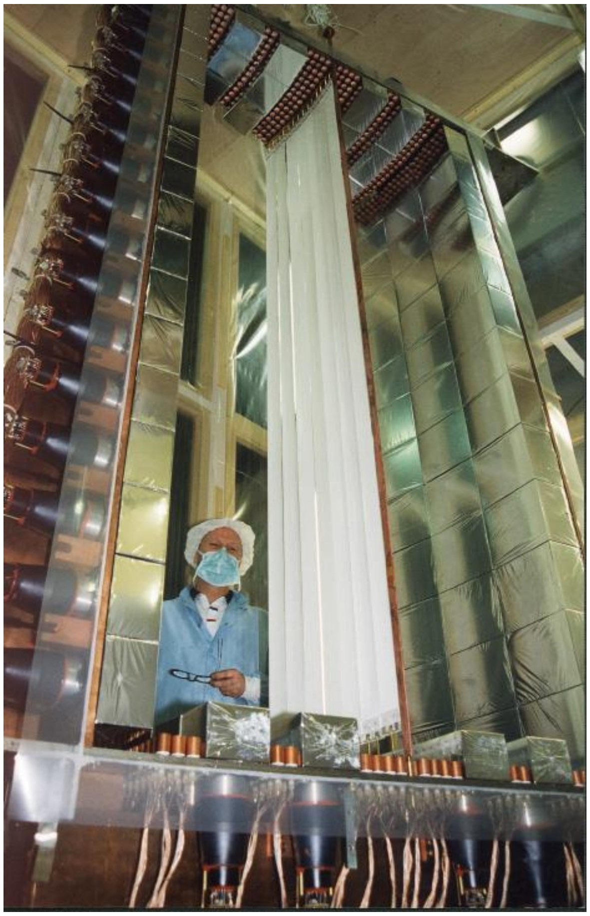

Figure 1.14 : View of the third sector in the source mounting room just after the installation of the tellurium source.

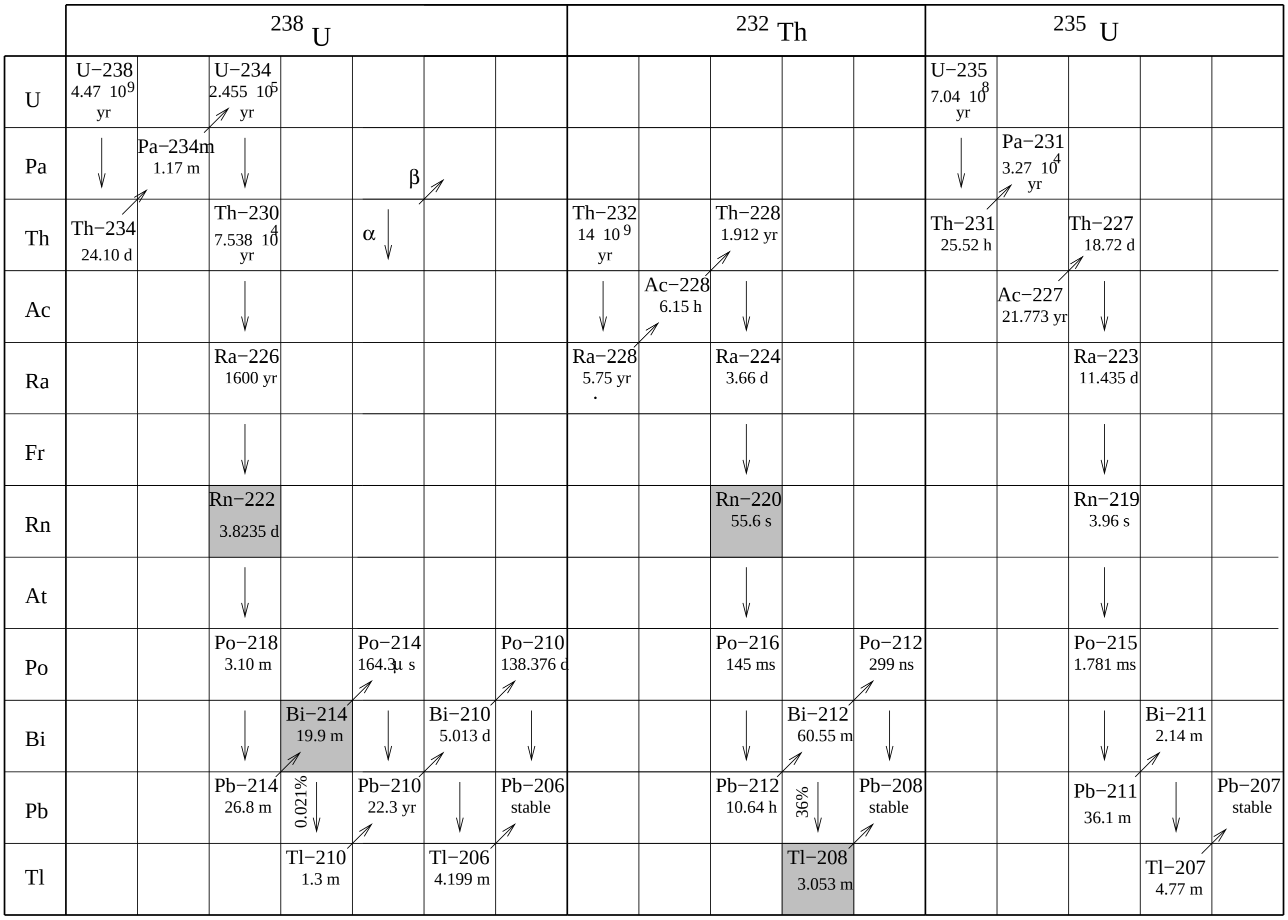

Figure 1.15: The three main decay chains of natural radioactivity (uranium, thorium and actinium series). The isotopes in gray produce the main background contribution to the NEMO 3 data ($^{222}$Rn (radon), $^{220}$Rn (thoron), $^{214}$Bi and $^{208}$Tl) [17].

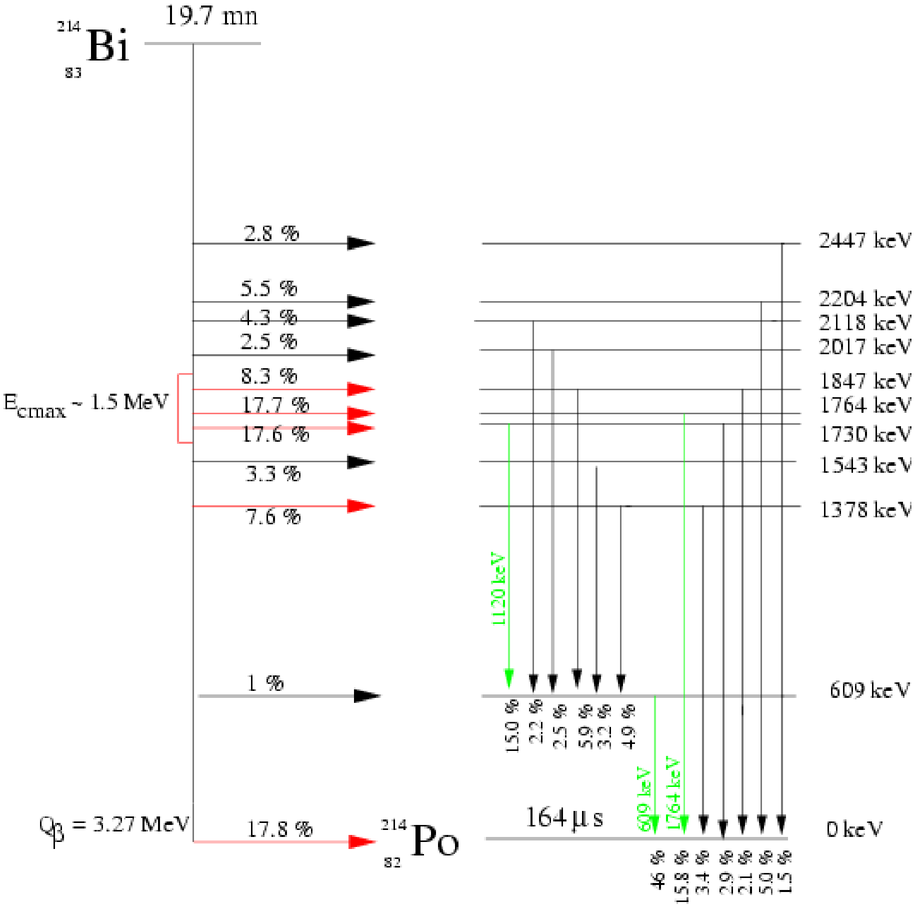

Figure 1.16 : Decay scheme for $^{214}$Bi [17].

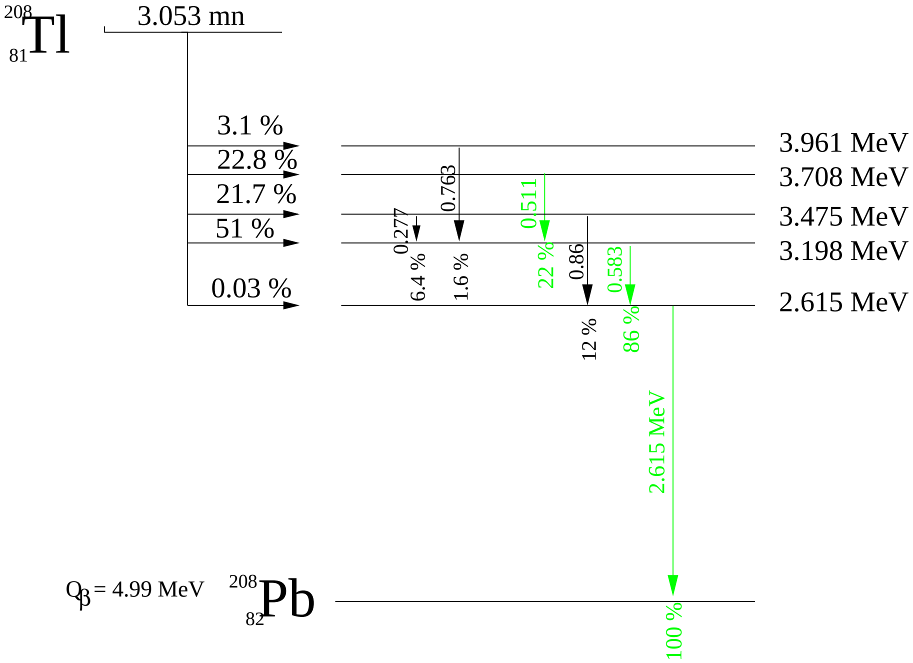

Figure 1.17 : Decay scheme for $^{208}$Tl [17].

| Nuclei | Energy in keV | $\gamma$ intensity (in %) | Nuclei | Energy in keV | $\gamma$ intensity (in %) | Nuclei | Energy in keV | $\gamma$ intensity (in %) |
|---|---|---|---|---|---|---|---|---|
| $^{238}$U | | | $^{232}$Th | | | Other radioisotopes | | |
| $^{234}$Th | 63.3 | 4.8 | $^{228}$Ac | 338.3 | 11.3 | $^{235}$U | 143.8 | 11.0 |
| | 92.6 | 5.6 | | 911.2 | 25.8 | | 163.4 | 5.1 |
| $^{234m}$Pa | 1001.0 | 0.84 | | 964.8 | 5.0 | | 185.7 | 57.2 |
| $^{226}$Ra | 186.2 | 3.6 | | 969.0 | 15.8 | | 205.3 | 5.0 |
| $^{214}$Pb | 242.0 | 7.4 | $^{212}$Pb | 238.6 | 43.3 | $^{40}$K | 1460.8 | 11.0 |
| | 295.2 | 19.3 | $^{212}$Bi | 727.3 | 6.6 | $^{60}$Co | 1173.2 | 99.97 |
| | 351.9 | 37.6 | $^{208}$**Tl** | 583.191 | 84.5 | | 1332.5 | 99.99 |
| $^{214}$**Bi** | 609.3 | 46.1 | | **2614.533** | **99** | $^{137}$Cs | 661.7 | 85.1 |
| | 1120.3 | 15.1 | | | | $^{152}$Eu | 121.8 | 28.6 |
| | 1764.5 | 15.4 | | | | | 344.3 | 26.5 |
| | 2204.2 | 5.1 | | | | | 867.4 | 4.245 |
| | | | | | | | 964.1 | 14.6 |
| | | | | | | $^{207}$Bi | 569.7 | 97.7 |
| | | | | | | | 1063.7 | 74.5 |

Table 1.2: Main $\gamma$-rays used for spectroscopy analysis [18]. Most intensive and energetic rays come from $^{214}$Bi and $^{208}$Tl, with the most energetic $\gamma$-ray for the thallium emitter, at 2615 keV, and nearly 100% in intensity compared to other rays.

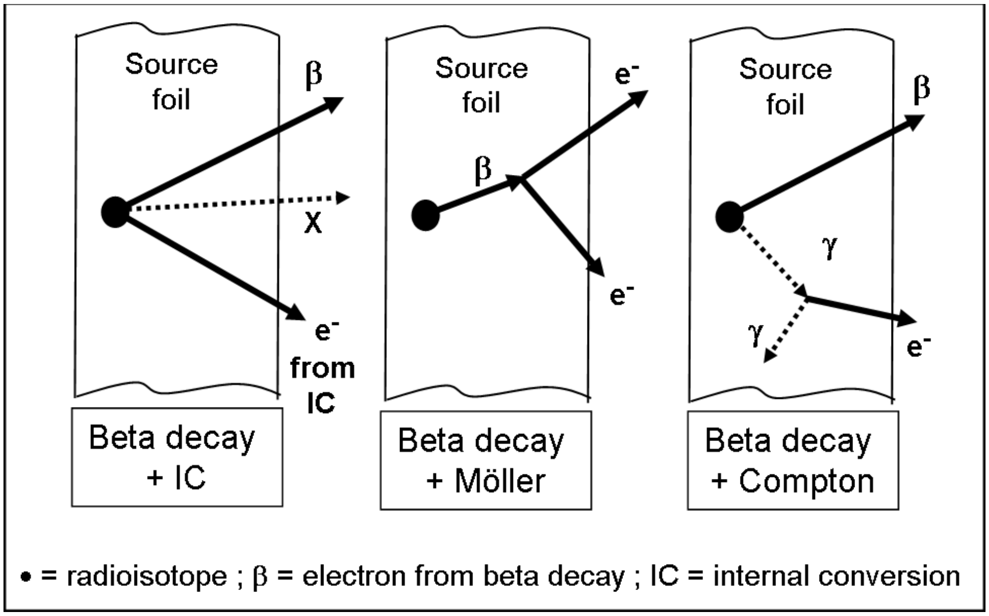

Figure 1.18: Internal background production.

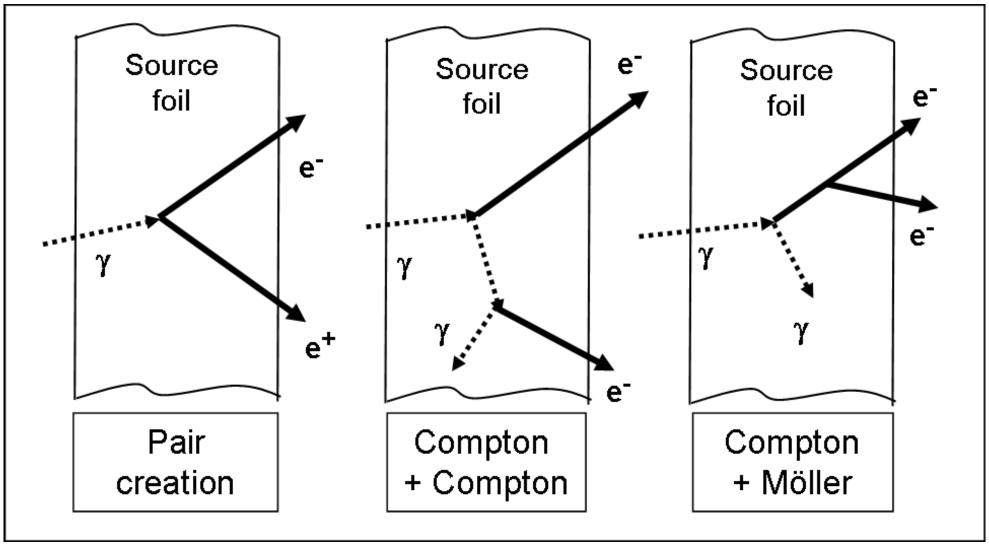

Figure 1.19: External background production.

# Chapter 2

# Technical design of the NEMO 3 detector

In this section, the sources and the different parts of the NEMO 3 detector are described with explanations of the choices made for the realization of the detector, for both materials and geometry. The main findings from this Section are already published in Ref. [19].

## 2.1 Principle of the NEMO 3 realization

As it was explained in the introduction, the NEMO 3 detector is divided into 20 identical sectors, except for the source foil, which is distinct and introduced just before the installation of the sector in a specified position. The principle of the sector construction is described in this section. As it will be shown all the pieces of the detector have been realized in the different laboratories of the NEMO collaboration. Then each sector was assembled at LAL Orsay and the final installation in the LSM (see Section 2.8).

### 2.1.1 Assembly of the sectors

The schematic view of one of the NEMO 3 sectors is shown in Fig. 1.13, with the two petals in iron and the two walls in copper, which compose the frame of the sector. The pieces in iron and copper were made in JINR Dubna (see Fig. 2.1) and then transported to LAL for the assembly of each sector by the NEMO group of the SECAP[1] in the "Hall IN2P3".

In LAL, the first step was the computerized machining at the SRM[2] of the 2,000 holes needed for passing the Geiger wires in each petal (see Fig. 2.2). Then all the pieces were assembled, marked and finally dismounted for a cleaning operation. It consisted of putting the pieces in a ultrasonic wash bath, which allowed to remove the grease deposits and machining debris (this operation was realized with LURE[3] materials). After each step of the construction and before the final assembly of each sector, a measurement of the pieces and machinings was made to check the tolerances.

The petals were then sent to IReS (Strasbourg) and the walls sent to CENBG (Bordeaux) for the installation of the light guides and scintillator blocks, which form the calorimeter part of the

---

[1] Service d'Etudes et de Construction d'Appareillages pour la Physique

[2] Service des Réalisations Mécaniques

[3] Laboratoire pour l'Utilisation du Rayonnement Electromagnétique

Figure 2.1 : Test of the assembly as a sector of the first walls and petals realized at JINR Dubna.

NEMO 3 sectors (see Section 2.3). Note that light guides were manufactured at the SRM and the scintillator blocks were manufactured in JINR for the walls and in Ukrainia for the petals.

After tests, the petals and walls with blocks were sent back to LAL, transported to the "Hall IN2P3" (see Fig. 2.3) and screwed and glued together to form the two petals and walls of a sector. where the sector was definitively assemblied (screwed and glued). An assembly support was build to ensure the right registration of parts (see Fig. 2.4). After assembly, a glue was used to seal connections and finally the rail for the source foil installation was mounted. Next the sector was transported in a clean room for wiring as well as more tests and gluing as described in Section 2.4. Then the sector was transported again to the "Hall IN2P3" for cabling of the tracking detector. During these operations and before its transportation to LSM, the sector was filled with gaseous nitrogen to ensure a clean environment.

Finally the sector was transported to LSM (see Section 2.8) in a dedicated frame to the blows of quick vibrations in the truck, which was bought by the LAL for the numerous trips between the laboratory and the LSM. The first sector, used as a prototype, was assemblied at the beginning of 1997 and allowed to validate the room for the assembly and all the operations. In LAL, the assembly of the 20 sectors was finished at the end of 1999.

A summary of "who did what" is presented in Fig. 2.5.

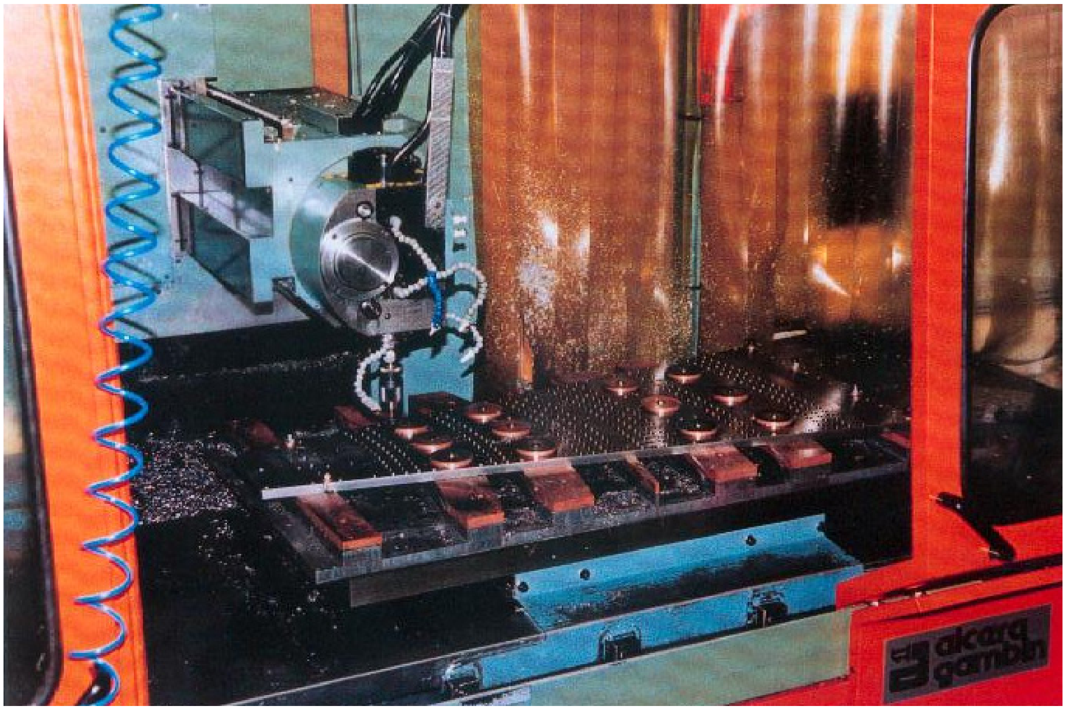

Figure 2.2: View of the computerised machining of the 2,000 holes for petal wiring, in the SRM (LAL).

Figure 2.3: Picture of portion of the "Hall IN2P3" dedicated to the NEMO 3 sector assembly in LAL.

Figure 2.4 : Zoom on the assembly support in the “Hall IN2P3”.

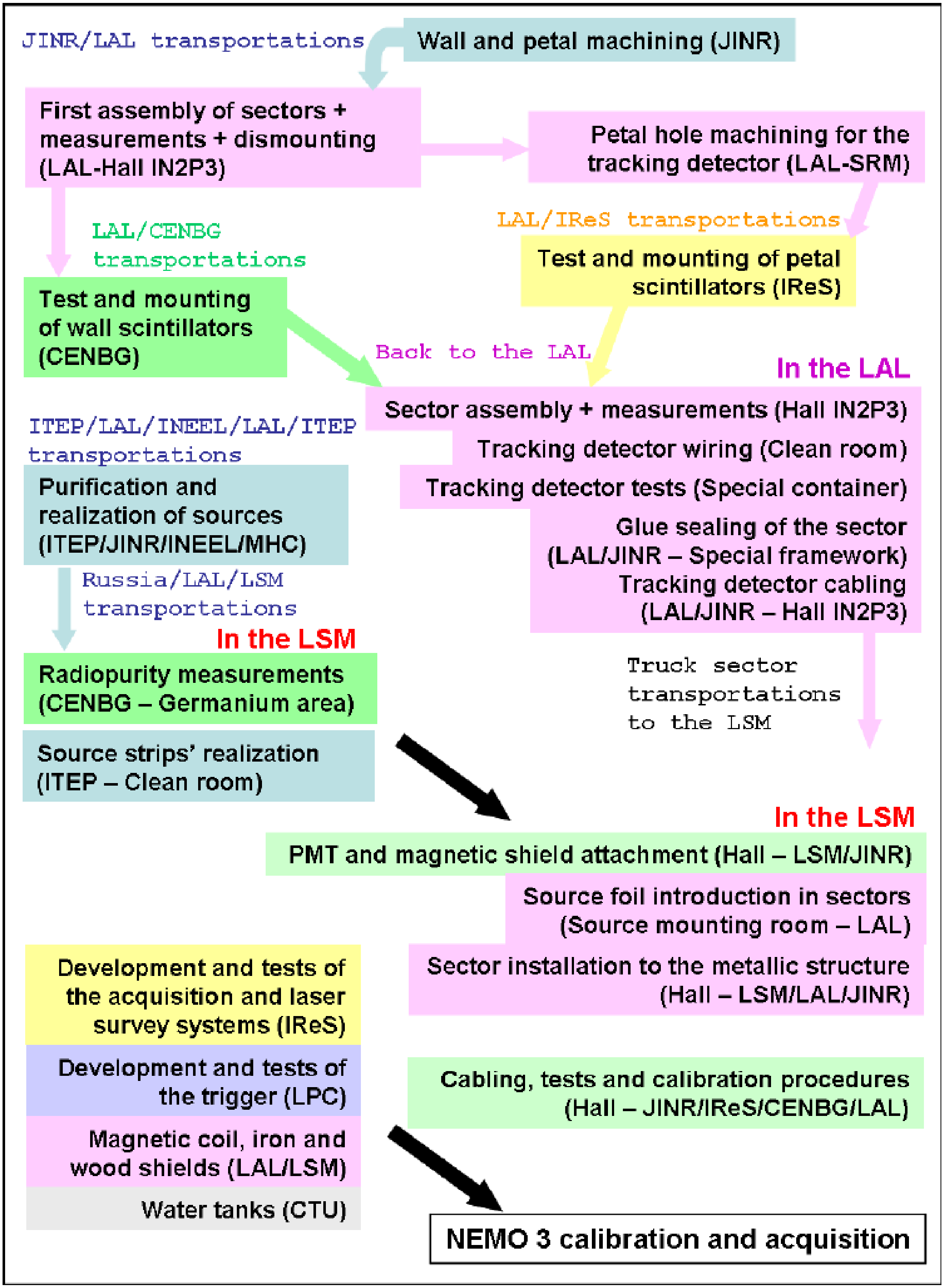

Figure 2.5 : Tasks of completing one sector in the different laboratories of the NEMO collaboration.

## 2.2 The NEMO 3 sources

### 2.2.1 Introduction

The primary design feature of the NEMO 3 experiment was to have the detector and the source of the double beta decay independent, unlike the case of the $^{76}$Ge experiments. This permits one to study several double beta decay isotopes. A critical point is to be able to confirm an excess of $\beta\beta0\nu$ events from one isotope with another isotope. It also reduces the dependence of the interpretation of the result on the nuclear matrix elements. Furthermore, a more detailed study of the backgrounds and systematic effects is possible.

The choice of nuclei was affected by several factors. These included the transition energy ($Q_{\beta\beta}$), the phase space factors ($G^{0\nu}$ and $G^{2\nu}$) and nuclear matrix elements ($M_{0\nu}$ and $M_{2\nu}$) of the transitions for $\beta\beta0\nu$ and $\beta\beta2\nu$ decays, the background in the energy region surrounding the $Q_{\beta\beta}$ value, the possibility of reducing the radioactivity of the isotope to acceptable levels, and finally the natural isotopic abundance. Basing the choice singularly on $M_{0\nu}$ is not advisable because the calculations are too uncertain. A good criterion for isotope selection is the $Q_{\beta\beta}$ value with respect to backgrounds. As explained in Section 1.3, the 2.615 MeV $\gamma$-ray produced in the decay of $^{208}$Tl is consistently a troublesome source of background and it is important to select $\beta\beta$ candidates with a $Q_{\beta\beta}$ value above this transition or to ensure an ultra high radiopurity level of the $\beta\beta$ candidates for this contaminant. The natural isotopic abundance is another useful criterion because in general the higher the abundance the easier the enrichment process. Typically only isotopic abundances greater than 2% were considered. As shown in Table 1.1, only five nuclei satisfy these two criteria: $^{116}$Cd, $^{82}$Se, $^{100}$Mo, $^{96}$Zr and $^{150}$Nd. Given this list and the availability of $^{100}$Mo, much effort has been focused by the NEMO collaboration on this isotope (it had already been studied by the NEMO 2 prototype [13]). However the focus is not exclusively on $^{100}$Mo, in view of the fact that the detector can house several different sources.

There have been improvements in the isotopic enrichment processing in Russia, where all the double beta decay sources were produced. Thus the $^{48}$Ca isotope has been added to the list of interesting sources. Note that $^{48}$Ca fails to meet the abundance selection criterion but has an impressive $Q_{\beta\beta}$ value ($Q_{\beta\beta}$ = 4272.0 keV). Finally, $^{130}$Te has been added for $\beta\beta2\nu$ studies. Historically, $^{130}$Te has had two different geochemical half-life measurements [20, 21], which are inconsistent with each other and a reliable one is sought here. Double beta decay isotopes used in NEMO 3 are summarized in Table 2.1.

| Transition | $Q_{\beta\beta}$ (keV) | Abundance(%) |
|---|---|---|
| $^{130}$Te → $^{136}$Xe | $2528.8 \pm 2.1$ | 33.8 |
| $^{116}$Cd → $^{116}$Sn | $2804.7 \pm 4.2$ | 7.5 |
| $^{82}$Se → $^{82}$Kr | $2995.2 \pm 3.3$ | 9.2 |
| $^{100}$Mo → $^{100}$Ru | $3034.8 \pm 6.3$ | 9.6 |
| $^{96}$Zr → $^{96}$Mo | $3350.0 \pm 3.5$ | 2.8 |
| $^{150}$Nd → $^{150}$Sm | $3367.1 \pm 4.9$ | 5.6 |
| $^{48}$Ca → $^{48}$Ti | $4272.0 \pm 4.1$ | 0.187 |

Table 2.1 : Double beta decay isotopes used in the NEMO 3 detector. Except for $^{130}$Te, all $Q_{\beta\beta}$ values are greater than the $^{208}$Tl 2.615 MeV $\gamma$-ray which is the most energetic $\gamma$-ray of natural radioactivity and producing background events.

A description of the current configuration of the 20 sectors of NEMO 3 is given in Table 2.1. To study the $\beta\beta0\nu$ processes 6914 g of $^{100}$Mo and 932 g of $^{82}$Se are housed in twelve and two and a third sectors, respectively. The objective here is to reach a sensitivity for the effective neutrino mass of the order of 0.1 eV. Several other $\beta\beta$ decay isotopes in smaller quantities have been introduced to study the $\beta\beta2\nu$ processes which will complement the very detailed studies provided by the $^{100}$Mo and $^{82}$Se on angular distributions and single electron energy spectra. This second tier of isotope samples consists of 454 g of $^{130}$Te (2 sectors), 405 g of $^{116}$Cd (1 sector), 37 g of $^{150}$Nd, 9 g of $^{96}$Zr and 7 g of $^{48}$Ca. Finally, source foils with high levels of radiopurity, so they are effectively void of internal backgrounds, will measure the external background in the experiment. This not only accounts for the presence of 621 g of copper but also a very pure oxide of natural tellurium, which permits one to study the background near 3 MeV. This natural tellurium also allows an investigation of the $\beta\beta2\nu$ because the natural abundance of isotope 130 for tellurium is 33.8%, which gives 166 g of $^{130}$Te.

For each sector, a source frame was constructed on which seven strips were placed. The mean length of the strips is 2480 mm with a width of 63 mm if they are on the edges of the frame or 65 mm for the five strips in the middle of the frame. All the strips were attached to the frames in a clean room at the LSM where they were then introduced into the sectors. The so-called "NEMO 3 camembert" depicts the distribution of the sources in the 20 sectors, Fig. 2.6.

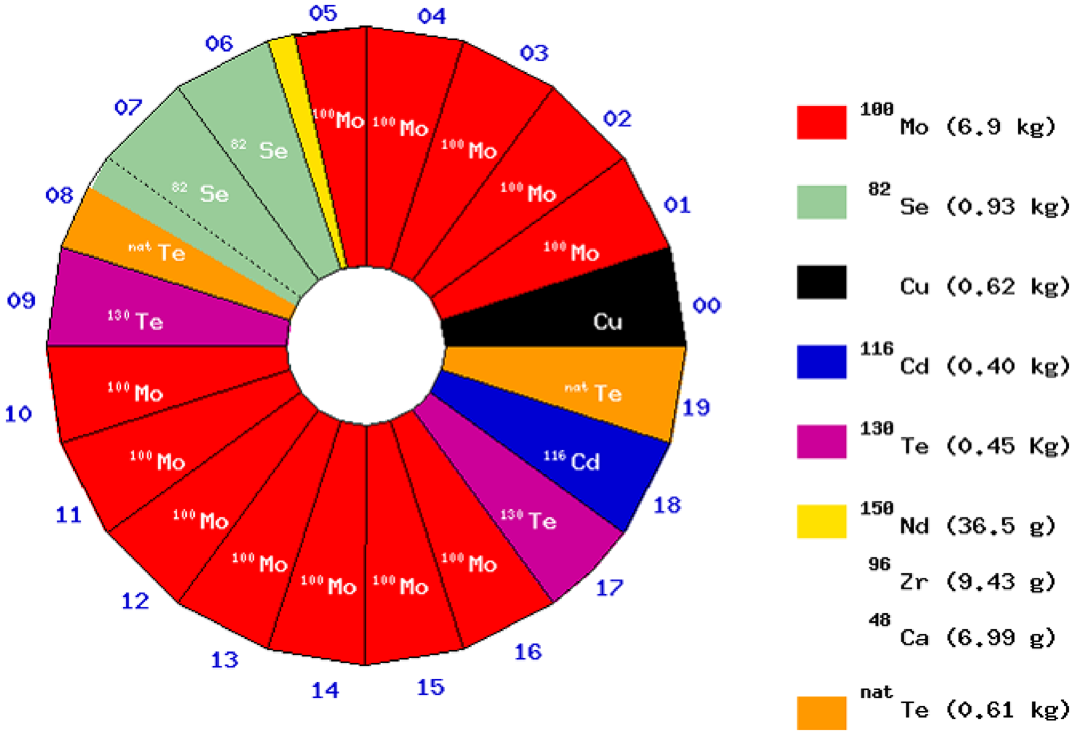

Figure 2.6: The source distribution in the 20 sectors of NEMO 3.

The thickness of the source foils was chosen to take into account the energy resolution, which is fixed by the calorimeter design. Monte-Carlo simulations have shown that the detector efficiency for the $\beta\beta0\nu$ process is not compromised as long as the surface densities of the foils do not exceed

60 mg/cm$^2$. As a consequence the source foils have surface densities between 30 and 60 mg/cm$^2$, which means a thickness lower than 60 $\mu$m for the metallic foils (density of $\sim$ 10 g/cm$^3$) and lower than 300 $\mu$m for composite foils (density of $\sim$ 2 g/cm$^3$).

As indicated above, NEMO 3 sources are metallic or composite. Cadmium, copper and a fraction of the molybdenum foils are metallic sources. Composite foils are a mixture of source powder and organic glue. For the $^{100}$Mo 64% are in the form of composite strips. The selenium, tellurium, zirconium, neodymium and calcium foils are all composite foils.

For composite foils, the glue is made from water and some percentage of PVA (polyvinyl alcohol). This mixture is laid down on a Mylar sheet and then covered by another sheet forming a sandwich-like structure. These sheets are often referred to as backing films, which provide mechanical rigidity. The Mylar sheets have undergone a special processing in which a large number of microscopic holes (around 0.4 $\mu$m in diameter) have been created to insure a good bond with the glue. There are three types of backing film used in the experiment. Type 1 has a thickness of 18 $\mu$m and around $7 \times 10^7$ holes/cm$^2$. Type 2 has a thickness of 19 $\mu$m and around $2 \times 10^7$ holes/cm$^2$. Type 3, which is 23 $\mu$m thick, has around $7 \times 10^7$ holes/cm$^2$. The holes were made first by irradiating the Mylar at JINR with a $^{84}$Kr ion beam of 3 MeV/nucleon and a total beam intensity on target of respectively $2.4 \times 10^{10}$ ions/s (for Type 2) and $8.4 \times 10^{10}$ ions/s (for Type 1 and Type 3 backing films). For each point on the Mylar surface, $3.6 \times 10^9$ ions and $1.3 \times 10^{10}$ ions were incident during an exposure time of 0.15 s corresponding to ion track densities in the film of $2 \times 10^7$ and $7 \times 10^7$ holes/cm$^2$ respectively. The next step in preparing the film was chemically etching it with NaOH (5 M) at 70$^o$ C, then the film was washed with water and 1% CH$_3$COOH (acetic acid) and finally dried with hot air. All the products (Mylar, water, acid...) used to process the backing film have been selected for their radiopurity with High Purity Germanium (HPGe) detector measured at the LSM (the HPGe detectors are from Canberra Mesures Company). The characteristics of all the source foils' strips in the 20 sectors are summarized in Tables 2.2 and 2.3.

### 2.2.2 Radiopurity of the sources with respect to $^{214}$Bi and $^{208}$Tl

As presented in Section 1.3, the presence of impurities in the source foils may give rise to two-electron events which mimic $\beta\beta$ decay and produce background events in the region of the $\beta\beta0\nu$ signal. These impurities have been sufficiently reduced that given the energy resolution of the calorimeter, the ultimate background for the $\beta\beta0\nu$ signal is the tail of the $\beta\beta2\nu$ decay distribution. This is why acceptable levels of $^{214}$Bi and $^{208}$Tl in the foils depends on the number of $\beta\beta2\nu$ events in the region 2.8 to 3.2 MeV. For 10 kg of $^{100}$Mo ($Q_{\beta\beta}$ = 3.035 MeV)[4], one background event/yr is expected from the $\beta\beta2\nu$ process above 2.8 MeV, corresponding to the $\beta\beta2\nu$ period of $^{100}$Mo of $0.95 \times 10^{19}$ years as measured with the NEMO 2 detector [13]. As a consequence, the maximum levels of $^{214}$Bi and $^{208}$Tl contaminations in the Mo source have been calculated to ensure that $^{214}$Bi and $^{208}$Tl should yield less than 0.4 background events/yr above 2.8 MeV for 10 kg of $^{100}$Mo, ensuring that $\beta\beta2\nu$ process is the limiting background, with 1 background event/yr expected above 2.8 MeV. The associated allowed limits for $^{214}$Bi and $^{208}$Tl contaminations are thus:

$$A_{(^{100}\mathrm{Mo})}(^{214}\mathrm{Bi}) \; < \; 0.3 \text{ mBq/kg} \tag{2.1}$$

$$A_{(^{100}\mathrm{Mo})}(^{208}\mathrm{Tl}) \; < \; 0.02 \text{ mBq/kg} \tag{2.2}$$

---

[4] Monte-Carlo simulations were done initially with the 10 kg maximal allowed mass of $^{100}$Mo in the NEMO 3 detector

| Sector | Source strips | $\eta$ (%) | M$_1$ (g) | M$_2$ (g) | M$_3$ (g) |
|---|---|---|---|---|---|
| 00 | 7 of $^{nat}$Cu **(M)** | / | 620.8 | 620.8 | 620.8 $^{\mathrm{nat}}$**Cu** |
| 01 | 5 of $^{enr}$Mo **(M)** | 95.14 | 424.21 | 423.22 | 401.76 $^{100}$**Mo** |
| | 2 of $^{enr}$Mo **(C)** | 95.14 | 176.22 | 145.08 | 137.72 $^{100}$**Mo** |
| 02 | 7 of $^{enr}$ Mo **(M)** | 1 and 2 : 96.81 | 186.44 | 186.06 | 179.76 $^{100}$**Mo** |
| | | 3 to 7 : 98.51 | 434.88 | 434.40 | 426.94 $^{100}$**Mo** |
| 03 | 7 of $^{enr}$Mo **(M)** | 98.90 | 697.32 | 696.47 | 686.29 $^{100}$**Mo** |
| 04 | 7 of $^{enr}$Mo **(M)** | 97.90 | 614.63 | 614.14 | 600.05 $^{100}$**Mo** |
| 05 | 2 of $^{enr}$Mo **(M)** | 1 and 2 : 98.20 | 188.27 | 187.89 | 184.14 $^{100}$**Mo** |
| | 3 of $^{enr}$Mo **(C)** | 3 : 96.66 | 109.22 | 90.07 | 86.89 $^{100}$**Mo** |
| | | 4 : 98.20 | 108.76 | 90.16 | 88.34 $^{100}$**Mo** |
| | | 5 : 95.80 | 87.00 | 70.85 | 67.73 $^{100}$**Mo** |
| | 1 of $^{enr}$Nd$_2$O$_3$ **(C)** | 6 : 91.0 | 56.68 | 40.18 | 36.55 $^{150}$**Nd** |
| | 1/2 of $^{enr}$ZrO$_2$ **(C)** | 57.3 | 11.57 | 7.15 | ITEP : 4.10 $^{96}$**Zr** |
| | (2 parts) | 57.3 | 14.94 | 9.27 | INR : 5.31 $^{96}$**Zr** |
| | 1/4 of $^{enr}$CaF$_2$ **(C)** | 73.1 | 18.516 | 9.572 | 6.997 $^{48}$**Ca** |
| | 1/4 of back. film | | | | |
| 06 | 7 of $^{\mathrm{enr}}$Se **(C)** | 97.02 | 455.67 | 385.31 | 373.80 $^{82}$**Se** |
| 07 | 7 of $^{\mathrm{enr}}$Se **(C)** | 96.82 | 535.04 | 460.65 | 446.03 $^{82}$**Se** |
| 08 | 2 of $^{\mathrm{enr}}$Se **(C)** | 1 : 96.95 | 73.58 | 63.24 | 61.31 $^{82}$**Se** |
| | | 2 : 97.02 | 62.78 | 52.82 | 51.25 $^{82}$**Se** |
| | 5 of $^{\mathrm{nat}}$TeO$_2$ **(C)** | 3 to 7 : 33.8 | 346.44 | 189.19 | 63.94 $^{130}$**Te** |
| 09 | 7 of $^{\mathrm{enr}}$TeO$_2$ **(C)** | 89.4 | 380.86 | 255.77 | 228.61 $^{130}$**Te** |

Table 2.2: Characteristics of the source strips for each of the NEMO 3 sectors 00-09: $\eta$ is the percentage of $\beta\beta$ decay isotope in the enriched sample; $M_1$, $M_2$ and $M_3$ are respectively the **t**otal mass of material in the foils, the mass of the investigated **e**lement in the foils, and the mass of the relevant $\beta\beta$ decay **i**sotope in the foils. In this table, **(M)** and **(C)** identify the metallic and composite foil.

For $^{82}$Se the $T^{2\nu}_{1/2}$ is 10 times longer than for $^{100}$Mo ($0.83 \times 10^{20}$ years as measured with the NEMO 2 detector [15]), however the available mass of this isotope is only 1 kg. Similarly, simulations have given the maximum levels of contamination for $^{214}$Bi and $^{208}$Tl in a 1 kg Se source foil:

$$A_{(^{82}\mathrm{Se})}(^{214}\mathrm{Bi}) \; < \; 0.7 \ \mathrm{mBq/kg} \tag{2.3}$$

$$A_{(^{82}\mathrm{Se})}(^{208}\mathrm{Tl}) \; < \; 0.05 \ \mathrm{mBq/kg} \tag{2.4}$$

No specific limits for activities of these contaminants were required for the other isotopes. Given the low mass of these isotopes, the $\beta\beta0\nu$ limits obtained are not expected to be as competitive with the Mo and Se sources.

| Sector | Source | $\eta$ (%) | $M_1$ (g) | $M_2$ (g) | $M_3$ (g) |
|---|---|---|---|---|---|
| 10 | 7 of $^{enr}$Mo **(C)** | 1 and 2 : 95.14 | 205.9 | 170.14 | 161.51 $^{100}$**Mo** |
| | | 3 to 6 : 96.66 | 414.68 | 339.94 | 327.92 $^{100}$**Mo** |
| | | 7 : 96.32 | 102.91 | 84.73 | 81.45 $^{100}$**Mo** |
| 11 | 7 of $^{enr}$Mo **(C)** | 5 : 95.14 | 107.88 | 89.44 | 84.92 $^{100}$**Mo** |
| | | others : 96.66 | 614.12 | 503.73 | 485.93 $^{100}$**Mo** |
| 12 | 7 of $^{enr}$Mo **(C)** | 95.14 | 728.25 | 601.59 | 571.89 $^{100}$**Mo** |
| 13 | 7 of $^{enr}$Mo **(C)** | 2 and 4 : 98.95 | 213.73 | 177.74 | 175.46 $^{100}$**Mo** |
| | | others : 96.20 | 508.93 | 420.9 | 404.1 $^{100}$**Mo** |
| 14 | 7 of $^{enr}$Mo **(C)** | 98.95 | 735.11 | 608.07 | 601.00 $^{100}$**Mo** |
| 15 | 7 of $^{enr}$Mo **(C)** | 96.20 | 753.85 | 627.59 | 602.62 $^{100}$**Mo** |
| 16 | 7 of $^{enr}$Mo **(C)** | 1, 2, 4, 7 : 95.14 | 391.64 | 318.97 | 302.79 $^{100}$**Mo** |
| | | 3 and 5 : 96.20 | 217.74 | 181.23 | 174.0 $^{100}$**Mo** |
| | | 6 : 95.30 | 102.35 | 84.49 | 80.34 $^{100}$**Mo** |
| 17 | 7 of $^{enr}$TeO$_2$ **(C)** | 89.4 | 375.52 | 252.01 | 225.29 $^{130}$**Te** |
| 18 | 7 of $^{enr}$Cd **(M)** | 93.2 | 491.18 | 434.42 | 404.89 $^{116}$**Cd** |
| 19 | 7 of $^{nat}$TeO$_2$ **(C)** | 33.8 | 547.18 | 301.89 | 102.04 $^{130}$**Te** |

Table 2.3: Characteristics of the source strips for each of the NEMO 3 sectors 10-19: $\eta$ is the percentage of $\beta\beta$ decay isotope in the enriched sample; $M_1$, $M_2$ and $M_3$ are respectively the **t**otal mass of material in the foils, the mass of the investigated **e**lement in the foils, and the mass of the $\beta\beta$ decay **i**sotope in the foils. In this table, **(M)** and **(C)** are written respectively for metallic and composite foil.

### 2.2.3 Production and enrichment of molybdenum

The isotopic abundance of $^{100}$Mo is 9.6% in $^{nat}$Mo. Using enrichment processes in Russia under the control of ITEP, Mo samples with levels of 95.14 ± 0.05% to 98.95 ± 0.05% $^{100}$Mo were produced having a total mass of 10 kg.

The enrichment process involved the production of MoF$_6$ gas from natural Mo. This gas was then centrifuged to isolate the heavier Mo isotope such as $^{100}$Mo. The next step was an oxidation-reduction reaction on the enriched $^{100}$MoF$_6$ gas which yields $^{100}$MoO$_3$ and finally $^{100}$Mo metallic powder.

Radioactivity measurements of this enriched Mo powder have shown that the enrichment process must be complemented with a purification process, more specifically thorium extraction. However the best measurements obtained with the HPGe spectrometer ($\sim (1-8)$ mBq/kg for $^{214}$Bi and $\sim (0.4-2)$ mBq/kg for $^{208}$Tl) did not satisfy the specific requirements for NEMO 3 given in Eq. 2.1 and Eq. 2.2. To reach these levels, the collaboration decided to investigate two different purification methods in parallel: a physical process and a chemical process. The methods were refined using samples of natural molybdenum. HPGe measurements were made before and after processing to identify improvements in the purification processes (see Section 2.9).

### 2.2.4 Physical purification of the enriched Mo powder and metallic strip fabrication

Enriched Mo powder was used directly to both purify and produce metallic foils. This purification process, developed by ITEP, involved transforming the powder into an ultrapure monocrystal with a mass of around 1 kg.

The powder was first pressed to obtain a solid Mo sample. Then the Mo was locally melted in a vacuum with an electron beam and a monocrystal was drawn from the liquid portion. Impurities coming from natural radioactivity decay chains made a migration towards the crystal extremities, because these are more soluble in the melting zone than molybdenum. Finally, cutting the skin of impurities off the crystal and repeating the process, one obtained a very pure sample, from which an enriched purified Mo monocrystal could be grown, with a 20 mm diameter and a 200 to 500 mm length.

"Short" metallic strips, which were between 44 and 63 $\mu$m thick and between 64 and 1445 mm long, were fabricated from the cut monocrystal by heating and rolling it in a vacuum to avoid pollution. The next step was to trim the edges to obtain short strips 63 to 65 mm wide. Wastes from each step could be recycled, either by the physical or chemical method. The whole process is presented in Fig. 2.7.

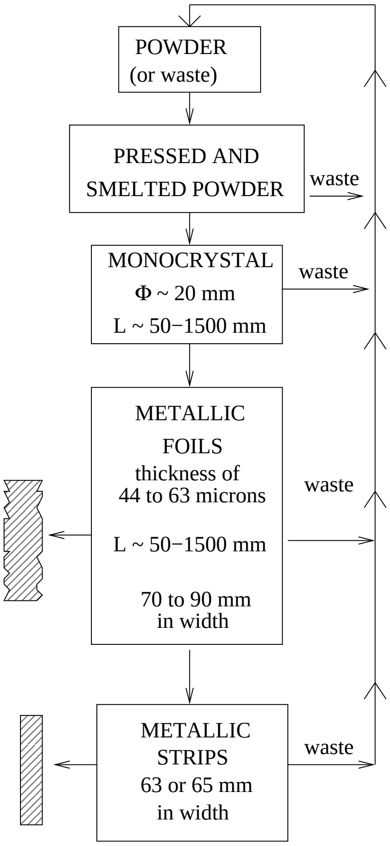

Figure 2.7: Schematic of Mo powder physical purification by monocrystal growth to obtain metallic strips.

After the radioactivity measurements (see Table 2.35 in Section 2.9 for the four sendings to LSM, respectively called "metallic 1" to "metallic 4"), which all present only upper limits for $^{214}$Bi activity (0.68 to 0.37 mBq/kg) and $^{208}$Tl activity (0.17 to 0.11 mBq/kg), three to five short strips were attached end-to-end in the clean room at the LSM to create a NEMO 3 strip with a mean length of around 2480 mm (see Fig. 2.8 for the definitions of the lengths). Seven of these NEMO 3 strips were installed in a frame to produce a source foil for one sector.

Introduction of source foils in sectors is described in Section 2.8. Metallic Mo strips were placed in sectors 02, 03 and 04. There are also five additional strips in sector 01 and two strips in sector 05, which give a combined mass of (2479 ± 5) g of $^{100}$Mo.

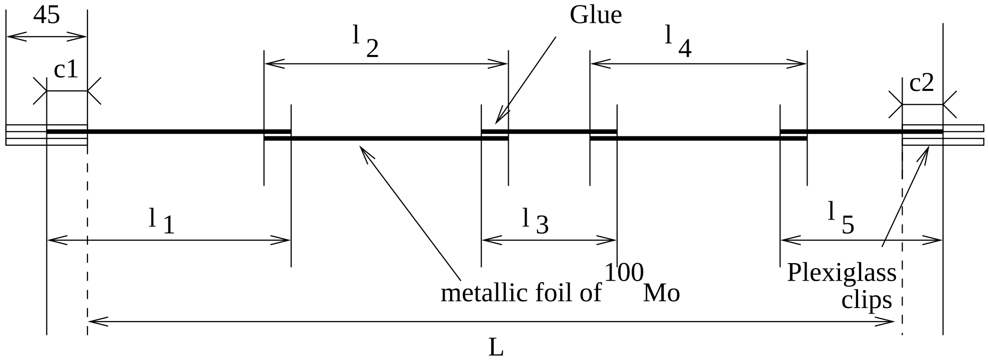

Figure 2.8: Principle of metallic strip assembly for $^{100}$Mo, with Araldite AW106/Hardener HV953U glue.

### 2.2.5 Chemical purification of the enriched Mo powder and fabrication of composite strips

The chemical purification process also started with the metallic powder. The focus of this method was to remove long lived radioactive isotopes of the $^{238}$U and $^{232}$Th decay chains while filling Ra sites with Ba by spiking the sample during the processing. It is important to remove from the source sample all long lived naturally occurring radioactive isotopes. These ones are U, Th and Ra (see Fig 1.15). This is in order to avoid the background coming from the decay of the short lived daughter products $^{214}$Bi (from $^{226}$Ra with half-life of 1600 yr) and $^{208}$Tl (from $^{232}$Th and $^{228}$Th, and from $^{228}$Ra with half-life of 5.75 yr). The process takes advantage of an equilibrium break in the $^{238}$U and $^{232}$Th decay chains, which can selectively transform these chains to non-equilibrium states in which only short lifetime daughters exist.

The purification process was carried out in a class 100 clean room at INL [22]. It is described in Fig. 2.9. A solution containing the enriched Mo metal powder, ultra pure $H_2O$, Quartz Distilled (Q.D.) $HNO_3$, and a very small sample of very pure $Ba(NO_3)_2$ (a salt nearly Ra-free) was heated until the Mo dissolved. Then the acid strength was increased and the volume was reduced by heating until Mo precipitates as $MoO_3$. The baryum salt was added to block sites on the $MoO_3$ as it precipitated that would otherwise carry Ra. A view of the purification system is given in Fig. 2.10. The $MoO_3$ slurry was filtered to separate the Mo from the impurity radioisotopes, as most of the impurities are acid soluble. The resulting filter cake was then washed, dried, inserted into a quartz-lined tube furnace and heated. The first step involved He at 200$^o$C which was needed to further dry the $MoO_3$, a second step with $H_2$ with successively higher temperatures permitted the reduction of the $MoO_3$ to purified metal powder. This powder typically contained less than 2% $O_2$.

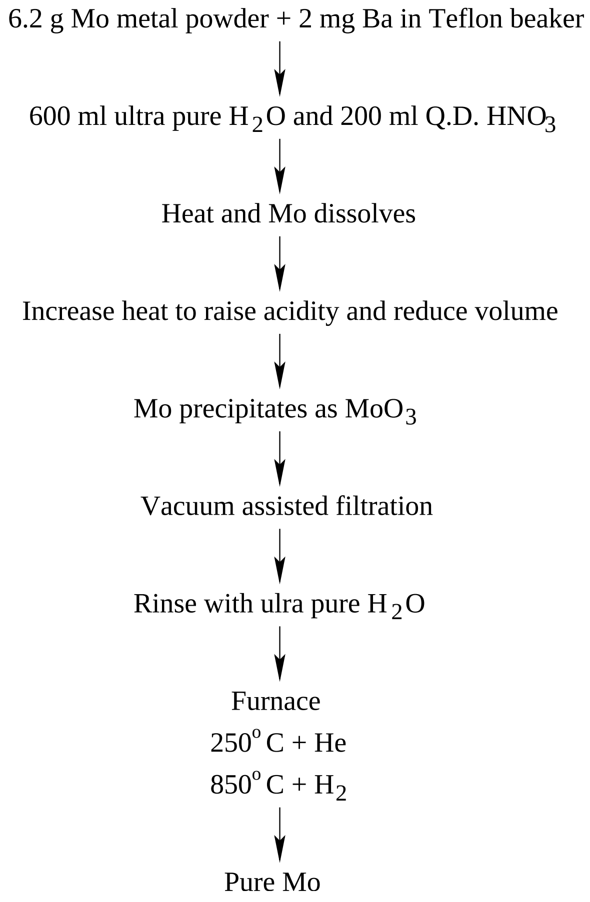

Figure 2.9: Flow chart of $^{100}$Mo chemical purification.

Radioactivity measurements of the purified enriched Mo powder samples were made with HPGe spectroscopy in the LSM for the five batchs (1, 2, 3-1, 3-2, 4). Results are given in Table 2.36 of Section 2.9 and present only upper limits for $^{214}$Bi activity (0.3 to 0.2 mBq/kg) and $^{208}$Tl activity (0.17 to 0.05 mBq/kg), except for batch 4 ($^{214}\mathrm{Bi} = 1.0 \pm 0.3$ mBq/kg)[5]. The best limits, $A(^{214}\mathrm{Bi}) < 0.2$ mBq/kg and $A(^{208}\mathrm{Tl}) < 0.05$ mBq/kg, were the achievable levels for the HPGe detectors. The required limit on $^{214}$Bi (Eq. 2.1) was directly measurable. The task of measuring the required limit for $^{208}$Tl (Eq. 2.2) was beyond the practical measuring limits of the HPGe detectors in the LSM. However, the chemical extraction factors (see Table 2.4 for K, U, Th and Ra contaminants) defined as the ratio of contamination before and after purification were measured for natural and enriched Mo [22]. This study implied by Ra extraction limits and indirectly inferred by measurable quantities of $^{235}$U in the enriched Mo samples, showed that

---

[5] Note that this small $^{214}$Bi contamination value ($3\sigma$ effect), which was measured for batch 4, was not shown after composite strip realization. Thus radon pollution of HPGe detector can not be excluded for batch 4 measurement, even if precautionary measures were taken to avoid such a pollution.

Figure 2.10: View of the chemical purification system for $^{100}$Mo (INL, Idaho, USA).

there was strong evidence that the $^{208}$Tl contamination would be below the NEMO 3 design criteria. Ultimately, the NEMO 3 detector now produces measurements of this activity (see Section 4.1.1).

| Isotope | $^{nat}\text{Mo}_{purified}$ | $^{enr}\text{Mo}_{purified}$ |
|---|---|---|
| $^{40}$K | $> 80$ | $> 21$ |
| $^{238}$U | $100 \pm 30$ | $> 16$ |
| $^{235}$U | $140 \pm 20$ | $80 \pm 30$ |
| $^{228}$Th | $> 95$ | $> 8$ |
| $^{226}$Ra | $> 39$ | $> 12$ |
| $^{228}$Ra | $> 34$ | $> 2$ |

Table 2.4: Reduction factors of contaminant content measured after purification from chemical processing for both natural Mo and enriched Mo.

The chemically purified $^{100}$Mo was used to make composite foils in the method previously discussed. There were two types of backing film used, Type 1 for sector 01 and Type 2 for sectors 05 and 10 through 16.

To produce the composite strips, the first step involved sieving the powder to keep only grains with diameters smaller than 45 $\mu$m. Then, the residual was ground up and several additional sieving processes were undertaken so the grains were small enough to ensure a good bond to the backing foil. Next the powder was mixed with the glue (water and PVA). The mixture was introduced into a syringe, which was heated with ultra-sound to obtain a paste. This paste of desired thickness was uniformly spread onto one of the two Mylar foils (backing film) and then covered with the second one. After 10 hours of drying, the composite strip was cut to length $L$ with a surface density lower than 60 mg/cm$^2$ (see Fig. 2.11).

After the radioactivity measurements (see Section 2.9 for results in Table 2.37) as with the metallic foils, a group of seven composite strips was installed in a frame to produce a source foil, which was then introduced into the sector.

The total mass of $^{100}$Mo in composite foils is $(4435 \pm 22)$ g.

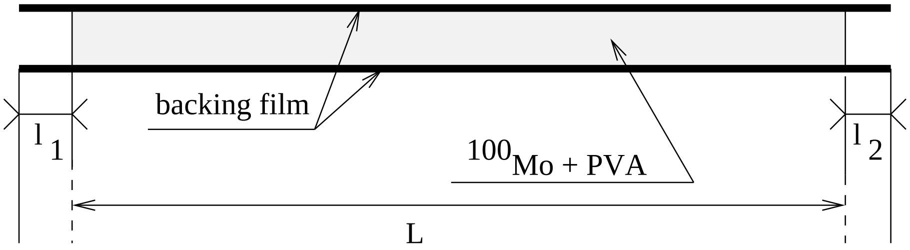

Figure 2.11 : View of composite strip assembly for $^{100}$Mo : powder mixed with PVA is glued between two backing film foils.

### 2.2.6 Production, enrichment and purification processes for other isotopes

#### 2.2.6.1 $^{82}$Se source

A similar enrichment process that for the Mo was used to produce $^{82}$SeF$_6$ gas. The next step was an electrical discharge in the gas to obtain the enriched Se powder.

Two different production runs of 500 g for $^{82}$Se powder, Se(I) and Se(II), were carried out in ITEP. They had an enrichment factor of $97.02 \pm 0.05\%$ for run 1 (Se(I)) and $96.82 \pm 0.05\%$ for run 2 (Se(II))[6]. No subsequent purification process was carried out. A portion of run 1 was already used in the NEMO 2 prototype and a value for the $^{214}$Bi contamination was measured, but the contaminants were found to be concentrated in small "hot spots" and rejected in the analysis via identification of the vertex of the candidate events [15]. The $^{82}$Se used in NEMO 2 foils was recovered and used to produce composite strips for NEMO 3. The sample of material from run 2 plus the remaining part of run 1 were also used to produce composite strips.
Low activities in $^{214}$Bi (1.2$\pm$0.5 mBq/kg) and $^{208}$Tl (0.4$\pm$0.1 mBq/kg) were measured for 0.8 kg of $^{82}$Se strips (both Se(I) and Se(II) strips) with the HPGe detector, as shown in Table 2.38 in Section 2.9 (the NEMO 3 required limits for selenium are given in Eq. 2.3 and 2.4). These

---

[6] Proportions of $^{80}$Se is also present, which is 2.94% for Se(I) powder and 3.06% for Se(II) respectively

correspond to an expected background of 0.2 events/yr/kg from $^{214}$Bi and 1 event/yr/kg from $^{208}$Tl, but it is expected that the measured contamination in these Se foils might again be localized and would be suppressed through data analysis.
In the mean time a purification process is being developed at INL for potential future runs with several kilograms of Se.

Se enriched powder was used to make composite strips at ITEP, with the Type 3 backing film in sectors 06 (with Se(I)) and 07 (with Se(II)), and Type 1 in sector 08 (with both Se(I) and Se(II)). The total mass of $^{82}$Se is $(932 \pm 5)$ g.

#### 2.2.6.2 $^{130}$Te source

The Te was enriched ($89.4 \pm 0.5\%$ of isotope 130) by the production of $^{130}TeF_6$ gas, followed by oxidation and reduction to obtain enriched $TeO_2$ powder. The reason for $^{130}TeO_2$ versus $^{130}$Te is that it is easier to work. The Kurchatov Institute (Moscow, Russia) provided this powder to the NEMO collaboration after three separate purifications. For this sample the radioactivity limits for $^{214}$Bi and $^{208}$Tl were measured and a small contamination of $^{228}$Ac ($^{232}$Th decay chain) was detected suggesting that the limit on $^{208}$Tl is close to a value which NEMO 3 should measure (see Table 2.38 in Section 2.9). Composite strips were made with the Type 1 backing film. A total mass of $454 \pm 2$ g of $^{130}$Te was placed in sectors 09 and 17.

#### 2.2.6.3 $^{116}$Cd source

Metallic enriched cadmium ($93.2 \pm 0.2$ % of isotope 116)[7] from ITEP was obtained again by the centrifuged separation method. Part of the sample had been measured with the NEMO 2 prototype [14]. Another part was purified by a distillation technique. A shown in Table 2.38 of Section 2.9, radioactivity limits in $^{214}$Bi and $^{208}$Tl are below the allowed levels of contamination for both Cd(I) and Cd(II) measurements. Small $^{137}$Cs contaminations were found of $4 \pm 1$ mBq/kg for Cd(I) and $2 \pm 1$ mBq/kg for Cd(II).

Despite the metallic quality of the cadmium source, strips were glued between Mylar foils to provide mechanical strength in the vertical position. A total mass of $(405 \pm 1)$ g of $^{116}$Cd was placed in sector 18.

#### 2.2.6.4 $^{150}$Nd source

The $^{150}Nd_2O_3$ powder was provided by INR (Moscow, Russia), after enrichment ($91.0 \pm 0.5\%$ of isotope 150)[8] by electromagnetic separation and chemical purification. Radioactivity measurements (see Table 2.38 in Section 2.9) showed $A(^{214}\mathrm{Bi}) < 3.0$ mBq/kg (the maximum level of contamination required for NEMO 3 is 83 mBq/kg) but there was a small contamination of $^{208}$Tl ($(10 \pm 2)$ mBq/kg instead of $A(^{208}\mathrm{Tl}) < 5.5$ mBq/kg for NEMO 3). As a consequence, this source is now used to check the ability of NEMO 3 to measure internal backgrounds. Other radioactivity measurements were obtained for $Nd_2O_3$: $A(^{137}\mathrm{Cs}) < 3$ mBq/kg, $A(^{60}\mathrm{Co}) < 2$ mBq/kg, $A(^{212}\mathrm{Pb}) = (30 \pm 5)$ mBq/kg, $A(^{152}\mathrm{Eu}) = (40 \pm 5)$ mBq/kg and $A(^{207}\mathrm{Bi}) = (130 \pm 5)$ mBq/kg.

The one neodymium composite strip (number 6 of sector 05) was made with 40.2 g of enriched $Nd_2O_3$ powder and backing films of Type 1. This gives a total mass of $37.0 \pm 0.1$ g of $^{150}$Nd.

---

[7] Proportions of $^{114}$Cd, $^{113}$Cd and $^{112}$Cs are also present, which represent respectively 3.28%, 0.89% and 1.55%

[8] Proportions of isotopes 148, 146, 144 and 142 were also present in the neodynium powder, which represent respectively 2.19%, 2.09%, 1.92% and 1.11%

#### 2.2.6.5 $^{96}$Zr source

Enriched zirconium was obtained by an electromagnetic separation technique, with the samples averaging $57.3 \pm 1.4\%$ $^{96}$Zr[9] . The samples were a powder of $^{96}ZrO_2$, from two different origins.

The first sample came from ITEP and was measured in the NEMO 2 prototype. Some contamination of $^{40}$K, $^{228}$Ac and $^{208}$Tl was measured. Similar to the Se contaminants they were concentrated in "hot-spots" and removed in data analysis [16]. The $^{96}ZrO_2$ powder was recovered from NEMO 2 foils and purified using a chemical process. It represents 9.6 g of $ZrO_2$ or $4.1 \pm 0.1$ g of $^{96}$Zr. The second sample comes from INR (Moscow, Russia) and is 12.4 g of $ZrO_2$ or $5.3 \pm 0.1$ g of $^{96}$Zr. Radioactivity measurements for these two production samples, which are shown in Table 2.38 of Section 2.9, are below the allowed levels of contamination.

The zirconium composite strips were made with enriched $ZrO_2$ powder and backing films of Type 2. The strip is the 7th in sector 05. The total mass of $^{96}$Zr is $9.4 \pm 0.2$ g.

#### 2.2.6.6 $^{48}$Ca source

A $CaCO_3$ sample was enriched in the isotope calcium 48 ($73.2 \pm 1.6\%$)[10] . It was produced by electromagnetic separation methods. Additionally, a purification process was developed collaboratively by JINR and the Kurchatov Institute. It removed $^{226}$Ra, $^{228}$Ra, $^{60}$Co and $^{152}$Eu, as well as elements from the uranium and thorium decay chains. The measured purification factors for $^{226(228)}$Ra, $^{60}$Co and $^{152}$Eu were greater than 1300, 3300 and 250 respectively. After the purification process, with 64 g of enriched $CaCO_3$, JINR had a yield of 42.1 g of enriched $CaF_2$ powder.

The first portion (24.6 g of enriched $CaF_2$) of this powder was used for radioactivity measurements with HPGe studies in the LSM. Only limits were obtained for $^{214}$Bi and $^{208}$Tl (see Table 2.38 in Section 2.9). Other radioactivity measurements obtained for $CaF_2$ powder were: $A(^{137}\mathrm{Cs}) < 3$ mBq/kg, $A(^{60}\mathrm{Co}) < 2$ mBq/kg and $A(^{152}\mathrm{Eu}) = (30 \pm 5)$ mBq/kg.

The second portion of this powder (17.5 g) was used to make nine 40 mm diameter disks. Mylar was again used and cut in the shape of the disks. To create the calcium portion of strip 25% of the 7th foil was populated with this material in sector 05 (see Fig.2.12). The disks were glued between two Type 2 backing films. In total there is $6.99 \pm 0.05$ g of $^{48}$Ca.

#### 2.2.6.7 $^{nat}$Te and copper sources

The foils of $^{nat}TeO_2$ from ITEP and placed in the detector allow the NEMO collaboration to measure the external background for $^{100}$Mo. The effective $Z$ of these foils ($Z(^{nat}TeO_2) = 43.2$) is nearly the same as that of the molybdenum foils ($Z$(Mo)= 42). This is useful because the external $\gamma$-ray background can give rise to contamination processes, which are all proportional to $Z^2$. Thus, the background for $^{100}$Mo and $^{nat}TeO_2$ foils should give rise to similar event rates. In addition, $^{nat}TeO_2$ has 33.8% $^{130}$Te[11] and the $\beta\beta2\nu$ process expected has $Q_{\beta\beta} = 2.53$ MeV. Thus these events would not enter the $\beta\beta0\nu$ region of interest for $^{100}$Mo. Consequently, a background subtraction is possible for the $^{100}$Mo foils using an analysis of the $^{nat}TeO_2$ spectrum.

---

[9] Proportions of isotopes 94, 92, 91 and 90 were also present in the zirconium powder, which represent respectively 9.38%, 8.28%, 5.28% and 19.75%

[10] Two other isotopes $^{44}$Ca and $^{40}$ were also present in the enriched calcium powder, which represent respectively 1.98% and 24.43%

[11] Composition of this natural tellurium is: 33.8% of isotope 130, 31.69% of isotope 128, 18.95% of isotope 126, and respectively 7.14%, 4.82% and 2.60% of isotopes 125, 124 and 122

Figure 2.12: View of source foil production for sector 05, by attachment of the seven strips in the LSM clean room (see the calcium portion' strip with the nine 40 mm diameter disks).

It is also useful to study $\beta\beta$ processes for the $^{130}$Te part of $^{nat}$TeO$_2$ (33.8%) compared to enriched TeO$_2$. Foils of $^{nat}$TeO$_2$ were not purified, but radioactivity measurements showed limits lower than 0.17 and 0.09 mBq/kg for $^{214}$Bi and $^{208}$Tl respectively, as shown in Table 2.38 of Section 2.9 (semi-conductor purity levels).

The $^{nat}$TeO$_2$ composite strips were made with Type 1 backing films for 5 strips in sector 08 and Type 3 for the 7 strips in sector 19. This gives a total mass of 614 g of $^{nat}$TeO$_2$ or 166 g of $^{130}$Te.

The copper foil (standard copper from France) provides a similar study of external backgrounds for a smaller value of $Z$. The metallic copper source is very pure ($A(^{214}\mathrm{Bi}) < 0.12$ mBq/kg and $A(^{208}\mathrm{Tl}) < 0.04$ mBq/kg as shown in Section 2.9) with a mass of 621 g and was placed in sector 00.

#### 2.2.6.8 Others

The NEMO collaboration decided to put six Type 2 backing film layers in the 7th strip of sector 05 (the same strip already used for zirconium and calcium, where there was a 635 mm long free space) to check radioactivity measurements of the backing film with the NEMO 3 detector. Small $^{214}$Bi contaminations were found in this backing film from HPGe measurements ($1.0 \pm 0.3$ mBq/kg).

### 2.2.7 Summary of the source foil properties

Properties of the seven strips for each sector's foils are given in Tables 2.5 (for sector 00) to 2.25 (for sector 19): composition, total lengths (with partial lengths for metallic strips), mass of each strip ($M_1$, $M_2$ and $M_3$ as defined in Tables 2.2 and 2.3), and percentage of $\beta\beta$ decay isotope in the enriched sample. Comments are added to give further informations and help the reader to refer to radiopurity measurements of the samples. Concerning radiopurity of these source foils, all results can be found in Tables 2.35, 2.37 and 2.38 (see Section 2.9).

| Sector 00 | | | | | | | |
|---|---|---|---|---|---|---|---|
| Material | Metallic foil Cu | | | | | | |
| Strip number | 1 | 2 | 3 | 4 | 5 | 6 | 7 |
| Total length L(mm) | 2445 | 2445 | 2445 | 2445 | 2445 | 2445 | 2445 |
| Width (mm) | 63 | 65 | 65 | 65 | 65 | 65 | 63 |
| $M_1$(g) $= M_2$(g) $= M_3$(g) | 86.63 | 89.57 | 89.27 | 88.98 | 89.57 | 89.96 | 86.82 |
| Radiopurity | see Table 2.38 | | | | | | |

Table 2.5: Composition, total length (with partial lengths for metallic strips) and mass of the seven strips of **sector 00**: $\eta$ is the percentage of $\beta\beta$ decay isotope in the enriched sample; $M_1$, $M_2$ and $M_3$ are respectively the **t**otal mass of material in the foils, the mass of the investigated **e**lement in the foils, and the mass of the $\beta\beta$ decay **i**sotope in the foils. Note that $M_1 = M_2 = M_3$ for copper foils.

| Sector 01 | | | | | | | |
|---|---|---|---|---|---|---|---|
| Material | $^{100}$Mo metallic foil | | | | | $^{100}$Mo composite strip | |
| Strip number | 1 | 2 | 3 | 4 | 5 | 6 | 7 |
| Total length L(mm) | 2463 | 2468 | 2468 | 2480 | 2476 | 2435 | 2430 |
| (Top) $L_1$(mm) | 475 | 451 | 211 | 350 | 290 | | |
| $L_2$ (mm) | 966 | 950 | 633 | 1175 | 761 | | |
| $L_3$ (mm) | 680 | 640 | 1245 | 701 | 718 | | |
| $L_4$ (mm) | 210 | 324 | 308 | 231 | 616 | | |
| $L_5$ (mm) | 172 | 143 | 111 | 64 | 131 | | |
| Width (mm) | 63 | 65 | 65 | 65 | 65 | 65 | 63 |
| $M_1$ (g) | 80.77 | 85.39 | 84.99 | 85.83 | 87.23 | 96.96 | 79.26 |
| $M_2$ (g) | 80.57 | 85.19 | 84.75 | 85.67 | 87.04 | 80.36 | 64.72 |
| $M_3$ (g) | 76.48 | 80.87 | 80.45 | 81.33 | 82.63 | 76.29 | 61.43 |
| $\eta$ (%) | 95.14 | 95.14 | 95.14 | 95.14 | 95.14 | 95.14 | 95.14 |
| Comments | Samples 328-4 and 328-5 | | | | | Batch 1 | |
| Radiopurity | see “metallic 1” in Table 2.35 | | | | | see Table 2.36 | |

Table 2.6 : Composition, total length (with partial lengths for metallic strips), mass and abundance of the seven strips of **sector 01**: $\eta$ is the percentage of $\beta\beta$ decay isotope in the enriched sample; $M_1$, $M_2$ and $M_3$ are respectively the **t**otal mass of material in the foils, the mass of the investigated **e**lement in the foils, and the mass of the $\beta\beta$ decay **i**sotope in the foils.

| Sector 02 | | | | | | | |
|---|---|---|---|---|---|---|---|
| Material | Metallic foil $^{100}$Mo | | | | | | |
| Strip number | 1 | 2 | 3 | 4 | 5 | 6 | 7 |
| Total length L(mm) | 2479 | 2497 | 2499 | 2485 | 2485 | 2478 | 2465 |
| $L_1$(mm) | 95 | 69 | 262 | 201 | 474 | 444 | 570 |
| $L_2$(mm) | 361 | 950 | 1197 | 1180 | 1021 | 1083 | 1084 |
| $L_3$(mm) | 549 | 1014 | 1060 | 1124 | 1010 | 971 | 831 |
| $L_4$(mm) | 1103 | 494 | | | | | |
| $L_5$(mm) | 411 | | | | | | |
| Width(mm) | 63 | 65 | 65 | 65 | 65 | 65 | 63 |
| $M_1$(g) | 87.67 | 98.77 | 88.43 | 88.26 | 87.55 | 87.54 | 83.10 |
| $M_2$(g) | 87.47 | 98.59 | 88.32 | 88.22 | 87.46 | 87.40 | 83.00 |
| $M_3$(g) | 84.51 | 95.25 | 86.80 | 86.71 | 85.96 | 85.90 | 81.57 |
| $\eta$ (%) | 96.81 mean | 96.81 mean | 98.51 | 98.51 | 98.51 | 98.51 | 98.51 |
| Samples | 328-4, 328-5<br>374 | | 329 | | | | |
| Radiopurity | see “metallic 2” in Table 2.35 | | | | | | |

Table 2.7 : Composition, total length (with partial lengths for metallic strips), mass and abundance of the seven strips of **sector 02**: $\eta$ is the percentage of $\beta\beta$ decay isotope in the enriched sample; $M_1$, $M_2$ and $M_3$ are respectively the **t**otal mass of material in the foils, the mass of the investigated **e**lement in the foils, and the mass of the $\beta\beta$ decay **i**sotope in the foils.

| | | | | | | | |
|---|---|---|---|---|---|---|---|
| Sector 03 | | | | | | | |
| Material | Metallic foil $^{100}$Mo | | | | | | |
| Strip number | 1 | 2 | 3 | 4 | 5 | 6 | 7 |
| Total length L(mm) | 2473 | 2488 | 2466 | 2510 | 2466 | 2472 | 2482 |
| $L_1$(mm) | 1335 | 1380 | 1175 | 1204 | 1453 | 125 | 1271.5 |
| $L_2$(mm) | 657 | 962 | 1082 | 1044 | 543 | 1412 | 460 |
| $L_3$(mm) | 499 | 166 | 229 | 282 | 489 | 818 | 393.5 |
| $L_4$(mm) | | | | | | 145 | 385 |
| Width(mm) | 63 | 65 | 65 | 65 | 65 | 65 | 63 |
| $M_1$(g) | 98.24 | 97.11 | 100.09 | 99.04 | 101.21 | 103.10 | 98.55 |
| $M_2$(g) | 98.12 | 96.96 | 100.00 | 98.93 | 101.08 | 102.91 | 98.47 |
| $M_3$(g) | 96.44 | 95.70 | 98.70 | 97.64 | 99.77 | 100.84 | 97.20 |
| $\eta$ (%) | 98.9<br>for $L_1$, $L_2$<br>96.8<br>for $L_3$ | 98.9 | 98.9 | 98.9 | 98.9 | 98.9<br>for $L_1$, $L_2$, $L_4$<br>96.8<br>for $L_3$ | 98.9 |
| Comments | Samples 314 and 363-bis | | | | | | |
| Radiopurity | see “metallic 3” in Table 2.35 | | | | | | |

Table 2.8: Composition, total length (with partial lengths for metallic strips), mass and abundance of the seven strips of **sector 03**: $\eta$ is the percentage of $\beta\beta$ decay isotope in the enriched sample; $M_1$, $M_2$ and $M_3$ are respectively the **t**otal mass of material in the foils, the mass of the investigated **e**lement in the foils, and the mass of the $\beta\beta$ decay **i**sotope in the foils.

| Sector 04 | | | | | | | |
|---|---|---|---|---|---|---|---|
| Material | Metallic foil $^{100}$Mo | | | | | | |
| Strip number | 1 | 2 | 3 | 4 | 5 | 6 | 7 |
| Total length L(mm) | 2480 | 2490 | 2460 | 2474 | 2461 | 2480 | 2480 |
| L1(mm) | 632 | 1445 | 58 | 224 | 1220 | 844 | 1112 |
| L2(mm) | 1398 | 1055 | 1126 | 1396 | 1251 | 1646 | 1378 |
| L3(mm) | 470 | | 1296 | 874 | | | |
| Width(mm) | 63 | 65 | 65 | 65 | 65 | 65 | 63 |
| $M_1$(g) | 85.98 | 89.20 | 89.98 | 90.78 | 90.47 | 86.31 | 81.91 |
| $M_2$(g) | 85.89 | 89.16 | 89.86 | 90.68 | 90.43 | 86.25 | 81.87 |
| $M_3$(g) | 83.92 | 87.12 | 87.79 | 88.60 | 88.35 | 84.27 | 79.99 |
| $\eta$ (%) | 97.9 | 97.9 | 97.9 | 97.9 | 97.9 | 97.9 | 97.9 |
| Comments | From the wastes | | | | | | |
| Radiopurity | see “metallic 4” in Table 2.35 | | | | | | |

Table 2.9 : Composition, total length (with partial lengths for metallic strips), mass and abundance of the seven strips of **sector 04**: $\eta$ is the percentage of $\beta\beta$ decay isotope in the enriched sample; $M_1$, $M_2$ and $M_3$ are respectively the **t**otal mass of material in the foils, the mass of the investigated **e**lement in the foils, and the mass of the $\beta\beta$ decay **i**sotope in the foils.

| Sector 05 | strips 1 → 6 | | | | | |
|---|---|---|---|---|---|---|
| Material | $^{100}$Mo metallic foils | | $^{100}$Mo composite strips | | | $^{150}Nd_2O_3$ composite strip |
| Strip number | 1 | 2 | 3 | 4 | 5 | 6 |
| Total length L(mm) | 2478 | 2480 | 2412 | 2421 | 2429 | 2340 |
| $L_1$(mm) | 386 | 423 | | | | |
| $L_2$(mm) | 263 | 372 | | | | |
| $L_3$(mm) | 562 | 561 | | | | |
| $L_4$(mm) | 512 | 450 | | | | |
| $L_5$(mm) | 425 | 316 | | | | |
| $L_6$(mm) | 380 | 406 | | | | |
| Width(mm) | 63 | 65 | 65 | 65 | 60 | 65 |
| $M_1$(g) | 92.06 | 96.21 | 109.22 | 108.76 | 87.00 | 56.68 |
| $M_2$(g) | 91.91 | 95.98 | 90.07 | 90.16 | 70.85 | 40.18 |
| $M_3$(g) | 90.08 | 94.06 | 86.89 | 88.34 | 67.73 | 36.55 |
| $\eta$ (%) | 98.2 | 98.2 | 96.66 | 98.2 | 95.8 | 91.0 |
| Comments | From the wastes | | Batch 3.1 | Batch 3.1<br>3.2 | Batch 3.1<br>2 | $M(Nd_2O_3)$<br>46.63 g |
| Radiopurity | see “metallic 4” in Table 2.35 | | see column $^{100}$Mo (2) in Table 2.37 | | | see Table 2.38 |

Table 2.10: Composition, total length (with partial lengths for metallic strips), mass and abundance of strips 1 to 6 of **sector 05**: $\eta$ is the percentage of $\beta\beta$ decay isotope in the enriched sample; $M_1$, $M_2$ and $M_3$ are respectively the **t**otal mass of material in the foils, the mass of the investigated **e**lement in the foils, and the mass of the $\beta\beta$ decay **i**sotope in the foils.

| Sector 05 strip 7 (from top to bottom) | | | | | | | |
|---|---|---|---|---|---|---|---|
| Material | backing film (2 layers) | $^{96}ZrO_2$ ITEP | backing film (2 layers) | $^{96}ZrO_2$ INR | backing film (2 layers) | $^{48}CaF_2$ JINR 9 disks $\phi = 40$ mm | backing film (6 layers) |
| Total length L(mm) | 85 | 437 | 30 | 637 | 95 | 515 | 635 |
| Width(mm) | 63 | 63 (40 for powder) | 63 | 63 (40 for powder) | 63 | 63 | 63 |
| $M_1$(g) | | 11.57 | | 14.94 | | 18.516 | |
| $M_2$(g) | | 7.15 | | 9.27 | | 9.572 | |
| $M_3$(g) | | 4.10 | | 5.31 | | 6.987 | |
| $\eta$ (%) | | 57.3 | | 57.3 | | 73.1 | |
| Comments | | $M(ZrO_2)$ = 9.58 g | | $M(ZrO_2)$ = 12.42 g | | $M(CaF_2)$ = 17.506 g | |
| Radiopurity | see Table 2.38 | | | | | | |

Table 2.11: Composition, total length (with partial lengths for metallic strips), mass and abundance of strip 7 of **sector 05**: $\eta$ is the percentage of $\beta\beta$ decay isotope in the enriched sample; $M_1$, $M_2$ and $M_3$ are respectively the **t**otal mass of material in the foils, the mass of the investigated **e**lement in the foils, and the mass of the $\beta\beta$ decay **i**sotope in the foils.

| Sector 06 | | | | | | | |
|---|---|---|---|---|---|---|---|
| Material | Composite strips $^{82}$Se - Se(I) | | | | | | |
| Strip number | 1 | 2 | 3 | 4 | 5 | 6 | 7 |
| Total length L(mm) | 2425 | 2425 | 2423 | 2426 | 2425 | 2425 | 2426 |
| Width(mm) | 63 | 65 | 65 | 65 | 65 | 65 | 63 |
| $M_1$(mm) | 58.34 | 62.15 | 65.15 | 75.03 | 71.33 | 62.88 | 60.79 |
| $M_2$(mm) | 48.83 | 52.23 | 55.08 | 64.41 | 60.91 | 52.92 | 50.93 |
| $M_3$(mm) | 47.37 | 50.67 | 53.43 | 62.49 | 59.09 | 51.34 | 49.41 |
| $\eta$ (%) | 97.02 | 97.02 | 97.02 | 97.02 | 97.02 | 97.02 | 97.02 |
| Radiopurity | see Table 2.38 | | | | | | |

Table 2.12: Composition, total length (with partial lengths for metallic strips), mass and abundance of the seven strips of **sector 06**: $\eta$ is the percentage of $\beta\beta$ decay isotope in the enriched sample; $M_1$, $M_2$ and $M_3$ are respectively the **t**otal mass of material in the foils, the mass of the investigated **e**lement in the foils, and the mass of the $\beta\beta$ decay **i**sotope in the foils.

| Sector 07 | | | | | | | |
|---|---|---|---|---|---|---|---|
| Material | Composite strips $^{82}$Se - Se(II) | | | | | | |
| Strip number | 1 | 2 | 3 | 4 | 5 | 6 | 7 |
| Total length L(mm) | 2426 | 2423 | 2424 | 2423 | 2423 | 2423 | 2425 |
| Width(mm) | 63 | 65 | 65 | 65 | 65 | 65 | 63 |
| $M_1$(g) | 74.60 | 77.31 | 77.54 | 78.05 | 77.66 | 76.90 | 72.98 |
| $M_2$(g) | 64.21 | 66.58 | 66.79 | 67.28 | 66.91 | 66.19 | 62.69 |
| $M_3$(g) | 62.19 | 64.46 | 64.67 | 65.14 | 64.78 | 64.09 | 60.70 |
| $\eta$ (%) | 96.82 | 96.82 | 96.82 | 96.82 | 96.82 | 96.82 | 96.82 |
| Radiopurity | see Table 2.38 | | | | | | |

Table 2.13: Composition, total length (with partial lengths for metallic strips), mass and abundance of the seven strips of **sector 07**: $\eta$ is the percentage of $\beta\beta$ decay isotope in the enriched sample; $M_1$, $M_2$ and $M_3$ are respectively the **t**otal mass of material in the foils, the mass of the investigated **e**lement in the foils, and the mass of the $\beta\beta$ decay **i**sotope in the foils.

| Sector 08 | | | | | | | |
|---|---|---|---|---|---|---|---|
| Material | composite strips $^{82}$Se | | composite strips $^{nat}TeO_2$ | | | | |
| Strip number | 1 | 2 | 3 | 4 | 5 | 6 | 7 |
| Total length L(mm) | 2428 | 2428 | 2436 | 2434 | 2435 | 2424 | 2146 |
| Width(mm) | 63 | 65 | 65 | 65 | 65 | 65 | 63 |
| $M_1$(g) | 73.58 | 62.78 | 70.78 | 73.93 | 72.65 | 71.94 | 57.14 |
| $M_2$(g) | 63.24 | 52.82 | 48.29 | 50.66 | 49.67 | 49.15 | 38.72 |
| $M_3$(g) | 61.31 | 51.25 | 16.32 | 17.12 | 16.79 | 16.61 | 13.09 |
| $\eta$ (%) | 96.95 mean value | 97.02 | 33.8 | 33.8 | 33.8 | 33.8 | 33.8 |
| Comments | Se(I) $\eta = 97.02\%$ L$_{top}$ = 1600 mm<br>Se(II) $\eta = 96.82\%$ L$_{bottom}$ = 828 mm | Se(I) | $M(TeO_2)$ = 60.40 g | $M(TeO_2)$ = 63.37 g | $M(TeO_2)$ = 62.15 g | $M(TeO_2)$ = 61.48 g | $M(TeO_2)$ = 48.43 g |
| Radiopurity | see Table 2.38 | | | | | | |

Table 2.14 : Composition, total length (with partial lengths for metallic strips), mass and abundance of the seven strips of **sector 08**: $\eta$ is the percentage of $\beta\beta$ decay isotope in the enriched sample; $M_1$, $M_2$ and $M_3$ are respectively the **t**otal mass of material in the foils, the mass of the investigated **e**lement in the foils, and the mass of the $\beta\beta$ decay **i**sotope in the foils.

| Sector 09 | | | | | | | |
|---|---|---|---|---|---|---|---|
| Material | Composite strips $^{130}$Te$0_2$ | | | | | | |
| Strip number | 1 | 2 | 3 | 4 | 5 | 6 | 7 |
| Total length L(mm) | 2424 | 2425 | 2426 | 2425 | 2425 | 2425 | 2425 |
| Width(mm) | 63 | 65 | 65 | 65 | 65 | 65 | 63 |
| $M_1$(g) | 54.01 | 56.65 | 54.50 | 55.15 | 54.18 | 53.62 | 55.66 |
| $M_2$(g) | 36.35 | 35.93 | 36.58 | 37.07 | 36.33 | 35.91 | 37.60 |
| $M_3$(g) | 32.50 | 32.12 | 32.70 | 33.10 | 32.48 | 32.10 | 33.61 |
| $\eta$ (%) | 89.4 | 89.4 | 89.4 | 89.4 | 89.4 | 89.4 | 89.4 |
| Comments $M(TeO_2)$ (g) | 45.31 | 44.79 | 45.60 | 46.21 | 45.29 | 44.76 | 46.87 |
| Radiopurity | see Table 2.38 | | | | | | |

Table 2.15: Composition, total length (with partial lengths for metallic strips), mass and abundance of the seven strips of **sector 09**: $\eta$ is the percentage of $\beta\beta$ decay isotope in the enriched sample; $M_1$, $M_2$ and $M_3$ are respectively the **t**otal mass of material in the foils, the mass of the investigated **e**lement in the foils, and the mass of the $\beta\beta$ decay **i**sotope in the foils.

| Sector 10 | | | | | | | |
|---|---|---|---|---|---|---|---|
| Material | Composite strips $^{100}$Mo | | | | | | |
| Strip number | 1 | 2 | 3 | 4 | 5 | 6 | 7 |
| Total length L(mm) | 2426 | 2428 | 2427 | 2426 | 2426 | 2427 | 2428 |
| Width(mm) | 63 | 65 | 65 | 65 | 65 | 65 | 63 |
| $M_1$(g) | 103.21 | 102.69 | 101.99 | 102.63 | 105.30 | 104.76 | 102.91 |
| $M_2$(g) | 85.45 | 84.69 | 83.47 | 84.05 | 86.45 | 85.97 | 84.97 |
| $M_3$(g) | 81.12 | 80.39 | 80.52 | 81.08 | 83.39 | 82.93 | 81.45 |
| $\eta$ (%) | 95.14 | 95.14 | 96.66 | 96.66 | 96.66 | 96.66 | 96.32 mean value |
| Batch | 2 | 2 | 3.1 | 3.1 | 3.1 | 3.1 | 2 + 3.1 |
| Radiopurity | see Table 2.36 and column $^{100}$Mo (1) in Table 2.37 | | | | | | |

Table 2.16: Composition, total length (with partial lengths for metallic strips), mass and abundance of the seven strips of **sector 10**: $\eta$ is the percentage of $\beta\beta$ decay isotope in the enriched sample; $M_1$, $M_2$ and $M_3$ are respectively the **t**otal mass of material in the foils, the mass of the investigated **e**lement in the foils, and the mass of the $\beta\beta$ decay **i**sotope in the foils.

| Sector 11 | | | | | | | |
|---|---|---|---|---|---|---|---|
| Material | Composite strips $^{100}$Mo | | | | | | |
| Strip number | 1 | 2 | 3 | 4 | 5 | 6 | 7 |
| Total length L(mm) | 2430 | 2428 | 2426 | 2316 | 2430 | 2427 | 2424 |
| Width(mm) | 63 | 65 | 65 | 65 | 65 | 65 | 63 |
| $M_1$(g) | 95.72 | 102.83 | 105.34 | 110.03 | 107.88 | 101.97 | 98.23 |
| $M_2$(g) | 76.06 | 84.23 | 86.50 | 91.14 | 89.44 | 83.47 | 80.33 |
| $M_3$(mm) | 75.30 | 81.26 | 83.44 | 87.92 | 84.92 | 80.52 | 77.49 |
| $\eta$ (%) | 96.66 | 96.66 | 96.66 | 96.66 | 95.14 | 96.66 | 96.66 |
| Batch | 3.1 | 3.1 | 3.1 | 3.1 | 2 | 3.1 | 3.1 |
| Radiopurity | see Table 2.36 and columns $^{100}$Mo (2) in Table 2.37 | | | | | | |

Table 2.17: Composition, total length (with partial lengths for metallic strips), mass and abundance of the seven strips of **sector 11**: $\eta$ is the percentage of $\beta\beta$ decay isotope in the enriched sample; $M_1$, $M_2$ and $M_3$ are respectively the **t**otal mass of material in the foils, the mass of the investigated **e**lement in the foils, and the mass of the $\beta\beta$ decay **i**sotope in the foils.

| Sector 12 | | | | | | | |
|---|---|---|---|---|---|---|---|
| Material | Composite strips $^{100}$Mo | | | | | | |
| Strip number | 1 | 2 | 3 | 4 | 5 | 6 | 7 |
| Total length L(mm) | 2428 | 2428 | 2430 | 2430 | 2425 | 2410 | 2428 |
| Width(mm) | 63 | 65 | 65 | 65 | 65 | 65 | 63 |
| $M_1$(mm) | 94.33 | 104.86 | 107.35 | 108.12 | 107.40 | 106.28 | 99.91 |
| $M_2$(mm) | 77.36 | 86.67 | 88.48 | 89.64 | 88.98 | 88.04 | 82.42 |
| $M_3$(mm) | 73.44 | 82.28 | 83.99 | 85.09 | 84.47 | 83.58 | 79.04 |
| $\eta$ (%) | 95.14 | 95.14 | 95.14 | 95.14 | 95.14 | 95.14 | 95.14 |
| Batch | 2 | 2 | 2 | 2 | 2 | 2 | 2 |
| Radiopurity | see Table 2.36 and column $^{100}$Mo (1) in Table 2.37 except for strip 4, see column $^{100}$Mo (2) | | | | | | |

Table 2.18: Composition, total length (with partial lengths for metallic strips), mass and abundance of the seven strips of **sector 12**: $\eta$ is the percentage of $\beta\beta$ decay isotope in the enriched sample; $M_1$, $M_2$ and $M_3$ are respectively the **t**otal mass of material in the foils, the mass of the investigated **e**lement in the foils, and the mass of the $\beta\beta$ decay **i**sotope in the foils.

| Sector 13 | | | | | | | |
|---|---|---|---|---|---|---|---|
| Material | Composite strips $^{100}$Mo | | | | | | |
| Strip number | 1 | 2 | 3 | 4 | 5 | 6 | 7 |
| Total length L(mm) | 2429 | 2426 | 2428 | 2337 | 2426 | 2430 | 2427 |
| Width(mm) | 63 | 65 | 65 | 65 | 65 | 65 | 63 |
| $M_1$(mm) | 97.32 | 105.21 | 104.45 | 108.52 | 108.36 | 104.57 | 94.23 |
| $M_2$(mm) | 80.33 | 87.19 | 86.60 | 90.55 | 90.15 | 86.68 | 77.14 |
| $M_3$(mm) | 77.13 | 86.07 | 83.14 | 89.39 | 86.55 | 83.22 | 74.06 |
| $\eta$ (%) | 96.20 | 98.95 | 96.20 | 98.95 | 96.20 | 96.20 | 96.20 |
| Batch | 4 | 3.2 | 4 | 3.2 | 4 | 4 | 4 |
| Radiopurity | see Table 2.36 and column $^{100}$Mo (4) in Table 2.37 | | | | | | |

Table 2.19 : Composition, total length (with partial lengths for metallic strips), mass and abundance of the seven strips of **sector 13**: $\eta$ is the percentage of $\beta\beta$ decay isotope in the enriched sample; $M_1$, $M_2$ and $M_3$ are respectively the **t**otal mass of material in the foils, the mass of the investigated **e**lement in the foils, and the mass of the $\beta\beta$ decay **i**sotope in the foils.

| Sector 14 | | | | | | | |
|---|---|---|---|---|---|---|---|
| Material | Composite strips $^{100}$Mo | | | | | | |
| Strip number | 1 | 2 | 3 | 4 | 5 | 6 | 7 |
| Total length L(mm) | 2426 | 2426 | 2428 | 2426 | 2373 | 2429 | 2269 |
| Width(mm) | 63 | 65 | 65 | 65 | 65 | 65 | 63 |
| $M_1$(g) | 95.93 | 105.03 | 107.07 | 110.57 | 109.95 | 102.71 | 103.85 |
| $M_2$(g) | 78.98 | 87.01 | 88.88 | 90.08 | 91.71 | 84.91 | 86.50 |
| $M_3$(g) | 77.97 | 85.90 | 87.75 | 88.93 | 90.54 | 83.83 | 86.08 |
| $\eta$ (%) | 98.95 | 98.95 | 98.95 | 98.95 | 98.95 | 98.95 | 98.95 |
| Batch | 3.2 | 3.2 | 3.2 | 3.2 | 3.2 | 3.2 | 3.2 |
| Radiopurity | see Table 2.36 and column $^{100}$Mo (3) in Table 2.37 | | | | | | |

Table 2.20 : Composition, total length (with partial lengths for metallic strips), mass and abundance of the seven strips of **sector 14**: $\eta$ is the percentage of $\beta\beta$ decay isotope in the enriched sample; $M_1$, $M_2$ and $M_3$ are respectively the **t**otal mass of material in the foils, the mass of the investigated **e**lement in the foils, and the mass of the $\beta\beta$ decay **i**sotope in the foils.

| Sector 15 | | | | | | | |
|---|---|---|---|---|---|---|---|
| Material | Composite strips $^{100}$Mo | | | | | | |
| Strip number | 1 | 2 | 3 | 4 | 5 | 6 | 7 |
| Total length L(mm) | 2429 | 2427 | 2425 | 2361 | 2426 | 2427 | 2428 |
| Width(mm) | 63 | 65 | 65 | 65 | 65 | 65 | 63 |
| $M_1$(mm) | 104.38 | 108.14 | 108.76 | 109.51 | 109.93 | 108.15 | 104.98 |
| $M_2$(mm) | 86.79 | 89.96 | 90.52 | 91.45 | 91.58 | 89.96 | 87.33 |
| $M_3$(mm) | 83.32 | 86.37 | 86.91 | 87.79 | 87.92 | 86.37 | 83.34 |
| $\eta$ (%) | 96.20 | 96.20 | 96.20 | 96.20 | 96.20 | 96.20 | 96.20 |
| Batch | 4 | 4 | 4 | 4 | 4 | 4 | 4 |
| Radiopurity | see Table 2.36 and column $^{100}$Mo (5) in Table 2.37 | | | | | | |

Table 2.21 : Composition, total length (with partial lengths for metallic strips), mass and abundance of the seven strips of **sector 15**: $\eta$ is the percentage of $\beta\beta$ decay isotope in the enriched sample; $M_1$, $M_2$ and $M_3$ are respectively the **t**otal mass of material in the foils, the mass of the investigated **e**lement in the foils, and the mass of the $\beta\beta$ decay **i**sotope in the foils.

| Sector 16 | | | | | | | |
|---|---|---|---|---|---|---|---|
| Material | Composite strips $^{100}$Mo | | | | | | |
| Strip number | 1 | 2 | 3 | 4 | 5 | 6 | 7 |
| Total length L(mm) | 2427 | 2428 | 2427 | 2424 | 2428 | 2429 | 2427 |
| Width(mm) | 63 | 65 | 65 | 65 | 65 | 65 | 63 |
| $M_1$(mm) | 87.71 | 100.46 | 108.98 | 109.65 | 108.76 | 102.35 | 93.82 |
| $M_2$(mm) | 69.89 | 82.68 | 90.72 | 91.05 | 90.51 | 84.49 | 75.35 |
| $M_3$(mm) | 66.34 | 78.49 | 87.10 | 86.43 | 86.90 | 90.34 | 71.53 |
| $\eta$ (%) | 95.14 | 95.14 | 96.20 | 95.14 | 96.20 | 95.3 mean value | 95.14 |
| Batch | 1 | 2 | 4 | 2 | 4 | 1 + 2 + 3.2 + 4 | 1 |
| Radiopurity | see Table 2.36 and column $^{100}$Mo (6) in Table 2.37 | | | | | | |

Table 2.22 : Composition, total length (with partial lengths for metallic strips), mass and abundance of the seven strips of **sector 16**: $\eta$ is the percentage of $\beta\beta$ decay isotope in the enriched sample; $M_1$, $M_2$ and $M_3$ are respectively the **t**otal mass of material in the foils, the mass of the investigated **e**lement in the foils, and the mass of the $\beta\beta$ decay **i**sotope in the foils.

| Sector 17 | | | | | | | |
|---|---|---|---|---|---|---|---|
| Material | Composite strips $^{130}TeO_2$ | | | | | | |
| Strip number | 1 | 2 | 3 | 4 | 5 | 6 | 7 |
| Total length L(mm) | 2423 | 2422 | 2423 | 2315 | 2425 | 2424 | 2424 |
| Width(mm) | 63 | 65 | 65 | 65 | 65 | 65 | 63 |
| $M_1$(mm) | 53.44 | 52.99 | 56.17 | 57.29 | 52.49 | 52.40 | 50.74 |
| $M_2$(mm) | 35.91 | 35.43 | 37.85 | 38.91 | 35.06 | 34.98 | 33.87 |
| $M_3$(mm) | 32.10 | 31.67 | 33.84 | 34.79 | 31.34 | 31.27 | 30.28 |
| $\eta$ (%) | 89.4 | 89.4 | 89.4 | 89.4 | 89.4 | 89.4 | 89.4 |
| Comments $M(TeO_2)$ (g) | 44.77 | 44.17 | 47.18 | 48.50 | 43.70 | 43.61 | 42.22 |
| Radiopurity | see Table 2.38 | | | | | | |

Table 2.23: Composition, total length (with partial lengths for metallic strips), mass and abundance of the seven strips of **sector 17**: $\eta$ is the percentage of $\beta\beta$ decay isotope in the enriched sample; $M_1$, $M_2$ and $M_3$ are respectively the **t**otal mass of material in the foils, the mass of the investigated **e**lement in the foils, and the mass of the $\beta\beta$ decay **i**sotope in the foils.

| Sector 18 | | | | | | | |
|---|---|---|---|---|---|---|---|
| Material | $^{116}$Cd metallic foils + mylar | | | | | | |
| Strip number | 1 | 2 | 3 | 4 | 5 | 6 | 7 |
| Total length L(mm) | 2432 | 2458 | 2456 | 2458 | 2458 | 2458 | 2433 |
| Width(mm) | 63 | 65 | 65 | 65 | 65 | 65 | 63 |
| $M_1$(g) | 56.03 | 68.64 | 70.39 | 83.96 | 78.11 | 69.47 | 64.58 |
| $M_2$(g) | 47.69 | 59.76 | 61.45 | 76.09 | 70.50 | 61.88 | 57.05 |
| $M_3$(g) | 44.45 | 55.70 | 57.27 | 70.92 | 65.71 | 57.67 | 53.17 |
| $\eta$ (%) | 93.2 | 93.2 | 93.2 | 93.2 | 93.2 | 93.2 | 93.2 |
| Comments | Cd(I) | Cd(I) | Cd(I)<br>3<br>Cd(II)<br>1, 2 | Cd(II) | Cd(I)<br>1, 2<br>Cd(II)<br>3 | Cd(I)<br>3<br>Cd(II)<br>1, 2 | Cd(I)<br>1<br>Cd(II)<br>2, 3 |
| Radiopurity | see Table 2.38 | | | | | | |

Table 2.24: Composition, total length (with partial lengths for metallic strips), mass and abundance of the seven strips of **sector 18**: $\eta$ is the percentage of $\beta\beta$ decay isotope in the enriched sample; $M_1$, $M_2$ and $M_3$ are respectively the **t**otal mass of material in the foils, the mass of the investigated **e**lement in the foils, and the mass of the $\beta\beta$ decay **i**sotope in the foils.

| Sector 19 | | | | | | | |
|---|---|---|---|---|---|---|---|
| Material | Composite strips $^{nat}TeO_2$ (33.8 % $^{130}Te$) | | | | | | |
| Strip number | 1 | 2 | 3 | 4 | 5 | 6 | 7 |
| Total length L(mm) | 2433 | 2435 | 2434 | 2434 | 2434 | 2433 | 2410 |
| Width(mm) | 63 | 65 | 65 | 65 | 65 | 65 | 63 |
| $M_1$(g) | 81.51 | 85.48 | 71.14 | 68.38 | 71.31 | 84.53 | 84.53 |
| $M_2$(g) | 56.54 | 59.39 | 48.54 | 46.45 | 48.67 | 58.67 | 59.10 |
| $M_3$(g) | 19.11 | 20.07 | 16.41 | 15.70 | 16.45 | 19.83 | 19.98 |
| $\eta$ (%) ($^{130}$Te) | 33.8 | 33.8 | 33.8 | 33.8 | 33.8 | 33.8 | 33.8 |
| Comments $M(TeO_2)$ (g) | 70.72 | 74.28 | 60.71 | 58.10 | 60.88 | 73.38 | 73.92 |
| Radiopurity | see Table 2.38 | | | | | | |

Table 2.25: Composition, total length (with partial lengths for metallic strips), mass and abundance of the seven strips of **sector 19**: $\eta$ is the percentage of $\beta\beta$ decay isotope in the enriched sample; $M_1$, $M_2$ and $M_3$ are respectively the **t**otal mass of material in the foils, the mass of the investigated **e**lement in the foils, and the mass of the $\beta\beta$ decay **i**sotope in the foils.

## 2.3 Design of the calorimeter

### 2.3.1 Description

The three functions of the NEMO 3 calorimeter are to measure the particle energy, make time-of-flight measurements and give a fast trigger signal. The calorimeter is constructed with 1940 counters, each of which is made with a plastic scintillator, light guide and PMT (3" or 5") as shown in Fig. 2.13. The gains of the PMTs have been adjusted to cover energies up to 12 MeV. The plastic scintillators were chosen to minimize backscattering and for their radiopurity. The scintillators completely cover the two cylindrical walls which surround the tracking volume. There is also partial coverage of the top and bottom end-caps (also called petals).

The scintillator blocks are inside the helium-alcohol gas mixture of the tracking detector in order to minimize energy loss in the detection of electrons. The blocks are supported by a rigid frame, which allows the PMTs to be outside the helium environment. This configuration prevents rapid aging of the PMTs due to the helium.

The detailed characteristics and nomenclature for the calorimeter scintillator arrays are best studied through Table 2.26 and Table 2.27 along with the graphical representation of Fig. 1.13. The arrays of scintillator for the calorimeter's petals are identified as L1 through L4 as one goes out radially. For the cylindrical walls of a sector, the internal wall array is designated IN and for the external wall there are the center (EC) and the edge (EE) arrays. There are seven types of scintillator which are distinguished by their different shapes which have been designed to fit the circular geometry of the NEMO 3 detector. All the scintillator blocks have a thickness of 10 cm which is a compromise to obtain a high enough efficiency (50% at 500 keV) for $\gamma$-ray tagging with plastic scintillators without loss of transparency of the scintillation light for the electron energy resolution (electrons from double beta decay being detected only in the entrance face of the scintillator block). The $\gamma$-ray tagging allows the measurement of the residual radioactivity of the source foil as well as rejecting background events.

### 2.3.2 Scintillator and light guide characteristics

The INR Kiev-Kharkov collaboration (Ukraine, with AMCRYS Institute of Kharkov) was given the charge of producing the 480 end-cap scintillators and JINR was assigned the 1460 wall scintillators. The preparation and installation of the scintillator blocks were under CENBG responsibility for the walls and IReS for the petals. Serge Jullian, the spokesman of the NEMO collaboration was given the charge of the global oversight. Finally, 28 working meetings took place between 1994 and 1999, in order to optimize the scintillators, to compare the test measurements realized in the different laboratories and to follow the realization of the 1940 blocks. The scintillator composition and their arrangment as well as those for the light guides and the interface guides are the result of these five years of R&D.

#### 2.3.2.1 Scintillator characteristics

The NEMO 3 scintillator was produced by conventional methods of styrene ($C_6H_5CH{=}CH_2$ with a mean Z value of 3.7 per atom) polymerization. Even if one to two centimeters of scintillators are enough to stop electrons with energies up to 12 MeV, the low density of polystyrene reduce the probablity of $\gamma$-ray interaction. Thus it was necessary to use a bigger width of 10 cm. It must be noted that even with this width, which results of a compromize, the efficiency is only 50% for 500 keV $\gamma$-rays.

| | |
|---|---|
| Thickness of one block | 100 mm |
| Length of one block (between layers of wires) | 126 mm |
| Total number of scintillators | 480 |
| Total mass of end-cap scintillators | 1 ton |
| **Layer L1** | |
| Number of L1 blocks per sector for two petals | 6 |
| Width of one block | 113/126 mm |
| Volume of one scintillator | 1.5 l |
| Associated PMT | 3” |
| Total number of L1 blocks | 120 |
| **Layer L2** | |
| Number of L2 blocks per sector for two petals | 6 |
| Width of one block | 133/146 mm |
| Volume of one scintillator | 1.8 l |
| Associated PMT | 3” |
| Total number of L2 blocks | 120 |
| **Layer L3** | |
| Number of L3 blocks per sector for two petals | 6 |
| Width of one block | 174/188 mm |
| Volume of one scintillator | 2.3 l |
| Associated PMT | 3” |
| Total number of L3 blocks | 120 |
| **Layer L4** | |
| Number of L4 blocks per sector for two petals | 6 |
| Width of one block | 195/208 mm |
| Volume of one scintillator | 2.5 l |
| Associated PMT | 5” |
| Total number of L4 blocks | 120 |

Table 2.26 : End-cap scintillator characteristics. The block composition is 98.75% of polystyrene with 1.2% of PTP and 0.05% of POPOP.

Concerning electrons or positrons, a charged particle moving inside the polystyrene loses its energy very quickly by ionization and the number of excited molecules is proportional to the deposited energy. De-excitation of the molecules use fluorescence principle, with a characteristic time of few nanoseconds. Concerning $\gamma$-rays, the dominant interaction in polystyrene is the Compton effect, due to its low mean Z, and the scintillator only detect the Compton electron coming of the $\gamma$-ray scattering. Thus, in usual conditions only a few part of the photon energy is detected.

The molecules excited by passing through polystyrene use thermal dissipation for their de-excitation (that means collisions between same type molecules). Thus, the chemical nature of the material used for scintillator production is the solid solution in polystyrene of a scintillating agent p-Terphenyl (PTP), which recovers the excitation energy before dissipation, and a wavelength shifter 1.4bis (5-phenyl-2-oxazoly)benzene (POPOP), which moves the fluorescence spectrum to a frequency better suited for the PMT photocathode.

| | |
|---|---|
| Total number of scintillators | 1460 mm |
| Total mass of wall scintillators | 5.4 tons |
| **Internal vertical wall** | |
| Number of **IN** blocks per sector for 17 layers | 34 |
| Thickness of one block | 110 mm |
| Height of one block | 153 mm |
| Width of one block | 154/138 mm |
| Volume of one scintillator | 2.4 l |
| Associated PMT | 3” |
| Total number of IN blocks | 680 |
| **External vertical wall** | |
| Number of **EC** blocks per sector for 13 layers | 13 |
| Thickness of one block | 99 mm |
| Height of one block | 200 mm |
| Width of one block | 218/228 mm |
| Volume of one scintillator | 4.5 l |
| Associated PMT | 5” |
| Total number of EC blocks | 260 |
| Number of **EE** blocks per sector for 13 layers | 26 |
| Thickness of one block | 99/123 mm |
| Height of one block | 200 mm |
| Width of one block | 218/230 mm |
| Volume of one scintillator | 5.0 l |
| Associated PMT | 5” |
| Total number of EC blocks | 520 |

Table 2.27: Vertical wall scintillator characteristics. The block composition is 98.49% of polystyrene with 1.5% of PTP and 0.01% of POPOP.

During the fabrication, optical tranmission measurements were made for different wavelengths between 300 and 500 nm on styrene before and after distillation, on the mixing after addition of the scintillating and shifter agents and finally on the polymerized block. The rate of residual monomere was also measured because its value governs the stability of plastic scintillators. The average value was $(0.78 \pm 0.06)\%$ for JINR blocks.

A lot of studies were accomplished, concerning the concentration, the temperature, the cycle duration for the polymerization, the heating, ... JINR group showed during these R&D studies that 2% of PTP associated with 0.05% of POPOP were equivalent to 1.5% of PPO (2,5-Diphenyl-oxazole) associated with 0.05% of POPOP, because PPO and PTP play the same role in the mixing. The best mixing chosen by JINR is 1.5% of PTP associated with 0.01% of POPOP. Some improvements were made also for the realization, as the use of an automatic mixer in inert atmosphere and the use of new moulds to obtain a better uniformity of the temperature inside a block during the polymerization.

After studies in both production laboratories, the mass fractions of polystyrene, PTP and POPOP were finally chosen: for the end-cap scintillator blocks, the composition is 98.75% of polystyrene with 1.2% of PTP and 0.05% of POPOP; for the wall scintillator blocks, the composition is 98.49% of polystyrene with 1.5% of PTP and 0.01% of POPOP.

The realization of a big plastic scintillator block of 72 kg cut to obtain the NEMO 3 wall scintillators used a four step method. First a vacuum distillation of 85 l of the styrene monomer under gaseous nitrogen, was carried out at heating temperature of $50^o$ C, with a rythm of 4 l distillated in 1h30 (that means 31 hours for 85 l). Next PTP and POPOP were dissolved in the styrene during 3 h at $80^o$ C. Then the solution was filtered and finally placed in an automated heating system in aluminium box to promote polymerization during 120 hours (with first a linear increasing of the temperature during 32 h, then 48 h at $180^o$ C and finally decreasing of the temperature in 40 h).

The big blocks from JINR were 29 cm high, 52 cm thick and a depth of 46 cm for EE and EC blocks of external walls and a depth of 52 cm for IN blocks of internal walls[12]. Blocks realized in Dubna were then cut and machined to obtain EE, EC and IN scintillator blocks for NEMO 3.

As performance objectives, the energy resolution $\sigma(E)/E$ for 1 MeV electrons had to be better than 6.2%. This resolution was checked during production using 482 and 976 keV conversion electrons produced by a $^{207}$Bi source. After etching the blocks under water to obtain diffusive reflection at the surfaces, there was an improvement in the resolution by about 1%. The average values of the energy resolution were respectively 5.1% for IN blocks and 5.5% for EE and EC blocks. To ensure the use of scintillators with the best resolution, a greater number of scintillator blocks was produced than necessary: 1093 IN blocks for 680 used (62%), 994 EE blocks for 520 used (52%) and 428 EC blocks for 260 used (61%) (histograms of the number of blocks versus their resolution (FWHM) are shown in Fig. 2.14). Note that energy resolution of the end-cap blocks was not measured in Kiev but only in IReS after depolishing, and before housing and mechanical arrangement of the petal scintillators.

In order to compare the performance of the different types of scintillator several tests were made such as optical transmission. The emission peak of photons associated with the NEMO 3 scintillators is centered at 420 nm with an efficiency of around 1 photon when the incident charged particle has an energy loss of 100 eV. This wavelength corresponds to the maximal sensitivity of the PMT photocathode. For a 10 cm thick sample from Dubna, the light transmission was on average 75% and always greater than 70% for the wavelength of 420 nm (see Fig. 2.15).

The radiopurity of the scintillator was also measured and found to be respectively 430 and 60 times lower in $^{214}$Bi and $^{208}$Tl activity than the PMTs used to read it out, which are also low radioactivity PMTs (see Tables 2.39, 2.40 and 2.42 in Section 2.9).

The scintillator blocks were then sent to CENBG and IReS. The blocks to mount with the best resolution were installed on the walls and petals of the detector.

#### 2.3.2.2 Light guide characteristics

For the light guides a special optical PMMA (poly(methyl methacrylate)) plexiglass 60 mm in thickness was manufactured for the experiment and used for the scintillator-PMT interface. This also protects the PMTs from helium. For the 5” PMTs, a second interface guide in PMMA had to be constructed to be adapted to the shape of the photocathode.

For the design of the experiment, the LAL proposed light guides glued in petals and walls as a transition between the scintillators (inside the gas volume) and the PMTs (outside the detector). During the search of manufacturers, an optics’ expert engineer allowed us to find a factory to realize this specific PMMA. The definition of the different surface states was made in CENBG

---

[12] The dimensions of the big blocks were changed during the production, with 26 cm thick and a depth increased to 92 cm for external blocks and 104 cm for internal blocks in order to improve the temperature uniformity during the polymerization.

and IReS. The machining and thermal treatments for the 1940 light guides were realized at the SRM (LAL).

The best characteristics of the light guide are a good seal against helium and a good light transmission, which is 98% through the guides in the wavelength range 380-420 nm. To ensure rigidity the light guide was glued to an iron ring, which provides a pressfit between the guide and the petal or wall. This iron ring is also useful to complete the magnetic shield surrounding the PMTs. A second iron ring was required for the L4 row of counters on the petals. This ring was glued on the 5" PMT's light guide.

### 2.3.3 Photomultiplier tube characteristics

As explained in Section 1.3, the dominant external background comes from the relatively strong activities in the PMTs. Studies with the NEMO 2 detector showed that the main external backgrounds came from standard RTC-XP2312 PMTs of the experiment, with a great activity in the glass bulb (53 g, $^{40}$K $\sim$ 1760 Bq/kg, $^{214}$Bi $\sim$ 25 Bq/kg and $^{208}$Tl $\sim$ 1.5 Bq/kg) and the entrance window (78 g, $^{40}$K $\sim$ 25 Bq/kg, $^{214}$Bi $\sim$ 3 Bq/kg and $^{208}$Tl $\sim$ 0.17 Bq/kg). Data from copper foil (1 m$^2$ and 70 $\mu$m in thickness) and Monte-Carlo simulations have shown that these big activities produced in NEMO 2 around 0.1 two-electron events per hour, for an energy threshold of 400 keV. This background was able to simulate $\beta\beta 2\nu$ signal with period of $3 \times 10^{19}$ years. Thus it was decided to select low radioactivity PMTs for the NEMO 3 detector.

Development of low background PMTs was begun in 1992, in a collaboration between different manufacturers and physicists studying dark matter, double beta decay and neutrino oscillations. The selection criterion for the low radioactivity glass was for the contamination in $^{40}$K, $^{214}$Bi and $^{208}$Tl to be lower than 1.7, 0.83 and 0.17 Bq/kg respectively. The Hamamatsu company was chosen to produce the PMTs for NEMO 3, with the radiopurity of their glass being 100 to 1000 times better than standard glass. The other parts of their PMTs also have very low contamination (see Tables 2.39 and 2.40 in Section 2.9 for the radioactivity measurements of the PMTs).

The IN, L1, L2 and L3 scintillator blocks identified above were coupled to R6091 3" PMTs (230 g[13], 1040 pieces). These tubes have 12 dynodes and a flat photocathode ($\phi = 76$ mm). The EE, EC and L4 scintillator blocks were coupled to R6594 5" PMTs (385 g[14], 900 pieces). These 5" tubes have 10 dynodes and a hemispherical photocathode ($\phi = 127$ mm) for structural integrity and thus need a second interface guide to match the design between the PMT and the light guide.

The Hamamatsu PMTs were chosen not only for their low background but also for their performance (quantum efficiency and gain of the photocathode; excellent linearity up to 4 MeV, with a maximal energy measurement of 12 MeV; low electronic noise (around 10 Hz) at minimal threshold).

The PMT energy resolution can be written as:

$$R^2 = \frac{(2.35)^2}{N_{ph} \times Q.E \times c} \left( \frac{\delta}{\delta - 1} \right) \tag{2.5}$$

where $N_{ph}$ is the number of incident photons arriving on the photocathode ($\sim 2 \times 10^3$ at 1 MeV for NEMO 3 PMTs), $Q.E$ is the quantum efficiency ($\sim$ 20%)[15], $c$ is the collection efficiency of

---

[13] Type 2Q glass bulb for 85.6 g, type A glass window for 70 g, foot for 18.2 g and ceramic for 23.1 g

[14] Type 2Q glass bulb and window for 263.6 g, foot for 41.8 g and ceramic for 86 g

[15] Quantum efficiency for best PMTs is around 34%

multiplication chain $(0.7-0.9)$ and $\delta$ is the coefficient of secondary emission for dynodes ($\delta \sim 5$). From this formula it is clear than improvements in PMT resolution are related to the increasing of the quantum efficiency and collection efficiency. The PMT response as a function of the entrance point on the photocathode must also present a very good homogeneity.

In order to check the PMT production conformity, a dedicated test station using a $H_2$ lamp was developed in IReS (see Fig. 2.16) to evaluate the PMTs.

#### 2.3.3.1 PMT dedicated test station

The station used as light source a self-triggered $H_2$ lamp ($\sim$ 150 Hz) with a filter centered to 420 nm, which gave an electrical signal proportional to the number of photons emitted during a discharge. Attenuators allowed the calibration of the photon flux, using results obtained with 1 MeV electrons from spectrometer. The goal was that the lamp yields the equivalent photon flux on the PMT that is produced by a 1 MeV electron in a NEMO 3 scintillator block, around $2 \times 10^3$ collected photons per MeV. A beam separator guided a fraction of the light to a reference 3/4" PMT.

There was a discrete variation of the photon flux between 0 and 12 MeV using calibrated optical attenuators on a motorized disk. Collimators allowed the illumination of the whole PMT photocathode or the use of a small pencil of light ($\sim$3 mm in diameter) to scan the photocathode. A motorized stage ensured the pencil of light shifting in two directions perpendicular to the PMT axis. This system was put in a 1 $m^3$ black box.

Data acquisition and the HV and motor controls were ensured by a CES/FIC-8234 processor (OS9 system).

#### 2.3.3.2 Test procedure

Before its installation in the black box, the PMT to characterize was connected to a dedicated HV distribution circuit with 16 pins (the Hamamatsu PMTs were delivered without sockets due to low radioactivity requirements).

Hamamatsu PMT informations were written in the program. Then, the evaluation proceeded by first identifying the high-voltage to obtain a charge[16] $Q$ of 125 pC at 1 MeV (gain[17] $G$ of around $2 \times 10^6$, $V \sim 1800$ V for 3" PMTs, $V \sim 1350$ V for 5" PMTs). The energy and time resolutions were then measured at 1 MeV, the average values were respectively 4% and 250 ps. The linearity of the response of the PMTs was studied as a function of energy between 0 and 12 MeV. Also, the symmetry and the uniformity of the photocathode was investigated using the XY moving of the light pencil. Finally the electronic noise at the minimal threshold, 10 mV ($\sim$ 33 keV) was measured.

The test duration was 30 mn for 3" PMTs and 40 mn for 5" PMTs. Informations for each PMT were written in a file for further analysis. Results were summarized, as presented in Fig. 2.17 for a 5" PMT. As a consequence of one year of tests of the PMTs, 49 (2.5%) were rejected and replaced by Hamamatsu: five 5" PMTs (four with broken glass and one with asymmetric photo-

---

[16] The charge $Q$ collected at the anode PMT results of the product of the number $N_{pe}$ of photoelectrons collected by the first dynode by the gain $G$ of the multiplier, with the formula $Q = N_{pe}G$, where $G$ is the product of each individual dynode gain.

[17] The gain of each PMT is related to the working voltage $V$, with $G = \alpha V^\beta$, where the constants $\alpha$ and $\beta$ are related to the PMT and its base characteristics. The $V$ value was given by Hamamatsu for a gain of $3 \times 10^6$. Test measurements were made using a gain of $2 \times 10^6$, which allowed to measure the $\beta$ factors.

cathode) and 44 3" PMTs (one with broken glass, 23 with no-linearity and 20 with asymmetric photocathode).

Also were measured the transit times in the PMTs, with photoelectron collection times between 3 and 4 ns, and a transit time to the anode 50 ns in average for 3" PMTs and 45 ns for 5" PMTs. These time differences imposed to increase the signal cable lengths for 5" PMTs to have uniform transit times for the whole calorimeter.

To minimize the operation of assembling the PMTs in the LSM, the collaboration decided to equip them with their bases and a portion of their light-tight sleeves and nitrogen purge tubes before transportation to the LSM. The light guides were also wrapped with aluminized Mylar before being glued to the 5" PMTs. These operations occured at CENBG for the PMTs of the walls and at IReS for the petals.

### 2.3.4 Preparation and installation of the scintillator blocks

At reception in IReS, the Kharkov blocks were sanded off under water with P1200 paper (with a grain of 4.2 $\mu$m) to obtain diffusive reflection at the surfaces (this step was realized in JINR for the wall blocks sent to CENBG). Then a visual check on the color of the block was made. Five layers of 70 $\mu$m thick Teflon ribbon were wrapped around the four lateral faces of the scintillator block to diffusely scatter the scintillation light for improved light collection. That allows the fluorescence light which is not emitted in the solid angle of the PMT to diffusely scatter on Teflon.

Then, one temporary layer of 12 $\mu$m thick aluminized Mylar was wrapped around the six faces of the scintillator block to realize quality tests before the mounting of the blocks. The energy resolution and the peak position at 1 MeV were checked for several locations on the entrance face of the block with an electron spectrometer using a $^{90}$Sr source (see Section 2.6 for $^{90}$Sr characteristics). The spectrometer from IReS (26x17x21 cm$^3$) had an intrinsic energy resolution of 0.6%. This test identified and rejected blocks with inhomogeneities. All six faces of the selected blocks, with the exception of the contact region for the light guide, were then covered with sheets of aluminized Mylar.

For the petal blocks, two layers of single-sided 6 $\mu$m thick aluminized Mylar (300 nm of aluminium near the scintillator face) on the six faces.

For the wall blocks, two layers of single-sided 6 $\mu$m thick aluminized Mylar (40 nm of aluminium near the scintillator face) on the entrance face and one layer of double face 12 $\mu$m thick aluminized Mylar (500 nm of aluminium on each face of the foil) on the five other faces of the scintillator.

The Mylar not only protects the scintillators from ambient light and from light produced by Geiger propagation plasma in the tracking region, but also enhances the light reflection inside the scintillator, while minimizing energy lost by the electrons at the entrance face.

Attaching the scintillator block to the petals and the walls was made in several steps. First the PMMA light guide was glued[18] to the iron ring. Next the guide and the iron ring were attached to the petal or the wall with RTV filler/sealer[19]. Tests of the helium tightness were then realized. Finally, the guide was optically glued[20] to the scintillator and check for bubbles or irregularities. The last step was to create an external circular seal of RTV-141 on the light guide for future gluing of the PMTs in the LSM. A systematic check of the radiopurity for all the glues used in the NEMO 3 detector was carried out in the LSM [23].

---

[18] Epotek 310 glue with carbonate

[19] RTV-141

[20] Bicron BC600 with a thickness of 100 $\mu$m

Fig. 2.18 and Fig. 2.19 show pictures of the scintillator mounting systems, respectively for the walls at CENBG and for the petals at IReS.

After these operations and before transportation to LAL, the peak position and energy resolution at 1 MeV were measured at the center of each block, using the electron spectrometer. This information was used to identify particular scintillator block and PMT combinations so as to obtain an energy resolution for the calorimeter which was as uniform as possible. Distributions of energy resolution (FWHM) at 1 MeV for petal blocks L1 to L4 are given as a function of ADC channels in Fig. 2.20 (values of FWHM are between 12 and 17% at 1 MeV). This calibration was realized again in the LSM after the sector installation.

The paired scintillators and PMTs (see next Section) for the whole calorimeter gave an energy resolution $\sigma_E/E$ between 6.1 and 7.3% at 1 MeV. The time resolution is around 250 ps at 1 MeV. Detailed performance of the calorimeter are given in Section 3.4.

### 2.3.5 Coupling between scintillator and PMT

The goal was to obtain as uniform response for the calorimeter as possible, attaching PMTs which had a good quantum efficiency and a good electron colllection with scintillators which had a worse light efficiency, or the opposite. It allowed to make the energy resolution for all the scintillator blocks more uniform.

The association procedure was the following. The scintillator response was measured during validation tests and allowed to obtain the ADC response at 1 MeV for each block, with a gaussian distribution of mean value $< ADC >$ and covariance $\sigma_{ADC}$. It was then possible to define the $\mu$ variable for each block, which characterizes the light efficiency of the scintillator and corresponds to the deviation from the mean value.

$$\mu = \frac{ADC - < ADC >}{\sigma_{ADC}}$$

The PMT sensitivity is a ratio of the photocathode current to the photon flux, which characterizes the quantum efficiency of the photocathode and the photoelectron collection efficiency. This sensitivity is well measured by the Corning Blue value (sensitivity at 430 nm, in $\mu$A/lm) given by Hamamatsu for each PMT and checked with the test station. For each PMT one defined the $\nu$ variable, which gives its deviation to the mean CB value.

$$\nu = \frac{CB - < CB >}{\sigma_{CB}}$$

An equilibrated association gave a scintillator-PMT couple with $\nu \approx -\mu$. This procedure suffered from constraints due to the limited number of PMTs and to the fact that there are three PMTs per HV channel, for which their HV values cannot differ by more than 80 V.

The association was made for each type of blocks. Concerning 3" PMTs, L1, L2+L3 and IN blocks were separated. For 5" PMTs, L4 and EE+EC blocks were separated. The association was more difficult to realize for the last sectors, when the number of avalaible PMTs was too low to really satisfy these constraints.

### 2.3.6 Assembly of the PMTs in the LSM

The collaboration decided to have only one operation of gluing in the LSM. Thus the other operations were made in the different laboratories before the sector transportation. The light guides were glued at IReS and CENBG. The PMTs were equipped with their bases and light-tight sleeves (see Fig. 2.13). The iron rings for the petal interface guide in the L4 blocks were glued at LAL during the operations of the gas sealing. The interface guides were covered with aluminized Mylar and glued to their 5" PMTs. Finally, once a sector was transported to the LSM, it was positionned in different frameworks in horizontal and vertical positions using rocking and turning tools especially designed for the LSM site, to be equipped of its 97 PMTs (see Fig. 2.70 in Section 2.8). The 3" PMTs were glued directly to the light guides, while the interface guide already attached to the 5" PMTs were glued to the light guide. The procedure was done per wall and per petal. After two days of drying, the second part of the light-tight sleeve was installed and secured with RTV-141. After a check of light-tightness of the system using a box that was placed directly to the PMT bases, only one PMT was replaced. Next a $\mu$-metal magnetic shield was placed around each PMT. Finally, the gaps between the PMTs and their $\mu$-metal shields was filled with radioactively pure sponge-like material to provide additional isolation from light.

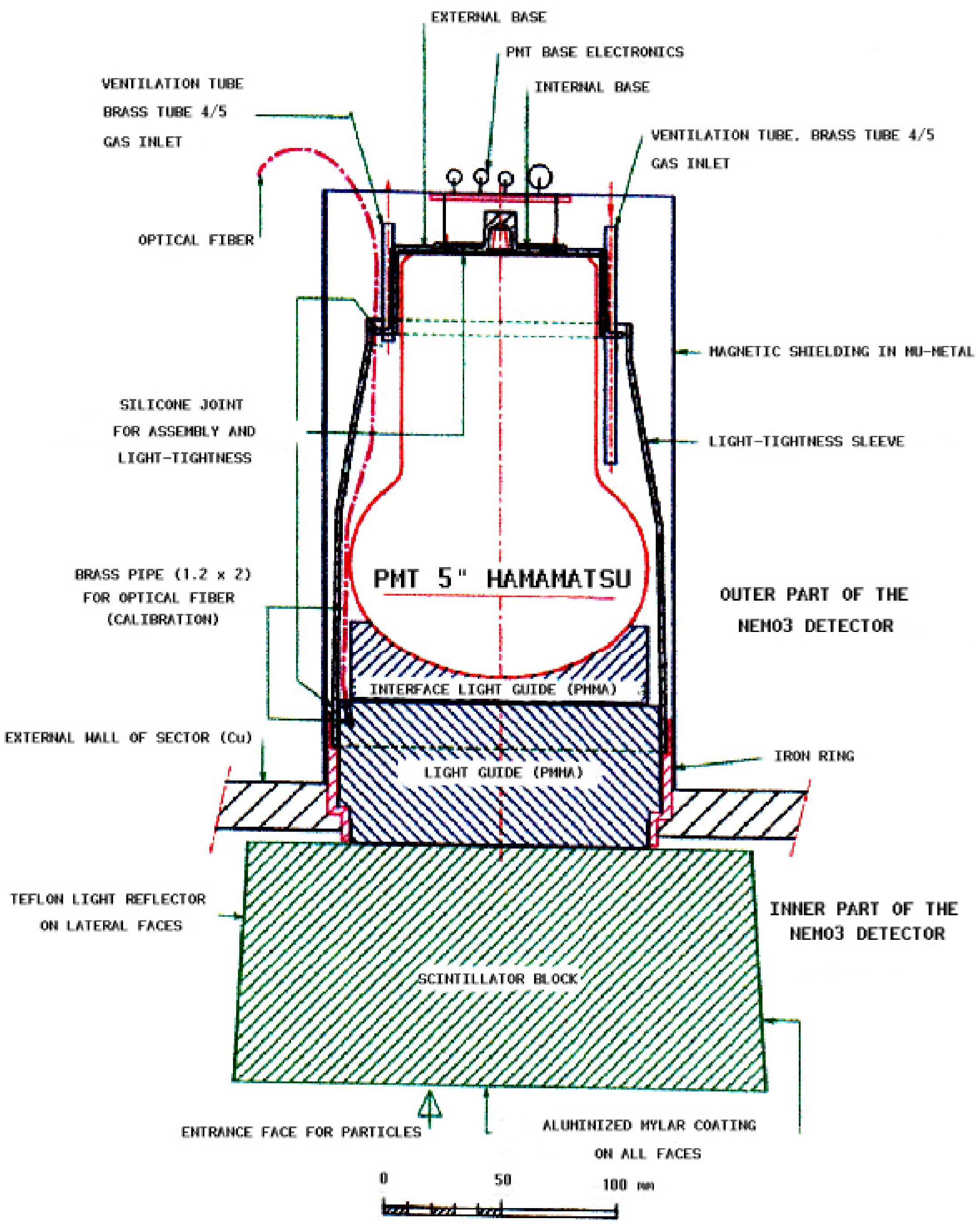

Figure 2.13: NEMO 3 scintillation counter unit for a 5” PMT.

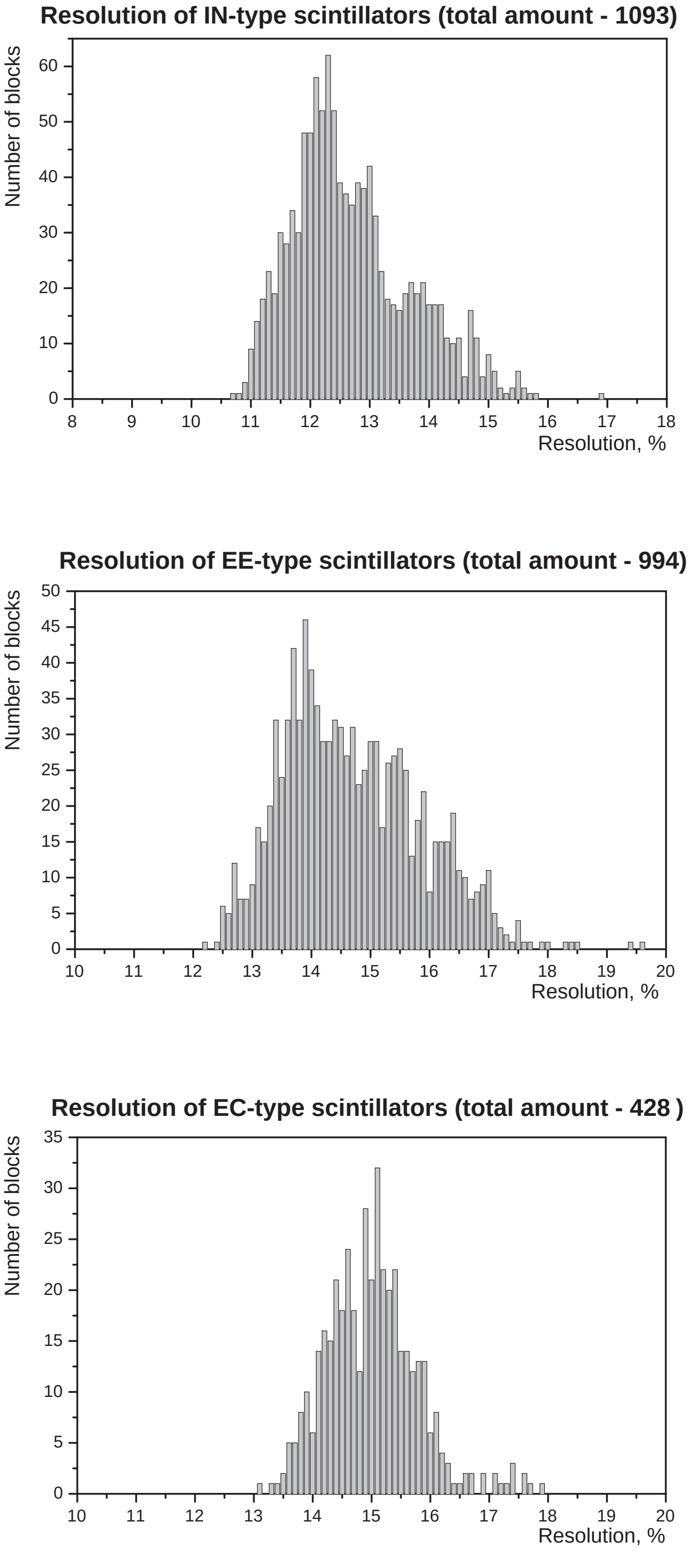

Figure 2.14: Energy resolution (FWHM) measurements from Dubna wall scintillators, respectively for IN, EE and EC blocks (with respectively 680, 520 and 260 blocks used for 20 sectors).

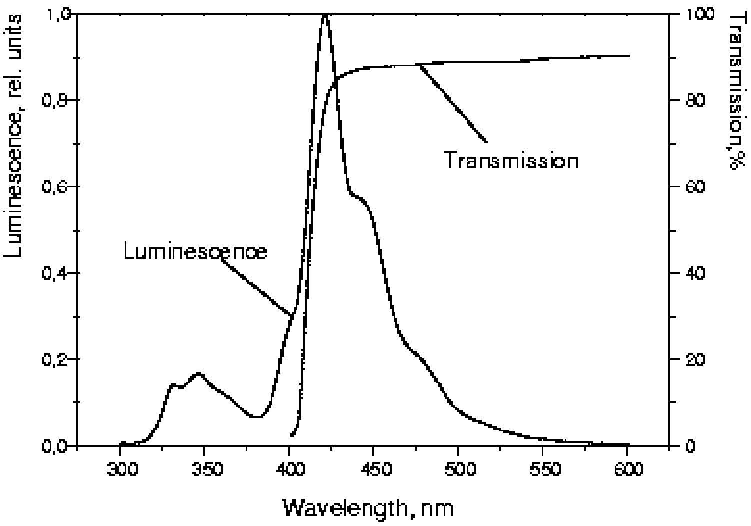

Figure 2.15: Luminescence and transmission spectra of polystyrene-based plastic scintillators, such as that used in the wall blocks, but not a NEMO 3 block, rather a cylinder 10 cm long and 3 cm in diameter.

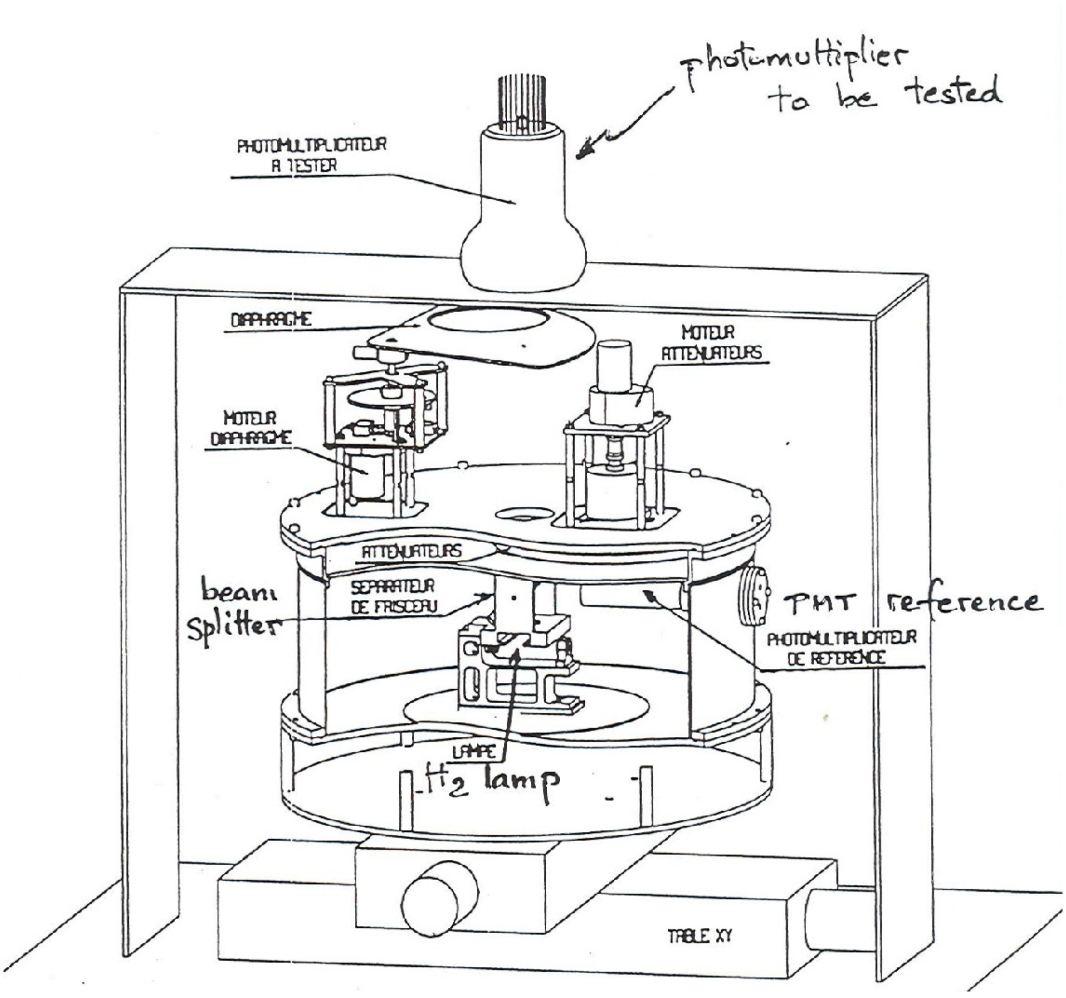

Figure 2.16 : Principle of the PMT dedicated test station at IReS.

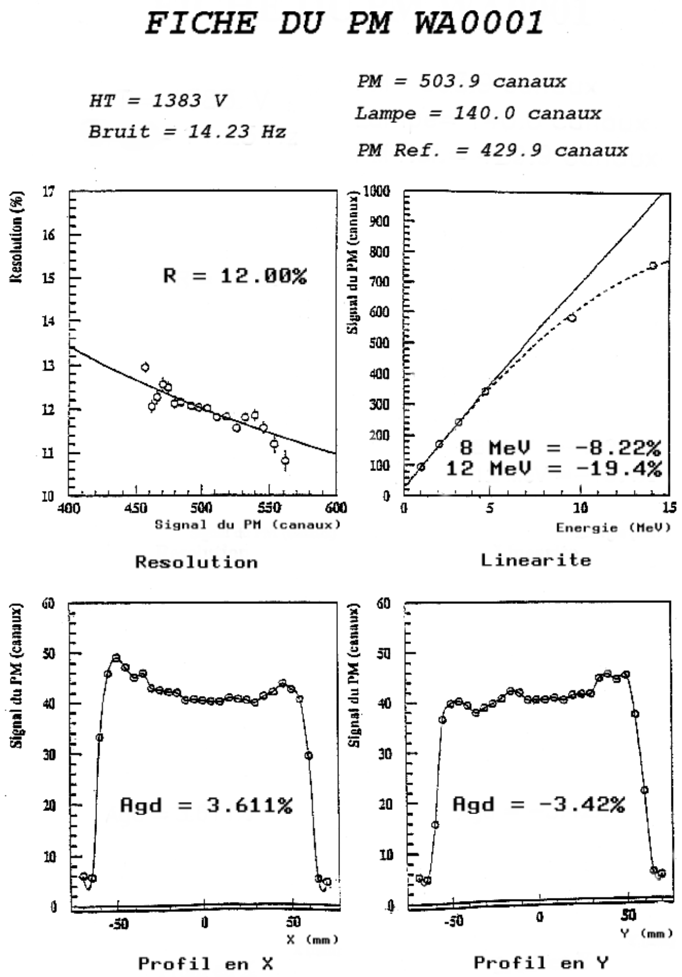

Figure 2.17 : Characteristics of a 5" PMT obtained with the test station. This figure presents the HV value for a gain of $2 \times 10^6$, the noise counts per second at minimal threshold of 33 keV (10 mV) and ADC channel number for PMT at 1 MeV energy, respectively written as "HT", "Bruit" and "PM". The four distributions show:

- on the left top, the energy resolution as a function of the ADC channels. At 1 MeV (500 channels) the typical resolution (FWHM) is 12%. A $1/\sqrt{E}$ fit is surimposed (where $E$ is the energy).

- on the right top, the linearity, which is the PMT response in ADC channels as a function of the energy. The straight line corresponds to a fit on the first points up to 4 MeV. The dotted curve results of a polynomial adjustment. One can see the good linearity up to 4 MeV. The two values give the deviation to the linearity respectively at 8 MeV and 12 MeV energy values.

- the two last distributions, which are respectively called X and Y profiles, show the PMT response in ADC channels for an XY moving of the light pencil on the photocathode, obtained from measurements each 5 mm on X or Y. The $A_{gd}$ value describes the left/right asymmetry for the PMT, with $A_{gd}$ = ((left-right)/(left+right).

Figure 2.18 : Scintillator mounting system on copper walls at CENBG.

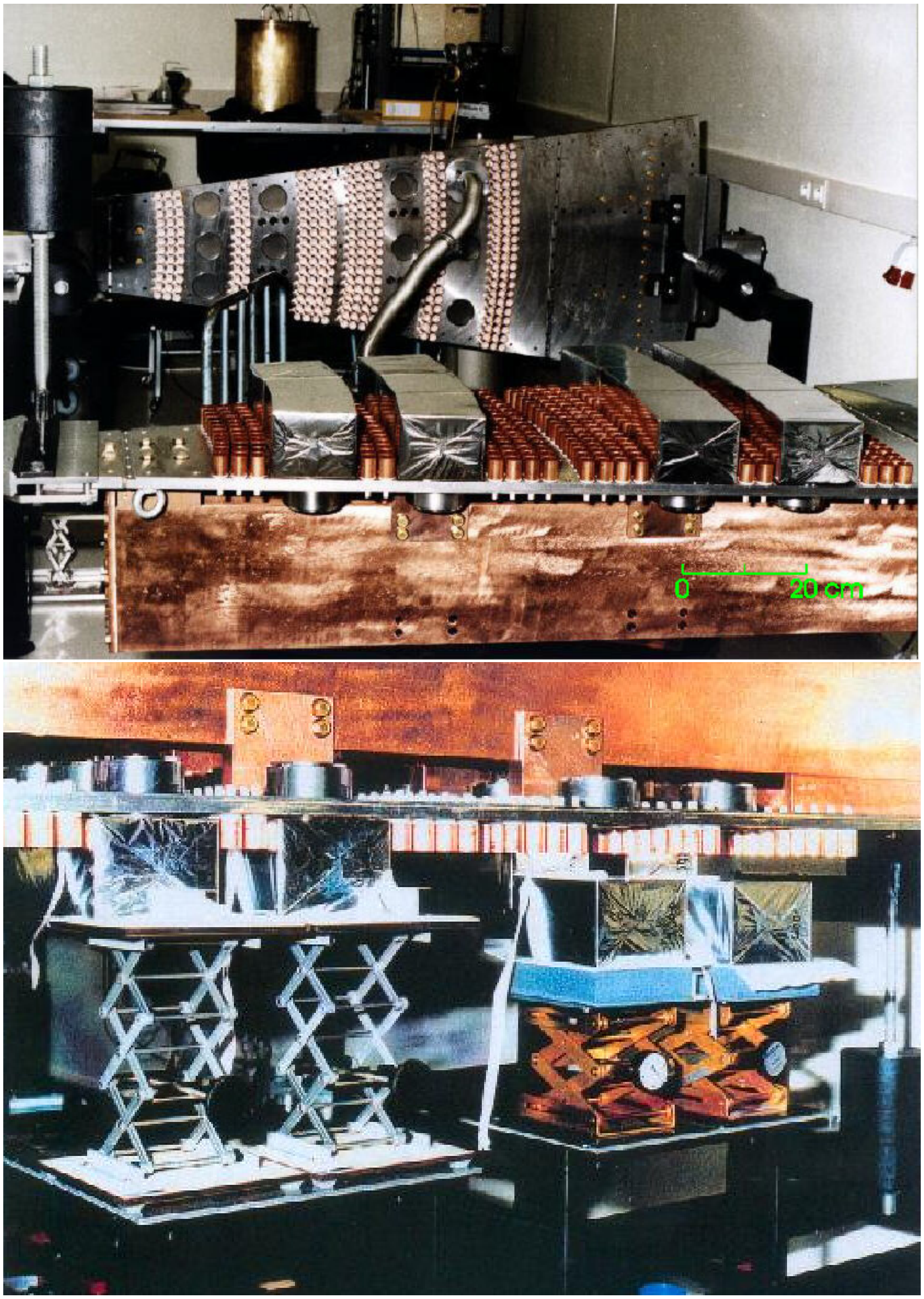

Figure 2.19: Scintillator mounting system on iron petals at IReS.

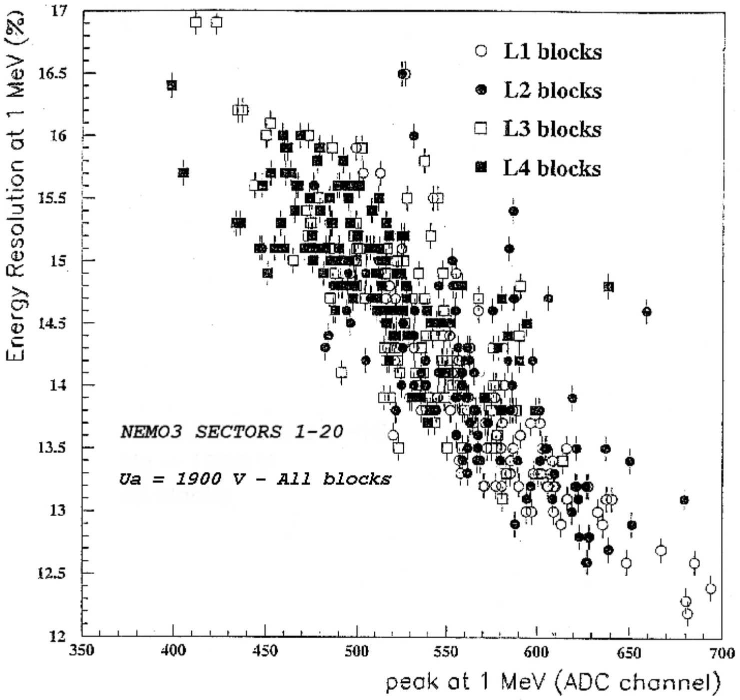

Figure 2.20 : Test results of petal scintillator block validation for the 20 NEMO 3 sectors using the same Phillips 3" PMT as a reference. Figure shows the 1 MeV energy resolution (FWHM) for L1 to L4 blocks as a function of ADC channel.

## 2.4 The tracking detector

### 2.4.1 Description

The tracking volume of the NEMO 3 detector is made of layers of vertical wire drift cells working in Geiger mode (6180 cells with 39820 wires, including anode and ground wires). After a long period of research and development at LAL, which had the responsibility for the tracking, the optimal parameters were identified for the best resolution and efficiency while minimizing multiple scattering effects. This optimization involved a balance between two parameters which contribute to aging effects of the wires. The first is the diameter of the cell's wires which needs to be as low as possible for better transparency in the tracking device. The second is the proportion of helium and alcohol in the gas mixture.

In 2003, it was finally decided to add 1% of argon and 1500 ppm of water in the gas mixture to improve the propagation efficiency and the stability of the tracking detector.

### 2.4.2 Elementary Geiger cell

The cross section of each cell is octagonal in shape with a diameter of 3 cm. It is outlined by 8 wires, as shown in Fig. 2.21. The basic cell consists of a central anode wire surrounded by the 8 ground wires, which belong to four adjacent cells to minimize the number of wires. However, tests on prototypes have shown an electrostatic cross talk between the cells of adjacent layers. As explained in Section 2.4.4, to avoid this problem and after electrostatic simulations with the Garfield software[21], an extra ground wire was added to each cell between the different layers (but not between the cells in the same layer).

All the wires are stainless steel, 50 $\mu$m in diameter and 2.7 m long. The wires are strung between the two iron petals of each sector which form the top and bottom of the detector (see Fig. 1.13). On each end of the cell, there is a cylindrical cathode probe, referred to as the cathode ring, shown in Fig. 1.14 and Fig. 2.21. The cathode ring is 3 cm in length and 2.3 cm in diameter. The anode wire runs through the center of this ring while the ground wires are supported just outside the ring.

Compared to the previous prototypes, NEMO 1 and NEMO 2, there is a new mechanism for securing the wires in the petals. The advantages of this new mechanism are that it allows easy wire installation, avoids the radioactivity of solder, and provides simple serviceability if replacement is necessary. This wire support mechanism is made of three parts as shown in Fig. 2.22 and it allows to secure the wire in a hole machined in the petal, 25 mm long and 3.2 mm in diameter, using three pieces. A Delrin piece acts as a guide to center the wire, then a small rectangular piece of copper, with an electrical contact pin carved into one end, is placed in contact with the centered wire. To firmly secure the wire in place, a tapered half-cylinder of copper is pressed into the mounting hole associated with each wire.

Drift chambers usually work in proportional mode, for which there is, in general, a direct relation between the particle deposited energy and the corresponding electrical signal. In NEMO experiments, one uses the Geiger mode. It allows a saturated amplification of the signal, which can be easily read out with simple electronics (RC circuit).

In the NEMO 3 detector, the cells work in the Geiger mode with a mixture of helium gas with ethyl alcohol and then with addition of argon and water. Under these running conditions, the characteristic operating voltage for the anode wires is now around +1620 V. When a charged

---

[21] Los Alamos National Laboratory, Los Alamos Accelerator Code Group

particle (e.g., a primary electron) crosses a cell, it ionizes some helium atoms. The ionized gas yields $He^+$ ions and around six secondary electrons per centimeter. When these electrons are far away from the anode wire the mean drift velocity is around 1 cm/$\mu$s. These electrons drift towards the anode wire at a speed of about 2.3 cm/$\mu$s when the electrons are close to the anode (around 100 $\mu$m), where the electric field is high. They are strongly accelerated and ionize gas, yielding to tertiary electrons, and so on. There is an avalanch effect, which produces UV photons (with a mean free path of around 1 mm). These UV photons in turn ionize gas around the anode wire producing photoelectrons.

These photoelectrons generate the primary avalanche. Readout electronics measures the arrival time of the avalanche on the anode wire. The anode signal is negative polarity (see Fig. 2.23), which is generated by the ions drifting in the wire chamber towards the anode wire. Measurements of these drift times are used to reconstruct the transverse position of the particle in the cells. The Geiger regime has a fast rise time for the anode pulse (around 10 ns) which can be used with a fixed threshold to provide a good time reference for the TDC measurements (see Section 2.5).

In the Geiger regime, the avalanche near the anode wire develops into a Geiger plasma which propagates along the wire with a speed of 5 cm/$\mu$s [22], depending on the working point (Geiger plateau) which is a function of the gas mixture and the operating voltage. Successive ionizations are created from UV photons produced in the Geiger plasma. The plasma creation and propagation yields a voltage generator, which becomes a current generator using the two cathode rings mentioned above. The electrons are collected by capacitive effect and form a positive cathode signal at each extremity of the wire. After the fast rise time of the current pulse at the anode wire (1), its amplitude is constant while the plasma propagates along the cell to both ends, as shown in part (2) of the pulse in Fig. 2.23. The amplitude of the anode pulse is halved when the plasma reaches one end of the wire (3) and is called the “one-plasma” amplitude. Then, the amplitude becomes zero when the plasma moving in the opposite direction reaches the other end of the cell (4). The arrival of the plasma at the ends of the wire is detected with the cathode rings and produce negative peaks on the anode signal as shown in Fig. 2.23. The propagation times are used to determine the longitudinal position of the particle as it passes through the cell.

The “one-plasma” amplitude of the NEMO 3 Geiger chamber is around 50 mV measured on 270 $\Omega$, that means a current of 200 $\mu$A on average for a total propagation time of 40 $\mu$s for initial gas mixture. The total charge of the plasma $Q$ (around $10^{-8}$ C, that means 0.5 $10^{11}$ charges) represents few 10-fold enhancement compared to proportional chambers.
After triggering the Geiger cell has a dead time of around 500 ms, corresponding to the total ion collection, but this big value is not a problem for the NEMO experiment. The anode and two cathode signals for fired cells are converted in drift and propagation times by the readout electronics, using a fast calorimeter signal as a trigger.

The tracking detector initially used the gas mixture with helium and ethyl alcohol. Helium is a rare gas with a low $Z$ value, which allows a good transparency of the chamber. Alcohol play the role of the quencher, which limits the photoionization process and the triggering of cells adjacent to a fired cell. Alcohol molecule has rotation and vibration energy levels. Thus it absorbs UV photons without emission of radiative energy, which could produce electrons from wires and trigger new avalanches. Alcohol also neutralizes He ions, which also could produce electrons from wires, leading to the use of alcohol ions as the charge carriers. When arriving on

---

[22] 6 to 7 cm/$\mu$s before argon addition in the gas mixture

ground wires, they extract electrons as He ions could do it, but the excess of energy only breaks the molecule producing simpler molecules without photon emission.

However it is necessary to avoid a too high alcohol content, which could produce a too short path length for the UV photons and stop the total propagation of the Geiger plasma along the anode wire. The selected proportion of alcohol results from a compromise to avoid cell aging (see Section 2.4.4).

In 2003 argon and then water were added to the gas mixture of helium and alcohol, in order to stabilize the cell's behavior (see Section 2.8.5). With these final operating conditions, the total propagation time along the anode wires is 52 $\mu$s.

### 2.4.3 NEMO 3 tracking device

Tracking in a 25 Gauss magnetic field were first investigated by Monte-Carlo simulations. The study revealed the optimum configuration of 18 layers of cells. Taking into account multiple scattering in the track reconstruction the result was four layers near the source foil (respectively of 16 and 18 cells for internal and external parts) followed by a gap, then two layers (respectively of 14 and 20 cells) and another gap followed by three layers (respectively of 12 and 23 cells) near the scintillator wall (the "4-2-3" layer configuration, see Fig. 2.21). Thus, there are nine layers on each side of the source foil and possibly 9 cell measurements to optimize track reconstruction. The gaps between the groups of cell layers is due to the position of the plastic scintillators on the petals. The four layers near the source foil are sufficient to provide a precise vertex position. Two layers in the middle and three layers close to the plastic scintillator walls provide good trajectory curvature measurements.

### 2.4.4 Choice of the wire and gas mixture [24]

Initially, NEMO 3 was proposed [12] with the tracking detector made of cells, 2.70 m long, with a nickel anode wire, 100 $\mu$m in diameter, and stainless steel ground wires, 30 $\mu$m in diameter, in a gas mixture with helium and ethyl alcohol at $10^o$ C. Studies with prototypes between 1993 and 1996 have shown that this proposal was not realistic. First prototype tests realized to choose the cell and wire configurations were carried out with the same gas mixture and temperature than in the NEMO 2 detector, that means helium gas with ethyl alcohol at $10^o$ C.

#### 2.4.4.1 Choice of the cell configuration

In the NEMO 3 proposal, an octagonal cell was designed with one anode wire surrounded by eight ground wires. Compare to NEMO 2 tracking chamber, where in worst configuration one 30 mm diameter cell had two neighboring cells only in the same layer with two common ground wires each, the NEMO 3 first proposal for cell configuration was defined to minimize the wire number. Thus, in the worst configuration, it was proposed to surround one 28 mm diameter cell by four cells (two in the same layer as in NEMO 2, and two from adjacent layers) with two common ground wires each.

In 1994, first prototype $9C30$ with 9 cells (3x3) as shown in Fig. 2.24 was realized and tested. There were 30 mm between two anode wires and same HV value put in all cells. It appeared there was a problem with central cell (wire 5), which was surrounded by the eight other cells, involving the need of much higher HV value to obtain the same propagation time and plasma amplitude than other cells.

This difference in working points ($\sim 130$ V for $HV = 1840$ V) for the middle wire was checked and explained using electrostatic simulations of this $9C30$ prototype with Garfield software, as shown in Fig. 2.25. The first conclusion was the need to use one HV value per layer.

These simulations also helped to define the new design for NEMO 3 in order to improve electrostatic separation between cells of adjacent layers and obtain nearly similar working points for all cells. By adding a third ground wire between neighboring cells of adjacent layers, the difference between working points became only 40 V, always for a $HV$ value of 1840 V (see Fig. 2.25). This behavior was then checked with a new prototype designed with this new configuration ($9C28$ as shown in Fig. 2.27). Putting a $HV$ value of 1840 V in anode wires of cells belonging to the two external layers and 1880 V for cells belonging to the middle layers, the nine cells of this prototype showed the same propagation times and amplitudes.

#### 2.4.4.2 Wire material and diameter

First, to avoid problems with magnetic field, it was necessary to use stainless steel not only for ground wires but also for the anode wires.

Second, studies with the $9C28$ prototype showed that for some wires Geiger plasma propagation was not always complete along the wire. This behavior, which could be explained by defects on the anode wires, was a very important problem and a long study was carried out to find the best quality wire, that means with no defect on the wire and with the best uniformity on the wire diameter. A special machine was build to test the quality of different production wires (see Fig. 2.28). Results of tests for numerous wire production (with different diameters and materials), it appeared that stainless steel wire from Trakus Company[23] was the best one for each tested diameter (30, 40, 50 and 100 $\mu$m). Moreover, after the final choice of wire diameter (see conclusions of this Section), Trakus factory realized a special production run of a 200 km long cold drawn stainless steel wire, to ensure the high quality needed and also the precision on the wire diameter.

Finally it was decided to build a bigger size prototype in LAL before the realization of the first NEMO 3 sector (with this new chosen configuration), in order to test with more cells the following points: the use of stainless steel anode wire (instead of nickel); the new gripping system for wires; gas contamination, which could explain the wire defects; electric connections, HV distributions and readout electronics; magnetic effects; etc...

This $20C28$ prototype (as shown in Fig. 2.29) consisted of four adjacent layers, which is the maximal configuration for NEMO 3, with 5 cells in each layer, 28 mm between two anode wires and one ground plane to simulate the NEMO 3 source foil. These studies showed a problem, which is well known for wire chamber: the aging.

#### 2.4.4.3 Compromise between gas mixture, wire diameter and wire material to solve aging problems

The use of the wire with diameters initially proposed for the NEMO 3 detector and the same gas mixture as in NEMO 2 was not possible due to mentionned aging problems, which produced deterioration of performances of the wire chamber. With ground wires 30 $\mu$m in diameter and anode wire 100 $\mu$m in diameter, in a wire chamber filled with the "NEMO 2 gas mixture" consisting of helium and ethyl alcohol at $10^o$ C, bad cell behavior appeared very fast, with high counting rates and breakdowns.

---

[23] Trakus factory, Germany

As a consequence, a exhaustive R&D program was realized in LAL to understand this wire chamber aging. Aging phenomena constitute one of the most complex and serious potential problems in a wire chamber. Studies began in the 50's and 60's on the dissociations of quenching vapors in Geiger tubes; in the 70's, studies of aging effects have been done in multiwire proportionnal chambers; finally, a good understanding with numerous tests apparead in the 80's (see [25] and [26] for reviews on wire chamber aging).

There are various possible explanations for aging. The "classical" aging effects could be attributed to the formation of polymeric deposits due to chemical reactions in the avalanche processes with two different effects for anode and ground wires: anode wire deposits decrease the gain (directly, by conducting deposits, or indirectly, by dipole charging up), when ground (cathode) wire deposits induce self-sustained discharges, because positive ion accumulation (which forms a thin insulator layer deposit) on ground wires creates high dipole field, inducing electron extraction (this is called the Malter effect since the explanation given by Malter in 1936 [27] for the aging of cathode surfaces for Geiger tubes).

Many experiments have demonstrated that the addition of alcohols and water tends to stabilize the detector operation, which is good for NEMO gas mixing using ethyl alcohol, but not to cure the Malter effect.

Also there were a lot of studies about the influence on anode aging of the wire surface quality, the nature and purity of the gas mixture, different additives and trace contaminants, construction materials, gas flow, high-voltage, anode and ground wire dimensions [25].

Using all these informations, various prototypes were realized to find at least one gas/wire combination allowing stable functioning of the chamber with full plasma propagation, avoiding aging (without high counting rates, discharges or breakdowns) and keeping a good transparency for the NEMO 3 tracking chamber (that means not increasing a lot the density of matter, but able to work without aging during at least five years). As a result of these NEMO 3 tests, it was found that:

- to avoid aging, it is important to increase the ground wire surfaces compare to the anode one;
- using "NEMO 2 gas mixture" and various combinations of wire diameters, for an anode wire of a given diameter (for example 100 $\mu$m), the ground wires should have at least the same diameter (that means 100 $\mu$m, so a lost of transparency if keeping both these proposed anode wire diameter and gas mixture);
- to improve the transparency, tests were done using copper coated ground wires in Nylon (sputtering technique was used for copper deposit on Nylon wire), 100 $\mu$m in diameter to keep the same 100 $\mu$m diameter for all the wires but using the low Z value of Nylon compare to stainless steel; this study also revealed the importance of the diameter homogeneity and mechanical properties for the wires;
- decreasing the diameters of both anode and ground wires, it was necessary to increase the proportion of alcohol quencher in the gas mixture (and then to add argon and water to stabilize the chamber functionning as explained in Section 2.8.5);
- to minimize the effect of contamination, which could stop the plasma propagation, it was very important to ensure the surface quality of the wires.

### 2.4.4.4 Conclusions

In conclusion of these three years of studies (with prototypes and with the first sector of NEMO 3, which is now used as a spare sector), all the wires in the NEMO 3 detector were chosen to be stainless steel (for the use of magnetic field), 50 $\mu$m in diameter, with gas mixture of helium, ethyl alcohol at 14$^o$ C (this temperature corresponds to alcohol with 40 mbars of partial pressure in the mixing and allows the use of 1,900 V as maximal HV in anode wires in the LSM[24]), with the addition of argon and water (see Section 2.8.5).

The studies have also shown that a new ground wire was necessary to avoid electrostatic cross-talks between the cells. Thus the octagone of ground wires was realized with 9 wires for layers with only one adjacent layer and with 10 wires for those with two adjacent layers. For cells in the same layer with common HV, no wire was added (see Fig. 2.21). It must be noted that this addition of wires degrades the transparency of the detector.

Finally, these studies with prototypes also confirmed the need for a very high quality wire to ensure proper plasma propagation. Precision in the 50 $\mu$m diameter of the chosen wire (special production run from Trakus company) is better than 1%. The ground wires were then cleaned with heptan. For the anode wires the same cleaning process was used but with the addition of heating (650$^o$ C) to bake impurities from the surface.

## 2.4.5 Assembly and wiring of a sector

To suspend the wire cells the iron petals have an intricate pattern of holes drilled in order to support the 4-2-3 layer configuration. The 1682 holes drilled per sector for the ground wires are 25 mm deep and 3.2 mm in diameter. These mate tightly with the wire securing mechanism. There are 309 larger central holes drilled in each sector, 16 mm in diameter, which were designed to receive a Delrin plug which insulates central anode wire at high voltage. The center of this plug contains a hole to receive the same wire securing device as the ground wires. This plug also holds the copper cathode ring, which protrudes into the tracking volume. To measure the arrival of the plasma at the cathode ring a copper connector passes through the Delrin plug and is attached to the cathod ring. In the construction of the sectors the machining of the 1991 holes were made at the SRM (LAL) and the central plugs were installed before they were sent to IReS where the scintillators were installed in the petals. Walls and petals were then transported to LAL where the sectors were erected and wired.

### 2.4.5.1 The dedicated zone

All the next operations on the sectors, from wiring to glue coating, were made in a dedicated area[25], as shown in Fig. 2.30. There were a class 10,000 clean room (1) with a surpressure system while each sector being supported horizontally in a gimble capable of rotating 360 degrees, a small room for the cleaning of the wires, an another room with a removable roof and a special container to test the sectors (2) and finally a surpressure framework (3) for the final gluing. Other parts of this area were used for moving and rotating of the sectors.

---

[24] Maximal allowed HV value from NEMO power supplies was 2,000 V

[25] Hall 1 of building 200, in LAL

#### 2.4.5.2 The wiring procedure

The sectors were wired in the clean room, using a rotating gimble allowing an optimal access to the holes for wiring (see Fig. 2.31).

The wire securing procedure was the same for the ground and anode wires but the wire spool had to be changed to take advantage of the heating of the anode wire. The wire was thread by a technician across the 2.7 m of the detector using a long needle. The wire was then secured first at one end and then prestressed with a tension of 50 g. Finally, the second end was secured. Wires were strung layer by layer, alternating ground and anode wires. After stringing a layer of the anode wires there were tests of the insulation of the central plug. This test was made by placing 2,500 V on the anode wire, which was a very sensitive test of the wire tension. It also excluded the possibility that the anode wire had been wind round a ground wire. The wiring of one sector took about four weeks for the 1991 wires. When it was completed a second impedance check was made on the anode wires and the resistance of the wires was measured ($\sim 1240\ \Omega$) to test the wire continuity. The sector was then stored with a nitrogen purge to elimate dust that might otherwise be deposited on the wires. Fig. 2.32 and Fig. 2.33 show pictures with details of petals during the sector's wiring.

Note that the collective tension of the 40,000 wires of NEMO 3 applies 2 tons of compression on the petals. To address this problem two copper stiffening ribs were placed on each petal (the ribs can be seen in Fig. 1.13).

#### 2.4.5.3 Test procedure for each sector

Cells were considered of high quality if at operating voltage two conditions were satisfied simultaneously: the counting rate was free of secondary triggers and electrical discharges while the Geiger plasma propagated to both ends of the cell. A special container measuring 6.4 $m^3$ (see Fig. 2.34 and Fig. 2.35) was manufacured at LAL and used to test each of the 20 sectors. The anode signals were checked with an oscilloscope, using cosmic rays and natural radioactivity as sources. During this test the cathode rings were connected to the ground, in order to see the two negative peaks on anode pulses confirming plasma propagation along the complete cell (as shown in Fig. 2.23).

The measured counting rate in the cells using cosmic rays was around 60 Hz compared to 2 Hz in the LSM before the coil and shields were added. Thus, a test for one week at LAL corresponded to several years of operation in the LSM. As a result of the anode tests, it was found that on average 10 of the 340 anode wires were replaced per sector. Fewer than 10 ground wires per sector needed to be replaced. This exercise also demonstrated the efficiency of cell repair.

#### 2.4.5.4 Gluing and cabling of the sectors

The final step, to ensure a tight seal to contain the helium, was the gluing of the wires, which used first silicon RTV to outline the regions to be sealed, and then Araldite. Tubes made of Rilsan that are 10 mm in length and 10 mm in diameter were first glued with standard Araldite around each anode signal pin. This provides electric insulation between the anode and ground pins. The next task was to seal the holes associated with the Geiger cells.

Given that the geiger cell layers have the 4-2-3 pattern and that the internal and external half sectors have their layers of four back to back with only the gap for the source foil, it was reasonable to seal these eight layers as one. Thus there were five arches of Geiger cells that need to be sealed instead of six (see Fig. 2.21). To accomplish this the silicon RTV was used to outline the regions to be sealed. The regions were then sealed with Araldite (Fig. 2.36 shows glue sealed regions for adjacent sectors in the LSM). A gas seal was also formed between the petals and walls, at the exterior of the sectors.

The iron disks were also glued onto the interface light guide for the three 5" PMTs which are the outmost layer of PMTs on the petals known as L4-type light guides.

Anode and cathode cables with one extremity connected to the distribution daughter boards were finally connected to each sector before its transportation to the LSM as shown in Fig.2.37.

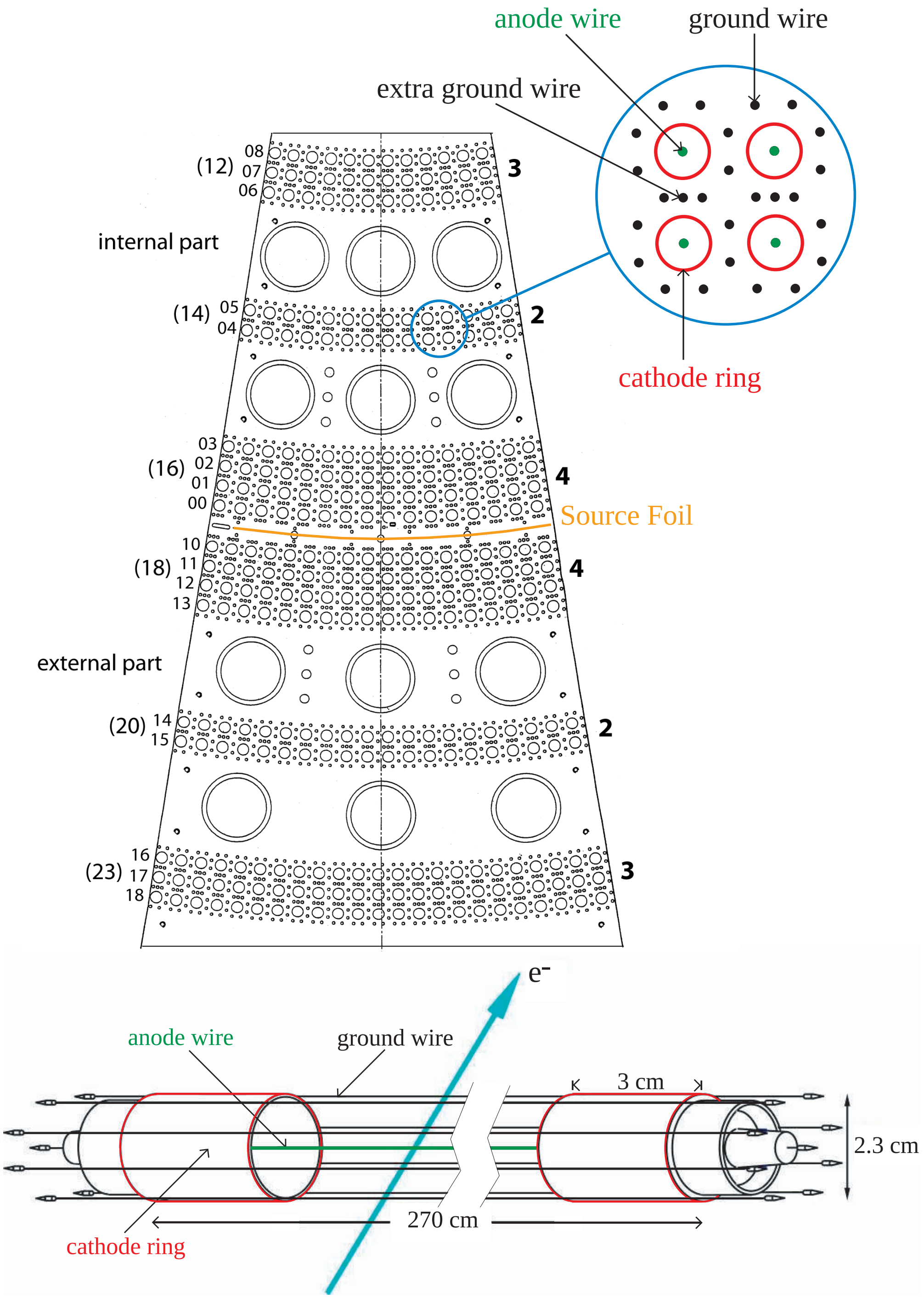

Figure 2.21 : Top view of one petal of the NEMO 3 sectors with a detail of four Geiger cells and view of an elementary Geiger cell. The basic cell consists of a central anode wire surrounded by 8 ground wires, which belong to four adjacent cells, with an extra ground wire between layers as detailed in the right top of the figure. All the wires are 50 $\mu$m in diameter and 2.7 m long. On each end of the cell is the cathode ring, 3 cm in length and 2.3 cm in diameter. The anode wire runs through the center of this ring while the ground wires are supported just outside the ring. One can see the “4-2-3” configuration, with nine layers on each side of the source foil numbered 00 to 08 and 10 to 18 respectively for the internal and external parts (in brackets are given the number of cells in each layer).

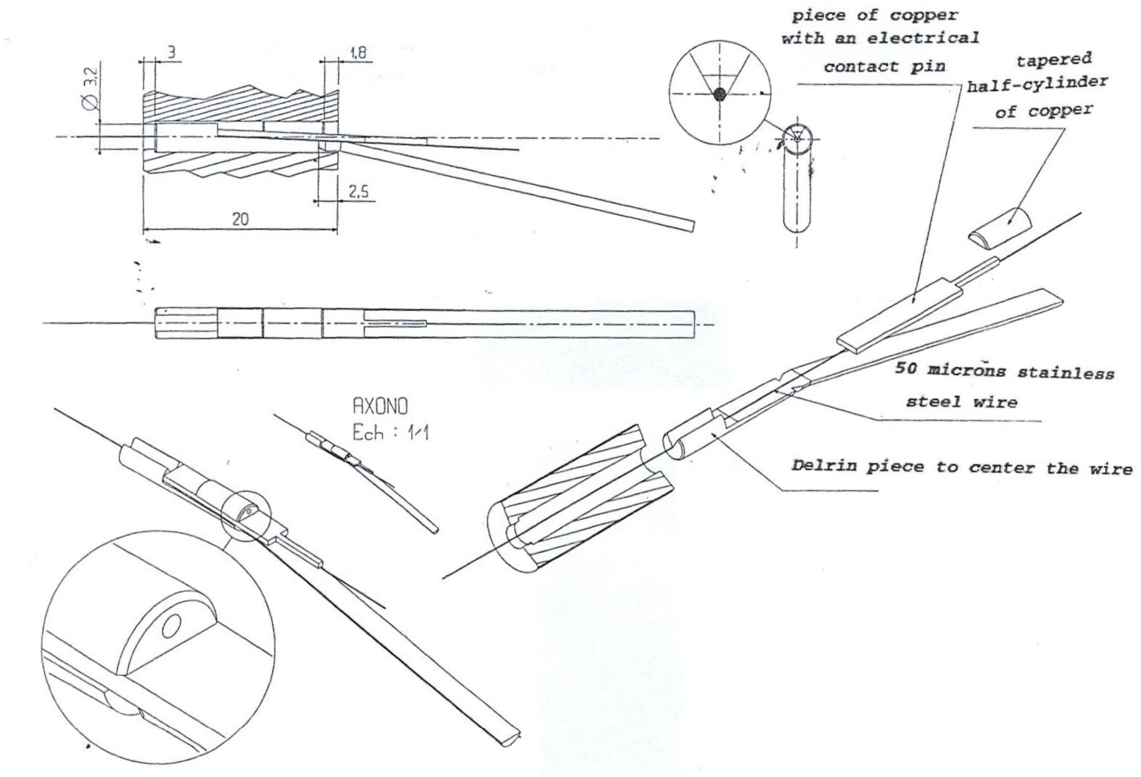

Figure 2.22: Wire support mechanism, with Delrin center, copper electrical pin and copper tapered half-cylinder.

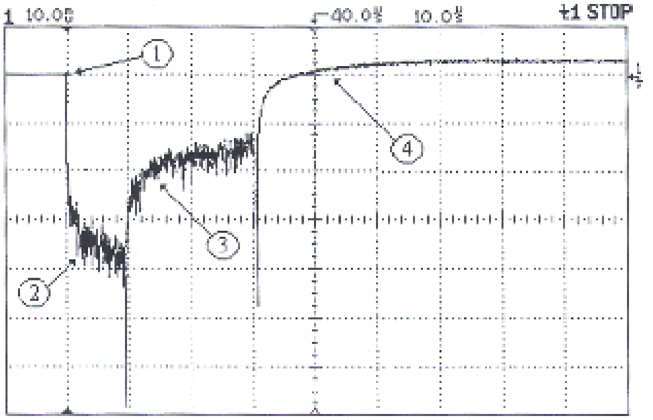

Figure 2.23: Anode pulse (on 270 Ω), with a "one-plasma" amplitude of around 50 mV, that means a current of 200 $\mu$A on average for a total propagation time of 40 $\mu$s, with a gas mixture of helium and alcohol.

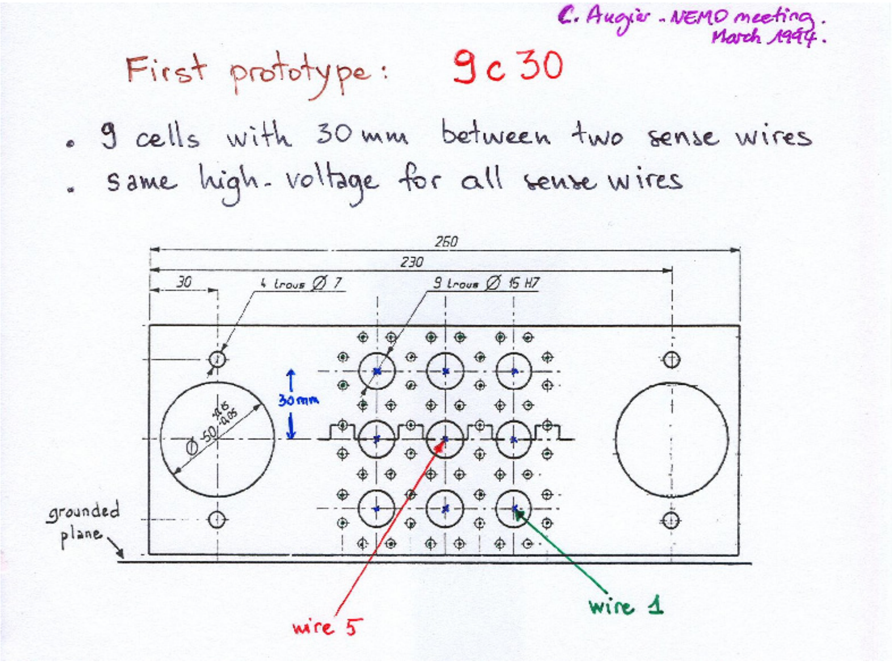

C. Augier - NEMO meeting.
March 1994.

First prototype : 9c30

- 9 cells with 30 mm between two sense wires
- same high-voltage for all sense wires

Figure 2.24: Configuration of the first prototype $9C30$ (side view), with 9 cells and 30 mm between anode wires. For the same $HV$ value put in all cells, it showed a very different behavior for wire 5 than for other wires, with a propagation time of 80 $\mu$s instead of 60 $\mu$s, and a 1-plasma amplitude of 5 mV instead of 10 mV.

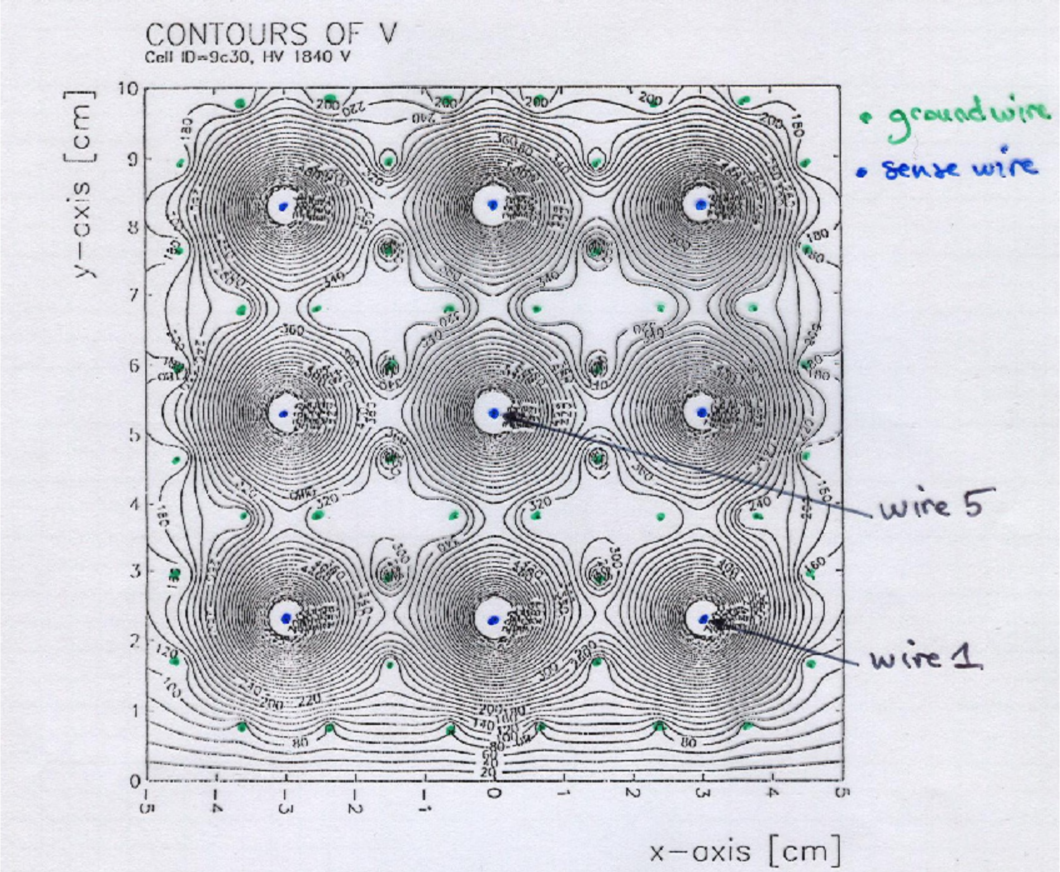

Figure 2.25: Garfield simulation of the $9C30$ prototype, showing that common equipotential lines between two adjacent cells of different layers were for $V = 340$ V (it was around 200 V for NEMO 1 configuration). Thus the gradient $\Delta V = HV - 340$ V was too low.

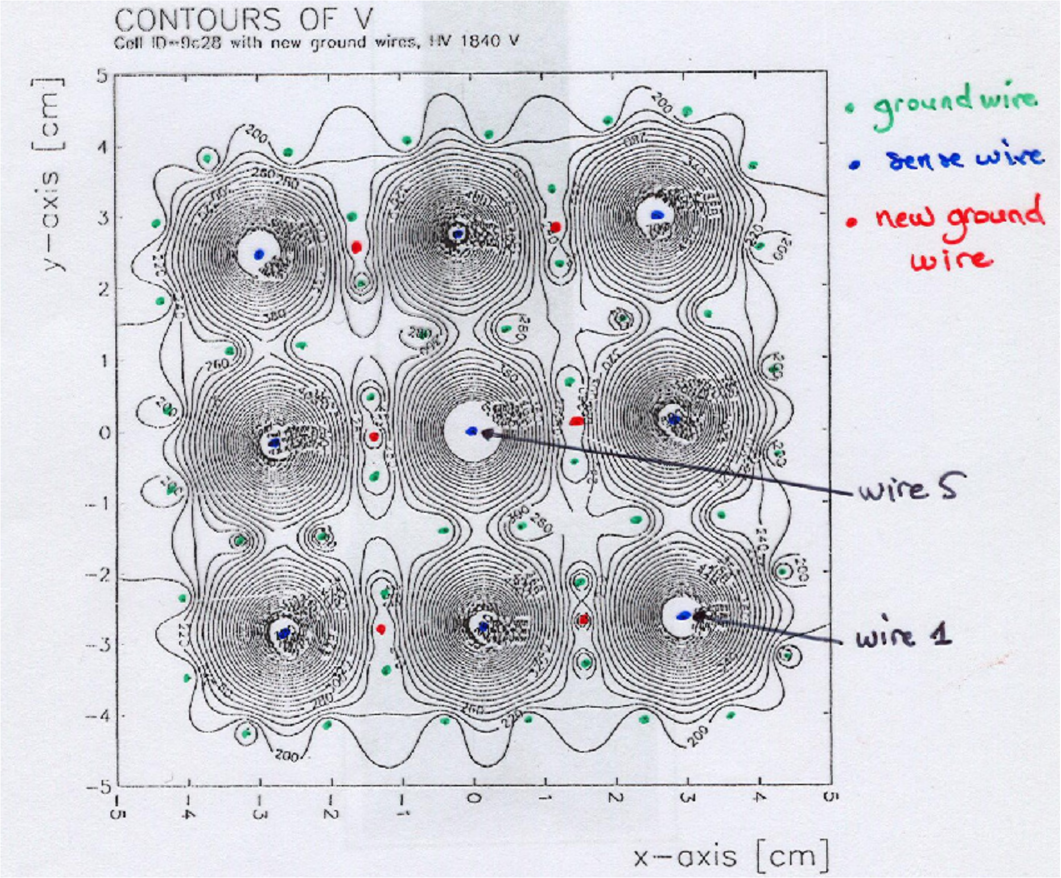

Figure 2.26 : Garfield simulation of a $9C28$ configuration with extra ground wire between cells of adjacent layers. In the same $HV$ conditions than in Fig. 2.25, common equipotential lines between two adjacent cells of different layers were now for $V = 260$ V. Thus the gradient $\Delta V = HV - 260$ V was higher than for $9C30$ configuration and implied a better electrostatic separation between cells with this extra ground wires.

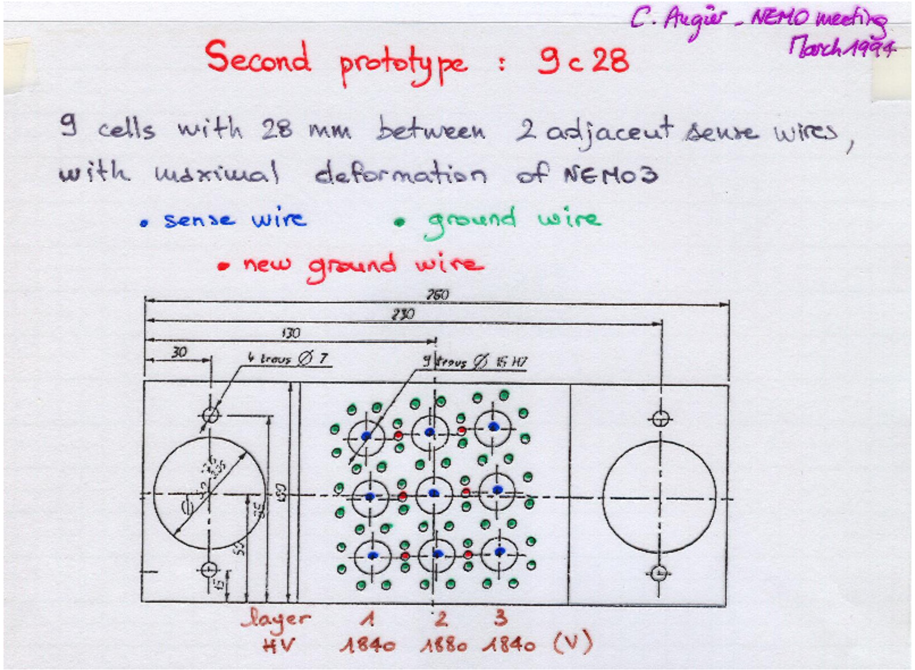

C. Augier - NEMO meeting
March 1994

Second prototype : 9c28

9 cells with 28 mm between 2 adjacent sense wires, with maximal deformation of NEMO3

Figure 2.27 : Configuration of the second prototype $9C28$ (side view), with 9 cells, 28 mm between anode wires and an extra ground wire added between cells of adjacent layers. For $HV$ values of 1880 and 1840 V as indicated on the figure, all cells showed the same propagation time of 60 $\mu$s and 1-plasma amplitude of 10 mV. It must be noted that compare to the $9C30$ prototype, the new distance of 28 mm between anode wires and the slightly deformed geometry reproduced the final design of the NEMO 3 sectors.

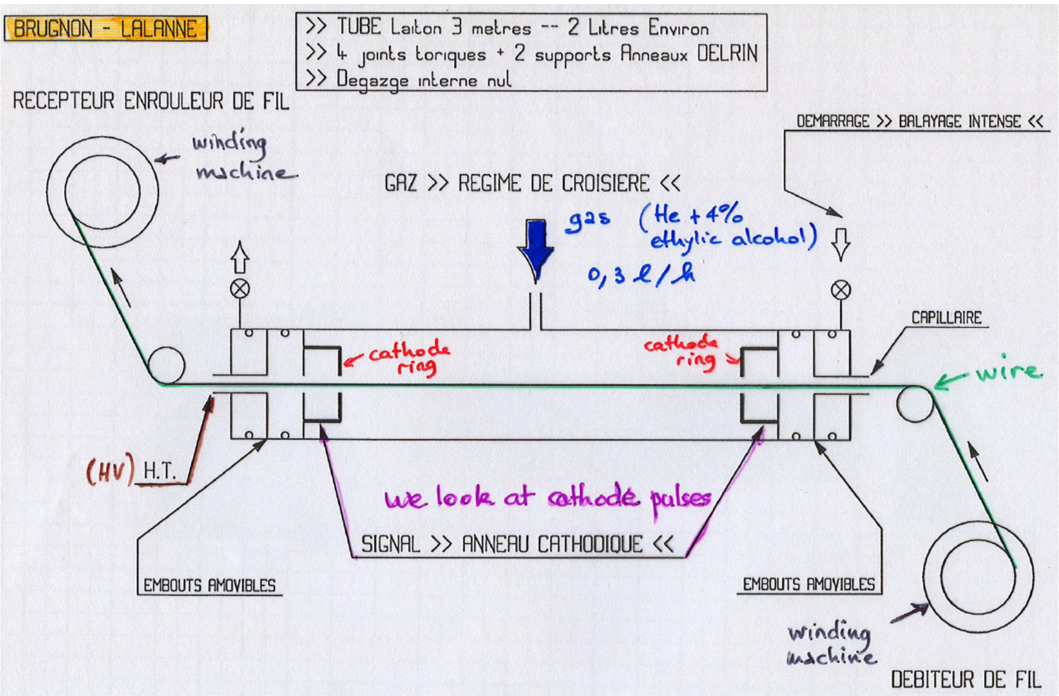

Figure 2.28 : Desig of the machine used to test the anode wire, which was passed through a brass tube, 3 m long, 28 mm in diameter and with cathode rings at both extremities to reproduce a NEMO 3 cell. The tube was filled with the same gas mixing than in prototypes (helium + alcohol at $10^o$ C, with a flux of 0.3 l/h). Putting HV on anode wire, presence of the two cathode peaks was checked on anode signal (as shown in Fig. 2.23) to ensure the full plasma propagation along the wire.

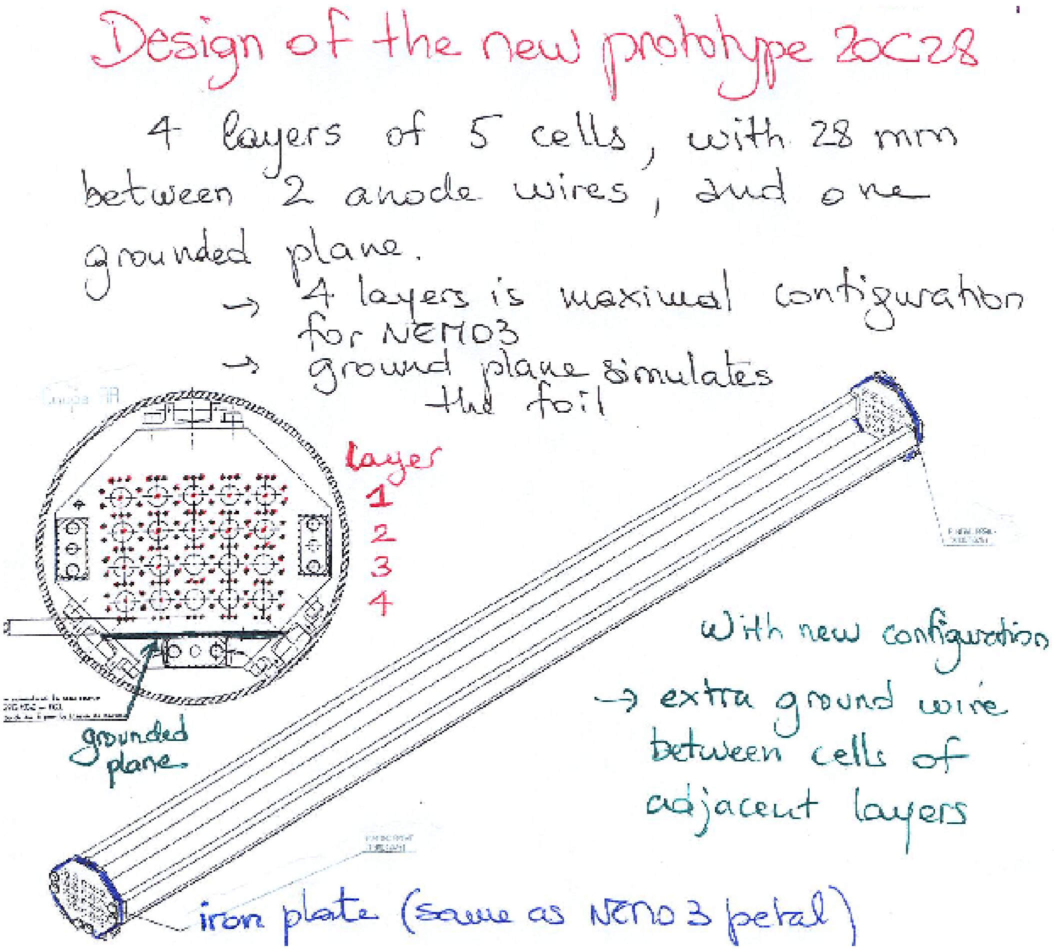

Design of the new prototype 20C28

4 layers of 5 cells, with 28 mm between 2 anode wires, and one grounded plane.

→ 4 layers is maximal configuration for NEMO3

→ ground plane simulates the foil

With new configuration

→ extra ground wire between cells of adjacent layers

iron plate (same as NEMO 3 petal)

Figure 2.29: Configuration of the third prototype $20C28$, with 20 cells (four layers of five cells each), 28 mm between anode wires and the extra ground wire added between cells of adjacent layers.

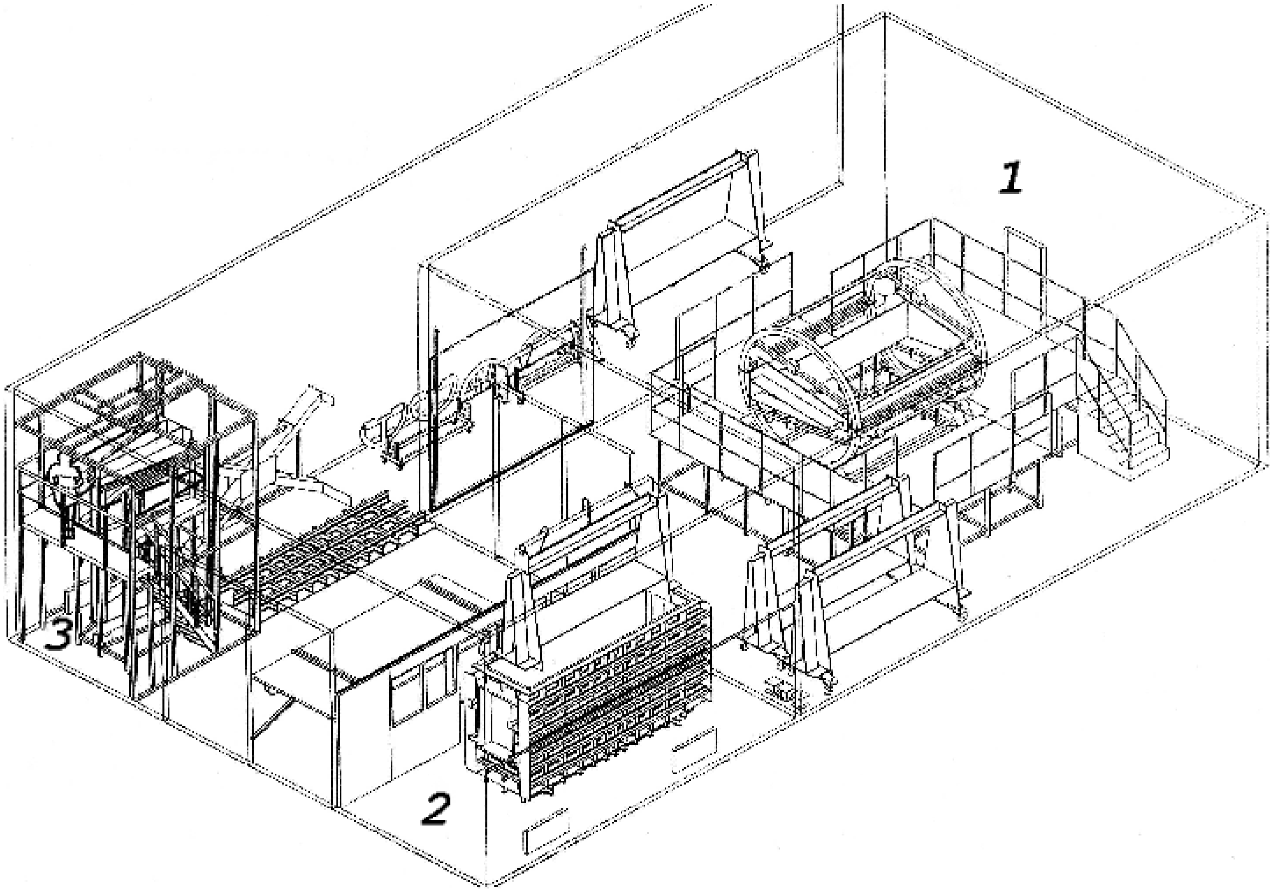

Figure 2.30 : General drawing of the "Hall 1" in LAL, dedicated to the NEMO 3 tracking detector realization of each sector. One can see the clean room (1) for the wiring and wire replacement, the test room (2) with a moving sector, and the glue coating framework (3).

Figure 2.31 : Photography of the gimble used for the wiring, installed in the clean room. The gimble was composed of two half-arches for an easy introduction of the sector. It used an electrical system for the 360$^o$ rotation and was surrounded by many removable platforms. One can see a sector in the gimble during wiring and on the left side an another sector with its protection shiels, waiting for bad wire replacement after the test procedure.

Figure 2.32: Photography of a petal sector during wiring. The operator blocked up the tapered half-cylinder in copper for an anode wire.

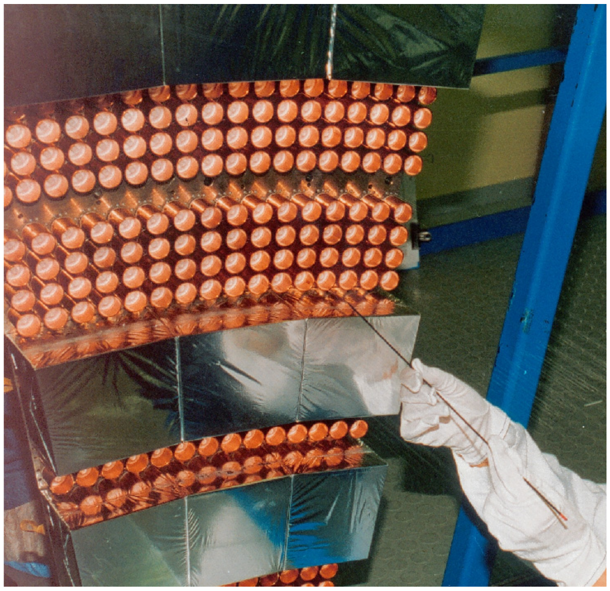

Figure 2.33: Photography of a petal sector during wiring. The operator passed the needle attached to stainless steel wire through the corresponding hole in the petal.

Figure 2.34: Realization of the special container used to test each sector after wiring.

Figure 2.35: Temporary cabling of one sector in the special container before tests of the wire chamber.

Figure 2.36 : View of the five sealed regions in the top petals of adjacent sectors in the LSM.

Figure 2.37 : Picture of the anode and cathode cabling in LAL.

## 2.5 Electronics, trigger and data acquisition systems

The NEMO 3 detector comprises of an independent calorimeter and a tracking detector. The readout electronics, data acquisition and a trigger system systems are inter-dependent. They are separated into modules which share a VME bus. This design permits not only $\beta\beta$ runs, but also different tests to adjust and calibrate the detector.

### 2.5.1 Calorimeter electronics

The choice of low radioactive materials was essential not only for the PMTs but also for their high voltage distributions bases. Thus, the PMT bases are made of FR2[26] printed circuits equipped with SMD[27] polycarbonate or polypropylene capacitors and resistors (see Table 2.41 for the radioactivity measurements of all the PMT components).

The PMT bases were designed with a tapered voltage divider to improve the linearity under conditions of high current. Fig. 2.38 shows the high-voltage (HV) distributions for 3" and 5" PMTs. R4 and R5 resistors could be removed, in order to change the $R_{base}$ value. Tests carried out at the IReS laboratory identified these fixed sets of resistors (chosen between only R3 resistor, R3 and R4, or R3, R4 and R5) for each PMT base which control the voltage between the photocathode and the first dynode so as to optimize the time resolution.

The HV cables[28] have a mean length of 11 m and the PMTs are run with positive HV so the photocathode is at ground. The signal cables[29] are connected to the calorimeter acquisition boards via Nicomatic multiaxial connectors (8 or 4 channels). The cable length is 11.30 m for the 5" PMTs and 10.60 m for the 3" PMTs. The difference in cable lengths corrects for the different transit times of the two different types of PMTs. It should also be noted that the HV decoupling capacitor for the signal cable is on the acquisition board.

The mean values of the HV is 1350 V for the 5" PMTs and 1800 V for the 3" PMTs, with the base currents being less than 350 $\mu$A for each. Three large power supplies from C.A.E.N.[30] are used to supply the HV for the 1940 PMTs. HV control is done using RS232 connection with a computer or using CANbus connection with the survey PC of the experiment (see Section 2.5.5). This control allows to set the HV values of the 24 channels of each power supply board with a resolution of 0.2 V. There is also a global current measurement with a resolution of 2 $\mu$A. Each HV channel is shared in parallel by three PMTs via a distribution board, using AMP multicontact connectors.

Each PMT is connected to its HV channel through two resistors $R_1$ and $R_2$ put on the associated distribution board. There are nine boards per sector, each corresponding to four HV channels. One channel allows the same HV value to be distributed to three sets of variable resistor $R = R_1' + R_2'$, one for each PMT, which is a voltage divider. Thus there are finally $9 \times 4 \times 3$ allowed distribution channels per sector, that means 108 channels to distribute 97 PMTs (see Fig. 2.39). The distributions boards are distributed in four racks, with one crate per two sectors (18 boards):

---

[26] phenolic paper

[27] Surface Mounted Device

[28] SM50 coaxial cable from AXON, with a diameter of 1.05 mm

[29] 50 $\Omega$ coaxial cable, type KX3B in polyethylene dielectric

[30] C.A.E.N. HV power supply type SY527 10 boards A938 AP, 24 channels each, with HV AMP 201310-3 multicontact connectors, at maximum 1.2 mA/channel and 2200 V max/channel, with one current channel in addition and less than 700 V as difference between HV channels. Thus it is impossible to use the same board for the 3" and 5" PMTs.

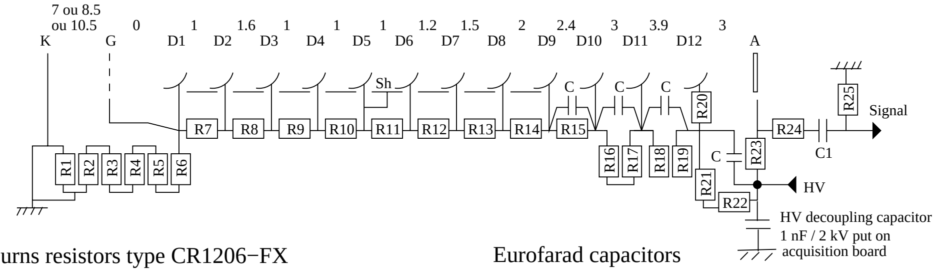

Bourns resistors type CR1206−FX

R1 = R3 = R4 = R5 = R14 = 402 kΩ

R2 = R13 = R16 = R17 = R19 = R21 = R22 = 301 kΩ

R5 = R6 = R9 = R10 = R11 = 200 kΩ

R8 = 324 kΩ    R12 = 237 kΩ

R15 = R18 = 475 kΩ

R20 = R24 = 49.9 Ω

R23 = R25 = 10 kΩ

Eurofarad capacitors

C = 22 nF / 250 V   type SP1792

C1 = 3.3 nF / 2 kV   type SP2488

a) Base for 3’’ Hamamatsu R6091 PMT

$R_{base}$ = 5925 kΩ   with R3
= 6226 kΩ   with R3 and R4
= 6628 kΩ   with R3, R4 and R5

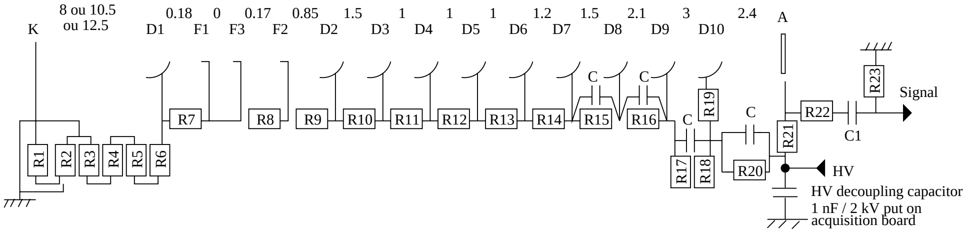

Bourns resistors type CR1206−FX

R1 = R3 = R4 = R5 = R6 = 402 k Ω

R2 = 499 kΩ    R7 = 35.7 kΩ

R8 = 34 kΩ    R8 = 169 kΩ

R10 = R15 = R17 = R18 = 301 kΩ

R11 = R12 = R13 = 200 kΩ

R14 = 237 kΩ    R16 = 422 kΩ

R19 = R22 = 49.9 Ω

R20 = 475 kΩ

R21 = R23 = 10 kΩ

Eurofarad capacitors

C = 22 nF / 250 V   type SP1792

C1 = 3.3 nF / 2 kV   type SP2488

b) Base for 5’’ Hamamatsu R6594 PMT

$R_{base}$ = 4784.7 k Ω   with R3
= 5283.7 k Ω   with R3 and R4
= 5685.7 k Ω   with R3, R4 and R5

Figure 2.38: Resistor and capacitor distributions for the 3” and 5” PMT bases of NEMO 3.

- rack B51, in two crates, for sectors 19, 00, 01 and 02;
- rack B22, in four crates, for sectors 03 to 09;
- rack B32, in four crates, for sectors 10 to 16;
- rack B41, in two crates, for sectors 17 and 18.

Let $R_{base}$ be the base resistor and $HV$ the high-voltage value delivered by the distribution channel, the voltage applied on PMT is:

$$V_{app} = HV \frac{R}{R + R_{base}}$$

The three PMTs from one distribution channel were coupled per sector, using the association defined in Section 2.3.5, the test measurements (HV, gain) at IReS, and the requirement to have a difference in their working HV less than 80 V. The HV tuning was done during the

PMT alignment procedure with $^{207}$Bi sources, changing the $R = R'_1 + R'_2$ value with a step of 10 k$\Omega$ corresponding to a voltage variation of 2 to 2.5 V and a precision of 3 to 5 channels (see Section 2.6).

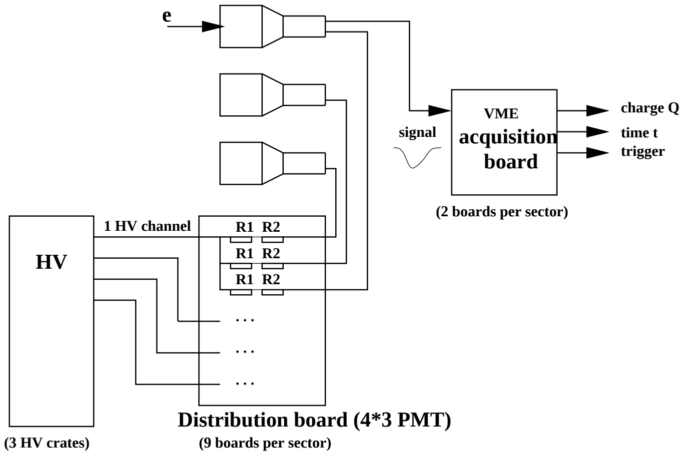

Figure 2.39: Calorimeter electronics distribution.

The calorimeter electronics was designed by a collaboration between LAL and IPNO [28] to fulfill three functions. First, energy measurements must be correlated with the charge pulses from the PMTs. Next, there must be time-of-flight (TOF) measurements which allow to distinguish between events in which the tracks come from the source and those that are from external backgrounds. Typically the difference of TOF measurements are from 0 to ±8 ns. Finally, the calorimeter electronics must provide a fast first level trigger.

The counting rates per PMT are a few tens of Hz during $\beta\beta$ runs and a few tens of kHz during calibration runs. The conversion times do not exceed 100 $\mu$s. A diagram of the system is shown in Fig. 2.40.

The 97 PMTs of each sector are divided by the source foil into the internal and external regions. A total of 46 PMTs are used for the internal region of which 12 PMTs are on the top and bottom petals. The external region is covered with 51 PMTs, again with 12 PMTs on the top and bottom petals (see Fig. 2.41 and Fig. 2.42 for numbering of the 97 PMTs of each sector). Thus, there is a total of 40 half-sectors for which front-end electronics boards were designed. The corresponding 40 mother boards[31] are housed in three VMEbus crates[32] and each mother board supports 46 or 51 analog-NEMO (ANEMO[33]) daughter boards. Positions of the 40 mother boards in the three VME crates are given in Table 2.28.

The ANEMO boards have both a low and a high threshold leading edge discriminator (the slewing issue will be addressed at Section 2.6.8). If the PMT signal exceeds the lower level threshold (with a minimal value of 7 mV or 23 keV) it starts a TDC measurement and opens a charge integration gate for 80 ns. The high threshold discriminator is adjustable up to 1 V but generally runs at 48 mV corresponding to 150 keV. The high threshold discriminator works as a one shot that delivers an event signal to the mother board.

---

[31] The calorimeter acquisition mother boards were designed at LAL.

[32] V430 type

[33] The ANEMO daughter boards, with a surface of 23 x 40 mm$^2$, were designed at IPNO. It was decided not to use an ASIC, due to the low number of circuits to realize.

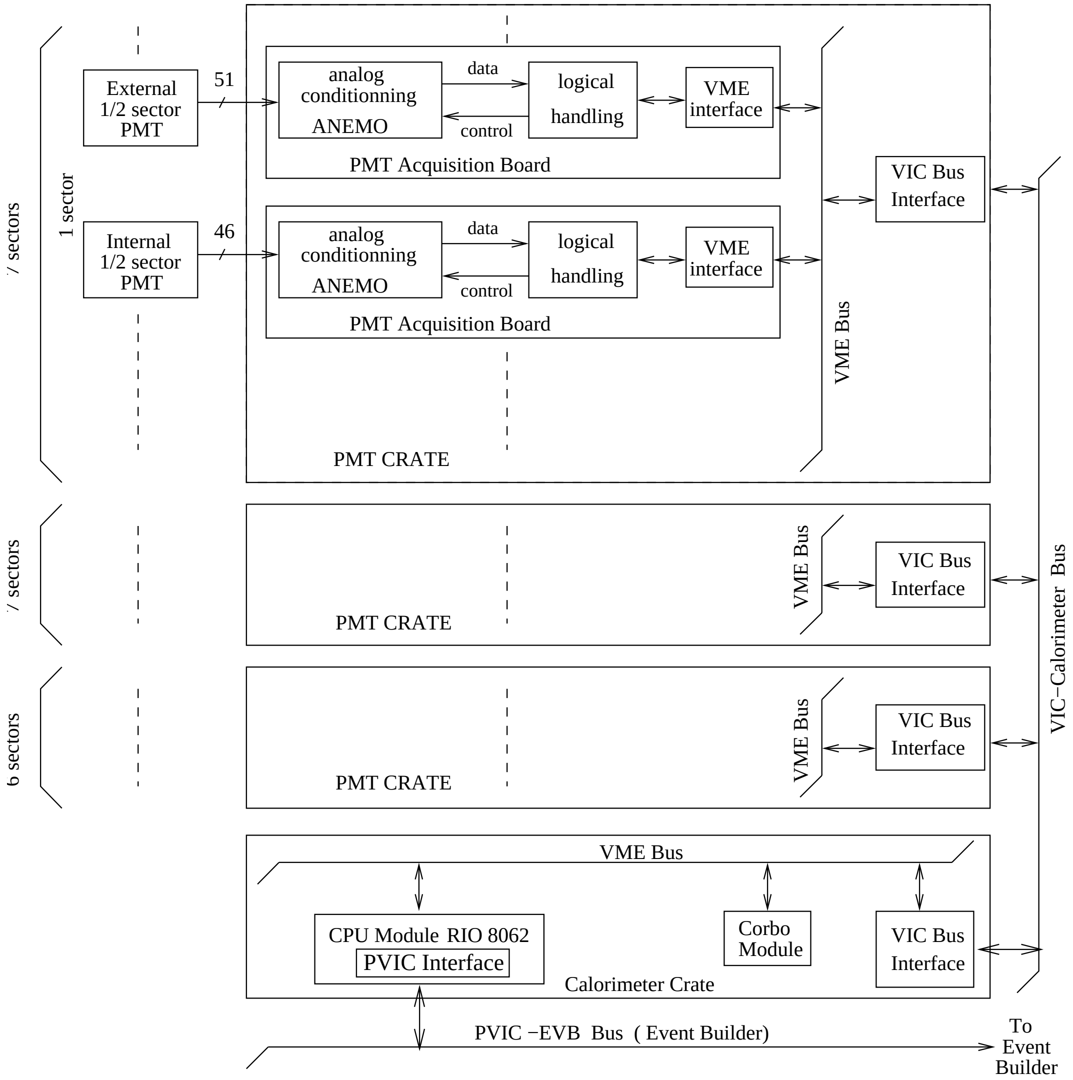

Figure 2.40: Calorimeter system electronics.

Each mother board provides an analog signal to the trigger logic which reflects the number of channels that have exceeded the upper threshold per event. The signal strength is 1 mA per PMT channel (50 mV/PMT on 50 Ω, with a non-linearity for more than 5 to 7 PMTs per event). This level is used to trigger the system (1st level trigger) if the desired multiplicity of active PMTs is achieved. This typically is one PMT.

The trigger logic then produces a signal called *STOP-PMT*, which is sent to all the calorimeter electronic channels, to save their data. So the TDCs are stopped and the integrated charge is stored. Then digital conversions begin after receiving the *TRIGGER-PMT* signal. At the same time, a signal called *INT-PMT* is sent to the calorimeter acquisition processor, which stops all others programs and permits the read out of the digitized times and charges for the active channels.

| Crate position | Crate number 31 in rack B31 | Crate number 21 in rack B21 | Crate number 51 in rack B51 |
|---|---|---|---|
| 20 | S16 external | S09 external | S02 external |
| 19 | S16 internal | S09 internal | S02 internal |
| 18 | S15 external | S08 external | S01 external |
| 17 | S15 internal | S08 internal | S01 internal |
| 16 | S14 external | S07 external | S00 external |
| 15 | S14 internal | S07 internal | S00 internal |
| 14 | S13 external | S06 external | S19 external |
| 13 | S13 internal | S06 internal | S19 internal |
| 12 | S12 external | S05 external | S18 external |
| 11 | S12 internal | S05 internal | S18 internal |
| 10 | S11 external | S04 external | S17 external |
| 09 | S11 internal | S04 internal | S17 internal |
| 08 | S10 external | S03 external | |
| 07 | S10 internal | S03 internal | |

Table 2.28: Position of the 40 PMT acquisition boards in the three VME crates (one per each internal or external half-sector, for sectors S00 to S19).

The analog-to-digital conversions of the charge and the timing signal are made with two 14-bit ADCs of which only 12 bits are used (to improve the linearity). As energy performance measurements, the resolution is 0.36 pC/channel ($\sim$ 3 keV/channel) for 12 bits, the integral linearity is less than 3 bits and the precision is better than $2.4 \times 10^{-4}$ up to 12 MeV. As time performance, the resolution is 53 ps/channel FWHM for 12 bits (for a total time of 200 ns) with a linearity better than 0.1%. The low threshold precision is 1 mV/bit for 8 bits, and the one for the high threshold is 4 mV/bit for 8 bits. The energy and time are corrected with information from calibration runs to obtain the true values for each PMT as described in Section 2.6. If any PMT signal exceeds the high level threshold then the TDC measurement and charge integration are aborted and the system resets after 200 ns.

### 2.5.2 Tracking detector electronics

The Geiger electronics, which was designed at LAL, has two types of boards.
The first is for the secondary voltage distribution (see Fig. 2.43), which provides around 1620 V to the anode wires and can provide between 0 and 100 V to the cathode rings. The feature of providing voltage to the cathode ring is not currently used. Included on the secondary distribution boards are the analog signals from the anode wire and the two cathode rings[34]. These boards receive high voltage from two of the C.A.E.N. power supplies[35]. There are two primary HV distribution card with 16 channels each. The current demands per layer of cells increases as the circumference given the greater number of cells at larger radii to have complete coverage. To address this problem a single channel of the primary supply powers a single layer of all the

---

[34] Anode coaxial cable is a type SM50 from AXON, connected to the anode pin with a 75543-006 connector from Berg; cathode coaxial cable is a type PK50 1-12 from UFA, connected to cathode pin with 47771-001 connector from Berg; all cables are soldered to the daughter boards of the secondary distribution board

[35] C.A.E.N. HV power supply type SY527 with A734P boards, 16 channels each

internal half-sectors. For the external half-sectors two channels power each of the 9 layers (see Fig. 2.44).

The second type of board is for the tracking electronics and is an acquisition board which is connected to the distribution board. It uses ASICs[36] and has an interface with a 50 MHz clock (TDCs provide a 20 ns LSB).

Two sectors and a half correspond to the 20 boards of one crate, for both distribution and acquisition boards. Thus Geiger cell electronics for the 20 sectors of the NEMO 3 are distributed in 16 crates:

- in rack B10, two distribution crates and two acquisition crates, for sectors 00 to 04;
- in rack B10, two distribution crates and two acquisition crates, for sectors 05 to 09;
- in rack B10, two distribution crates and two acquisition crates, for sectors 10 to 14;
- in rack B10, two distribution crates and two acquisition crates, for sectors 14 to 19.

The functions of the acquisition board are first amplification and then discrimination of analog signals coming from the distribution board. Time measurements for each cell are acquired for the anode wire and the two cathode rings. Note that the two cathode times are identified as $t_{LC}$ and $t_{HC}$ where $LC$ and $HC$ stand for low and high cathode times. The low one corresponds to the cathode ring on the bottom of the detector and the high for the top. The anode time, $t_A$, is the time difference between the anode signal and the *STOP-A* signal (coming from the trigger). This signal gives the transverse distance of the particle to the sense wire. This time ranges from 0 to 1.5 $\mu$s for cells of 3 cm in diameter. The low and high cathode times, $t_{LC}$ and $t_{HC}$, are the time differences between the anode signal and the cathode ring signals. These are used to measure the longitudinal position of the particle. The cathode times range from 0 to 82 $\mu$s, depending on the operating voltage and position of the through going particle. Delayed pulses, which occur for up to 710 $\mu$s after the trigger signal, are recorded in order to tag alpha particles coming from $^{214}$Bi contamination. The Bi-Po decay yields an $\alpha$-particle of 7.83 MeV with a time constant of 164 $\mu$s (see Section 1.3.0.3).

A scheme of the tracking detector system electronics is shown in Fig. 2.45. In summary each of the 20 sectors needs the following electronics. Eight secondary distribution boards receive a total of 15 daughter boards, of which five for the anode, five for $LC$ and five for $HC$ signals. The five sets of three different daughter boards services eight cells per set, so that there are 40 cells per distribution board. Then each sector also needs eight acquisition boards, which receive 10 analog ASIC and 10 digital ASIC circuits, with each ASIC handling four cells, so 40 cells per board.

Each of the four channels of the analog ASIC[37] is used to amplify the anode and two cathode signals by a factor of 60, and to compare them to anode and cathode thresholds generated by a software programable 8-bit DAC. The DAC's output signal is the same for both thresholds but by using different voltage dividers two threshold voltages are generated[38]. For signals exceeding the thresholds, a comparator provides a TTL signal which is sent to the TDC scalers of the digital ASIC. There are four TDCs for each of the four channels of the digital ASIC[39]. The first three are for the anode ($tdc_A$), low cathode ($tdc_{LC}$) and high cathode ($tdc_{HC}$) contents, which

---

[36] Application Specific Integrated Circuit

[37] 1.20 micron technology from AMS inside PLCC 44 boxes

[38] For example, a 160 channel's threshold corresponds to 6 mV and 20 mV for anode and cathode signals respectively

[39] 1.00 micron technology from ES2 inside PLCC 68 boxes

are measured with a 12-bit TDC and give times between 0 and 82 $\mu$s. The alpha TDC ($tdc_\alpha$) is 17-bits, which provides time measurements between 0 and 2.6 ms[40] (see Fig. 2.46).

The anode signal starts the TDCs and creates an OR signal (called *HIT-GG*) for all the cells of a layer of a given sector; so 360 TTL signals are sent to the T2 trigger (see Section 2.5.3). The propagation of the Geiger plasma is detected by the cathode rings. These signals stop their respective cathode TDCs and give $tdc_{LC}$ and $tdc_{HC}$ values. Physical propagation times are proportional to these values:

$$t_{LC} = [tdc_{LC} \times 20]\,\mathrm{ns} \tag{2.6}$$

$$t_{HC} = [(tdc_{HC} \times 20) - 17.5]\,\mathrm{ns} \tag{2.7}$$

The time constant, 17.5 ns, is removed from $t_{HC}$ to take into account the difference in cable lengths: the low cathode cables are 6 m and high cathode cables 9.5 m.

Concerning the anode signal, there are two cases which have to be distinguished. The anode signal can exceed its threshold before or after the arrival of the *STOP-A* signal which comes from the trigger (see Section 2.5.3).

In the first case, for $\beta$-type events, the *STOP-A* signal is used to stop the $tdc_A$ channels which have received an earlier start signal. Anode times $t_A$, correspond to the transverse drift time given by:

$$t_A = [(tdc_{max} - tdc_A) \times 20]\,\mathrm{ns} \tag{2.8}$$

where $tdc_{max}$ corresponds to 6.14 $\mu$s.

In the second case, for $\alpha$-type events, all Geiger cells not already triggered can register delayed hits which occur after the *STOP-A* has been received for up to $\sim$ 704 $\mu$s (with addition of the 6 $\mu$s between the trigger and *STOP-A* signals, it corresponds to the 710 $\mu$s as defined in Section 1.3.0.3. Anode signals exceeding their threshold start not only their anode and cathode TDCs but also their alpha TDCs ($tdc_\alpha$).

Cathode signals stop the cathode TDCs and give $tdc_{LC}$ and $tdc_{HC}$ values, but the anode and alpha TDCs are stopped by the *STOP-$\alpha$* signal coming from the trigger. As a consequence, in this case the $tdc_A$ and $tdc_\alpha$ have the same value modulo 4096 for these cells. The corresponding alpha time $t_\alpha$ is then given by:

$$t_\alpha = [(tdc_{\alpha\_max} - tdc_\alpha) \times 20]\,\mathrm{ns} \tag{2.9}$$

where $tdc_{\alpha\_max}$ corresponds to $\sim$ 704 $\mu$s. This value is measured from the alpha TDC spectra and then stored in the database.

For more information on the reconstruction of the transversal and longitudinal positions (respectively $r_\perp$ and $z$) for Geiger cells see Section 3.3.2.

### 2.5.3 The NEMO 3 trigger system

The trigger system [29] was developed by LPC. It is fairly flexible to a large number of searches. It receives one analog signal from each of the 40 half-sectors that is proportional to the number of PMTs that have exceeded their high threshold in that sector. The 40 signals are summed resulting in an analog signal. The trigger then goes onto the second level which involves the Geiger layers. In this case 360 channels of binary information are read out by treating each Geiger layer in each sector as a bit, which is on if the layer is hit. This information allows the

---

[40] This allowed long time measurement is due to the fact that the trigger was previously defined using a programmable delayed electronics up to 1.5 ms instead of a fixed delay of 710 $\mu$s after the trigger signal.

use of a rough track recognition program to be run on the available Geiger cell information (see Fig. 2.47 and 2.48). It is then possible to refine the identified tracks by spatially connecting the Geiger cells and triggered PMTs.

Timing constraints and trigger strategy lead to a two level trigger system (see Fig. 2.49) for normal running, where the level 1, T1, identifies the number of active scintillators (*PMT* multiplicity) and the level 2, T2, involves the Geiger cells (*GG*) and track pattern recognition that is done with a computer program using the 360 channels of Geiger information. There is a third level, T3, used only for calibration runs, which allows for spatial and timing *PMT/GG* correlations. The trigger system is composed of five 9U VME boards put in one crate in rack B41. There are two T2 boards, one for internal and one for external Geiger signals, and one T1-3 board. Finally, there are two interface boards, which receive the 360 differential TTL Geiger signals, transform them in monopolar TTL signals with a width between 1 and 3 $\mu$s, sort between internal and external signals and finally distribute these 360 signals to T2I and T2E boards (see below).

The **first level (T1)** of the trigger, is embedded on the T1-3 board, and is based on the number of PMTs required to initiate a readout. It is used to identify the number of active scintillators by using the summed current from the 40 analog signals to define the multiplicity of the event *(MULT)*. It can be greater than 1, 2,... $N$ PMTs, with the possibility of selecting the PMT positions to be on opposite sides of the source foil for $MULT \geq 2$. For hardware there is one 3-bit register *(MODE-SEUIL)* that records the intended trigger using:
- no trigger (000), *PMT* only (001), *GG* only (010), *PMT+GG* (011) or running calibration with laser (100)[41];
- if using *PMT*, set the multiplicity threshold (check of the multiplicity with fast ECL comparators during 20 ns);
- at the T3 level: ask for internal/external *PMT* temporal coincidence or not (during 10 ns).

If the trigger logic encounters a multiplicity higher than that set by the *MULT* threshold up to 20 ns after the first triggered PMT, T1 generates the *STOP-PMT* signal (see Section 2.5.1), which is the timing reference of the experiment, with an electronic accuracy better than 150 ps.

The **second level (T2)** consists of track recognition in the Geiger layers (*GG*), using the 40 half-sectors. The track recognition is first performed on a half-sector basis. Since the probability for an electron to cross more than one sector is high, the tracks that cross two adjacent half-sectors are searched for in a second step. Thus, there are two secondary steps.
First step of T2 level is the search between different possible tracking patterns, which correspond respectively to a long track, a short track near the foil or near the scintillator block, or no track. Second step consists of making special associations between adjacent half-sectors, which allows the trigger to select a full track contained in more than one sector.

The second trigger level T2 is embedded on the T2I (internal) and T2E (external) boards, which receive 180 *HIT-GG* signals each and provide nine logical signals from a logical OR which lasts for 3 $\mu$s on the cells of each layer. Users can choose different triggering conditions for one sector or for two adjacent sectors. If the trigger logic is satisfied for the chosen track condition, a second level local trigger is generated *(VALID-GG)*. From the hardware point of view, the T2 level conditions on the T2I/E boards are set in programmable memories. In the first step the track recognition per half-sector is done with the *MEM-1* memory (see Figure 2.50), using 360 *HIT-GG* signals to produce 40 signals, that means one per half-sector. In the second step one looks at tracks in adjacent sectors using the output of the previous step. This is done with the

---

[41] For this last case the trigger is an input from the NIM DecLaser

*MEM-2* memory (see Fig. 2.51, with possible pre-track selection, which correspond to the PT2 condition). A program file is used to generate the various configurations.

The **third level (T3)**, which is only used for calibration runs, is embedded on the T1-3 board and checks on the possible coincidence between pre-tracks from T2's second stage and fired *PMT* half-sectors. This level aims to select electron tracks coming from radioactive sources installed in the calibration tubes. It is implemented in hardware without the possibility of changing the algorithm.

Examples of the different trigger configurations used for NEMO 3 acquisition are presented in Section 3.2.

For the case of an active PMT and Geiger cell trigger condition (*PMT+GG*), if the second level trigger is detected, the *STOP-A* signal is sent to Geiger acquisition boards with the programmable delay. This delay is set to 6.14 $\mu$s after the *STOP-PMT* signal. Then two trigger signals (*TRIGGER-GG* and *TRIGGER-PMT*) are sent to the Geiger and calorimeter electronics with a programmable delay set to 6.14 $\mu$s after the *STOP-PMT* signal. The first signal stops the automatic time-out which occurs 102 $\mu$s after the *STOP-A* signal. The second permits the digitization of the analog signals of the activated PMTs. In case these signals are not received there is an automatic reset of each of the PMT channels which have started measurements. Finally, the *STOP-*$\alpha$ and *INT-GG* signals are sent to the Geiger acquisition boards with a fixed delay of 710 $\mu$s after the *STOP-PMT* signal. A chronogram for the trigger in the *PMT+GG* mode can be found in Fig. 2.52. Pictures of T2 and T1-3 boards are shown in Fig. 2.53 and 2.54 respectively.

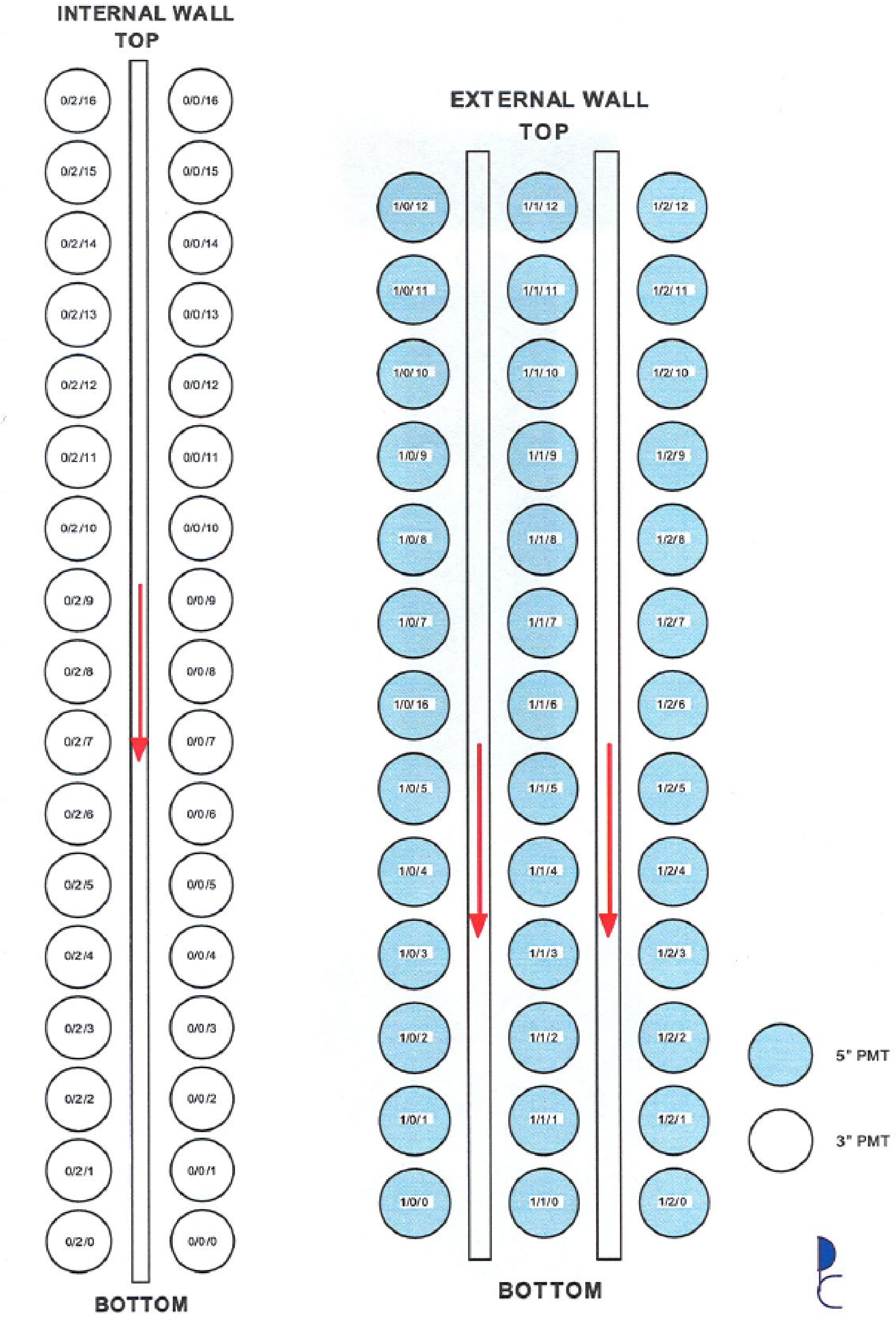

Figure 2.41 : Wall PMT numbering.

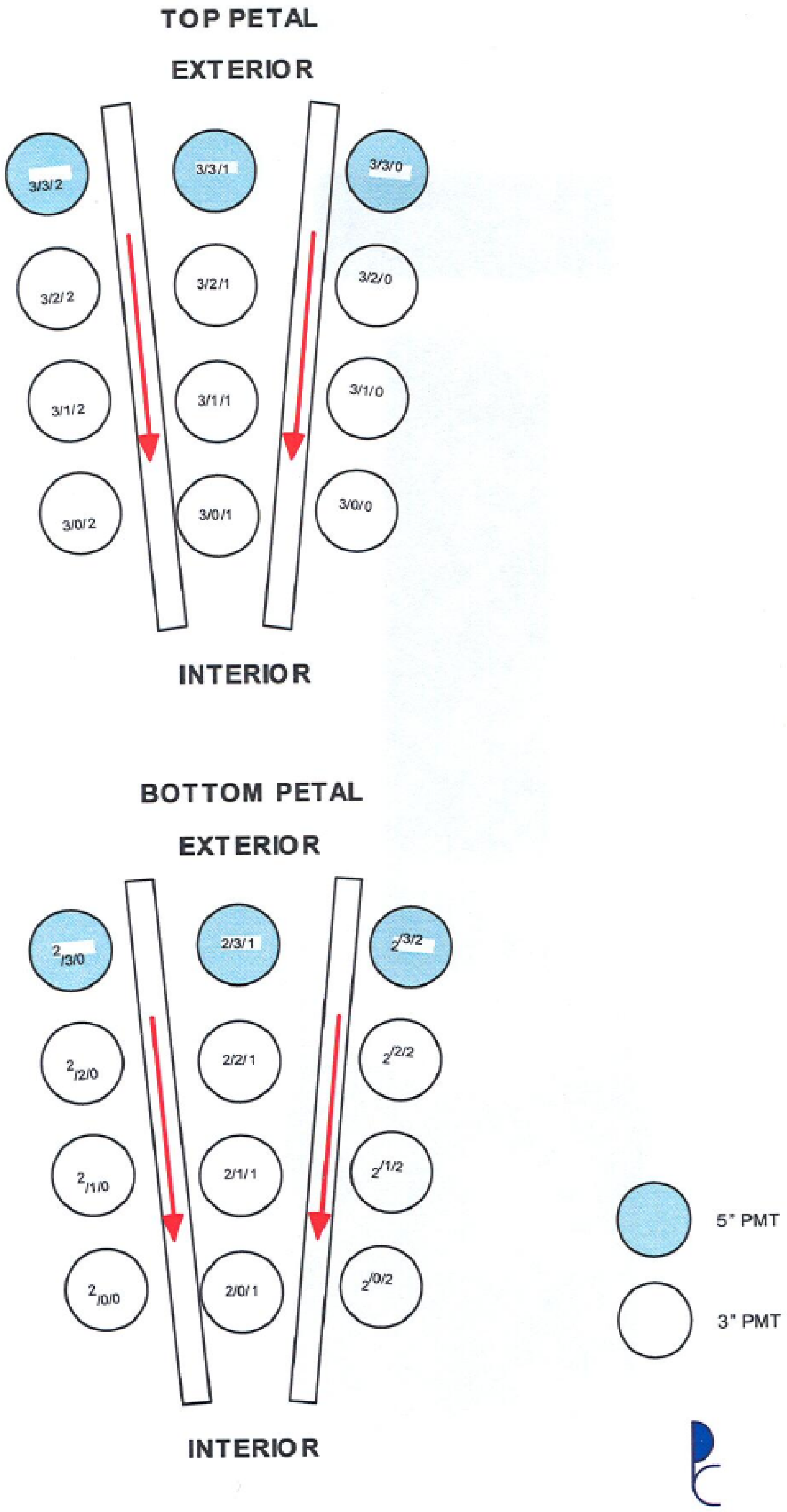

Figure 2.42: Petal PMT numbering.

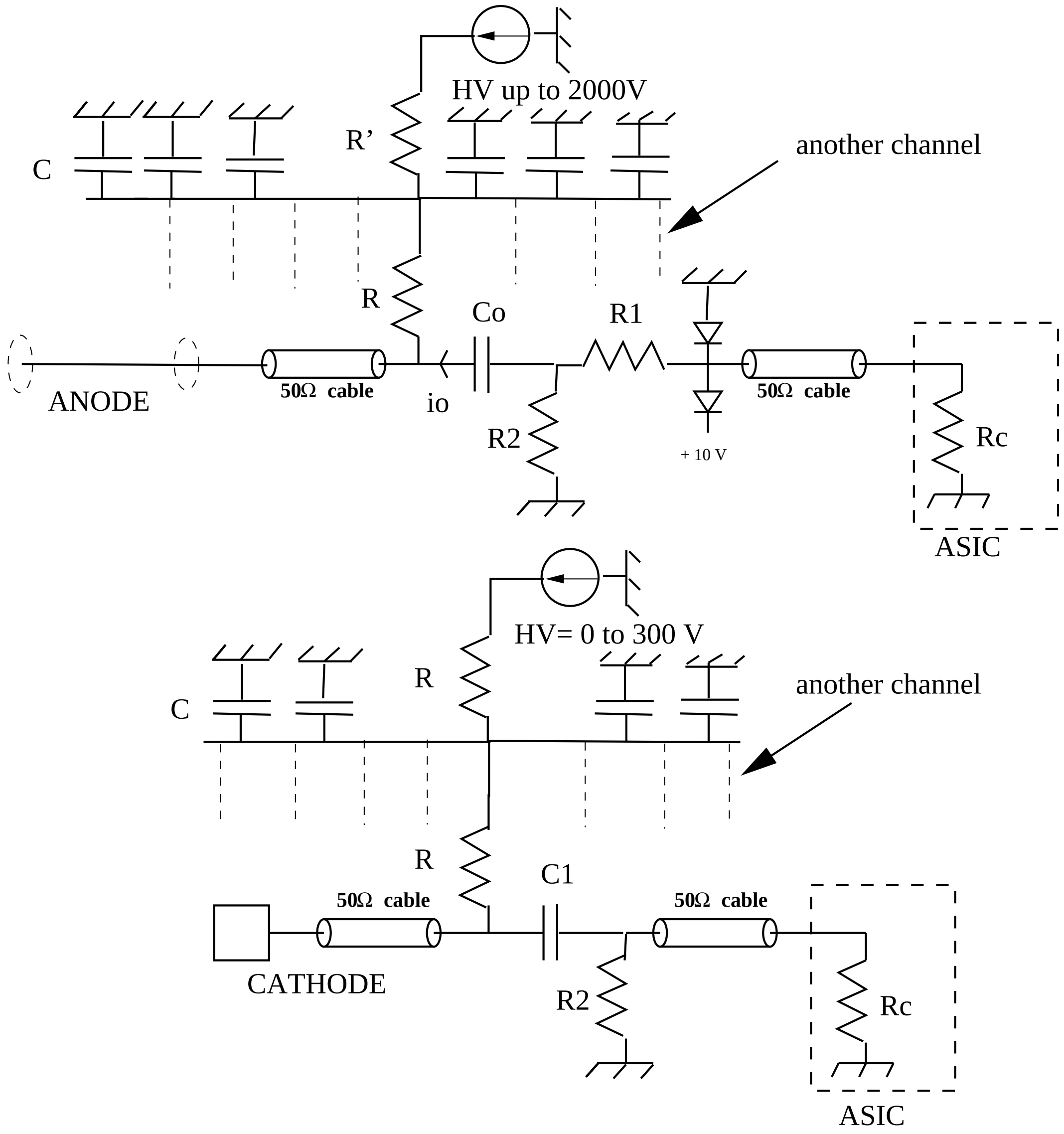

Figure 2.43: HV and signals distribution board principle for the tracking detector. The resistor values are $R = 220$ kΩ, $R' = 100$ kΩ, $R_1 = 100$ Ω, $R_2 = 820$ kΩ and $R_c = 270$ Ω. The capacitor values are $C = 10$ nF - 2 kV, $C_0 = 470$ pF - 2 kV and $C_0 = 1.5$ nF - 300 V.

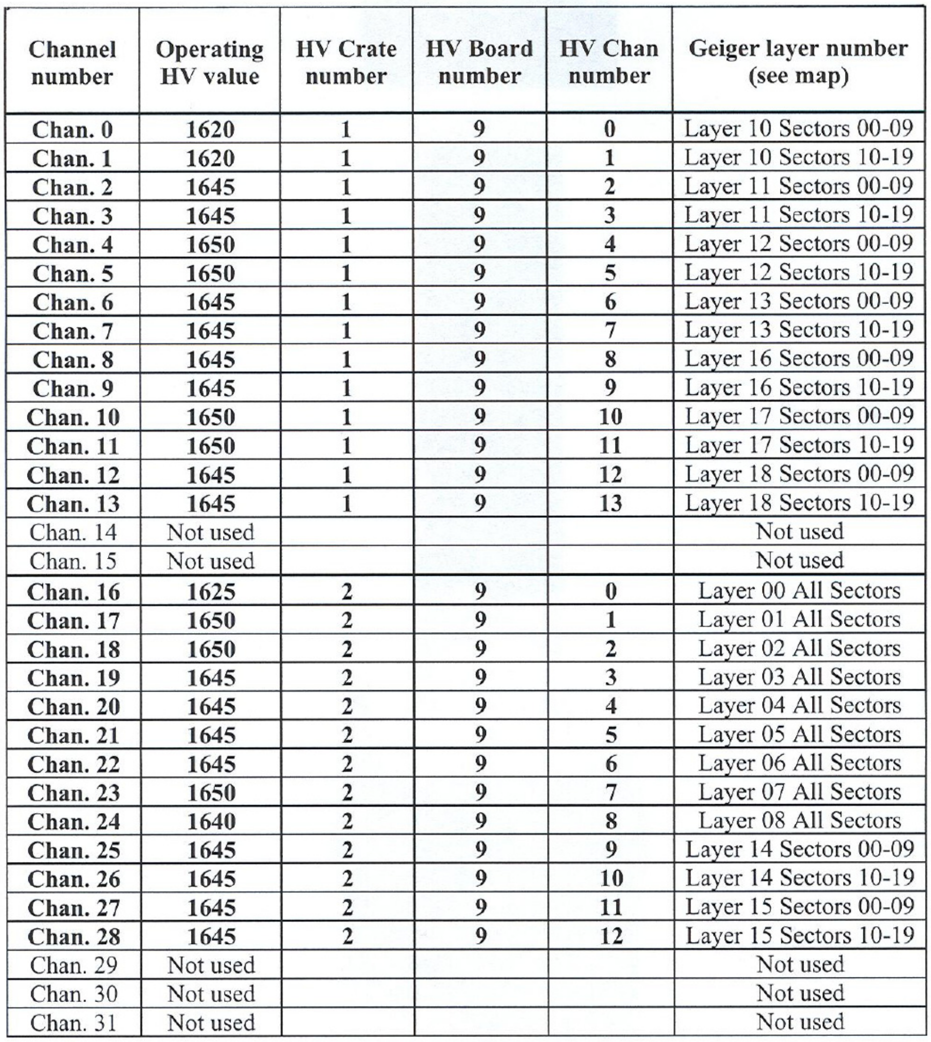

| Channel number | Operating HV value | HV Crate number | HV Board number | HV Chan number | Geiger layer number (see map) |
|---|---|---|---|---|---|
| **Chan. 0** | **1620** | **1** | **9** | **0** | Layer 10 Sectors 00-09 |
| **Chan. 1** | **1620** | **1** | **9** | **1** | Layer 10 Sectors 10-19 |
| **Chan. 2** | **1645** | **1** | **9** | **2** | Layer 11 Sectors 00-09 |
| **Chan. 3** | **1645** | **1** | **9** | **3** | Layer 11 Sectors 10-19 |
| **Chan. 4** | **1650** | **1** | **9** | **4** | Layer 12 Sectors 00-09 |
| **Chan. 5** | **1650** | **1** | **9** | **5** | Layer 12 Sectors 10-19 |
| **Chan. 6** | **1645** | **1** | **9** | **6** | Layer 13 Sectors 00-09 |
| **Chan. 7** | **1645** | **1** | **9** | **7** | Layer 13 Sectors 10-19 |
| **Chan. 8** | **1645** | **1** | **9** | **8** | Layer 16 Sectors 00-09 |
| **Chan. 9** | **1645** | **1** | **9** | **9** | Layer 16 Sectors 10-19 |
| **Chan. 10** | **1650** | **1** | **9** | **10** | Layer 17 Sectors 00-09 |
| **Chan. 11** | **1650** | **1** | **9** | **11** | Layer 17 Sectors 10-19 |
| **Chan. 12** | **1645** | **1** | **9** | **12** | Layer 18 Sectors 00-09 |
| **Chan. 13** | **1645** | **1** | **9** | **13** | Layer 18 Sectors 10-19 |
| Chan. 14 | Not used | | | | Not used |
| Chan. 15 | Not used | | | | Not used |
| **Chan. 16** | **1625** | **2** | **9** | **0** | Layer 00 All Sectors |
| **Chan. 17** | **1650** | **2** | **9** | **1** | Layer 01 All Sectors |
| **Chan. 18** | **1650** | **2** | **9** | **2** | Layer 02 All Sectors |
| **Chan. 19** | **1645** | **2** | **9** | **3** | Layer 03 All Sectors |
| **Chan. 20** | **1645** | **2** | **9** | **4** | Layer 04 All Sectors |
| **Chan. 21** | **1645** | **2** | **9** | **5** | Layer 05 All Sectors |
| **Chan. 22** | **1645** | **2** | **9** | **6** | Layer 06 All Sectors |
| **Chan. 23** | **1650** | **2** | **9** | **7** | Layer 07 All Sectors |
| **Chan. 24** | **1640** | **2** | **9** | **8** | Layer 08 All Sectors |
| **Chan. 25** | **1645** | **2** | **9** | **9** | Layer 14 Sectors 00-09 |
| **Chan. 26** | **1645** | **2** | **9** | **10** | Layer 14 Sectors 10-19 |
| **Chan. 27** | **1645** | **2** | **9** | **11** | Layer 15 Sectors 00-09 |
| **Chan. 28** | **1645** | **2** | **9** | **12** | Layer 15 Sectors 10-19 |
| Chan. 29 | Not used | | | | Not used |
| Chan. 30 | Not used | | | | Not used |
| Chan. 31 | Not used | | | | Not used |

Figure 2.44: Geiger HV values and correspondence between crate, board, channel number and Geiger layer number.

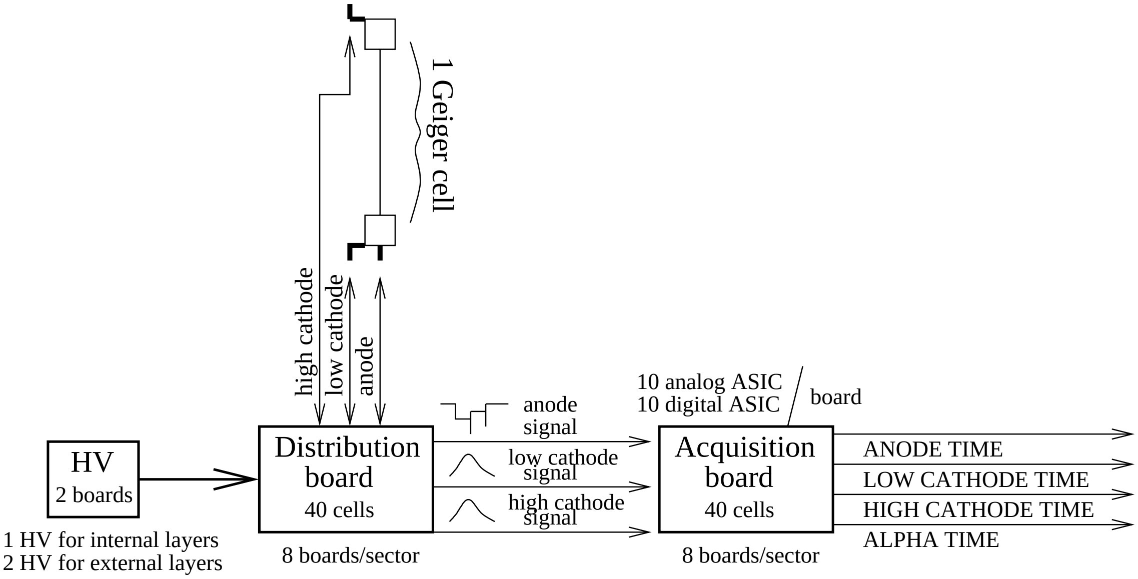

Figure 2.45: Tracking detector system electronics.

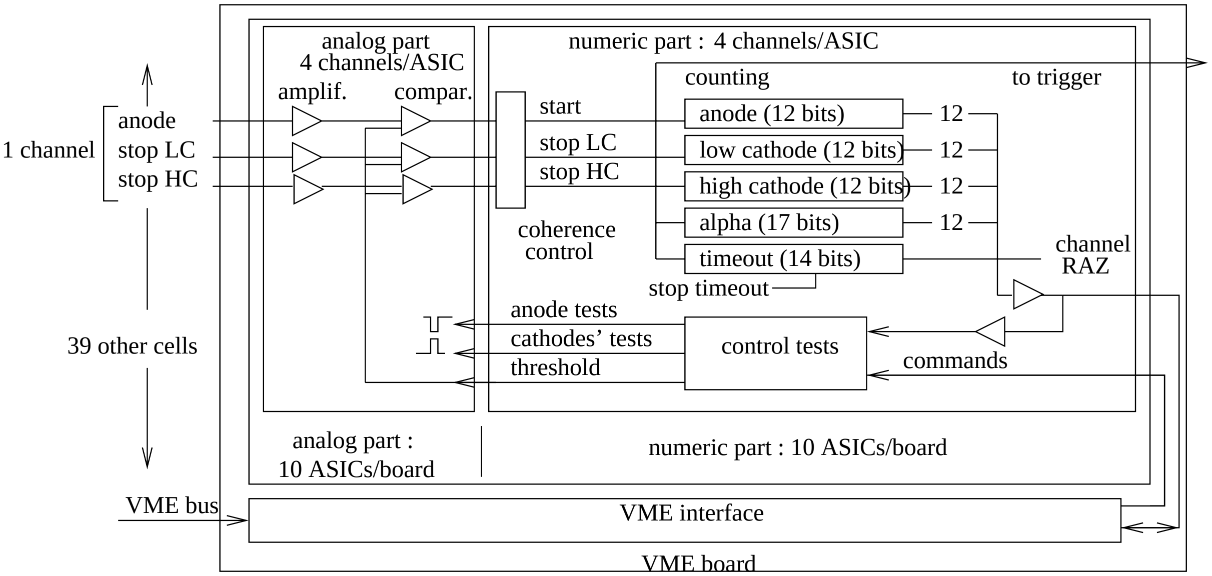

Figure 2.46: Principle of the Geiger cell acquisition board for one channel corresponding to 1 cell about 40.

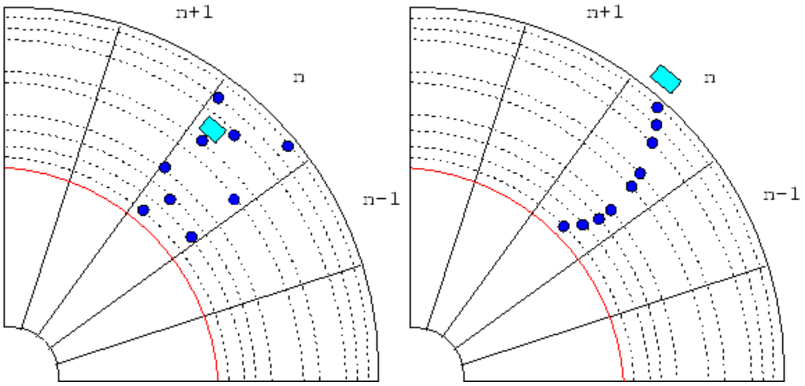

Figure 2.47: Two different Geiger cell and PMT configurations giving the same information to the trigger.

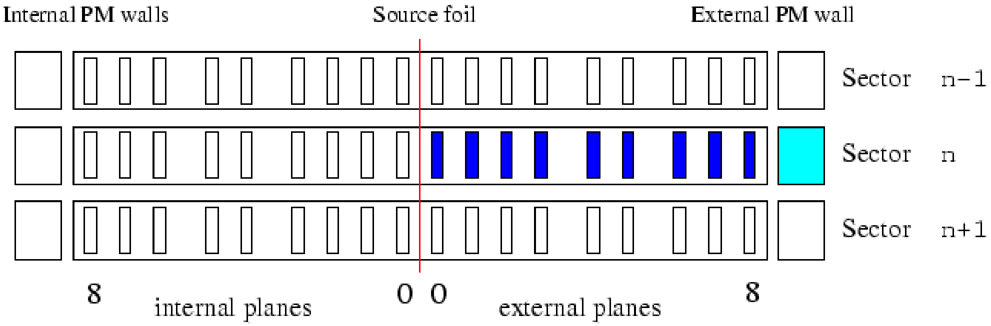

Figure 2.48: Information from trigger for the two event configurations from Fig. 2.47. Filled rectangles are triggered input signals for sectors n-1 to n+1.

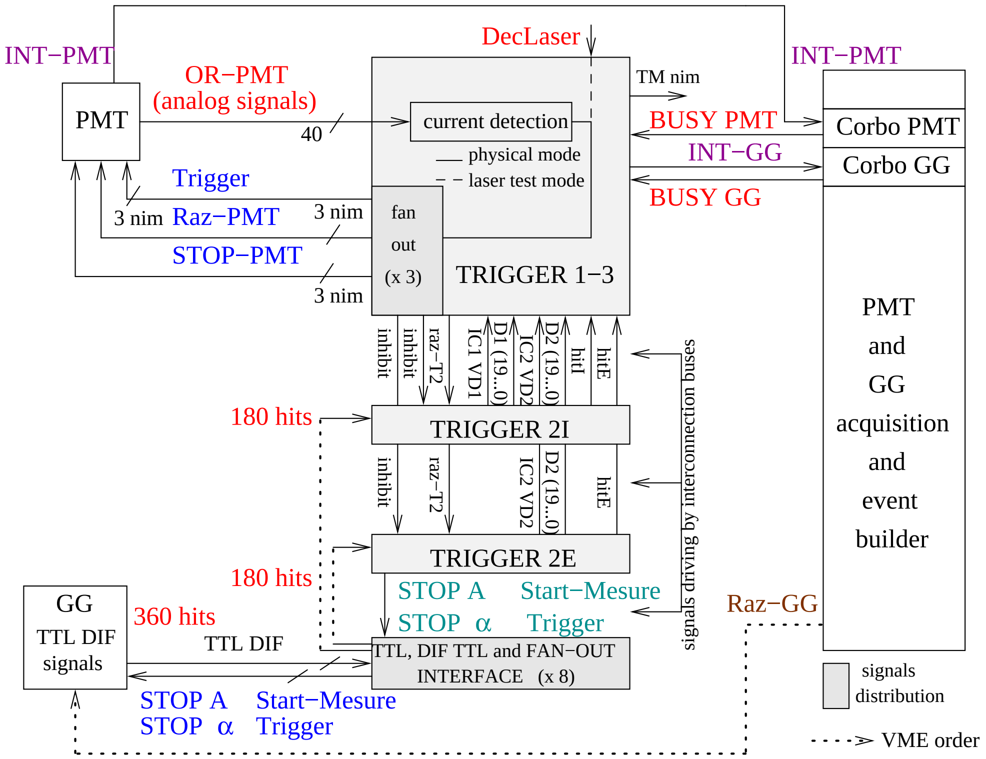

Figure 2.49: Overview of the NEMO 3 trigger system.

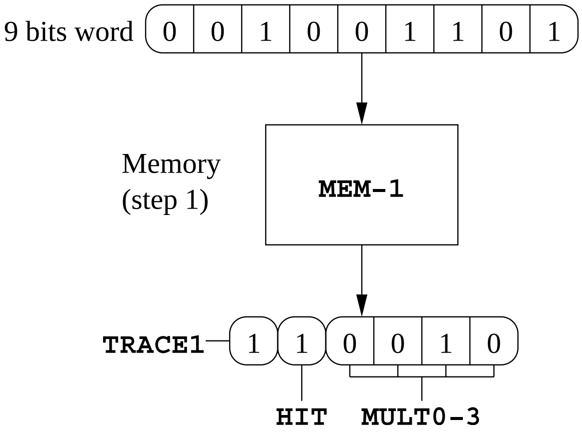

Figure 2.50: Configuration of the signals produced in exit of *MEM-1* memories: creation of one 6-bits word per half-sector.

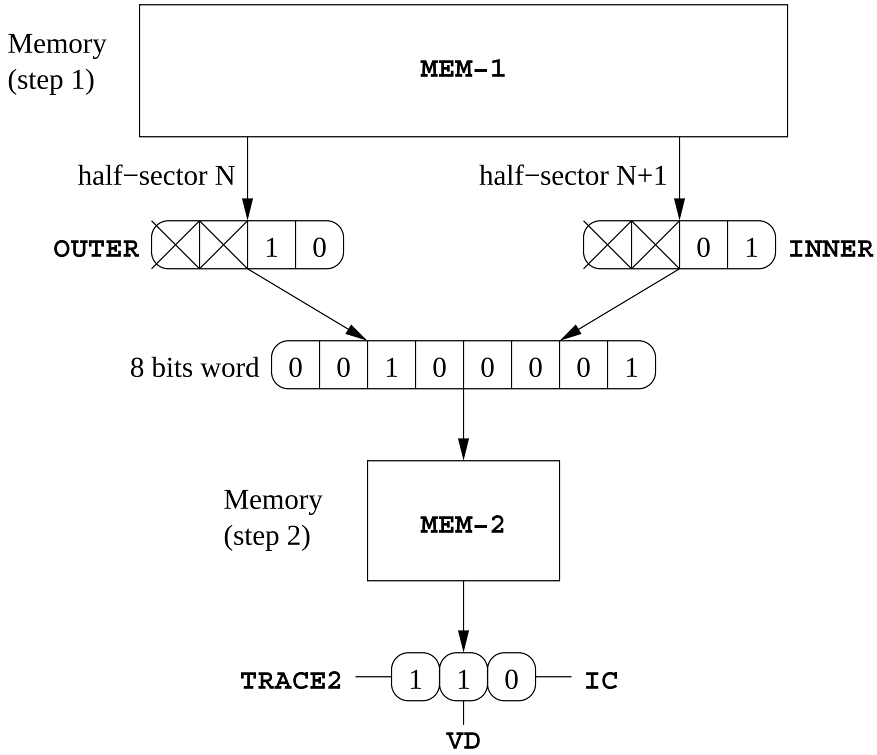

Figure 2.51 : Configuration of the signals produced in exit of *MEM-2* memories: creation of one 3-bits word per association of two half-sectors. Here is presented an example for trigger number *TRN*=21, where an **OUTER** pattern configuration is recognized in half-sector "N" and an **INNER** pattern configuration is recognized in half-sector "N+1". Thus bit **VD** is activated in exit of *MEM-2*, because an "interesting" track has been identified in these two adjacent half-sectors. Note that bit **IC** is not activated, meaning that coincidence between pre-tracks and fired PMT are required for validation of the third level T3 (see Section 3.2).

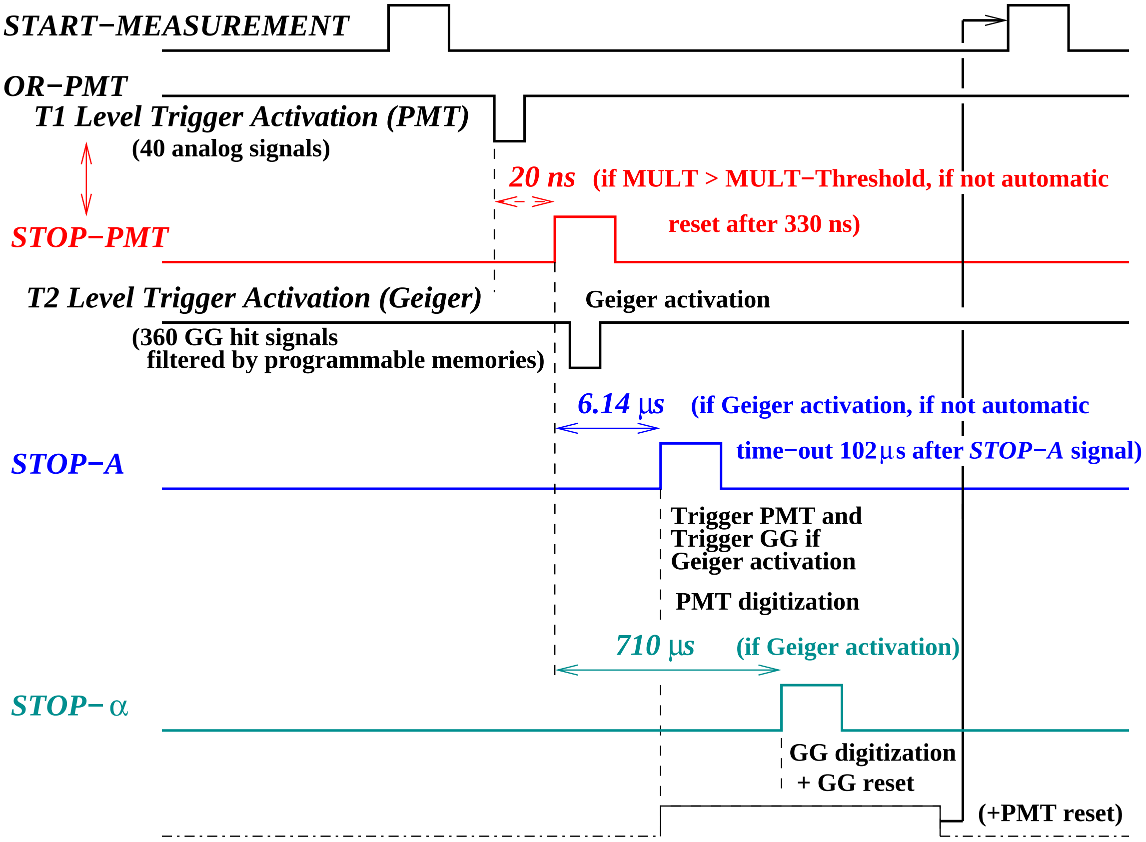

Figure 2.52: Chronogram for the trigger in the *PMT+GG* mode.

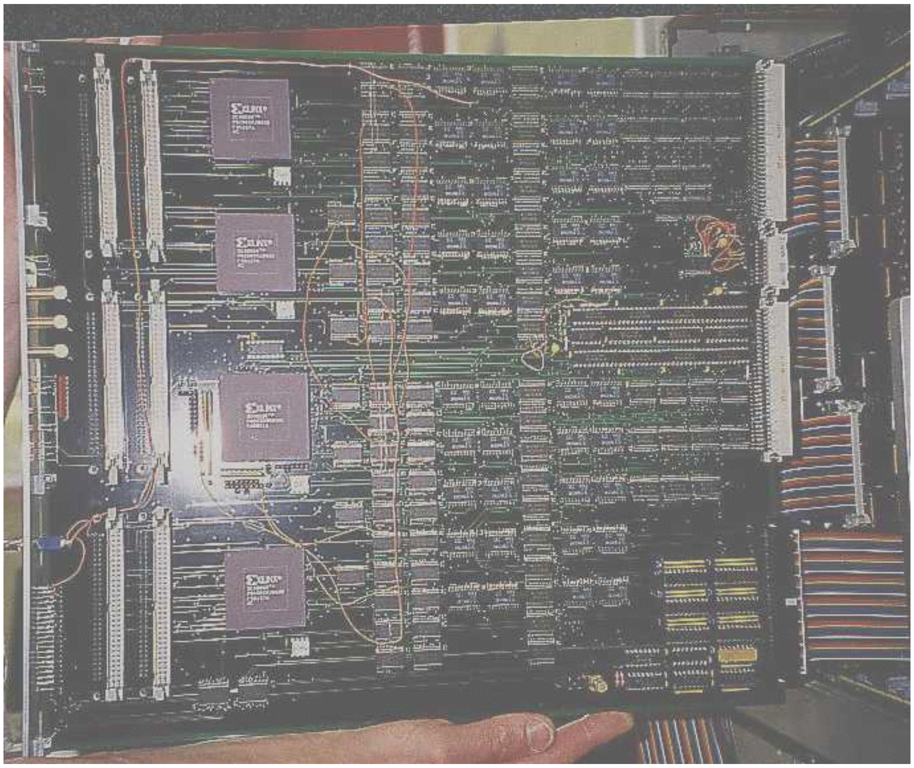

Figure 2.53 : Picture of the T2I trigger board.

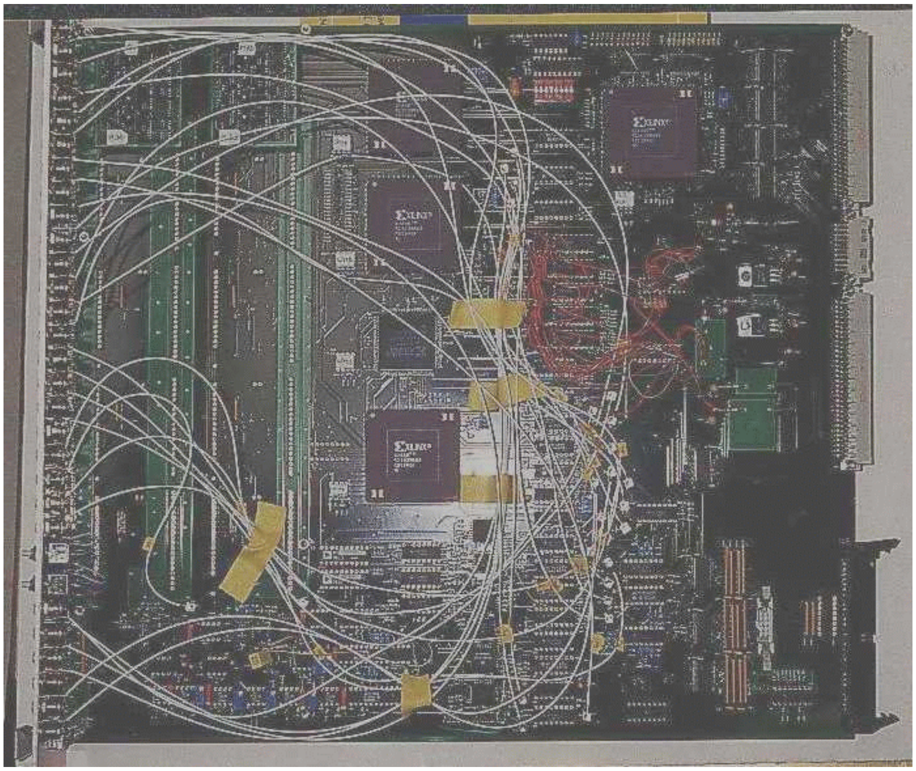

Figure 2.54: Picture of the T1-3 trigger board.

### 2.5.4 The NEMO 3 data acquisition system

An overview of the data acquisition system is presented in Fig. 2.55.
The control and readout of the calorimeter and Geiger cell crates is performed with the intercrate VICbus and two CES RIO 8062 computer modules equipped with PowerPC 604E-300MHz CPU chips. The data acquisition system is based on *Cascade* [30] operating under the Lynx-OS software package developed at CERN. It uses two boards: Corbo PMT for the calorimeter readout trigger and Corbo GG for the track detector readout trigger. The two independent acquisition processors collect information in parallel. After the processors have read out the event and de-activated their “busy” signal, the trigger system reinitializes its logic electronics for the next event. Data buffers for the calorimeter and Geiger cells are then sent to the event builder processor (EVB) via the PVIC bus (multidrop PCI-to-PCI high speed link), as described in Section 3.2.

### 2.5.5 Control of the experiment

Monitoring and control of the experiment from remote sites is possible with two dedicated PCs in the LSM. The two PCs also operate locally. The tasks of these two PCs are not overlapping. The first controls the gas system of the tracking chamber, the current in the magnetic coil and the high voltage on the Geiger and PMT boards. The second controls the on/off power for the acquisition boards and crates, the high voltage crates and the uninterruptible power supply. The principle of the system is shown in Fig. 2.56. The survey system was under LPC responsibility and the control programs were written in LAL[42].

### 2.5.6 The NEMO 3 database: *NEMO DB*

The choice of which database to use for the NEMO 3 experiment was defined by the requirement that it had to manage calibration parameters of the detector for data analysis (see section 2.6 for information about NEMO calibration setup). During the development, it was expanded to include additional information such as run information, monitoring parameters and other.

The MySQL database management system is used for NEMO 3 [31]. Data synchronization in the *NEMO DB* server network is based on the replication concept of the MySQL package. Here any number of servers can be replicated and can transfer data from one primary server. The structure of the NEMO MySQL servers, as shown in Fig. 2.57, includes the primary server at the LSM for information stored in the on-line database. The main server located at Lyon CCIN2P3[43] contains all the data, and a set of local servers mirroring the main server.

The *NEMO DB* contains the electronic logbook of the runs, the calibration parameters of scintillator counters and Geiger cells, as well as other information about the run conditions.

The scintillator counter calibration parameters include:

- Pedestal measurements, which are performed at least once a day. These special runs are automatically processed just after stop of DAQ and the parameters are saved in *pdRun* and *pd* tables.
- Absolute energy calibration parameters, which are derived from analysis of source and laser calibration runs. A few times per year, parameters below saturation energy (where

---

[42] by people from the “contrôle-commande” group

[43] Centre de calcul de l’IN2P3: computer center of the institute for nuclear and particle physics

the relationship between energy and ADC channel is linear) are obtained from runs with calibration sources, when parameters above are extracted from special laser runs. These parameters are stored in *ecRun* and *ec* tables.

- Time shift calibration parameters, which are extracted from sources and neutrons runs, are performed a few times per year. The associated parameters are stored in *tsRun* and *ts* tables.
- Laser correction parameters for the time and energy calibration are produced and stored off-line (later, it will be on-line). Laser measurements are performed at least once a day. The data is stored in *clRun* and *cl* tables.

The two types of Geiger calibration parameters are:

- Simplified calibration parameters consisting of the calculation of propagation times for each cell and in the determination of noisy wires. This monitoring is performed automatically during data processing for each $\beta\beta$ run. The data are placed in *gmRun* and *gm* tables.
- More sophisticated Geiger calibration parameters, which give the status of Geiger cells, are filled irregularly, when one needs to mark special notes about the cells (damaged, problem, recovering...). This status is stored in *gs* table.

The information about the run conditions include:

- Information about the run, which are recorded three times: at the start of the DAQ program in *RunStart* table, before the end of DAQ program in *RunStop* table and before storage of the file on tape in *RunStore* table.
- Information coming from the monitoring system used for the survey of the experiment. Data files dumped by the slow-control program are used to fill slow control tables, which contain the status of the scintillator counters and Geiger cells, the values of the high and low thresholds for the scintillator counters and the result of HV monitoring for the scintillator counters and Geiger cells.

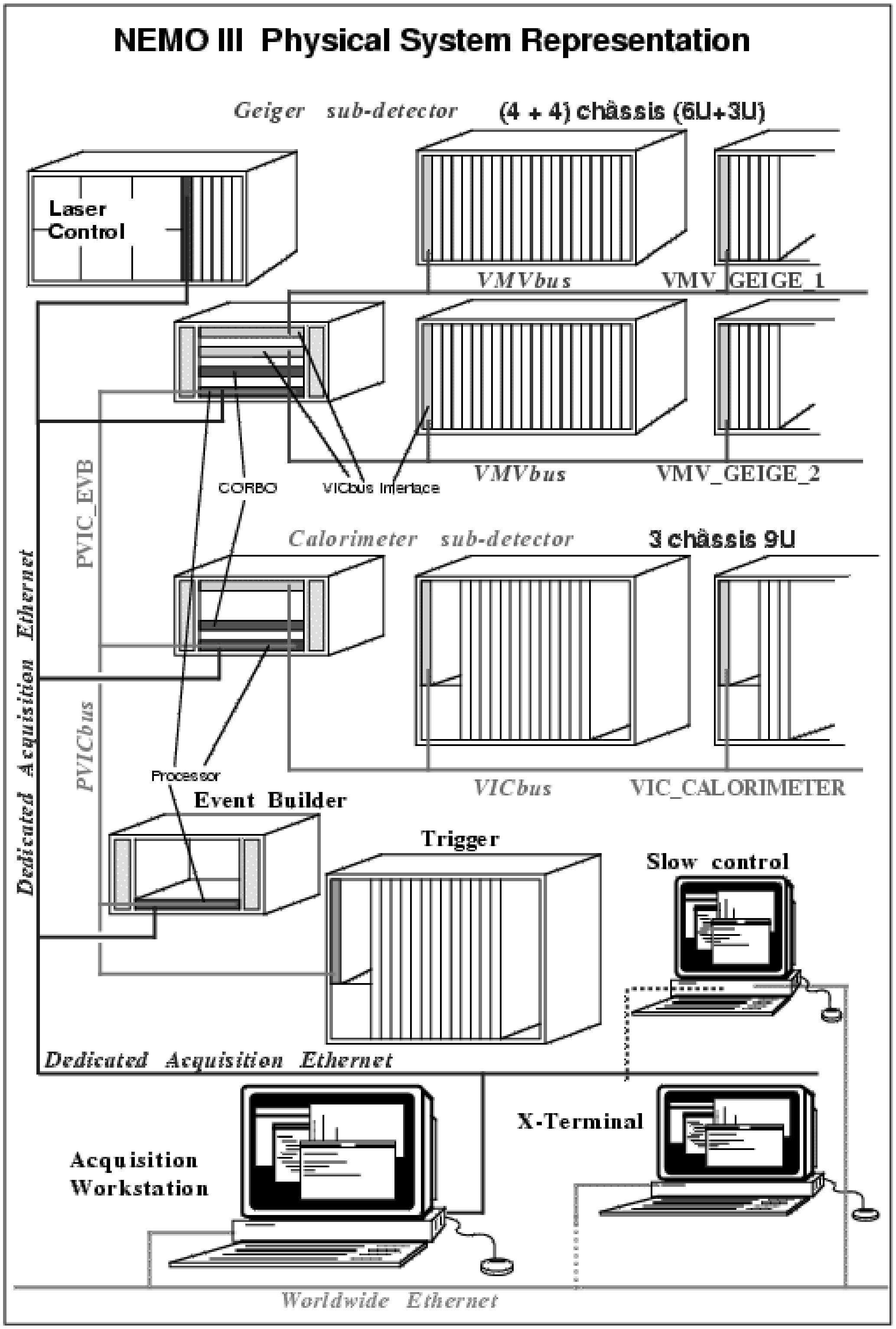

Figure 2.55: Synopsis of the NEMO 3 data acquisition system.

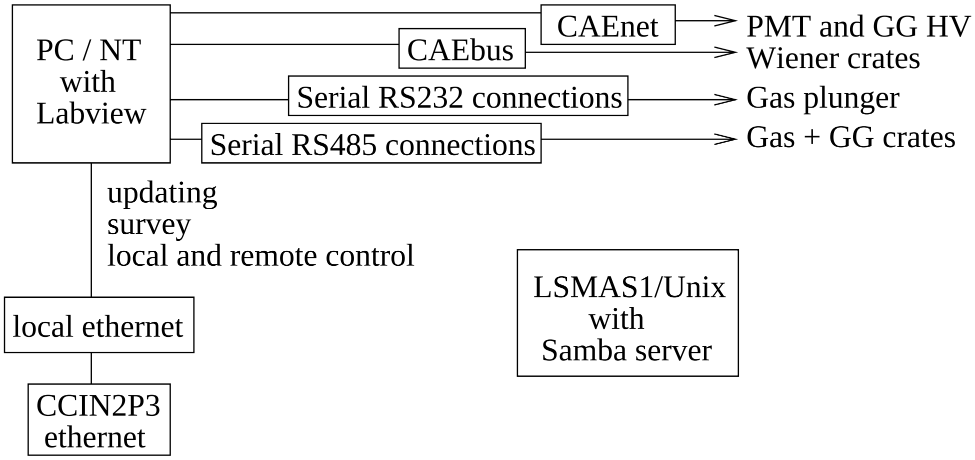

Figure 2.56 : Principle of the monitoring and control of the experiment.

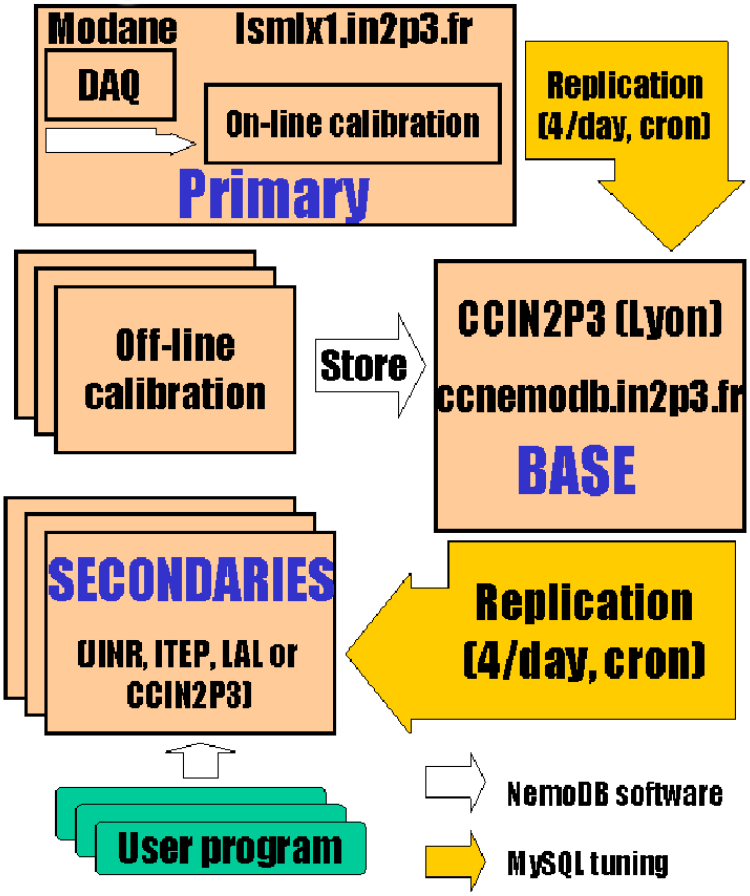

Figure 2.57 : Organization of the *NEMO DB* network.

## 2.6 Energy and time calibration of the counters

### 2.6.1 Introduction

In order to measure accurately the absolute energy released in a double beta decay ($Q_{\beta\beta}$), a calibration procedure was established. Putting a radioactive source in front of the NEMO 3 counters is not as easy as in NEMO 2 because of the scintillator location inside the gas. The solution for NEMO 3 is to use radioactive sources that can be introduced into the detector and present only during runs dedicated to calibration. These absolute energy measurements run for extended periods (at least three days) and take place around six times a year. Thus, daily studies of the stability of the counters are done with a laser survey system.

Timing information is used to discriminate between external and internal events for background studies (see Section 1.3). The relative timing offsets for each of the 1940 counters has to be determined using the measured times of particles emitted in coincidence from $^{60}$Co radioactive sources. Particle times-of-flight are also corrected for several effects: the amplitude corrections due to leading edge discriminators (called time-energy corrections) and TDC slope corrections. These corrections are also checked with the laser survey system.

All the calibration system and running are under IReS responsibility [32], in collaboration with JINR.

### 2.6.2 Mechanics of the calibration tubes

Each of the 20 sectors of the detector is equipped with a vertical tube[44] made of flattened high purity copper[45] that is located along the edge of the source foils (see Fig. 2.58). This tube, through which flows helium gas, is equipped with 3 pairs of Kapton windows, 25 $\mu$m in thick: one window of the pair is oriented towards the internal wall and the other towards the external one. The size of the windows ($26 \times 20$ mm$^2$) and their vertical positions ($z = -90$, 0 and $+90$ cm with an accuracy better than 1 mm) have been chosen to obtain an approximately uniform illumination of the scintillator blocks by three radioactive sources placed inside the tube in precise positions facing the windows. The source carrier is a long narrow Delrin rod[46] supporting three removable source holders, which is introduced into the copper tube from the top of the detector, after the removal of some shields on the top. The source holders, screwed onto the carrier for the calibration runs, are small Delrin frames[47] on which two Mylar foils (of 12 $\mu$m in thick each) sandwiching the centered radioactive source (with a diameter less than 1 mm to allow energy measurements) are glued[48].

This system allows to realize calibration runs of the detector and to put the radioactives sources near the $\beta\beta$ foils. Thus, it permits to obtain electron trajectories from these radioactive sources to the scintillator blocks very similar as those of $\beta\beta$ electrons from source foils.

### 2.6.3 Radioactive sources

Tests realized at IReS with $^{207}$Bi sources have shown that the calorimeter response was not the same for incident electron or $\gamma$-ray particles. This effect is probably the consequence of

---

[44] inner section of (24 x 4) mm$^2$

[45] Cu - OFHC, Cu + Ag 99.99%

[46] 3 m long, with a section of ($22.5 \times 3$) mm$^2$

[47] (26 x 17) mm$^2$

[48] Epotek 310

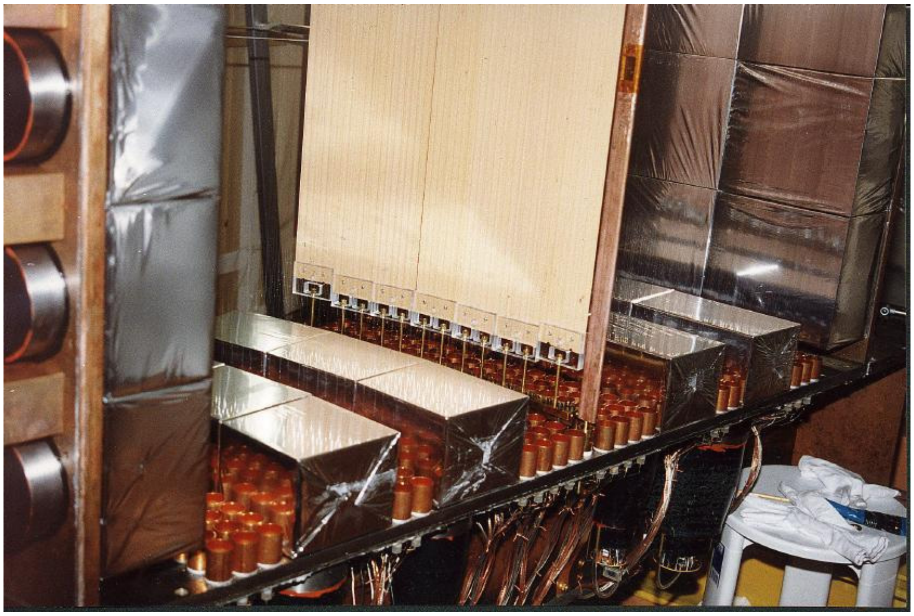

Figure 2.58: View of the calibration tube of one sector with the kapton window in bottom position ($z = -90$ cm).

different light collection for electrons directly absorbed by the entrance face of the scintillator block than for those produced in the plastic scintillator. The NEMO 3 experiment is mainly focused on electron energy measurements. Thus for energy calibration or alignment procedure of the counters, one needs radioactive sources which emit electrons. The choice was made to use $^{207}$Bi and $^{90}$Sr sources.

Decay of the first one provides conversion electrons of 482 and 976 keV energy (K-lines) suited for an energy calibration up to 1.5 MeV (see Table 2.29 and Fig. 2.59). The products in $^{207}$Bi decay are essentially $\gamma$-rays, thus the tracking chamber must be in operation to select electrons originating directly from these sources. As a consequence, counting rates has to be not too high when using the 60 source positions: each $^{207}$Bi source has an activity of 222 Bq (6 nCi). The energy loss distribution in glue has been measured and all 60 sources selected are such that $\Delta E < 6$ keV (the sources are numbered thus individual corrections can be applied, with an average value of 2 keV). During their flight towards the scintillator blocks, the electrons cross several materials (Mylar source support, kapton window, He gas, scintillator wrapping) where they lose energy. The mean energy losses are estimated to be 45 keV and 40 keV respectively for the 482 keV and 976 keV electrons.

To measure energies up to 3 MeV or more, one needs at least one additional calibration point, which is obtained using electrons from pure beta emitter $^{90}$Y (daughter of $^{90}$Sr, with a period of 2.671 days) and measuring the end-point of the $\beta$ spectrum at 2.283 MeV (with an intensity of 99.984%)[49]. This calibration does not require pattern recognition because the events of interest are located in the tail of the spectrum, which can only contain electrons coming directly from the sources. Relatively intense sources are used here for short runs with high speed event collection.

---

[49] $^{90}$Y has an other $Q_\beta$-value of 523 keV but the associated intensity is only 0.016%

For timing calibration, the relative offsets for each channel are determined with a $^{60}$Co source, which emits two coincident $\gamma$-rays with energies of 1332 and 1173 keV. Spectra of arrival time differences are collected to establish time delays between the 1940 channels. This time calibration does not require the use of the tracking chamber and allows the use of relatively intense sources.

| $E_\gamma$ (keV) | $I_\gamma$ (%) | $E_{e^-}$ (keV) | $I_{e^-}$ (%) |
|---|---|---|---|
| 569.7 | 97.74 | 481.7 (K) | 1.52 |
| | | 553.8 - 556.7 (L) | 0.440 |
| 1063.7 | 74.5 | 975.7 (K) | 7.03 |
| | | 1047.8 - 1050.6 (L) | 1.84 |
| 1770.2 | 6.87 | 1682.2 (K) | 0.02 |

Table 2.29: Energies and intensities (for 100 decays) for conversion electrons (K and L lines) and $\gamma$-rays emitted by $^{207}$Bi source [17].

Calibration source activities were $\gamma$ controlled with a Ge-Li detector, for which the efficiency was measured using calibrated reference sources ($^{152}$Eu, $^{60}$Co, $^{137}$Cs and $^{133}$Ba, with an activity of 74 to 111 Bq (2 to 3 nCi)). Each source activity was measured twice, during at least one hour, with a reproducibility better than 2.5%.

### 2.6.4 Laser calibration system

In an experiment such as NEMO 3, which requires stability for many years over a large number of PMTs, frequent tests of the detector's stability are of paramount importance. As in NEMO 2, it has been decided to use a laser system. The objectives of this system [33], as shown in Fig. 2.60, are first a daily check of the absolute energy and time calibration, which permits the calculation of the corrections according to the emission peak. Next, measurements of the PMTs linearity between 0 and 12 MeV are made and finally is determined the time-energy relation. To accomplish this, the shape of the laser signal has to be very similar to the one produced by an electron. Thus the laser light must be known with very high accuracy ($< 1\%$) and must be stable during the measurement. One needs also a precise calibration of the optical filter transmission for the energy range 0 to 12 MeV and a good common time reference (STOP). For safety reasons, two different laser systems are used for daily survey (see Tables 2.30 and 2.31).

| | |
|---|---|
| wavelength | 337.1 nm |
| peak output power | 200 kW |
| pulse energy | 130 $\mu$J |
| pulse duration | 700 ps |
| repetition rate | (1-20) Hz |
| beam dimensions | 2 mm$^2$ |
| beam divergence | 2 x 3 mm$^2$ |

Table 2.30: Laser characteristics for MNL 202 from Lasertechnik Berlin.

The $N_2$ laser wavelength of $337 \pm 15$ nm is selected after focalization of the laser light with an optical lens. Then the light beam is split into two parts. The first one is sent to a photodiode, which can monitor the laser light intensity. A variable optical attenuator can be used to adjust the flux. This attenuator is a glass disk 75 mm in diameter, covered with a sheet of aluminum

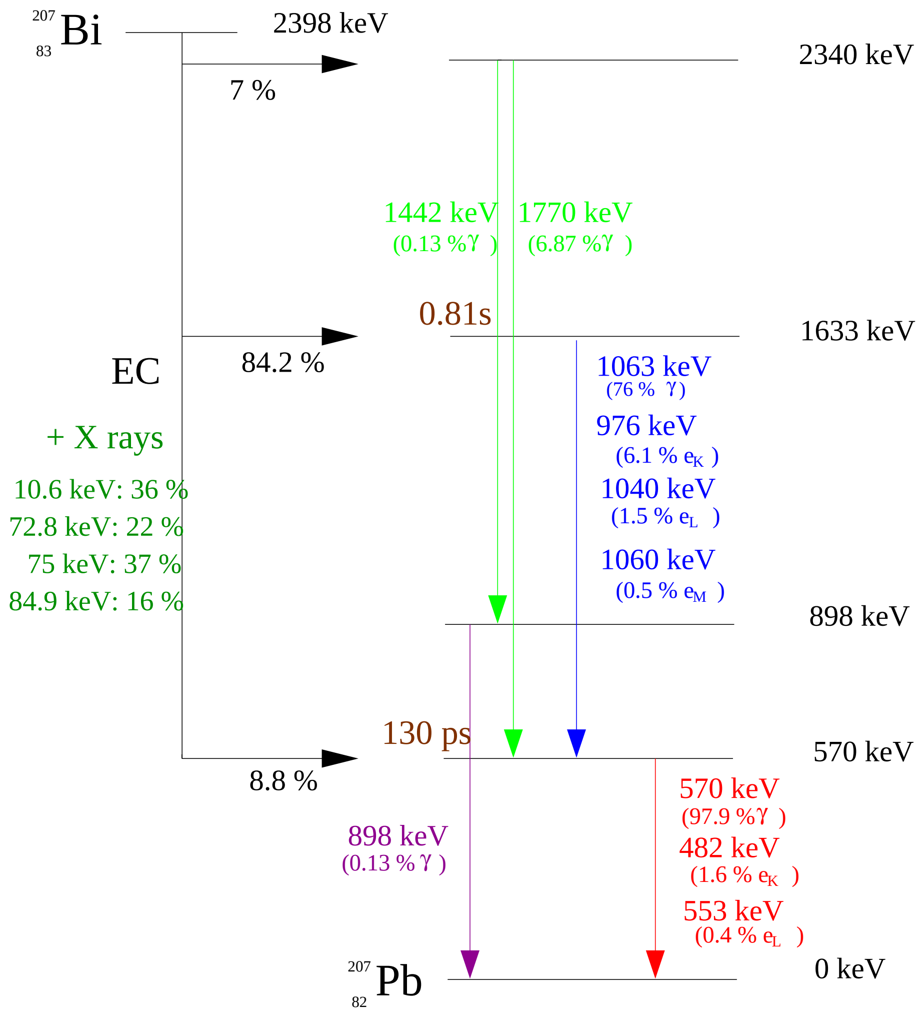

Figure 2.59 : Decay scheme for $^{207}$Bi [17].

| | |
|---|---|
| wavelength | 337.1 nm |
| peak output power | 30 kW |
| pulse energy | $> 120\ \mu$J |
| pulse duration | 4 ns |
| repetition rate | (1-20) Hz |
| beam divergence | 3 x 7 mm$^2$ |

Table 2.31 : Laser characteristics for sealed VSL-337 from Laser Science Inc.

of which the thickness is increased with the angle. The rotation of this continuous disk can be made using a stepping motor with an angular precision of $0.1^o$.

The second part of the laser beam goes through two optical filter wheels to simulate the full range of energy. This beam is then wavelength shifted to 420 nm and sent to the NEMO 3 PMTs by means of optical fibers. The shifter is a scintillator ball, wrapped in Teflon and aluminum to increase diffusive reflections, used to mimic the signal of electrons in the scintillators (see

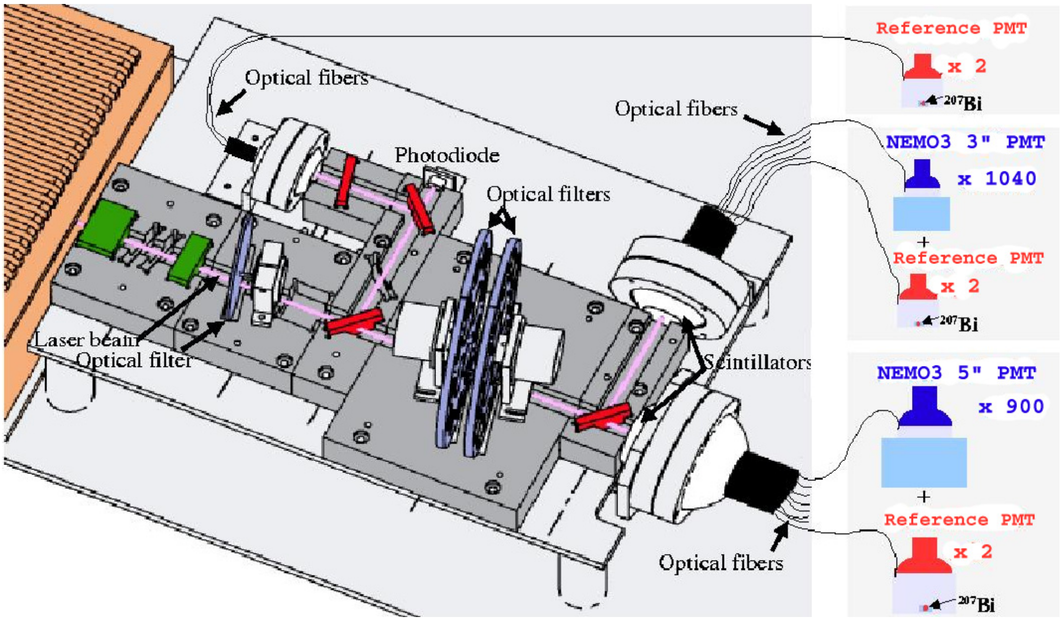

Figure 2.60 : The laser calibration system, with only one laser beam representation [33].

Fig. 2.61). Each optical fiber (see Table 2.32) is divided into two strands and the optical distance between these two is adjustable using individual attenuators, which allow the distribution of the same flux of light to all the counters (equivalent to around 1 MeV energy for daily procedure). Six reference counters (independent of the NEMO 3 calorimeter) equipped with $^{207}$Bi sources allow the monitoring of the laser by measuring energies of both the laser and the 976 keV conversion electrons emitted from $^{207}$Bi. Two of the six reference counters (one 3" PMT and one 5" PMT) receive the same light flux as the photodiode to check its stability and the four others (two 3" PMTs and two 5" PMTs) are used to check the light received by the NEMO 3 counters.

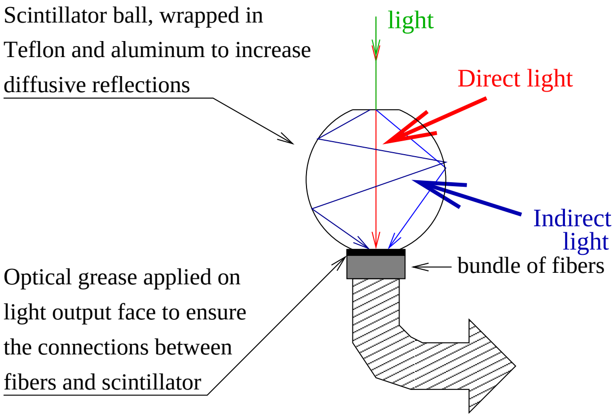

Figure 2.61 : Scintillator ball used as a wavelength shifter for the laser system, as well to format the laser light.

| | |
|---|---|
| core (polymethyl methacrylate) | 0.5 mm $\phi$ |
| cladding (fluorinated polymer) | step index |
| jacket (polyethylene) | 1.0 mm $\phi$ |
| numerical aperture | 0.46 |
| acceptance angle | $55^o$ |
| attenuation at 400 nm | 0.2 dB/m |
| allowable bending radius | $\geq$ 17 mm |
| temperature range | -40 to $85^o$ C |

Table 2.32: Characteristics of the optical fibers (Toray PFU-CD 501-10-E).

The electronic part of the laser system is a special one using two boards. The first board allows the conversion of the electrical charge from the photodiode into electrical voltage. The second board uses a 12-bits ADC. With a special laser processor, a common *STOP* is generated by the photodiode. For laser run, the trigger is made using only NIM *DecLaser*[50] input to generate the *STOP-PMT* signal, which gives the time precision.

The daily laser procedure is carried out in two steps. First, after stopping the current $\beta\beta$ run, the laser is stabilized for checking its parameters (pressure, frequency, ...). During this step the flux can be corrected if necessary. The second step consists of a pedestal measurement for the PMTs[51], which is followed by the acquisition of the laser and $^{207}$Bi events. Finally the laser is turned off and a new $\beta\beta$ run is started. For a "complete" calibration run up to 12 MeV, the procedure is only repeated few times during the year with different fluxes and changing the rotation of the two optical attenuator disks for each run. A webcam put in front of the laser system (http://www.lsmcam1.in2p3.fr) can be used to check that the laser system is off.

### 2.6.5 Energy alignment of the counters

As explained in paragraph 2.5, one high voltage channel supplies three PMTs. The individual gain adjustment of each PMT was done using spectra of conversion electrons emitted from $^{207}$Bi sources. An example of spectra and fitting procedure is shown in Fig. 2.62: for each PMT, one obtained the total one electron spectrum (1); 482 keV electron peak position was isolated (2) and its mean position was calculated (3) using a gaussian fit; from this result, 976 keV electron peak position was isolated (4) and its mean position was calculated using first probability distribution (5) and then a gaussian fit (6). The gain correction for each PMT, which was given by the procedure, was used to calculate the new values of the two appropriate resistors on the repartition board. After modification of the resistors, results of the alignment were checked with a new acquisition. In average, only two iterations were needed.

### 2.6.6 Absolute energy calibration method

Over the full 12 MeV range of energies measured by NEMO 3, the relation between the charge signal and energy deposited in the counter is not necessarily linear. The relation is, however, linear up to 4 MeV, where the greatest accuracy is required:

$$E = a\,(C - P) + b \tag{2.10}$$

---

[50] DecLaser = Déclenchement Laser, that means Laser Trigger

[51] 1940 PMTs from the NEMO 3 calorimeter and six PMTs for the reference counters

here $C$ is the ADC value of the scintillator and $P$ is the pedestal. The energy calibration constants $a$ and $b$ are determined using at least two points from measurements with radioactive sources, while the relation for the energies greater than 4 MeV is determined using a "complete" laser calibration run.

The energy resolution is defined from FWHM($E$) measured value, dividing it by 2.35, which results from a quadratic addition:

$$\mathrm{FWHM}(E) = AE \oplus B \oplus CE^2 \tag{2.11}$$

The energy resolution was initially assumed to have essentially the two first contributions. The principal component, which originates from the statistical fluctuations of the scintillation photons and from the number of photo-electrons at the PMT anode, increases as the square root of the energy. The second component is due to the instrumental effects which are energy independent. Finally, a third term has been added to the quadratic addition, which depends upon the gain fluctuations, presence of non-uniformity and non-linearity as well as calibration method and results.

Using 60 $^{207}$Bi sources ($\sim$ 220 Bq each) with the high threshold set at 48 mV ($\sim$ 150 keV), a $\sim$ 72 hour run yields between 1,500 and 4,000 events for each PMT with identifiable not scattered tracks, depending on the block type and position. Then the positions of the two peaks, corresponding to the 482 and 976 conversion electrons, are extracted and the resolution is obtained (see Fig. 3.25 in Section 3.4).

Using four $^{90}$Sr sources simultaneously ($\sim$ 6 kBq each) eight runs were taken with the sources in different positions (see Table 2.33) and a threshold of 48 mV ($\sim$ 150 keV). For each PMT about $5 \times 10^4$ events are used to form a spectrum (see top of Fig. 3.26 in Section 3.4). A fit to the high-energy tail of the spectrum is made with a function describing the shape of a single $\beta$ spectrum of $^{90}$Y, convolved with the energy resolution function $\sigma(E)$ and taking into account the mean energy loss of the electrons in the gas of the wire chamber.

| | | | |
|---|---|---|---|
| 0T | 5B | 10T | 15B |
| 2T | 7B | 12T | 17B |
| 4T | 9B | 14T | 19B |
| 6T | 11B | 16T | 1B |
| 8T | 13B | 18T | 3B |
| 1C | 6C | 11C | 16C |
| 3C | 8C | 13C | 18C |
| 5C | 10C | 15C | 0C |

Table 2.33: $^{90}$Sr source positions for the 8 runs. Letters T, C and B refer respectively to $z = 90$, 0 and -90 cm for Top, Central and Bottom.

Finally, these three results (two peaks at 482 and 976 keV and one end-point at 2283 keV) from the calibration runs with $^{207}$Bi and $^{90}$Sr are combined to extract the parameters $a$ and $b$ of a linear calibration valid for the energy region up to 4 MeV. The results of energy calibration runs are presented in Section 3.4.

### 2.6.7 Energy corrections using the laser system

During calibration periods, laser runs are carried out every two hours. The last one is used as a reference just after the calibration runs and gives a fiducial reference energy, $E_0$, for each counter (one assumes there is no correction to be applied to the $b$ offset). Counters for which the corrected gains obtained from the laser survey system are different than those resulting from absolute calibration results, have a correction factor applied to their reference energy $E_0$. At a later time $t$ after calibration period, a new value of the energy, $E_t$, is measured:

$$E_0 = a_0(C_0 - P_0) + b \qquad \text{and} \qquad E_t = a_t(C_t - P_t) + b = e_{corr} \times a_0(C_t - P_t) + b$$

where $e_{corr}$ is the correction factor to be applied. It represents the variation of the calibration slope of the counter as a function of time between $t_0$ and $t$. This variation of the laser light is determined comparing the laser peak position ($C_{laser}$) and the 976 keV peak position from the $^{207}$Bi ($C_{Bi}$) between $t_0$ and $t$ for the six reference counters.

$$\frac{E_t}{E_0} = \frac{C_{lasert} - P_t}{C_{laser0} - P_0} \times \frac{C_{Bi0} - P_0}{C_{Bit} - P_t} \tag{2.12}$$

Results are then transferred to the database. Since 2004, a new program written at CENBG [34] is used for laser survey.

The “real” energy value $E^{(i)}_{(t)}$ for counter number $i$ at instant $t$ is finally given by:

$$E^{(i)}_{(t)} = [(C^{(i)}_{(t)} - P^{(i)}_{(t)}) \times a^{(i)} \times e^{(i)}_{corr_{(t)}}] + b^{(i)} \tag{2.13}$$

### 2.6.8 Time calibration

The timing response of two counters detecting two particles emitted in coincidence depends not only on the time-of-flight of each particle, but also on several effects which have to be corrected for.

#### 2.6.8.1 Time alignment of the counters

All PMTs must be aligned in time. The time taken for each PMT to respond to a signal depends on the individual characteristics of the counter. In order to use only one time scale, an alignment procedure has been developed to obtain the individual time shifts $\varepsilon^{(i)}$ ($i = 1$ to 1940).

Let $\varepsilon^{(i)}$ ($i = 1, 1940$) be this “intrinsic” unknown delay for each PMT. These delays are due to the small differences which can been found in cable lengths, in PMT transit times, in scintillator or light guide geometry, in PMT arrangement, etc... The procedure to find $\varepsilon^{(i)}$ uses the two $\gamma$-rays emitted in coincidence by a decay in a $^{60}$Co radioactive source (1173 keV and 1332 keV) and detected by a pair of scintillators. Both counter electronics have common *START* due to the decay mode and there is a common *STOP-PMT* for all the counters, which allows extracting the individual delays, by writing for each pair of PMTs:

$$TOF^{(i)} + tdc^{(i)} + \varepsilon^{(i)} = TOF^{(j)} + tdc^{(j)} + \varepsilon^{(j)}$$

where $TOF^{(i/j)}$ is the time-of-flight of the particle, $tdc^{(i/j)}$ is the time measured in the associated TDC counter and $\varepsilon^{(i/j)}$ is the individual delay to be found.

Since measured time and time-of-flight are known, one can call $\delta^{(ji)}$ the difference $(TOF^{(j)} + tdc^{(j)}) - (TOF^{(i)} + tdc^{(i)})$. Thus $\varepsilon^{(i)} = \varepsilon^{(j)} + \delta^{(ji)}$. If one considers all the events $N^{(i)}$ involving the counter $i$ and call sum over $i$ one gets:

$$N^{(i)} \cdot \varepsilon^{(i)} = \sum \delta^{(ji)} + \sum \varepsilon^{(j)},$$

$$\varepsilon^{(i)} = \frac{\sum \delta^{(ji)}}{N^{(i)}} + \frac{\sum \varepsilon^{(j)}}{N^{(i)}}$$

Using a "successive approximation" method and putting $\sum \varepsilon^{(j)} \sim 0$ due to its randomly distribution being the fluctuations in the apparatus set-up, the global formula to find $\varepsilon^{(i)}$ after $(n)$ iterations is:

$$\varepsilon^{(i)}_{(n)} = \frac{\sum \delta^{(ji)}}{N^{(i)}} + \frac{\sum \varepsilon^{(j)}_{(n-1)}}{N^{(i)}}$$

In order to calculate the time-of-flight correctly, only one $^{60}$Co source of 15.5 kBq is used per run. Ten runs with different source positions (five runs with this source in Top position in sectors 0, 4, 8, 12 and 16, and five runs in Bottom position in sectors 2, 6, 10, 14 and 18) are performed in order to cover all possible combinations of PMTs. A threshold of 150 mV ($\sim$ 500 keV) is set for the arrival time difference spectra and the relative timing offset $\varepsilon^{(i)}$ for each counter $i$ (see results in Section 3.4).

### 2.6.8.2 Others

The effect of leading edge discriminators is to induce a time-vs-energy dependence, which can be described with a formula using four parameters

$$t(C) = p_1 - \frac{p_2}{p_3\sqrt{C} + p_4} \tag{2.14}$$

and taking into account the pulse shape. Determination of the parameters $p_k^{(i)}$ ($k = 1$ to 4 for counter $i$) is accomplished through a "complete" laser run producing equivalent energies between 0 and 12 MeV. The relative timing offset $\varepsilon^{(i)}$ for counter $i$ is then included in the asymptotic value $p_1^{(i)}$.

The laser survey system is also used to obtain daily time response corrections for each counter, which correspond to TDC slope variations: $t_{corr} = tdc_t - tdc_0$.

Finally, the "real" time, $T_t^{(i)}$, used for a time-of-flight calculation for counter number $i$ at instant $t$ is:

$$T^{(i)}_{(t)} = tdc^{(i)}_{(t)} - t^{(i)}_{corr_{(t)}} - t(C^{(i)}_{(t)}) \tag{2.15}$$

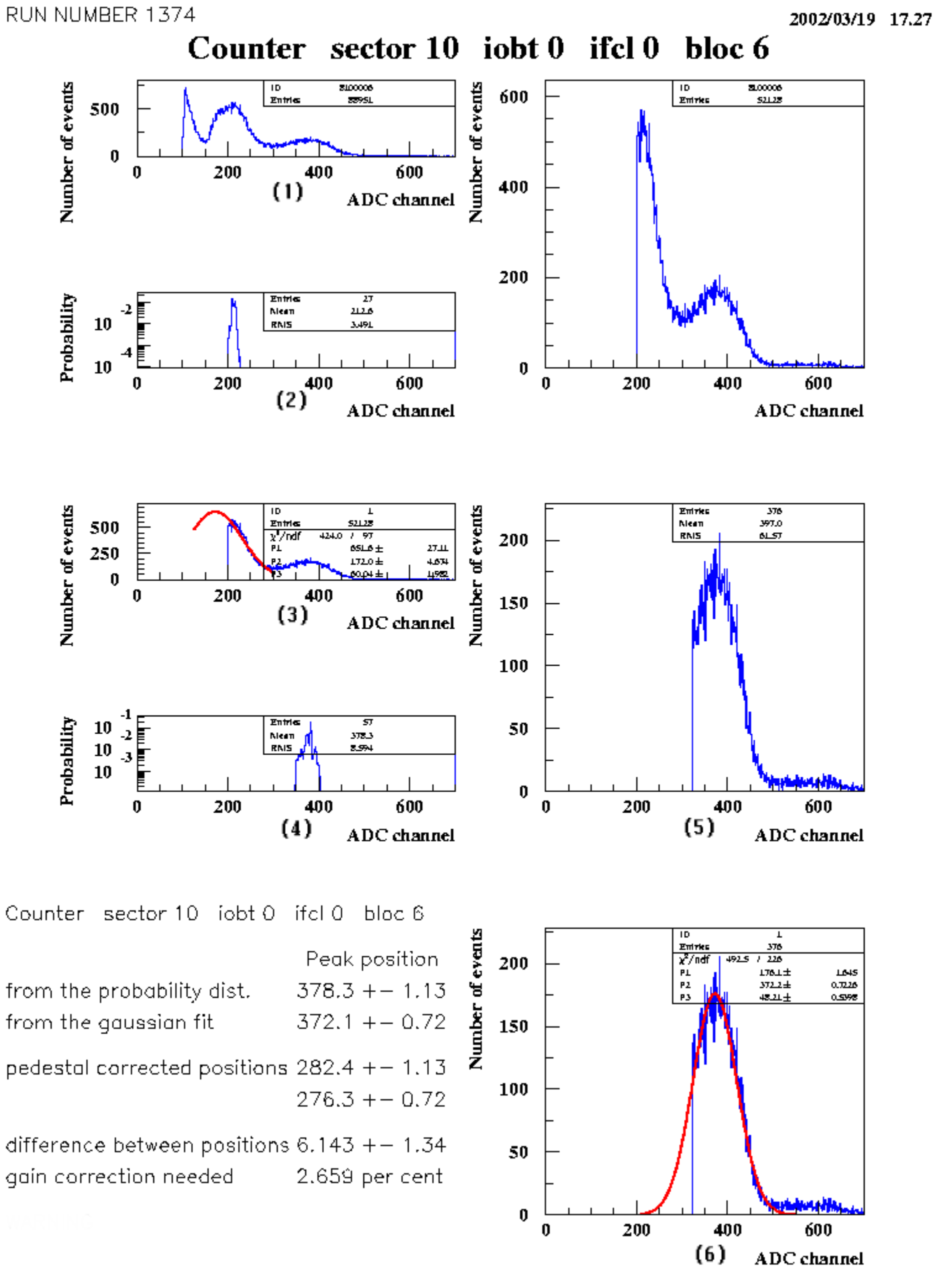
RUN NUMBER 1374

2002/03/19 17.27

Counter sector 10 iobt 0 ifcl 0 bloc 6

Counter sector 10 iobt 0 ifcl 0 bloc 6

| | Peak position |
|---|---|
| from the probability dist. | 378.3 +− 1.13 |
| from the gaussian fit | 372.1 +− 0.72 |
| pedestal corrected positions | 282.4 +− 1.13 |
| | 276.3 +− 0.72 |
| difference between positions | 6.143 +− 1.34 |
| gain correction needed | 2.659 per cent |

Figure 2.62: Alignment procedure: method to fit the peak positions of the 482 and 976 keV conversion electrons from $^{207}$Bi.

## 2.7 Coil and shields

### 2.7.1 Introduction

To reach the desired sensitivity for the effective neutrino mass, there must be no events ($< 0.1$) from external backgrounds in the energy range [2.8 - 3.2] MeV during five years of data collection. This external background corresponds to the two electron events created by interactions in the source foils of the $\gamma$-rays emitted by the surrounding materials after a radioactive decay or a neutron capture. The external background contribution coming from neutrons is due to $(\alpha, \mathrm{n})$ reactions, spontaneous fission of uranium and the interaction of cosmic ray muons in the rocks. The other external background contribution is the $\gamma$-ray flux produced in the LSM, which has been studied using a NaI detector surrounded by different shields [35]. The origins of these $\gamma$-rays are natural radioactivity, radiative neutron captures and the bremsstrahlung of muons. Below 4 MeV, the spectrum is dominated by radioactivity in the surrounding material and rocks. Between 4 and 6 MeV, the shape of the spectrum is well explained by U, Th and daughters, which are internal contaminations in the NaI crystal. Between 6 and 10 MeV, the flux is strongly correlated with neutron captures in the surrounding materials. Finally the flux above 10 MeV falls off and is related to the very weak cosmic muon flux via muon bremsstrahlung.

As shown in Section 2.9, the detector has been designed with stringent radiopurity for its construction materials. For the external background coming from $\gamma$-rays and neutrons, several studies were made with the NEMO 2 detector as well as the NEMO 3 simulations [36]. These have shown that there is a large reduction in these backgrounds given the following conditions to the experiment. A solenoid capable of producing a field of 25 G is surrounded by two external shields, the first one to reduce $\gamma$-ray and thermal neutron fluxes, the second to suppress the contribution of slow and fast neutrons. The design of the coil and shields allows for partial dismantling of the detector to access each sector.

### 2.7.2 The magnetic coil

The simulation of the fast neutrons coming from the laboratory into NEMO 3 was carried out with 20 cm of iron shield. The contribution to the $\beta\beta0\nu$ background by the $\gamma$-rays created from neutron captures leads mainly to $(e^+e^-)$ events and also to a few $(e^-e^-)$ events produced in the source foils. The detection by the calorimeter of the $\gamma$-rays associated with these events provides a high rejection efficiency (80%). A 25 G magnetic field, which provides the charge recognition rejects 95% of the $(e^+e^-)$ pair events.

The coil surrounds the entire detector but the detector access was a necessary design consideration. Thus, the coil is made of ten sections with 203 copper rings connecting every other sector to form one loop of the helix (see Fig. 2.63). The surface of one ring section is 100 mm$^2$ (10 mm in height and 10 mm in width) and the free space for isolating between rings is 3 mm long. Panels of iron of 10 mm in thick, as well as the iron petals of the NEMO 3 detector, are used for backfield. The finished coil is cylindrical, 5320 mm in diameter, 2713 mm in height and has a mass of 5 tons ($\sim 3.1$ tons of high radiopurity copper).

The electric current for a 25 G magnetic field is around 29 A ($V = 18.9$ V). The copper ring resistivity of $\sim 1.6 \times 10^{-8}$ $\Omega$.m leads to an electric resistance of around 0.6 $\Omega$ for the coil. This value has only a very small increase when connecting the system of 2,030 ring connections. The cooling of the coil and PMTs is possible using air fans installed in each iron shield's sector, which can provide an air flux of 1 m$^3$/s.

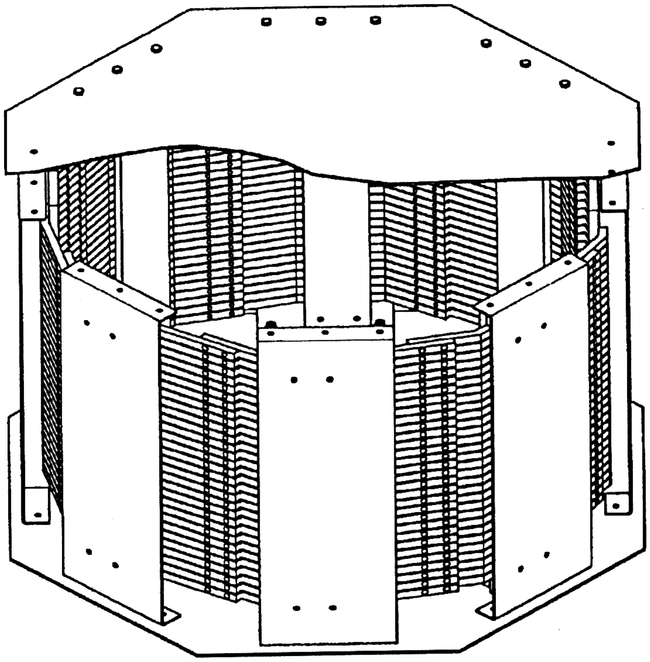

Figure 2.63: Design of the magnetic coil, with the copper rings.

### 2.7.3 Iron shield

The iron shield is also made in ten sections (165 tons) with two end-caps (6 tons each). The lower end-cap is fixed and the upper one is removable. The iron shield is 20 cm thick, except for a few places where it is 18 cm on account of mechanical supports. As other materials, the iron was selected for its radiopurity (see Table 2.43).

### 2.7.4 Neutron shield

The remaining $(e^+e^-)$ pair events (5% not rejected by curvature measurements) and the $(e^-e^-)$ events due to the $\gamma$-rays created by neutron capture can be suppressed only if the flux of neutrons inside the detector is decreased. NEMO 3's neutron shield is optimized to stop fast neutrons with an energy of a few MeV, it also suppresses thermal and epithermal neutrons.

The neutron shield is made of three parts, as shown in Fig. 1.11. The first one is situated below the central tower of the detector (not shown in the figure) and consists of paraffin 20 cm thick. The second part covers the end-caps below and above the detector, and consists of 28 cm of wood. The cylindrical external walls are covered with ten large tanks[52] containing borated water which are 35 cm thick and separated by wood 28 cm thick.

---

[52] from Czech Technical University (Prague, Czech Republic)

Figure 2.64: Detail of the copper rings used to realize the magnetic coil.

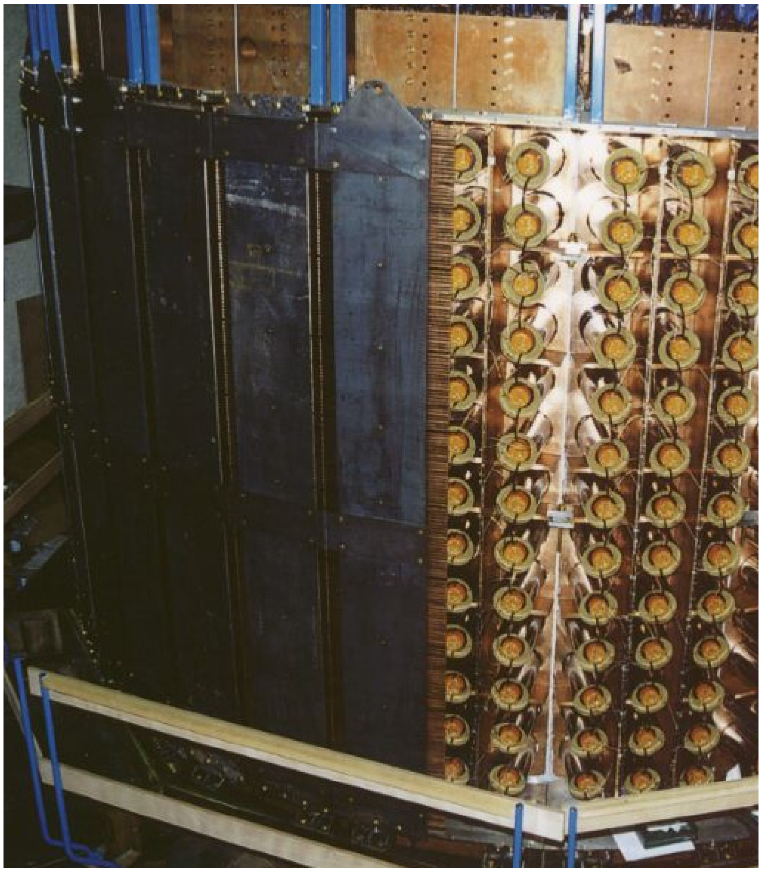

Figure 2.65 : Picture of the coil during its installation round about the detector.

## 2.8 Mounting and assembly of the detector in the LSM

### 2.8.1 Special arrangements of the Fréjus Underground Laboratory

Several arrangements were made in the LSM before the installation of the NEMO 3 detector. In the entrance, to permit the reception of the 13.5 m long semi-trailer, or in the big room, there were a lot of new installations as an overhead crane of 8 tons, a metallic reinforced floor of 2 tons/m$^2$, a new plane area to win 10 cm in height under the overhead crane. Also were realized a class 5,000 clean room to prepare the source foils and finally a clean frame with a light surpressure to install the foils inside each sector.

### 2.8.2 Supporting structure

The steel framework, which supports the NEMO 3 sectors, is made of two parts[53]. It was installed in the LSM at the end of 1998 and supports the 20 sectors of the detector, the magnetic coil and the various shields. All the components of the framework were selected for their radiopurity. To properly enclose the active detector and have access to readout electronics in the narrow experimental hall, the detector was raised off the ground two meters. Thus the control and readout electronics can be housed under the detector. This structure preserves proximity and serviceability of the electronics and detector (see Fig. 2.66).

### 2.8.3 Principle of the gas regulation system

The principle of the gas regulation system is described in Fig. 2.67.

Helium gas from bottles is sent through the flow meter and pressure gauge to a primary bubbler filled with pure ethyl alcohol. Next this mixing is sent inside a cooling box (called FRIGEBAC in the figure), which also contains pure ethyl alcohol at the chosen temperature. There are two cooling boxes and the gas regulation system can switch from one to other. These cooling boxes are able to maintain the needed temperature, which is now 14$^o$C, with a precision of 0.1$^o$C. In output of FRIGEBAC is the helium and alcohol gas mixture ready to be sent inside the NEMO 3 detector. For each sector, there are two gas inputs on the top petal and two gas outputs on the bottom petal. Addition of argon and water (see Section 2.8.5) is carried out just after the output of the mixture from the cooling box. The gas mixture can also be sent through a brass tube in order to test its specifications, before its input inside the NEMO 3 detector as at its output. This tube was initially realized in LAL to choose the wires for the tracking chamber (as presented in Section 2.4.4 and Fig. 2.28).

A view of the system in the LSM is shown in Fig. 2.68.

### 2.8.4 Placing of the sectors on the supporting structure

Once the sectors were made helium tight, the anode and cathode cables were connected at LAL before being transported to the LSM (see Fig. 2.69), where PMTs were attached (a sector in the LSM before PMTs attachment is shown in Fig. 2.70). After gluing (using RTV-615) and testing the PMTs (see Fig. 2.71), the sectors were carried inside the source mounting room and cleaned using alcohol and nitrogen gas.

The source frame, which supports the seven foils of each sector, was prepared simultaneously in the LSM clean room. There was a glove box between this room and the clean frame, to

---

[53] one part from JINR Dubna and the second one from CTU Prague

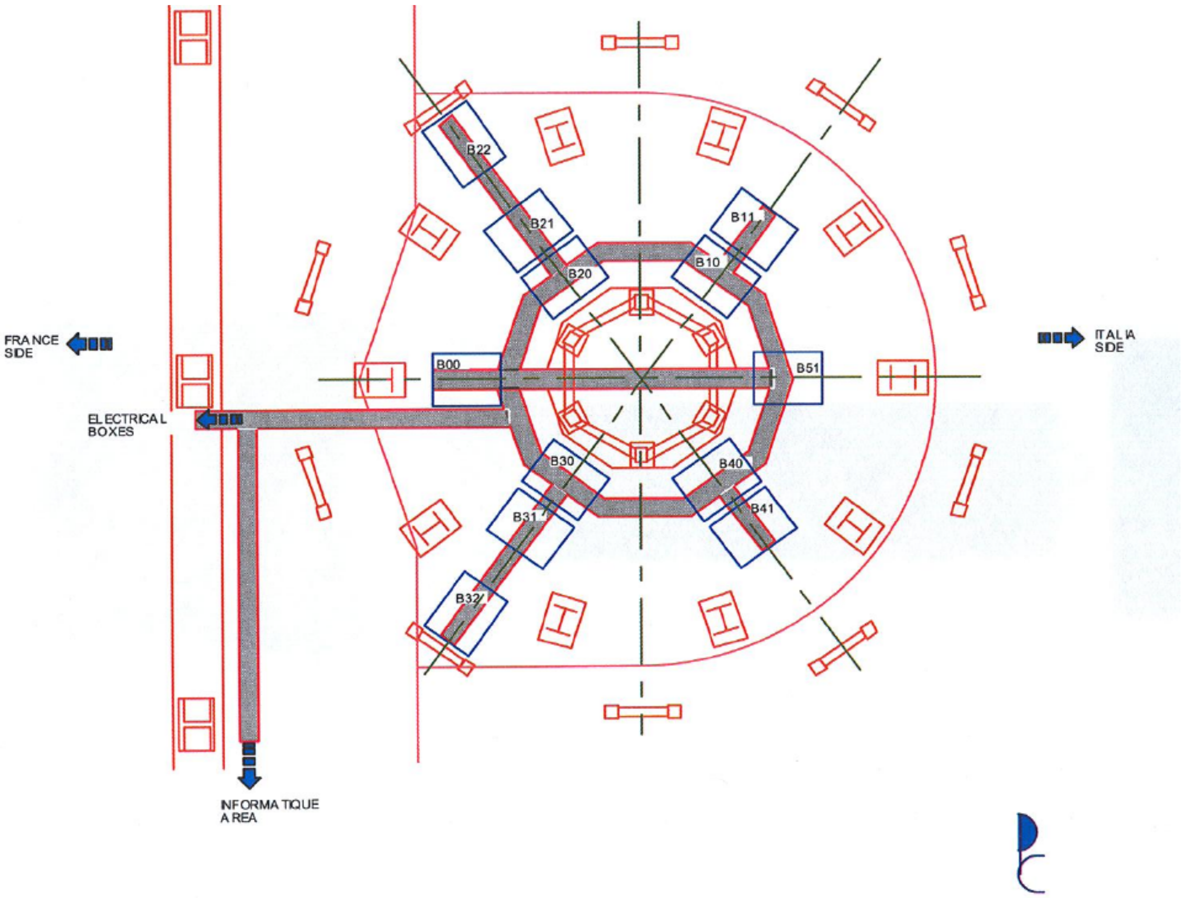

Figure 2.66 : Top view of the setting-up of the electronic racks for the NEMO 3 detector, which are all implemented under the metallic frame.

avoid pollution of the foils when introducing the source frame inside the sector. To minimize the thickness between the sectors during the mounting, a special mechanical system called “Marie-Louise” was chosen to separate the sectors. This is a frame containing a Mylar foil permitting to approach one sector at 1 mm from another one during the mounting, and which can be easily removed when moving the sectors in final position. This “Marie-Louise” frame was glued on both sides of the sector. After 24 h to ensure polymerization of the gluing, the tracking chamber was cleaned with a nitrogen flux to eliminate dust on the wires or on the scintillators. The source frame was then passed from the clean room to the clean frame and mounted in the sector. Finally, the calibration tube was set in position and the sector was cleaned once again with nitrogen and closed with sheets of Mylar glued to the “Marie-Louise” system.

The source mounting room was then opened to move the sectors to the supporting structure. The calorimeter cables (HV and signal) were soldered to the PMT bases and to the distribution daughter boards, when the distribution daughter boards for the tracking detector were installed on their mother boards. These operations were followed by the introduction of the plastic optical fibers into brass tubes which are present in each light guide of the calorimeter (20 mm long for 3”

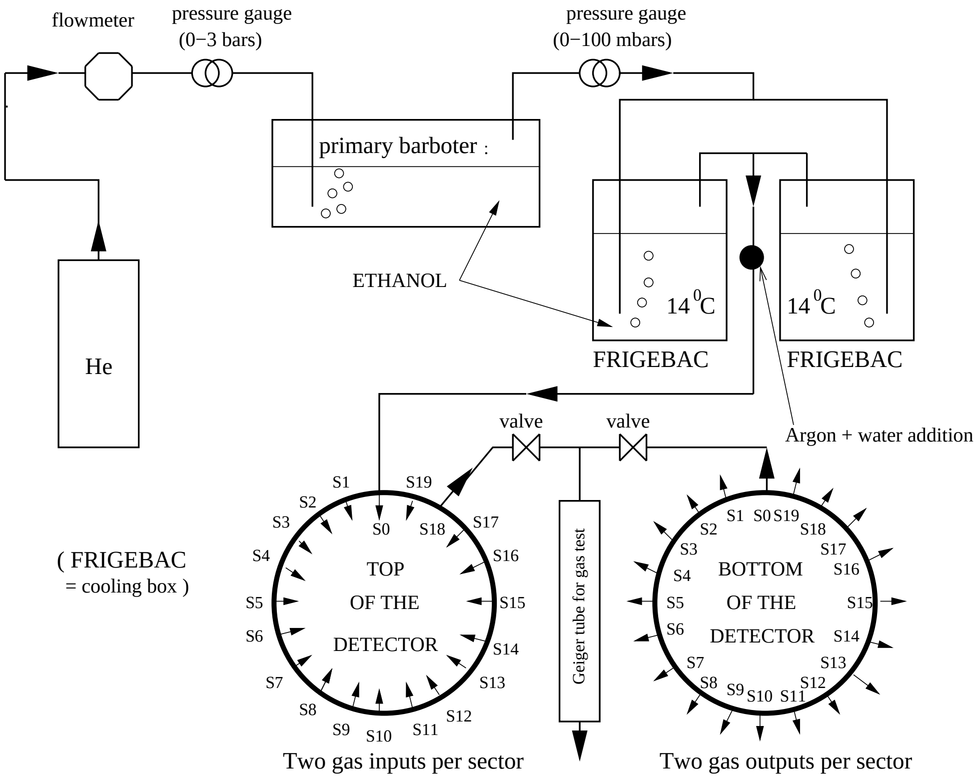

Figure 2.67: Scheme of the gas regulation system for NEMO 3.

PMTs and 25 mm long for 5” PMTs). The contact between the fiber and the guide was ensured by optical grease. Finally there was a thorough test of the connections for the calorimeter, the tracking detector and the laser system (both electrical and optical). During these procedures the sectors were filled with nitrogen to avoid deposition of impurities on the wires.
These tasks (construction of the sectors, installation on the metallic frame, helium integrity, filling of the sectors with helium and alcohol, triggering and acquisition) were previously checked in the year 2000 for three sectors (00, 18 and 19). The 17 remaining sectors of NEMO 3 were gradually installed and tested until August 2001. The 20 sectors were then placed in their final positions in cutting the “Marie-Louise” foils and the helium seals made using RTV glue.

### 2.8.5 Final installation and commissioning period

The total fiducial volume inside the tracking detector is 28 $m^3$. The detector was filled with gas in December 2001, using a fast flushing of helium gas (5 volumes), followed by introduction of ethyl alcohol in the gas regulation system. The whole process took approximately 24 h. A constant pressure of gas was maintained with a flux of the order of 130 l/h until December 2002. The magnetic coil was installed in February 2002 and $\gamma$-shield in April 2002. Finally, the installation of the neutron shield was completed in February 2003 and the boron was added the 1st March 2004, with 50 kg in each tank, both with addition of water to the top of the tanks when needed.

Between each step, $\beta\beta$ and calibration runs were taken to monitor stability and the effectiveness of the shields for comparisons with simulations (see Section 3.1.2).

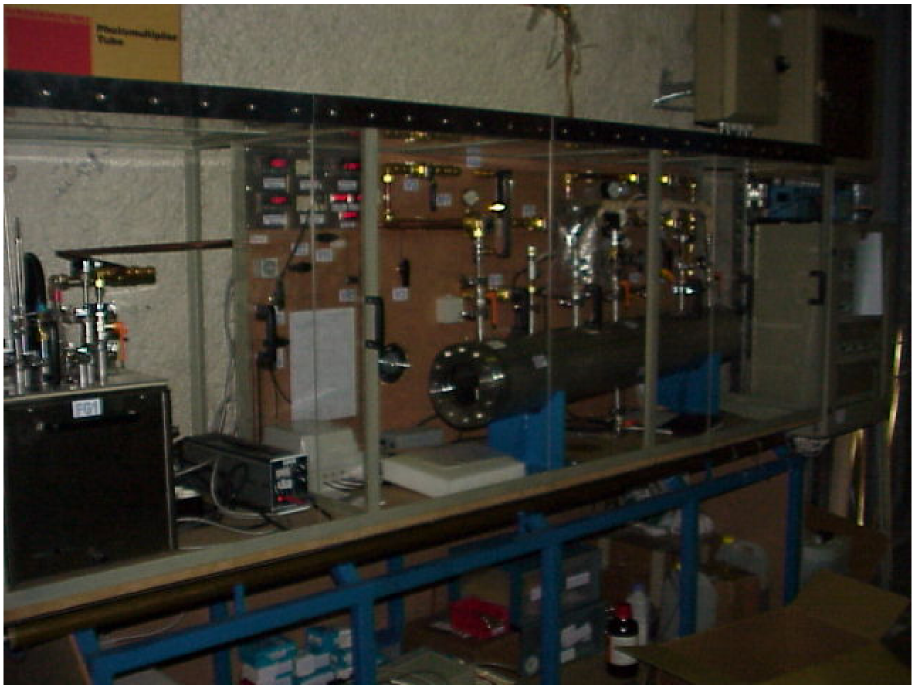

Figure 2.68: Picture of the gas regulation system for NEMO 3.

Data collection was temporarily stopped in December 2002 to make several improvements. These involved changes in HV power supplies for the calorimeter PMTs' overvoltage protection, while noise and gain adjustments were made on several PMTs. Helium leaks were also sealed.

High currents in Geiger cells were observed after rather short running time without full propagation efficiency. This situation was specially difficult during calibration runs with bismuth sources. Tests on small prototypes in Orsay [37] showed that the Geiger propagation was improved at smaller gain with the addition in the gas mixture of argon, which is easily photoionized. Thus the addition of 1% of argon into the gas mixture was carried out in order to improve the Geiger cell stability and efficiency of the plasma longitudinal propagation as well as limiting the aging problems. It also provides a decreasing of $\sim$ 150 V of the Geiger HV.
With this new gas (He + Ar + alcohol), the situation was improved but not really satisfactory. One month of cell "burning", that means a functioning of the tracking chamber with very high currents at high voltage, provided a big improvement and a quite good situation at full propagation efficiency.
Nevertheless, there were still currents, which appeared at some well known areas of the chamber after many hours of running (typically 10 hours). Self-sustained discharges from one cell spread very fast to neighboring cells and this contamination stopped always at the same place. Size of the affected area could be small and concern only few wires, but it could also be very large, with around three half-sectors affected by the contamination, i.e. $\sim$ 250 cells! It was possible to reset this situation by putting OFF/ON the high-voltage power, but it was a real problem during the calibration runs with Bi sources due to the increasing of the counting rates in the chamber, which produce high-currents.
Thus, using experience from other experiments with gas drift chambers [26], addition of $O_2$ in

Figure 2.69: One sector just after its transportation to the LSM.

the mixture was tried and finally addition of water, which improve cell stabilization without having effect on cell efficiency due to its electronegativity. A mass flow meter was installed in October 2003 to ensure a good control of the water content, which is now 1500 ppm. With this gas mixture of He, Ar, alcohol and $H_2O$, there is no obvious improvement for $\beta\beta$ running but the situation is slightly better for calibration runs with radioactive sources, for which there is a stabilization of the tracking chamber, even if the working conditions are not yet completely satisfactory.
The proportion of alcohol quencher in the mixture was also reduced from 40 to 39 mbars partial pressure (ethyl alcohol at $14^o$C instead of $15^o$C).

In mid-February 2003, new $\beta\beta$ runs commenced under improved conditions, with the coil and both shields (without boron, see above). The gas mixture used in the day-to-day running is now He with Ar (with $V(Ar)/V(He) = 1\%$) and ethyl alcohol as the quencher (at $14^o$C or 39 mbars of partial pressure) with the addition of 1500 ppm of water, at a flux of 240 l/h. An overpressure of $\sim 10$ mbars is maintained to flush contaminants from the surrounding gas volume.

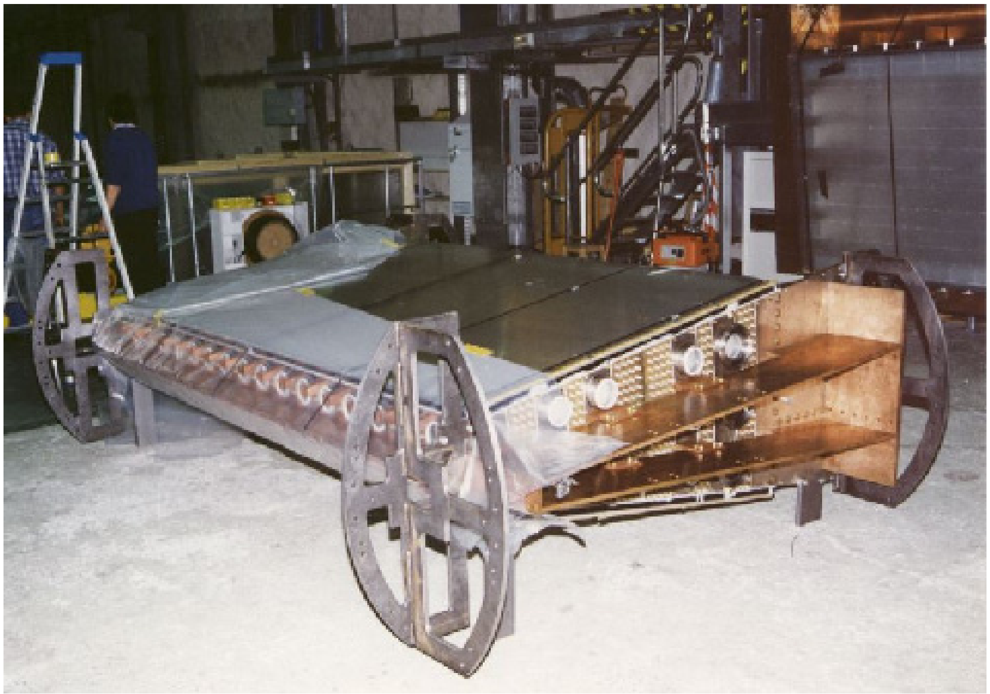

Figure 2.70 : One sector in the LSM with its half-wheel system for rocking motion.

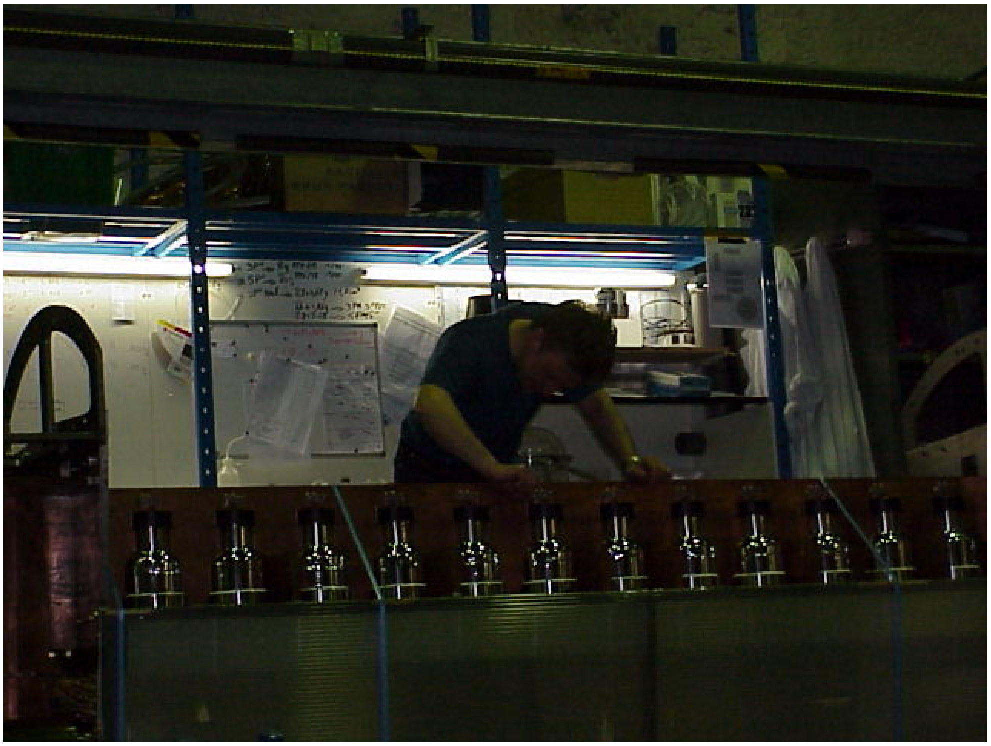

Figure 2.71 : One sector in the LSM during the internal wall PMT attachment.

## 2.9 Radiopurity of the detector

All radiopurity measurements were carried out by the NEMO collaborators from CENBG [38].

### 2.9.1 Introduction

As described in Section 1.3, for energy deposits in the range of a few MeV as it is the case in double beta decay experiments, radionuclide concentration has to be as low as possible in the materials used in the detector construction. A long-term program of material selection and control using the $\gamma$-ray detection technique has been initiated since many years in the LSM [39], leading to measurements of a very high number of samples. As a result, it has been shown that in order to minimize internal background the sources have to be purified, whereas to minimize external background it is necessary to control radioactivity in $^{208}$Tl, $^{214}$Bi and $^{40}$K for all detector materials including PMTs.

### 2.9.2 Measurement principle

#### 2.9.2.1 HPGe detectors

$\gamma$-ray spectra were acquired using four low background p-type HPGe detectors[54] at low temperature using liquid nitrogen (T = 77 K). One is located at CENBG (*Aubépine*) and has a 100 cm$^3$ crystal volume, with a cosmic veto which consists of an anticoincident detection of cosmic rays. The others are located in the LSM in order to suppress effects of the cosmic rays. One of these detectors has a 100 cm$^3$ crystal (*Géranium*) and there are two 400 cm$^3$ (*Iris* and *Jasmin*), which were used to reach the high sensitivity for $\beta\beta$ sources needed for high energy $\gamma$-rays (see Fig. 2.72 and Fig. 2.73). The cryostats of these HPGe detectors have a special configuration and are made of selected materials. The passive shield of the 1 m$^3$ structure of the detectors is made with radioactivity free materials and flushed with nitrogen to avoid radon deposit. External part is a standard lead shield, 15 cm in thickness. Central shield part is in OFHC copper, around 10 cm thick. And finally, archeological lead is used for the internal shield surrounding the crystal, 6 cm in thickness. The 400 cm$^3$ HPGe spectrometers typically use the "Marinelli" geometry[55] to measure the abundance of selected isotopes in the decay chains via the strength of selected gamma lines.

Energy range of interest for p-type HPGe detectors from NEMO is between 30 keV and 3000 keV. Some characteristics are given here as an example for one of the 400 cm$^3$ HPGe spectrometers in LSM. The counting rate associated with the background measurements is around 0.2 counts per minute for the whole spectrum. The relative photopeak efficiency depends on the detector, the sample and the $\gamma$-ray energy: a typical efficiency curve as a function of the $\gamma$-line energy is presented in Fig. 2.74. The energy resolution is 1.8 keV on 1332 keV $\gamma$-ray line of $^{60}$Co (this value is very stable and stays less than 2 keV after several months of data collection, without gain adjustment). This good energy resolution allows identification of all the $\gamma$-emitters present in the sample.

---

[54] High-Purity Germanium detectors, from the French company "Canberra-Eurisys Mesures"

[55] The "Marinelli" geometry consists in placing around the crystal a big quantity of investigated substance ($\sim$ 1 kg) to improve the detection efficiency. It was used for the measurements of the source components (powder, foil, Mylar, backing film, ...). All these samples were first placed during two weeks in a glove box under nitrogen atmosphere to allow the radon decay

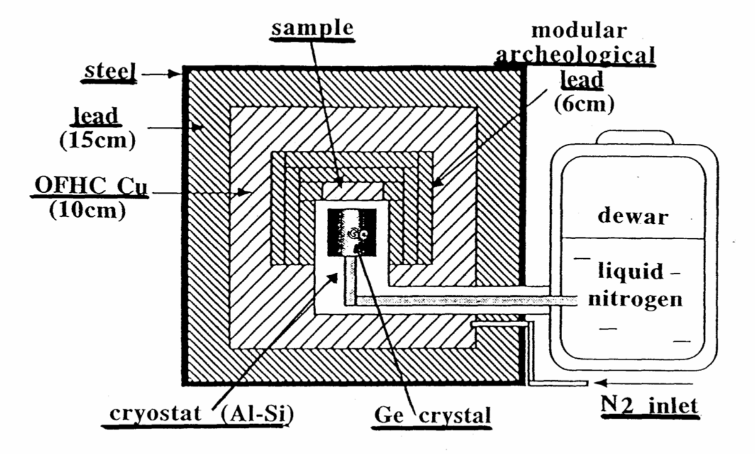

Figure 2.72: A schematic view of the HPGe detector.

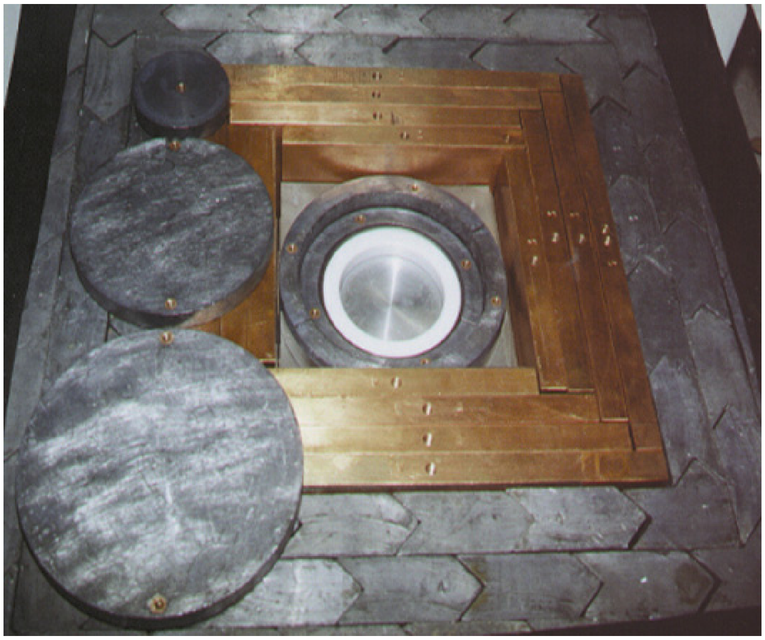

Figure 2.73: Picture showing a top view of *Iris* 400 cm$^3$ HPGe detector in LSM. The cryostat end-cap has a diameter of 11 cm.

As explained in Section 1.3, it was essential for the NEMO 3 experiment to measure $^{214}$Bi and $^{208}$Tl activities in all materials.

In Section 1.3.0.3, Fig. 1.15 presents the three natural decay series, and the energy and intensity for the main $\gamma$-rays from the most commonly observed radioisotopes are summarized in Table 1.2 [18].

Concerning uranium decay series, the precursor of the chain, $^{238}$U, does not yield any significant $\gamma$-lines and estimate of its activity has to be done by means of its progenies $^{234}$Th and

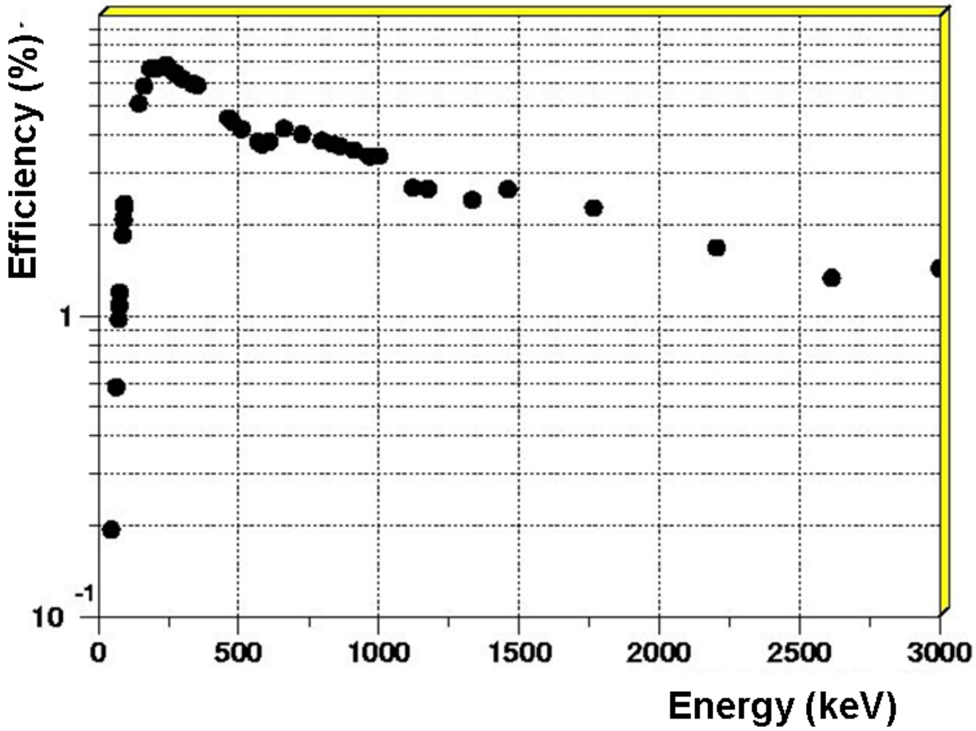

Figure 2.74 : Efficiency (in %) as a function of the $\gamma$-ray line energy, for a 400 cm$^3$ HPGe detector. The points are efficiency values calculated using Monte-Carlo simulations. The calculation has been done for Marinelli geometry with 673 g of $^{100}$Mo powder sample.

$^{234m}$Pa, both of which reaching secular equilibrium with $^{238}$U within $\sim$ 120 days in a closed system[56]. The radionuclides of this series with the most intense emission in the spectra are $^{214}$Pb and $^{214}$Bi. Due to the involved half-lives in the decay chain, these two radionuclides are in equilibrium with 226Ra in $\sim$ 20 days.
In the thorium chain, the longest half-lives are for $^{232}$Th, $^{228}$Ra and $^{228}$Th. The head of the chain, $^{232}$Th, can not be measured with gamma spectroscopy. The activity determination for $^{228}$Ra and $^{228}$Th can be determined assuming that they are in equilibrium with their progenies, $^{228}$Ac and $^{212}$Pb-$^{212}$Bi-$^{208}$Tl respectively.

It is also possible to measure directly the activities from $^{235}$U, $^{40}$K, $^{60}$Co, $^{137}$Cs, $^{152}$Eu or $^{207}$Bi radiocontaminants, as shown in Table 1.2.

#### 2.9.2.2 Sensitivity of the HPGe detectors

All the measurements done with the HPGe detectors allowed to check NEMO 3 specifications for all materials and sources used for the detector realization.

---

[56] The equilibrium is nearly reached after five progeny periods

The obtainable activity limit, $A_{lim}$ (90% C.L.), from characteristic $\gamma$-line is given by

$$A_{lim} = 1.6 \sqrt{\frac{bkg}{T_{stat}}} \frac{1}{\varepsilon \cdot BR \cdot M} \tag{2.16}$$

where $bkg$ is the HPGe background at the energy of interest $E$, $T_{stat}$ is the statistical time of exposure, $\varepsilon$ is the HPGe detection efficiency for associated $\gamma$-line energy, $BR$ is the branching ratio of the $\gamma$-line and $M$ the sample mass. Note that efficiency for each $\gamma$-ray line is calculated on the assumption that associated contaminations are evenly distributed in the measured sample.

| Activity in mBq/kg | $^{137}$Cs | $^{40}$K | $^{226}$Ra |
|---|---|---|---|
| 1) Sea-level detector, without cosmic veto | $< 50$ | $< 470$ | $< 80$ |
| 2) Sea-level detector, with cosmic veto | $< 20$ | $< 240$ | $< 30$ |
| 3) Detector in the LSM (4800 m.w.e.) | $< 8$ | $< 110$ | $< 15$ |

Table 2.34: Activities (in mBq/kg) measured with the same 100 cm$^3$ low background HPGe detector for three different configurations and the same 100 g sample during 4.7 days of data taking. In each step a gain of a factor around 2 was obtained on the sensitivity. The limits are given at the $2\sigma$ level (90% C.L.).

Example of the sensitivities obtained for one of the 100 cm$^3$ HPGe detector used to measure the NEMO 3 materials are presented in Table 2.34. The first line shows measurements at CENBG, without cosmic veto. The second measurement was with a cosmic veto and the third was the same detector put in LSM. Results present limits obtained for $^{137}$Cs, $^{40}$K and $^{226}$Ra activities, for a 100 g sample, 70 mm in diameter, 20 mm in height and a density of 1.3. The sample was put directly above the end-cap of the detector during 4.7 days of data collection. For this detector, the cryostat was realized using low background materials and placed inside a shield consisting of 10 cm thick standard lead and 4 cm thick archeological lead. The two measurements carried out in CENBG needed the addition of a neutron shield. Limits were calculated using the background spectra presented in Fig. 2.75. In each step a gain of a factor $\sim 2$ was obtained in the sensitivity.
Using 400 cm$^3$ HPGe detectors in LSM, the best sensitivities obtained for $^{214}$Bi and $^{208}$Tl activities for all the NEMO 3 measurements were 0.2 and 0.06 mBq/kg respectively, in one month of data collection for a 1 kg sample in Marinelli beaker.

### 2.9.3 Radioactivity measurements of the source foils

The maximum allowed levels of $^{214}$Bi and $^{208}$Tl contamination in the Mo sources are 0.3 and 0.02 mBq/kg respectively (as given in Eq. 2.1 and 2.2 of Section 2.2.2). The expected level of sensitivity was achieved for $^{214}$Bi, but not for $^{208}$Tl (there was a factor 3 between the experimental germanium sensitivity and the maximal allowed level). A solution could have been reached by using 1.5 kg samples or by counting for more than one month. But the collaboration has decided to make a compromize between the source measurement sensitivity and the detector construction, and thus to keep around one month of counting. Results of Mo source measurements after purification are given in Tables 2.35, 2.36 and 2.37 respectively for metallic foils, chemical purified powder and composite strips of $^{100}$Mo. Note that a $^{214}$Bi contamination was observed in batch 4, with a measured activity of 1.0 ± 0.3 mBq/kg (see Table 2.36), which was no more founded

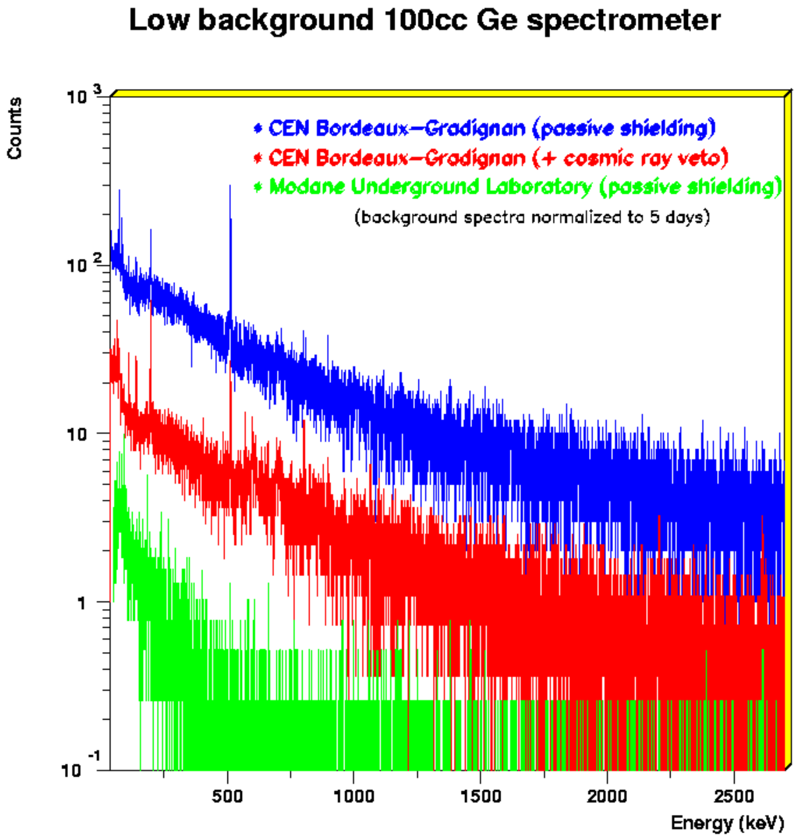

Figure 2.75 : Background spectra for the same 100 cm$^3$ low background HPGe detector in three different configurations. The spectra have been normalized to five days of data.

after composite strips realization (see Table 2.37). Thus one can not exclude there was a radon pollution inside the HPGe detector during measurement of this batch 4.

Radioactivity measurements for all the NEMO 3 sources are summarized in Table 2.38. Only the lower limits obtained for $^{100}$Mo are presented here, for both the metallic and composite strips. In this table it can be seen that for $^{208}$Tl only limits have been obtained except in $^{82}$Se and $^{150}Nd_2O_3$ strips. In the case of $^{82}$Se (Se(I) selenium), the presence of “hot-spots”, which can be suppressed by analysis, is anticipated. For $^{150}$Nd, it is not a problem because the $Q_{\beta\beta}$ value (3367.1 keV) is well above the 2615 keV $\gamma$-ray produced in the decay of $^{208}$Tl. Other contamination measurements obtained for calcium and neodymium can be found in the caption of Table 2.38.

It should be noted that HPGe method, which was used to measure radiopurities of all the NEMO 3 components, fails to measure pure beta emitter contaminations of the samples. Nevertheless, using NEMO 3 data, one-electron channel analysis showed a $^{90}$Sr ($^{90}$Y, 100%, $Q_\beta$ = 2.280 MeV) contamination of around 2 Bq/kg for the nine disk samples of $^{48}$Ca in the seventh strip of sector 05 (see Fig. 5.3 in Section 5.1).
In the $^{116}$Cd source foil in sector 18 a $^{234m}$Pa (99.84%, $Q_\beta = 2.196$ MeV) contamination of around

| Source<br>Activity (mBq/kg) | $^{100}$Mo<br>metallic 1<br>sector 01 | $^{100}$Mo<br>metallic 2<br>sector 02 | $^{100}$Mo<br>metallic 3<br>sector 03 | $^{100}$Mo<br>metallic 4<br>sector 04 |
|---|---|---|---|---|
| Mo mass (g) | 471 | 733 | 709 | 1014 |
| Exposure (days) | 30 | 35 | 25 | 17 |
| $^{40}$K | $< 5$ | $< 5$ | $< 5$ | $< 5$ |
| $^{235}$U | $6.3 \pm 0.5$ | $1.5 \pm 0.3$ | $1.3 \pm 0.3$ | $< 0.5$ |
| $^{238}$*U decay chain* | | | | |
| $^{234}$Th | $< 17$ | $< 15$ | $< 13$ | $< 17$ |
| $^{214}$Pb,Bi | $< 0.68$ | $< 0.39$ | $< 0.41$ | $< 0.37$ |
| $^{232}$*Th decay chain* | | | | |
| $^{228}$Ac | $< 0.7$ | $< 0.5$ | $< 0.7$ | $< 1.7$ |
| $^{208}$Tl | $< 0.13$ | $< 0.11$ | $< 0.17$ | $< 0.14$ |

Table 2.35: Radioactivity measurements of the $^{100}$Mo metallic source foils after physical purification (mBq/kg). The error bars are statistical uncertainties at the $1\sigma$ level while the limits are at the $2\sigma$ level. A systematic uncertainty of about 10% is associated with the Monte-Carlo calculations for the HPGe detector efficiencies.

22 mBq/kg was found using the same one-electron analysis channel, which is in agreement with the upper limit given by HPGe measurements (see $A(^{234m}\mathrm{Pa}) \equiv A(^{234}\mathrm{Th}) < 56$ mBq/kg in Table 2.38).

It is important to note that these unexpected internal contaminations of the source foils are not a problem for $\beta\beta0\nu$ studies, because $\beta\beta$ isotopes in the NEMO 3 detector have corresponding energy windows greater than the $Q_\beta$ values of beta emitters and greater than the maximal $\gamma$-ray energy from natural decay chain at 2.615 MeV. The only exception is $^{130}$Te, which has a $Q_{\beta\beta}$ value of 2.5 MeV. Thus for this isotope, such internal contaminations could produce $\beta\beta$-like events in the $\beta\beta0\nu$ energy range.

Of course these internal contaminations modify $\beta\beta2\nu$ spectra. Nevertheless, using background analysis channels for NEMO 3 data (for example the one-electron channel for beta-emitter), it is possible to measure the associated activity and to subtract this background from the two-electron spectra.

The 400 cm$^3$ p-type HPGe detectors used for NEMO 3 source foils' measurements have a poor sensitivity for the $^{234m}$Pa $\gamma$-line at 1001 keV, which has a very low intensity (0.84%) associated to a relatively low efficiency of the germanium detector for this energy value (see Fig. 2.74). Thus only $^{234m}$Pa contaminations with a big activity could be directly measured with these detectors. Due to the shape of the efficiency curve presented in Fig. 2.74, these detectors also have a poor sensitivity for $\gamma$-ray energies below 100 keV. This implies a poor sensitivity to measure the precursor of the $^{238}$U decay chain (using $^{234}$Th characterized by 63 keV $\gamma$-line and the 93 keV doublet) and the end of the same serie ($^{210}$Pb characterized by a 46 keV line). Nevertheless, the first NEMO 3 results have shown that measurements of these isotopes are quite important, because $^{238}$U play a large role in the neutron backgrounds, and $^{210}$Pb plays a large role in the radon (and surfaces) contaminations. Note that both $^{238}$U and $^{232}$Th isotopes are sources of neutrons, which could provide external backgrounds for NEMO 3. First by spontaneous fission of $^{238}$U (even if spontaneous neutron emission by $^{238}$U is so sparse that ordinary detectors will not pick it up) and second because alpha decays of $^{238}$U and $^{232}$Th can provide neutrons through

| Source<br>Activity (mBq/kg) | $^{100}$Mo not pure batch 1 | $^{100}$Mo pure batch 1 | $^{100}$Mo pure batch 2 | $^{100}$Mo pure batch 3-1 | $^{100}$Mo pure batch 3-2 | $^{100}$Mo pure batch 4 |
|---|---|---|---|---|---|---|
| Mo weight(g) | 683 | 642.6 | 1250 | 1110 | 1005 | 1353 |
| Ge exposure (h) | 736 | 610.8 | 723 | 561 | 339 | 571 |
| Detector | Iris | Iris | Jasmin | Jasmin | Jasmin | Jasmin |
| $^{40}$K | $140 \pm 10$ | $< 6.6$ | $< 3$ | $< 3$ | $< 5$ | $< 3$ |
| $^{60}$Co | | $1.0 \pm 0.2$ | $< 0.1$ | $< 0.13$ | $< 0.3$ | $< 0.3$ |
| $^{235}$U | $83 \pm 7$ | $1.0 \pm 0.3$ | $0.7 \pm 0.2$ | $0.3 \pm 0.2$ | $< 0.5$ | $< 0.25$ |
| $^{238}U$ *chain* | | | | | | |
| $^{234}$Th | $270 \pm 30$ | $< 17$ | $< 8$ | $< 10$ | $< 17$ | $< 8$ |
| $^{234m}$Pa | $280 \pm 50$ | | | | | |
| $^{214}$Pb,Bi | $4.0 \pm 0.7$ | $< 0.3$ | $< 0.2$ | $< 0.3$ | $< 0.3$ | $1.0 \pm 0.3$ |
| $^{232}Th$ *chain* | | | | | | |
| $^{228}$Ac | $2.3 \pm 0.8$ | $< 1$ | $< 0.3$ | $< 0.7$ | $< 0.7$ | $< 0.8$ |
| $^{212}$Pb | $3.2 \pm 0.8$ | $< 1$ | $< 0.2$ | $< 0.2$ | $< 0.3$ | $< 0.2$ |
| $^{208}$Tl | $1.3 \pm 0.3$ | $< 0.17$ | $< 0.05$ | $< 0.08$ | $< 0.13$ | $< 0.12$ |

Table 2.36: Radioactivity measurements (mBq/kg) of the enriched Mo composite powder, after chemical purification at INL, for all batch productions. For batch 1, there is a comparison before and after purification. Error bars are the same as those in Table 2.35.

$(\alpha, n)$ reactions.

For the future, it will be very important to measure low energy $\gamma$-ray lines. It could be done with the use of low background large planar HPGe detectors[57], with a diameter of around 10 cm and a thickness of around 2 cm, which have a very good sensitivity at low energy associated with very good energy resolution ($\sim 0.6$ keV at 122 keV). These planar detectors will be coupled with classical 1,000 cm$^3$ crystal volume HPGe detectors, which will allow measuring higher energy $\gamma$-rays for big quantities of source samples.

### 2.9.4 Radioactivity measurements for the other components of NEMO 3

As explained in Section 2.3.3, the Hamamatsu company was chosen to produce the low background PMTs (see Table 2.39), with very low contamination in all the components (glass, insulator, ceramics, etc). In NEMO 3 the total mass of the PMTs is 239.2 kg for the 3" tubes and 346.5 kg for the 5" tubes, which yield the total activities presented in Table 2.40.

In Table 2.41 the measurements for all selected components of a 5" PMT are summarized. The two last lines of this table provide a comparison between the activity of the selected calorimeter materials and the total activity of the PMTs, the first one being at most of the same order as the PMTs. Radioactivity measurements for the NEMO 3 scintillators are recalled in Table 2.42.

After selection of the PMTs, the other materials (except shields) were chosen if their total activities in $^{40}$K, $^{214}$Bi and $^{208}$Tl were at most one tenth of the total activities for the PMTs. It was not always possible to satisfy this criterion for all three contaminants simultaneously. If $^{40}$K exceeds the threshold, the material may have been accepted but not for $^{214}$Bi and $^{208}$Tl which produce background events in the $Q_{\beta\beta}$ region.

---

[57] Planar detectors with such performances are relatively new detectors

| Source<br>foils<br>Activity (mBq/kg) | $^{100}$Mo (1)<br>7/10 | $^{100}$Mo (2)<br>7/11 | $^{100}$Mo (3)<br>7/7 | $^{100}$Mo (4)<br>7/7 | $^{100}$Mo (5)<br>7/7 | $^{100}$Mo (6)<br>7/7 |
|---|---|---|---|---|---|---|
| $^{100}$Mo mass (g)<br>Exposure (days) | 733<br>26 | 732<br>29 | 745<br>20 | 735<br>27 | 761<br>13 | 721<br>23 |
| $^{40}$K | $< 6$ | $< 5$ | $< 7$ | $< 6$ | $< 7$ | $13 \pm 5$ |
| $^{235}$U | $< 0.4$ | $< 0.3$ | $< 0.3$ | $< 0.3$ | $< 0.5$ | $< 0.5$ |
| $^{137}$Cs | $< 0.3$ | $< 0.3$ | $< 0.3$ | $< 0.3$ | $< 0.3$ | $1.2 \pm 0.3$ |
| $^{60}$Co | $< 1$ | $< 0.1$ | $< 0.1$ | $< 0.1$ | $< 0.1$ | $< 0.1$ |
| $^{238}$*U decay chain* | | | | | | |
| $^{234}$Th | $< 13$ | $< 10$ | $< 23$ | $< 15$ | $< 17$ | $< 13$ |
| $^{214}$Pb,Bi | $< 0.41$ | $< 0.36$ | $< 0.38$ | $< 0.34$ | $< 0.52$ | $< 0.34$ |
| $^{232}$*Th decay chain* | | | | | | |
| $^{228}$Ac | $< 0.8$ | $< 0.5$ | $< 0.9$ | $< 0.3$ | $< 0.7$ | $< 0.5$ |
| $^{212}$Pb | $< 0.5$ | $< 0.5$ | $< 0.7$ | $< 0.3$ | $< 0.5$ | $< 0.3$ |
| $^{208}$Tl | $< 0.18$ | $< 0.18$ | $< 0.29$ | $< 0.10$ | $< 0.34$ | $< 0.12$ |

Table 2.37 : Radioactivity measurements (mBq/kg) of the enriched Mo composite strips, after chemical purification and strips production from powder. Error bars are the same as those in Table 2.35.

Finally, to conclude the NEMO 3 radiopurity report, a summary of the radioactivity measurements is given in Table 2.43 for the majority of the components of the detector.

| Source sample Activity (mBq/kg) | Meas. mass (g) | Exp. (h) | $^{40}$K | $^{235}$U | $^{238}$U chain | | $^{232}$Th chain | |
|---|---|---|---|---|---|---|---|---|
| | | | | | $^{234}$Th | $^{214}$Pb $^{214}$Bi | $^{228}$Ac | $^{208}$Tl |
| $^{100}$Mo **(M)** **2479 g** | 733 | 840 | $< 5$ | 1.5 $\pm 0.3$ | $< 15$ | $< 0.39$ | $< 0.5$ | $< 0.11$ |
| $^{100}$Mo **(C)** **4435 g** | 735 | 648 | $< 6$ | $< 0.3$ | $< 15$ | $< 0.34$ | $< 0.3$ | $< 0.10$ |
| $^{82}$Se **(C)** **932 g** | 800 | 628 | 55 $\pm 5$ | 20.0 $\pm 0.7$ | $< 18$ | 1.2 $\pm 0.5$ | $< 1$ | 0.4 $\pm 0.1$ |
| $^{130}$TeO$_2$ **(C)** **454 g of $^{130}$Te** | 633 | 666 | $< 8$ | $< 0.5$ | $< 20$ | $< 0.67$ | 1.7 $\pm 0.7$ | $< 0.46$ |
| $^{116}$Cd **(M)** + mylar Cd(I) | 299 | 368 | $< 20$ | $< 1$ | $< 56$ | $< 1.7$ | $< 4$ | $< 0.83$ |
| **405 g of $^{116}$Cd** Cd(II) | 257 | 778 | $< 13$ | $< 0.5$ | $< 12$ | $< 1.5$ | $< 2$ | $< 0.51$ |
| $^{150}$Nd$_2$O$_3$ **(C)** **37.0 g of $^{150}$Nd** | 58.2 | 458 | $< 70$ | $< 1$ | $< 66$ | $< 3.0$ | 20 $\pm 7$ | 10 $\pm 2$ |
| $^{96}$ZrO$_2$ ITEP **(C)** **4.1 g of $^{96}$Zr** | 13.7 | 624 | $< 217$ | $< 7$ | $< 222$ | $< 16$ | $< 23$ | $< 10$ |
| $^{96}$ZrO$_2$ INR **(C)** **5.3 g of $^{96}$Zr** | 16.6 | 456 | 583 $\pm 167$ | $< 10$ | $< 211$ | $< 14$ | $< 27$ | $< 5.5$ |
| $^{48}$CaF$_2$ **(C)** **6.99 g of $^{48}$Ca** | 24.56 | 1590 | $< 50$ | $< 2$ | $< 15$ | $< 4$ | $< 6$ | $< 2$ |
| $^{nat}$TeO$_2$ **(C)** **166 g of $^{130}$Te** | 620 | 700 | 8 $\pm 3$ | $< 0.3$ | $< 17$ | $< 0.17$ | $< 0.9$ | $< 0.090$ |
| Cu **(M) 621 g** | 1656 | 853 | $< 8$ | $< 0.2$ | $< 5$ | $< 0.12$ | $< 0.4$ | $< 0.040$ |

Table 2.38: Radioactivity measurements for the NEMO 3 source foils (in mBq/kg). The total enriched mass of each isotope is given in bold characters. Error bars are the same as those in Table 2.35. Only the lower limits obtained for $^{100}$Mo are presented, for both metallic and composite strips. In the case of $^{48}$CaF$_2$ the results are for the powder. Also europium contamination was measured, with $A(^{152}\mathrm{Eu}) = 30 \pm 5$ mBq/kg (only limits were found for $^{137}$Cs and $^{60}$Co contaminants in calcium strips). For Nd$_2$O$_3$ sample, other contaminant measurements were obtained, which are $A(^{212}\mathrm{Pb}) = 30 \pm 5$ mBq/kg, $A(^{152}\mathrm{Eu}) = 40 \pm 5$ mBq/kg and $A(^{207}\mathrm{Bi}) = 130 \pm 5)$ mBq/kg (only limits were found for $^{137}$Cs and $^{60}$Co contaminants in neodymium strips).

| Activity in Bq/PMT | $^{40}$K | $^{214}$Bi | $^{208}$Tl |
|---|---|---|---|
| 3" PMT R6091 (230 g/PMT) | 0.34 | 0.083 | $5\ 10^{-3}$ |
| 5" PMT R6594 (385 g/PMT) | 0.53 | 0.24 | 0.014 |

Table 2.39: Radioactivity measurements (in Bq/PMT) for NEMO 3 Hamamatsu photomultipliers.

| Total activity in Bq | $^{40}$K | $^{214}$Bi | $^{208}$Tl |
|---|---|---|---|
| 3" PMTs | 354 | 86 | 5.2 |
| 5" PMTs | 477 | 216 | 12.6 |
| $\Sigma$ PMTs | 831 | 302 | 17.8 |

Table 2.40 : Total radioactivity, in Bq, for all NEMO 3 photomultipliers.

| Sample | Weight **(kg)** | $^{40}$K **(mBq/kg)** | $^{214}$Bi **(mBq/kg)** | $^{208}$Tl **(mBq/kg)** |
|---|---|---|---|---|
| Magnetic shield (1.5 mm thick) | 1.385 | $< 20$ | $< 2$ | $< 2$ |
| PMMA (light guide + interface) | 1.500 | $< 50$ | $< 5$ | $< 3$ |
| Iron ring for light guide | 0.555 | $< 35$ | $< 3$ | $< 3$ |
| Light-tightness sleeve | 0.191 | $< 80$ | $< 17$ | $< 12$ |
| PMT-Guide glue RTV 615 | 0.072 | $380 \pm 100$ | $< 40$ | $< 7$ |
| Light-protection glue for PMT RTV 106 | 0.025 | $250 \pm 70$ | $< 20$ | $< 7$ |
| Teflon ribbon (5 layers) | 0.023 | $< 170$ | $< 20$ | $< 5$ |
| Guide-Iron ring glue Epotek 310 | 0.017 | $< 110$ | $< 15$ | $< 3$ |
| Isolated circuit FR2 for PMT divider | 0.0105 | $320 \pm 100$ | $57 \pm 8$ | $10 \pm 3$ |
| Light-protection glue RTV 116 | 0.006 | $< 830$ | $< 45$ | $< 4$ |
| Scintillator-Guide glue BC 600 | 0.004 | $< 235$ | $< 42$ | $< 7$ |
| Aluminized mylar | 0.004 | $< 700$ | $< 35$ | $< 20$ |
| White RTV 160 | 0.003 | $370 \pm 130$ | $35 \pm 10$ | $< 4$ |
| Capacitor 3.3 nF - 2 kV (1 piece) | 0.003 | $< 230$ | $< 17$ | $48 \pm 5$ |
| Capacitor 22 nF - 250 V (4 pieces) | 0.002 | $< 1300$ | $< 80$ | $< 55$ |
| *"Radial"* solder Sn(63%) Pb(37%) | 0.002 | $< 400$ | $< 50$ | $< 30$ |
| CMS resistors (23 pieces) | $21\ 10^{-5}$ | $< 9200$ | $1400 \pm 500$ | $< 600$ |
| Total activity of these components **in Bq/PMT** | | $< 0.25$ | $< 0.028$ | $< 0.016$ |
| Total activity for one Hamamatsu 5" PMT **in Bq/PMT** | | 0.53 | 0.24 | 0.014 |

Table 2.41 : Radioactivity measurements for 5" PMT components (in mBq/kg). Total radioactivity of these components is compared to the radioactivity of one PMT (in Bq/PMT).

| Activity | $^{40}$K | $^{214}$Bi | $^{208}$Tl |
|---|---|---|---|
| Dubna scintillators | $(17 \pm 2)$ mBq/kg | $< 0.1$ mBq/kg | $< 5\,10^{-2}$ mBq/kg |
| Kharkov scintillators | $< 10$ mBq/kg | $< 0.7$ mBq/kg | $< 0.3$ mBq/kg |
| 5.4 tons of Dubna scintillators **(Bq)** | $92 \pm 11$ | $< 0.5$ | $< 0.3$ |
| 1 ton of Kiev/Kharkov scintillators **(Bq)** | $< 10$ | $< 0.7$ | $< 0.3$ |
| Compare to $\Sigma$ PMT **(Bq)** | 831 | 302 | 17.8 |

Table 2.42: Scintillator radioactivity measurements (in mBq/kg) and for the whole detector (in Bq).

| Components of NEMO 3 | Weight in kg | Total radioactivity (Bq) | | | |
|---|---|---|---|---|---|
| | | $^{40}$K | $^{214}$Bi | $^{208}$Tl | $^{60}$Co |
| **Photomultiplier Tubes** | 600 | 831 | 302 | 17.8 | not measured |
| Scintillator blocks | 6400 | $< 102$ | $< 1.2$ | $< 0.6$ | $< 3$ |
| Copper | 25000 | $< 125$ | $< 25$ | $< 10$ | $< 6$ |
| Iron petals | 10000 | $< 50$ | $< 6$ | $< 8$ | $17 \pm 4$ |
| $\mu$-metal PMT shield | 2000 | $< 40$ | $< 4$ | $< 4$ | $< 4$ |
| Tracking detector wires | 1.7 | $< 8\,10^{-3}$ | $< 10^{-3}$ | $< 6\,10^{-4}$ | $< 10^{-2}$ |
| Iron shield | 180000 | $< 3000$ | $< 400$ | $< 300$ | $< 600$ |

Table 2.43: Total radioactivity for the components. The PMT activities are lower than the design specification. Moreover, with the exception of the iron shield, all activities are clearly lower than the PMT's. Note that new measurements of $^{214}$Bi activity were realized for tracking detector wires, in order to understand the residual radon value inside the NEMO 3 detector. Only limits were obtained once again corresponding to a total activity of 1.2 mBq which is in very good agreement with the limit of 1 mBq as put in this Table.

# Chapter 3

# Performance of the detector

Up to now there were three phases of data acquisition with the NEMO 3 detector. The first one, up to December 2002, which was the commissioning period, was used to study the performance of the detector and results are presented in Ref. [19]. Second period, between February 2003 and September 2004, allowed data collections to improve calibrations, to study $\beta\beta2\nu$ decays of all the isotopes housed in the detector, and to provide the best actual limits on $\beta\beta0\nu$ modes for both $^{100}$Mo and $^{82}$Se isotopes. Technical performance presented in this report is based mainly on data from this second period.

Data analyses during these two periods showed that the main background came from radon contaminations. Thus the collaboration decided to design and build a radon purification facility (as explained in Section 4.2). Data collections and results for the third period, which began in October 2004, are not described in the report, except to show, also in Section 4.2, that the NEMO 3 detector is now nearly free of radon.

## 3.1 Monte-Carlo simulations

### 3.1.1 The simulation program

The NEMO 3 simulation program [41] has been developed in the framework of GEANT 3 [42], with the EUCLID industrial software and the EUCLID-GEANT interface [43]. The description of the NEMO 3 device (geometric information, description of more than 60 materials and tracking media) is given with 20 identical sectors, except for the source foils which are placed in their exact positions inside the detector. The code consists in a description of the geometry of the experimental setup; the generation of the initial kinematics of the event; the transport of particles through the various regions of the setup; the recording of tracks produced by particles hitting sensitive detectors and the description of the response of these detectors; the visualization of the detectors. Simulation events are used to test the reconstruction and analysis programs, as well as to study the acceptance of the detector to background and rare process.

The event generator of the program, called *GENBB*, provides the possibility of generating different double beta decays ($0\nu$, $2\nu$, Majorons). Also internal and external background events due to decay of radioactive nuclei may be generated. This event generator also generates the kinematics of special events, such as Compton scattering of external $\gamma$-rays or Möller scattering of external electrons, thereby speeding up the computations compared to the simulated events with GEANT.

### 3.1.2 Neutron simulations and shields' effectiveness

Important work has been done for the simulation of neutron interactions using the GEANT/-MICAP code [44]. This code tracks neutrons from 20 MeV to $10^{-5}$ eV. It also takes into account $\gamma$-ray emission from (n,$\gamma$) captures and (n,n'$\gamma$) scatterings. Using the results of several tests done with a Germanium detector and the NEMO 2 detector [36], the $\gamma$-ray generation subroutines were improved by including additional spectroscopic information related to nuclei. Also a new library, GAMLIB, was developed taking into account branching ratios down to as low as 0.1%. This library takes into account the possibility of emission of conversion electrons, which is particularly important for neutron captures with the large internal conversion coefficients observed in many nuclei. A comparison between the simulation and the data with a Am-Be neutron source, with a flux of 220,000 neutrons per second, using the magnetic field and no shield, is presented in Fig. 3.1 and shows the excellent agreement for high energy one crossing electron events $e_{cross}$ (with $E_e > 3.2$ MeV) [45].

In Table 3.1, the experimental number of ($e_{cross}N\gamma$) events (with $N \geq 0$) observed per hour without a shield is compared to the expected number of events from simulations. These simulations take into account the $\gamma$-ray flux in the laboratory as well as thermal, epithermal and fast neutron fluxes, for which the respective proportions are given in this table. It was assumed that the epithermal neutron flux was equal to the thermal one. The resulting number of ($2.19 \pm 0.17$) observed events is compared to ($2.05 \pm 0.25$) simulated events per hour. The agreement is still very good with the $\gamma$-ray shield, which provides an attenuation factor of $3.2 \pm 0.4$ with a 1200 rejection factor for $\gamma$-rays and a 100 one for thermal neutrons. The number of associated two-electron background events due to the neutron flux, with the $\gamma$-ray shield, is $13.6 \pm 4.4$ for the summed electron energies greater than 2.75 MeV [45].

| Type of events | Simulated flux (x $10^{-6}$ $s^{-1}cm^{-2}$) | $e_{cross}N\gamma$ events in 1 h ($N \geq 0$) ($E_e > 3.2$ MeV) without shield | Attenuation factor with $\gamma$ shield |
|---|---|---|---|
| $\gamma$-rays from laboratory | $3.2 \pm 0.9$ | $0.20 \pm 0.05$ | 1176 |
| Thermal neutrons ($E \leq 0.1$ eV) | $1.6 \pm 0.1$ | $0.50 \pm 0.05$ | 98 |
| Epithermal neutrons (0.1 eV $< E <$ 1 MeV) | $1.6 \pm 0.1$ | $0.8 \pm 0.2$ | 3.2 |
| Fast neutrons ($E \geq 1$ MeV) | $4 \pm 1$ | $0.55 \pm 0.15$ | 1.1 |
| Simulation total | | $2.05 \pm 0.25$ | 2.7 |
| Experiment total | | $2.19 \pm 0.17$ | 3.2 |

Table 3.1: Comparison between simulated data and experimental data that studies the neutron contamination, without shield (3rd column) and with the $\gamma$-ray shield (4th column).

Recollect that the experiment requires that there be no external background.
A new study was realized after addition of the neutron shield, comparing events from runs with the Am-Be source corresponding to three different periods [46]. The first one was in July 2002 without neutron shield (with only the $\gamma$-ray shield). The second one was in February 2004, with the neutron shield composed of wood and tanks of water (no boron). And finally the third one

was in March 2004, after putting boron inside the water tanks, with 50 kg in each tank, both with addition of water to the top of the tanks when needed.
For each of the three periods, the Am-Be source was put in two different positions, in the top of the detector or in the middle height near sectors 14-15, in order to compare the top and side shields' effectiveness (one with only wood and the second with water tanks and wood).
Analyses from each neutron run consisted to search for one crossing electrons (OCE) as external events and two-electrons or $e^+e^-$ pair creation as internal events.

Fig. 3.2 shows the comparison between the energy sum spectra for OCE events, normalized to 1800 s, for the three periods of runs with neutron source, as defined above. The top figure corresponds to data collections with the neutron Am-Be source placed in the top position and the bottom figure to runs with the neutron source in side position. Comparing the top and bottom figures show that the neutron shield is much more efficient on sides than on the top. The same runs were used to also study internal events ($e^-e^-$ and $e^+e^-$). All the results are summarized in Table 3.2, which present the number of measured events normalized to 1800 s, for both the source in top and side positions and for the three different periods. It can be concluded that without neutron shield, there were around two times more OCE events with energy greater than 2.7 MeV for runs with the neutron source placed on the top position than for runs with the source on the side (1350 events on the top compare to 725 events on the side), when with the complete neutron shield, there are around 12 times more OCE events (486 for runs with source on the top compare to 39 events with source on the side). These results also confirmed than the neutron shield is more efficient on sides than on the top. This Table 3.2 also shows that the effect of boron and more water addition in the tanks when needed (third period) is the same for side and top shields and produces an attenuation factor of around 1.5 more. Finally, concerning the attenuation factor with this complete neutron shield, one has to distinguish top shield with only wood, which provides an attenuation factor of $\sim 5$ for internal events and $\sim 3$ for OCE events, from the side shield with wood and tanks full of water and boron, which gives an attenuation factor of $\sim 30$ for internal events and $\sim 18$ for OCE events. Note that the expected attenuation factor of $\sim 70$ coming from Monte-Carlo simulations [45] is not achieved, which can be explained by two facts. The first one is that the mean neutron energy is not the same for Am-Be source ($\sim 5$ MeV) than for the LSM neutron background ($\sim 3$ MeV). Fortunately, new Monte-Carlo simulations showed than the neutron shield is less efficient with high energy neutrons. Thus, one can expect a better attenuation factor for neutrons from the LSM than for neutrons for Am-Be source. Second, real data are well reproduced by these new Monte-Carlo simulations for side shield, which is mainly composed of tanks full of water and boron, but the agreement is not good for top shield, which is only composed of wood. Thus the wood is not well reproduced by simulations (wood composition has possibly changed). Due to this problem it could be possible that the wood thickness, which was chosen to completely remove neutron backgrounds, had been underestimated. New simulations are needed to adjust wood composition [46].

Neutron external background contribution was also studied by another analysis of OCE events produced from Am-Be neutron source run. When 1,000 OCE events with energy greater than 4 MeV were produced, this analysis showed that 5 $\beta\beta$-like events were produced in $^{100}$Mo foils in the $\beta\beta0\nu$ energy window [2.8 - 3.2] MeV. In 270 days of $\beta\beta$ data collection, 47 OCE events with energy greater than 4 MeV have been found in the $^{100}$Mo data. Thus, the number of expected events in the $\beta\beta0\nu$ window due to neutron external backgrounds is 0.235, which correspond to a neutron background value of 0.05 counts.kg$^{-1}$.yr$^{-1}$, which is negligible [47]. Precision could be improved by analysis of longer runs with neutron source.

| Am-Be source | in TOP position | | | in SIDE position | | |
|---|---|---|---|---|---|---|
| Events | No neutron shield | Neutron shield | Neutron shield + full water tanks + boron | No neutron shield | Neutron shield | Neutron shield + full water tanks + boron |
| Internal $e^-e^-$ | $4.9 \pm 1.6$ | $1.5 \pm 0.3$ | $0.9 \pm 0.2$ | 0.0 | $0.08 \pm 0.05$ | $0.06 \pm 0.04$ |
| Internal $e^+e^-$ | $12.0 \pm 2.6$ | $5.5 \pm 0.6$ | $4.0 \pm 0.4$ | $7.4 \pm 2.0$ | $0.54 \pm 0.14$ | $0.25 \pm 0.09$ |
| External OCE | $1349 \pm 27$ | $784.9 \pm 7.7$ | $486.6 \pm 4.4$ | $725.4 \pm 19.6$ | $50.0 \pm 1.4$ | $39.1 \pm 1.1$ |

Table 3.2 : Number of measured events with summed energy greater than 2.7 MeV and normalized to 1800 s, for both the Am-Be neutron source in top and side positions and for the three different shield periods. Comparison between top and side shield is done for $e^-e^-$ and $e^+e^-$ internal events as for OCE external events. See text for details [46].

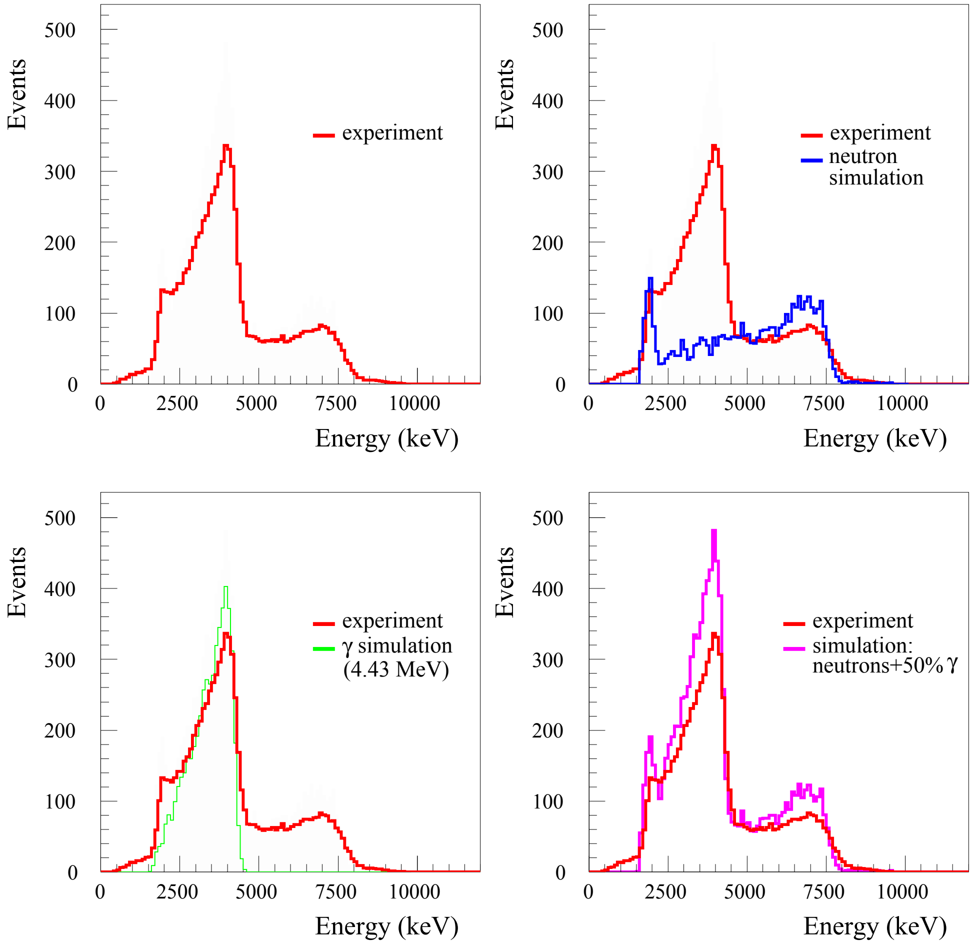

Figure 3.1 : Comparison between simulation and experimental data with a magnetic field and no shield, for one-crossing-electron events (with and without $\gamma$-rays) obtained with a neutron Am-Be source. The spectra are normalized to 8 minutes. Left, top: experimental spectrum; Right, top: superposition of experimental and simulated spectra, where the simulation corresponds to neutron events from Am-Be source; Left, bottom: superposition of experimental and simulated spectra, where the simulation corresponds to 4.43 MeV $\gamma$-ray events emitted by $^{12}$C from Am-Be source; Right, bottom: superposition of experimental and simulated spectra, where the simulation corresponds to both neutron and $\gamma$-ray events from Am-Be source, assuming a neutron flux two times greater than the $\gamma$-ray flux (this factor is not well known but the chosen value of two reproduces the data).

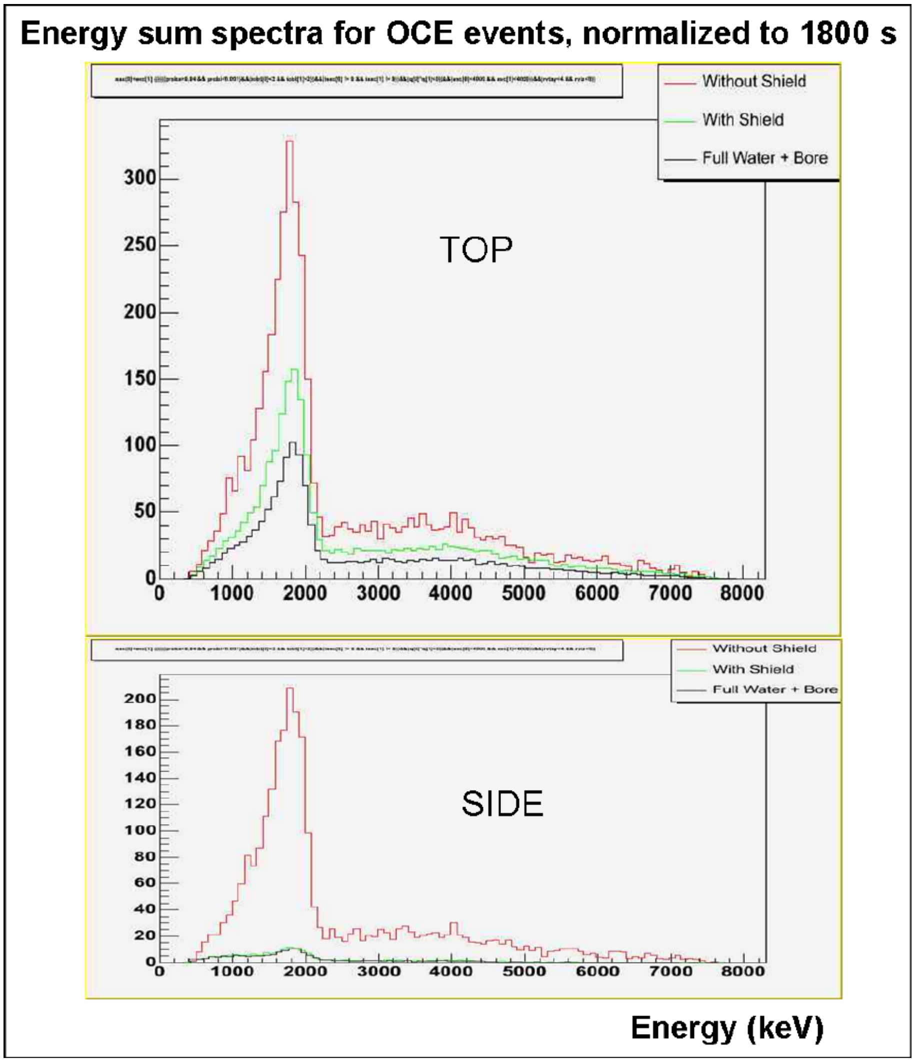

Figure 3.2: Comparison between the energy sum spectra for OCE events, normalized to 1800 s, for the three different periods as defined in the text. The top figure corresponds to data collections with the neutron Am-Be source in top position, and the bottom figure to runs with the neutron source in side position. Comparing the top and bottom figures show that the neutron shield is much more efficient on sides than on the top. See text for more details [46].

## 3.2 Trigger and data acquisition

### 3.2.1 Acquisition and data file building

Data transfer is achieved via a dedicated Ethernet. The EVB (400 MHz, with a Powerful Ethernet controller) sends data event by event to a PC running Linux. In the transfer, Linux processes the data by decoding it and re-organizing it into Random Access ZEBRA files. The initial format of *Cascade* events uses a 12-byte header, followed by calorimeter and Geiger cell information with variable lengths (two bytes per triggered PMT and three bytes per fired cell), and finally a 3-byte trailer. The final format is an “ntuple” format for data analysis. The ntuple building is done on the local acquisition disc and the Zebra file is written every 5000 events with an hrout procedure.

An example of the ntuple variables obtained after first data processing is given in Fig. 3.3 and Fig. 3.4 respectively (see captions). This pre-analysis allows to obtain particles’ energy and time in each event using calibration factors, as well as beta and alpha particle’s tracking informations using cell parameters.

### 3.2.2 The $\beta\beta$ acquisition

#### 3.2.2.1 The $\beta\beta$ trigger configuration

The $\beta\beta$ trigger is the usual one for double beta studies. During the $\beta\beta$ runs, the trigger configuration *TRN*=25 uses only the two first levels (see Section 2.5.3 for the description of the different trigger levels), which enables the readout of events with at least one electron or electron-gamma event. The associated counting rate was (7.4 ± 0.1) Hz with radon contamination inside the detector, and is now around 5.7 Hz, as explained in Section 4.
Trigger *TRN*=25, which is used for $\beta\beta$ runs, is defined as below:

- Mode: **PMT+GG**
- Level 1 (PMT multiplicity): at least one triggered PMT with energy deposited greater than 150 keV,
- Level 2 (track recognition pattern):
  - Step 1 defines two types of tracks in each half-sector:
    - **FULL**:
      long track between the source foil and the calorimeter wall in one half-sector:
      activation of Geiger cells in at least three of the nine layers,
      with at least two fired cells in neighbouring layers (using at least two out of the four layers near the source foil 0 to 3, the two intermediate layers 4-5, or at least two out of the three layers near the calorimeter wall 6 to 8),

Example:

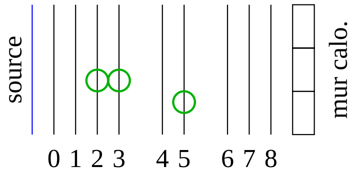

- **VOID**:

  no identifiable track (complementary part of the **FULL** type).

  Example:

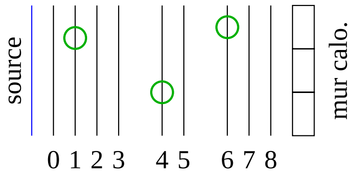

- Step 2 validates any identifiable long track in one half-sector.
  - **T2**: validation of any event with at least one **FULL** pattern.
  - **PT2**: not used in this configuration (no required coincidence),
  - **VOID**: no identifiable track (complementary part of **T2**).

- Level 3 is validated as soon as Level 2 is (no GG/GG or GG/PMT required coincidence).

The $\beta\beta$ trigger efficiency [48] was estimated by applying trigger criteria to simulated signal and background events with at least one fired Geiger plane and at least one active PMT. The trigger efficiency check was made with $\beta\beta0\nu$ or $\beta\beta2\nu$ events from the $^{100}$Mo source foils, $^{214}$Bi and $^{208}$Tl background events from the $^{100}$Mo source foils, and $^{214}$Bi decays in the gas. The number of generated events for each type was 10000. The results are summarized in Table 3.3, for events with at least one PMT or two PMTs. The proportion of accepted simulated events are given in the first and third columns for at least one and two PMT(s) respectively. The lost events are mainly due to geometrical cuts. The proportion of accepted events after applying the trigger criteria are given in the second and fourth columns. It represents the trigger efficiency (the error bars are statistical uncertainties). The efficiency relative to the number of events with exactly two fired PMTs is the number between squared brackets in the last column. This study shows that trigger criteria do not provide additional cuts and allows one to keep data for further analysis of all interesting events. The trigger efficiency relative to the number of events with exactly two fired PMTs (criterium for $\beta\beta$ analysis) are 100% for $\beta\beta$ events (both $0\nu$ and $2\nu$), 96.7% and 94% for $^{214}$Bi and $^{208}$Tl in the sources and 74.5% for $^{214}$Bi in the gas.

In the usual trigger conditions of $\beta\beta$ runs ($TRN$=25), dead time is due both to the 710 $\mu$s delay devoted to the search for alpha particles and to the Geiger readout dead time, which is at least 587.5 $\mu$s for three triggered Geiger cells. For each event the Geiger processor reads the 160 Geiger acquisition cards' status bits and five counters for each fired cell. This is accomplished through a VICbus single read cycle which needs 2.5 $\mu$s. Finally the interrupt handling and Cascade overhead take around 150 $\mu$s.

$$160 \times 2.5 + 16 \times 5 \times 2.5 + 150 \sim 750 \ \mu\text{s}$$

Thus a $\beta\beta$ event with two triggered PMTs and an average of 16 triggered Geiger cells has a 1.1% dead time of 1.5 ms (710+750 $\mu$s).

#### 3.2.2.2 Proportion of events in a $\beta\beta$ run

The combination of a tracking volume, delayed tracking electronics, calorimeter and a magnetic field allows NEMO 3 to identify electrons, positrons, $\gamma$-rays and $\alpha$-particles. The characteristics of events with these particles are outlined below.

| Type of events | Percentage of events with at least one PMT (simulation output) | Associated trigger efficiency (%) | Percentage of events with at least two PMTs (simulation output) | Associated trigger efficiency (%) [see caption] |
|---|---|---|---|---|
| $\beta\beta0\nu$ (in Mo foils) | 96.1 | $96.1 \pm 1.0$ | 56.8 | $56.8 \pm 0.7$ [100] |
| $\beta\beta2\nu$ (in Mo foils) | 73.6 | $73.0 \pm 0.9$ | 22.7 | $22.7 \pm 0.5$ [100] |
| $^{208}$Tl (in Mo foils) | 65.7 | $63.5 \pm 0.8$ | 16.9 | $16.3 \pm 0.4$ [96.7] |
| $^{214}$Bi (in Mo foils) | 58.7 | $56.0 \pm 0.8$ | 13.8 | $12.9 \pm 0.4$ [94.0] |
| $^{214}$Bi (in gas) | 79.4 | $60.0 \pm 0.8$ | 20.7 | $15.4 \pm 0.4$ [74.5] |

Table 3.3: Results of simulations giving trigger efficiencies relative to the number of events coming from $\beta\beta0\nu$, $\beta\beta2\nu$, $^{208}$Tl and $^{214}$Bi impurities from Molybdenum source foils and finally $^{214}$Bi impurities from gas. The number of generated events for each case is 10000.

- electron (positron): one $e^-$ ($e^+$) is reconstructed as a track, defined by active Geiger cells in time, with negative (positive) curvature starting from the source foil, passing through the wire chamber and being detected by only one scintillator given that electrons and positrons have a low probability of emitting bremsstrahlung $\gamma$-rays, which could trigger neighboring scintillators.

- alpha particle from the source foil: an $\alpha$-particle is reconstructed as at least one delayed Geiger cell near an electron or a positron vertex, or as a short straight track defined with delayed hits within 1.5 $\mu$s of each other and passing through a fraction of the wire chamber.

- gamma: a $\gamma$-ray corresponds to one or two adjacent scintillators being triggered, without any associated track and without a single Geiger cell hit in front of the scintillator. If there are two active scintillators, they must have been simultaneously triggered, or equivalently their time differences must be lower than the sum of their temporal resolutions. Note that gamma energy measurements correspond to the energy deposited by electrons produced by Compton effect of $\gamma$-rays in the scintillator.

Fig. 3.5 and Fig. 3.6 show respectively a view and its zoom of a typical two electron event coming from a molybdenum source foil ($\beta\beta2\nu$ process). In Figs. 3.7, 3.8, 3.9 and 3.10 one can see events characteristic of some contamination associated with the detector: $e^-\gamma\gamma\gamma$ event, $e^+e^-$ pair production, $e^-\alpha$ event and finally an external source of background, which is a high energy crossing electron coming from a neutron capture in the detector. This type of events, which was used to establish reconstruction formulae for transverse and longitudinal positions in the tracking detector, can be distinguished from back-to-back electrons events emitted from the source by time-of-flight (TOF) measurements (see Section 3.4).

The proportion of different types of events in a $\beta\beta$ run is given in Table 3.4. Note that $\beta\beta$-like events represent 0.15% of the registered events, which means one $\beta\beta$-like event occurs every 1.5 minute.

| Type of event | Proportion (in %) |
|---|---|
| $1e^-$, no $\gamma$-ray | 7.7 |
| $1e^-$, $N\gamma$-rays, $N \geq 1$ | 2.0 |
| $1e^+$, no $\gamma$-ray | 1.4 |
| $1e^+$, $N\gamma$-rays, $N \geq 1$ | 0.66 |
| $e^+e^-$ pairs | 1.5 |
| One-crossing-electron | 1.1 |
| **Two-electron events, no $\gamma$-ray** | **0.15** |

Table 3.4: The proportions of events which are used for $\beta\beta$ and background analyses (see Table 3.7 for the associated trigger), for which $1e^-$ or $1e^+$ events are reconstructed with a single track between the source foil and an associated PMT on one side of the detector (values correspond to the radon period as explained in Section 4). $\sim$ 90% of the events do not pass the cuts because the trigger imposes very loose constraints so most of the events have only a few triggered cells which are not sufficient to reconstruct tracks or correspond to events reconstructed with more than one track on one side of the detector. These last events are due to electron backscatterring at the scintillators or other mechanisms such as the magnetic field turning electrons back towards the source foil. Note that $e^+e^-$ or $e^-e^-$ events created in the source foils and one-crossing-electron events are reconstructed with two single tracks.

### 3.2.3 Other acquisition types

With the same trigger configuration, one can have higher counting rates and lower dead times using acquisition processes without looking for delayed events. It is however impossible to remove the 710 $\mu$s fixed delay, but the Geiger readout can begin with the calorimeter interrupt. In this case the busy Geiger and the busy calorimeter are superimposed and the overlap is reduced to about 200 $\mu$s, which gives a dead time of $\sim$ 1 ms.

It is possible to realize data collection with just the calorimeter (with a counting rate about 600 Hz) or just the tracking detector. In the second case, for acquisition with only the tracking detector, trigger is made using the same two configurations (**FULL** and **VOID**) to build a track in a half-sector than for trigger number $TRN$=25 ($\beta\beta$ runs), without the condition imposing at least three different triggered layers.
For laser runs, the counting rate is 250 Hz, with 10 Hz/PMT of that being the laser data, and the remainder coming from $^{207}$Bi in the six reference counters.

For energy calibration runs with 60 $^{207}$Bi sources, with an acquisition rate of 240 Hz, acquisition is done using trigger number $TRN$=21, which is defined as below:

- Mode: **PMT+GG**
- Level 1 (PMT multiplicity): at least one triggered PMT with energy deposited greater than 150 keV,
- Level 2 (track recognition pattern):

- Step 1 defines four types of tracks in each half-sector (see Table 3.5):
    - **INNER**: short track near the source foil, with cells' activation of at least three out of the six layers near the foil,
    - **OUTER**: short track near the calorimeter wall, with cells' activation of at least three out of the five layers near the wall,
    - **FULL**: long track between the source foil and the calorimeter wall, with cells' activation of at least six out of the nine layers of the half-sector,
    - **VOID**: no identifiable track (this fourth type of tracks is the complementary part of the union of the three other types).

- Step 2 validates any full track in one half-sector and short tracks in adjacent half-sectors.
    - **PT2**: the tracks is validate if either there is at least one **FULL** pattern or there is one **INNER** pattern adjacent to one **OUTER** pattern,
    - **T2**: not used in this configuration (because coincidence between pre-tracks and fired PMT in the same half-sector is required, see below),
    - **VOID**: no identifiable track (complementary part of **PT2**).

- Level 3: required coincidence using **PT2** pre-tracks (GG internal/GG external or GG internal/PMT internal or GG external/PMT external).

| Label | Illustration | Multiplicity criterium | Description |
|---|---|---|---|
| **INNER** | 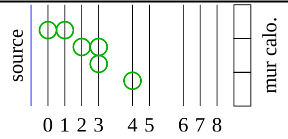 | `[3-6:0-5]-[3-5:4-8]` | Short track near the source foil |
| **OUTER** | 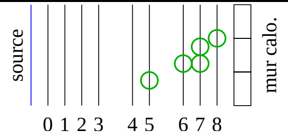 | `[3-5:4-8]-[3-6:0-5]` | Short track near the wall |
| **FULL** | 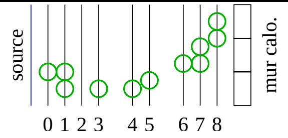 | `[7-9:0-8]` | Long track in one half-sector |
| **VOID** | 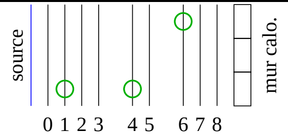 | complementary part | no identifiable track |

Table 3.5: The four tracking pattern configurations used for the first step of track recognition for trigger number $TRN$=21.

Table 3.6 presents the rules used for track selection in adjacent half-sectors.
Other calibration runs use only calorimeter acquisition, with a special one developed for $^{90}$Sr to determine the beta end-point. The acquisition of only the energy spectra is realized without ntuple building for the whole calorimeter, which permits very high counting rates (up to 30 kHz) with the smaller output files of 32 Mbytes. All of the 32 Mbytes of the calorimeter processor are used to construct histograms.

| `N×N+1` | `VOID` | `INNER` | `OUTER` | `FULL` |
|---|---|---|---|---|
| `VOID` | `VOID` | `VOID` | `VOID` | `PT2` |
| `INNER` | `VOID` | `VOID` | `PT2` | `PT2` |
| `OUTER` | `VOID` | `PT2` | `VOID` | `PT2` |
| `FULL` | `PT2` | `PT2` | `PT2` | `PT2` |

Table 3.6 : Validation for the second step of track recognition for trigger number $TRN=21$. `N` and `N+1` are respectively left and right half-sectors for any association between adjacent half-sectors.

Counting rates associated with different triggers and acquisition types are presented in Table 3.7.

| Type of run | Trigger conditions | Event type | Counting rate (Hz) |
|---|---|---|---|
| $\beta\beta$ **run** | $\geq$ (1 triggered PMT + 1 track)<br>with $E_{PMT} > 150$ keV<br>and at least 3 fired Geiger cells | (e), (e, e), (e, $N\gamma$), (e, e, $N\gamma$),<br>with $N \geq 1$ | **7.0 to 7.5** |
| Calo run | $\geq$ 1 triggered PMT<br>with $E_{PMT} > 150$ keV | PMT singles | 580 |
| Geiger run | $\geq$ 1 track | GG singles | 65 |
| | $\geq$ (2 triggered PMTs + 1 track)<br>with $E_{PMTs} > 150$ keV<br>and at least 3 fired Geiger cells | (e, e), (e, $N\gamma$), (e, e, $N\gamma$),<br>with $N \geq 1$ | 1.15 |

Table 3.7 : Different counting rates for different types of trigger.

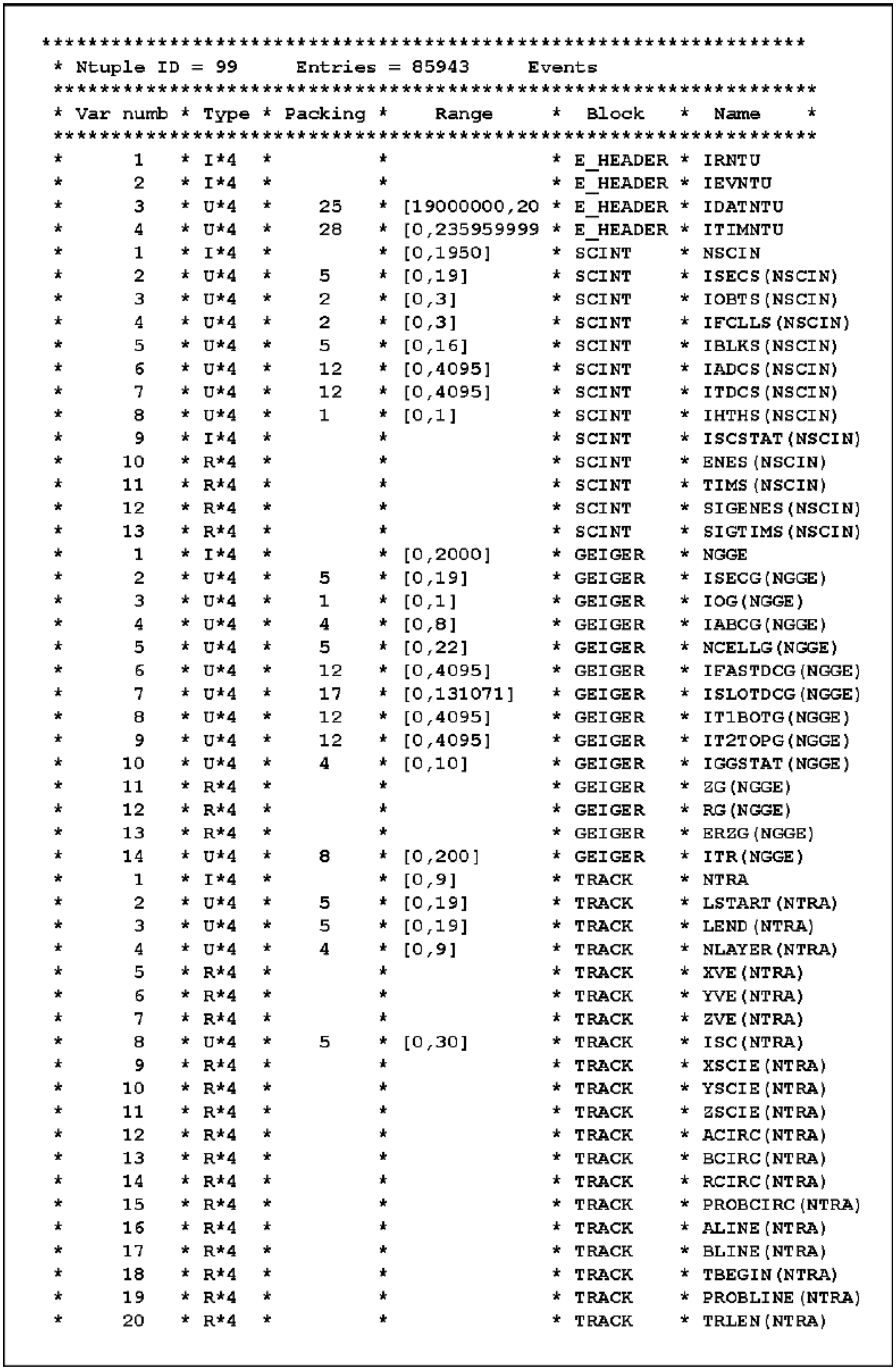

```
******************************************************************
 * Ntuple ID = 99     Entries = 85943     Events
 ******************************************************************
 * Var numb * Type * Packing *    Range      *  Block   *  Name    *
 ******************************************************************
 *      1   * I*4  *         *               * E_HEADER * IRNTU
 *      2   * I*4  *         *               * E_HEADER * IEVNTU
 *      3   * U*4  *    25   * [19000000,20 * E_HEADER * IDATNTU
 *      4   * U*4  *    28   * [0,235959999 * E_HEADER * ITIMNTU
 *      1   * I*4  *         * [0,1950]     * SCINT    * NSCIN
 *      2   * U*4  *    5    * [0,19]       * SCINT    * ISECS(NSCIN)
 *      3   * U*4  *    2    * [0,3]        * SCINT    * IOBTS(NSCIN)
 *      4   * U*4  *    2    * [0,3]        * SCINT    * IFCLLS(NSCIN)
 *      5   * U*4  *    5    * [0,16]       * SCINT    * IBLKS(NSCIN)
 *      6   * U*4  *    12   * [0,4095]     * SCINT    * IADCS(NSCIN)
 *      7   * U*4  *    12   * [0,4095]     * SCINT    * ITDCS(NSCIN)
 *      8   * U*4  *    1    * [0,1]        * SCINT    * IHTHS(NSCIN)
 *      9   * I*4  *         *              * SCINT    * ISCSTAT(NSCIN)
 *     10   * R*4  *         *              * SCINT    * ENES(NSCIN)
 *     11   * R*4  *         *              * SCINT    * TIMS(NSCIN)
 *     12   * R*4  *         *              * SCINT    * SIGENES(NSCIN)
 *     13   * R*4  *         *              * SCINT    * SIGTIMS(NSCIN)
 *      1   * I*4  *         * [0,2000]     * GEIGER   * NGGE
 *      2   * U*4  *    5    * [0,19]       * GEIGER   * ISECG(NGGE)
 *      3   * U*4  *    1    * [0,1]        * GEIGER   * IOG(NGGE)
 *      4   * U*4  *    4    * [0,8]        * GEIGER   * IABCG(NGGE)
 *      5   * U*4  *    5    * [0,22]       * GEIGER   * NCELLG(NGGE)
 *      6   * U*4  *    12   * [0,4095]     * GEIGER   * IFASTDCG(NGGE)
 *      7   * U*4  *    17   * [0,131071]   * GEIGER   * ISLOTDCG(NGGE)
 *      8   * U*4  *    12   * [0,4095]     * GEIGER   * IT1BOTG(NGGE)
 *      9   * U*4  *    12   * [0,4095]     * GEIGER   * IT2TOPG(NGGE)
 *     10   * U*4  *    4    * [0,10]       * GEIGER   * IGGSTAT(NGGE)
 *     11   * R*4  *         *              * GEIGER   * ZG(NGGE)
 *     12   * R*4  *         *              * GEIGER   * RG(NGGE)
 *     13   * R*4  *         *              * GEIGER   * ERZG(NGGE)
 *     14   * U*4  *    8    * [0,200]      * GEIGER   * ITR(NGGE)
 *      1   * I*4  *         * [0,9]        * TRACK    * NTRA
 *      2   * U*4  *    5    * [0,19]       * TRACK    * LSTART(NTRA)
 *      3   * U*4  *    5    * [0,19]       * TRACK    * LEND(NTRA)
 *      4   * U*4  *    4    * [0,9]        * TRACK    * NLAYER(NTRA)
 *      5   * R*4  *         *              * TRACK    * XVE(NTRA)
 *      6   * R*4  *         *              * TRACK    * YVE(NTRA)
 *      7   * R*4  *         *              * TRACK    * ZVE(NTRA)
 *      8   * U*4  *    5    * [0,30]       * TRACK    * ISC(NTRA)
 *      9   * R*4  *         *              * TRACK    * XSCIE(NTRA)
 *     10   * R*4  *         *              * TRACK    * YSCIE(NTRA)
 *     11   * R*4  *         *              * TRACK    * ZSCIE(NTRA)
 *     12   * R*4  *         *              * TRACK    * ACIRC(NTRA)
 *     13   * R*4  *         *              * TRACK    * BCIRC(NTRA)
 *     14   * R*4  *         *              * TRACK    * RCIRC(NTRA)
 *     15   * R*4  *         *              * TRACK    * PROBCIRC(NTRA)
 *     16   * R*4  *         *              * TRACK    * ALINE(NTRA)
 *     17   * R*4  *         *              * TRACK    * BLINE(NTRA)
 *     18   * R*4  *         *              * TRACK    * TBEGIN(NTRA)
 *     19   * R*4  *         *              * TRACK    * PROBLINE(NTRA)
 *     20   * R*4  *         *              * TRACK    * TRLEN(NTRA)
```

Figure 3.3: Variables in ntuple for data analysis - First part. This ntuple file was obtained after pre-analysis to obtain particles' energy and time in each event, as well as beta and alpha particle's tracking informations. In this part are given the event-header and the variables associated to calorimeter (SCINT) and tracking detector (GEIGER for cells' informations and TRACK for beta-type tracks' informations.

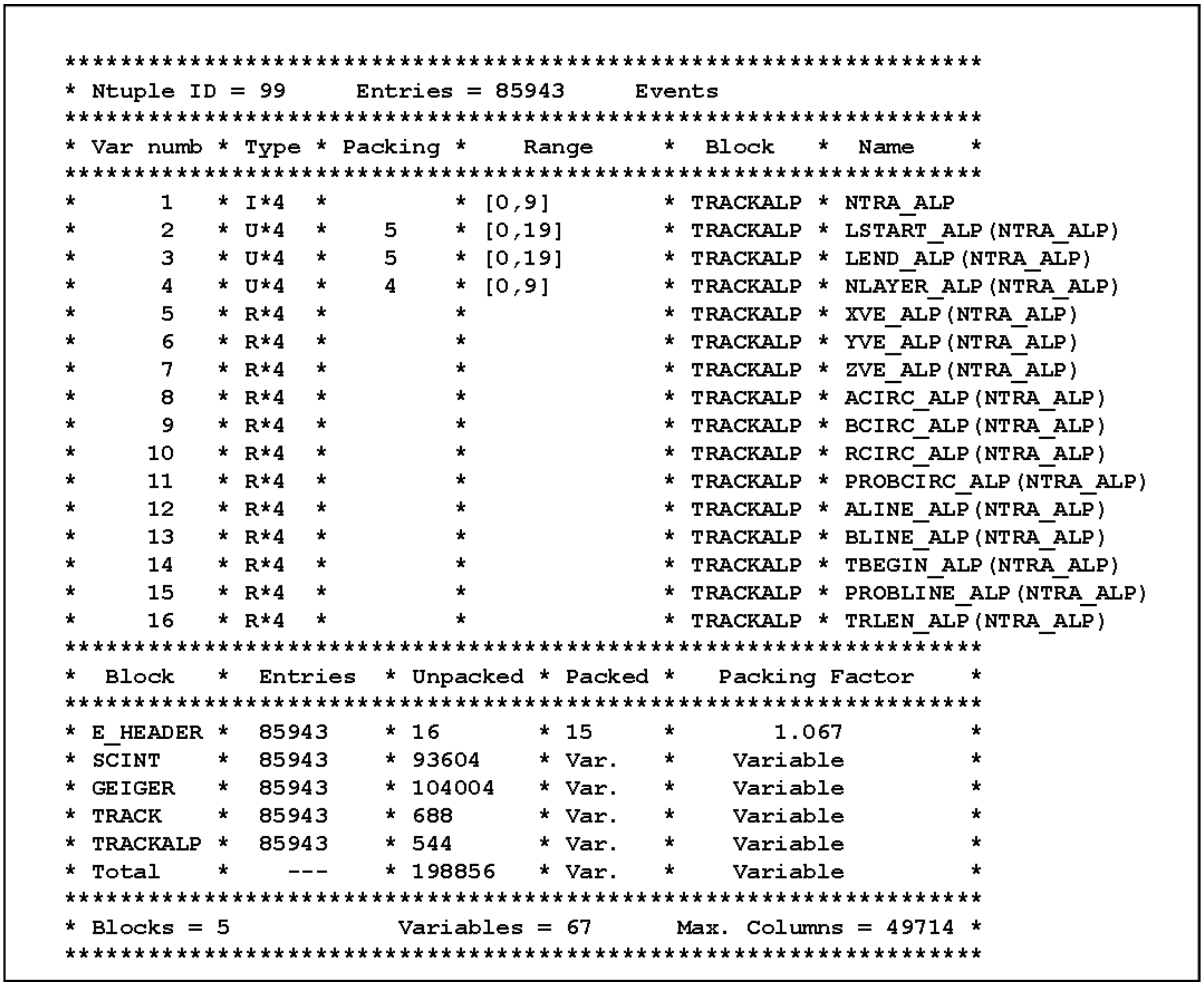

```
******************************************************************
* Ntuple ID = 99     Entries = 85943     Events
******************************************************************
* Var numb * Type * Packing *    Range     *  Block   *  Name    *
******************************************************************
*      1   * I*4  *         * [0,9]        * TRACKALP * NTRA_ALP
*      2   * U*4  *    5    * [0,19]       * TRACKALP * LSTART_ALP(NTRA_ALP)
*      3   * U*4  *    5    * [0,19]       * TRACKALP * LEND_ALP(NTRA_ALP)
*      4   * U*4  *    4    * [0,9]        * TRACKALP * NLAYER_ALP(NTRA_ALP)
*      5   * R*4  *         *              * TRACKALP * XVE_ALP(NTRA_ALP)
*      6   * R*4  *         *              * TRACKALP * YVE_ALP(NTRA_ALP)
*      7   * R*4  *         *              * TRACKALP * ZVE_ALP(NTRA_ALP)
*      8   * R*4  *         *              * TRACKALP * ACIRC_ALP(NTRA_ALP)
*      9   * R*4  *         *              * TRACKALP * BCIRC_ALP(NTRA_ALP)
*     10   * R*4  *         *              * TRACKALP * RCIRC_ALP(NTRA_ALP)
*     11   * R*4  *         *              * TRACKALP * PROBCIRC_ALP(NTRA_ALP)
*     12   * R*4  *         *              * TRACKALP * ALINE_ALP(NTRA_ALP)
*     13   * R*4  *         *              * TRACKALP * BLINE_ALP(NTRA_ALP)
*     14   * R*4  *         *              * TRACKALP * TBEGIN_ALP(NTRA_ALP)
*     15   * R*4  *         *              * TRACKALP * PROBLINE_ALP(NTRA_ALP)
*     16   * R*4  *         *              * TRACKALP * TRLEN_ALP(NTRA_ALP)
******************************************************************
*  Block   *  Entries  * Unpacked * Packed *   Packing Factor    *
******************************************************************
* E_HEADER *  85943    * 16       * 15     *       1.067         *
* SCINT    *  85943    * 93604    * Var.   *    Variable         *
* GEIGER   *  85943    * 104004   * Var.   *    Variable         *
* TRACK    *  85943    * 688      * Var.   *    Variable         *
* TRACKALP *  85943    * 544      * Var.   *    Variable         *
* Total    *    ---    * 198856   * Var.   *    Variable         *
******************************************************************
* Blocks = 5           Variables = 67      Max. Columns = 49714 *
******************************************************************
```

Figure 3.4: Variables in ntuple for data analysis - Second part. This ntuple file was obtained after pre-analysis to obtain particles' energy and time in each event, as well as beta and alpha particle's tracking informations. In this second part are given alpha tracks' informations and the summary about event-header, scintillators, Geiger cells, beta and alpha tracks.

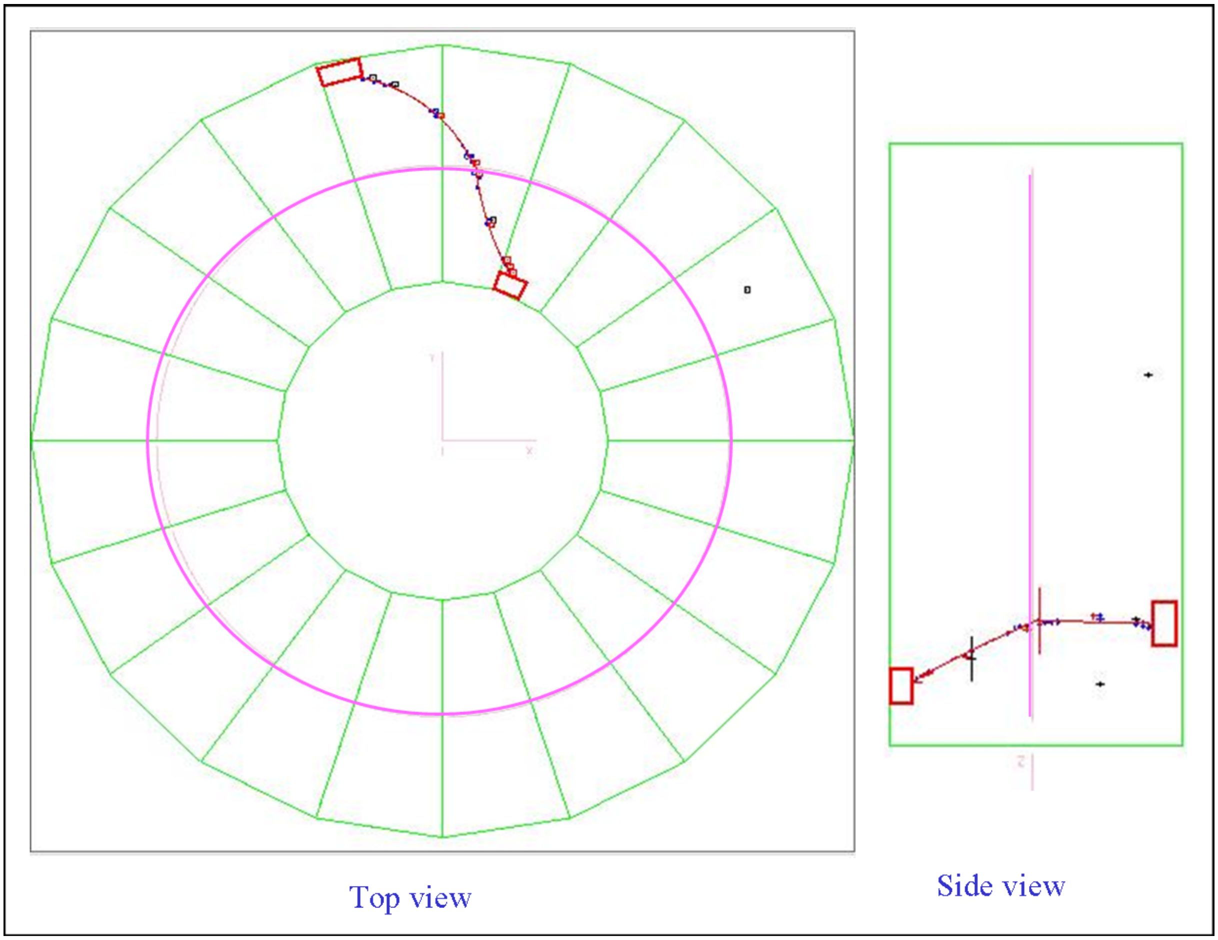

Figure 3.5: Two-electron event produced in molybdenum source foil (sector 04) [6]. The left portion of this figure shows the transverse top view of NEMO 3, while the right part presents the associated longitudinal side view. The source foil is in pink and the two red rectangles are fired scintillators with deposited energies of electrons. The circles radii correspond to the transverse distance from the anode wire for each fired cell, they are not error bars. The red curves are the tracks reconstructed using signals from Geiger cells. The curvature of the tracks due to the 25 G magnetic field is clearly seen on the transverse view and allows the charge recognition. Time-of-flight measurements allow to ensure that the source foil is the emission point of the two electrons (see zoom in Fig. 3.6 for event specifications.

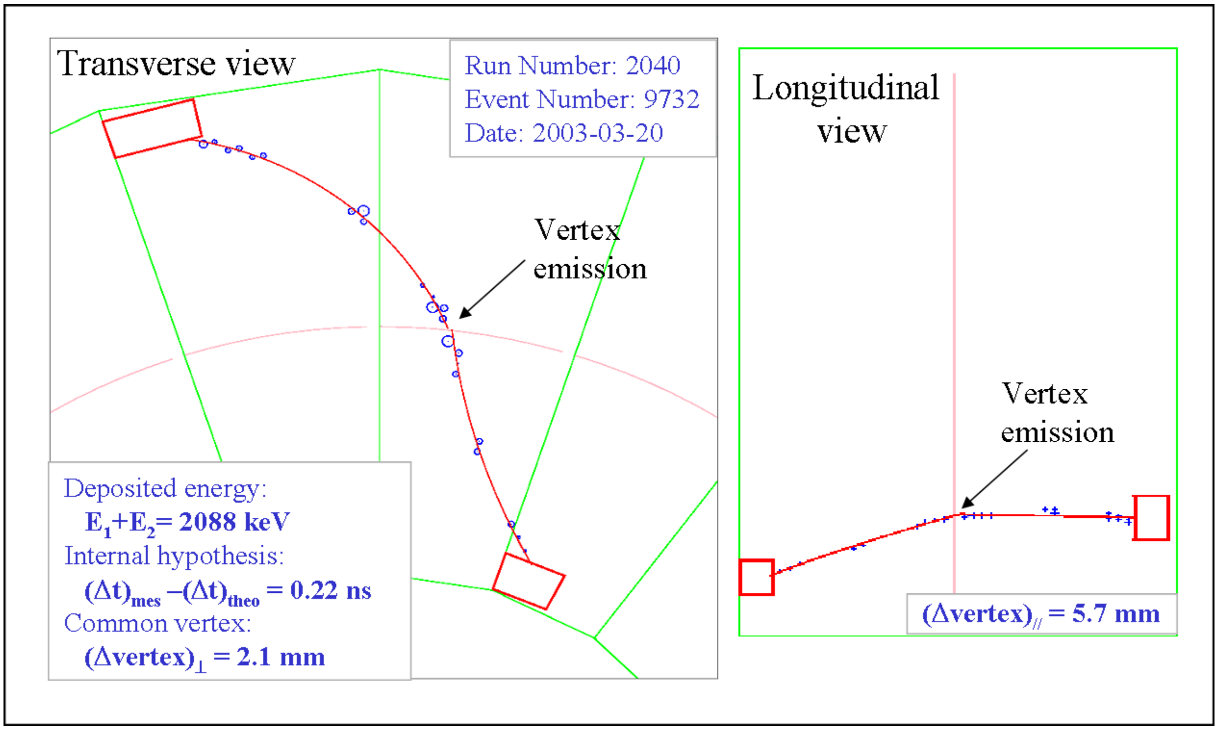

Figure 3.6 : Zoom on the same two-electron event than in Fig. 3.5 [6]. The two-electron deposited energy is 2088 keV. This event is associated to the internal hypothesis (it comes from the source foil, see Section 3.4.3 and Fig. 3.34) since $(\Delta T_{meas} - \Delta T_{cal})_{int} = 0.22$ ns, and finally the two electron tracks have a common vertex, distant from $\Delta R\phi = 2.1$ mm, as defined in Section 3.3.6. Thus this event satisfy the two-electron events' selection criteria, as presented in Section 4.1.3.

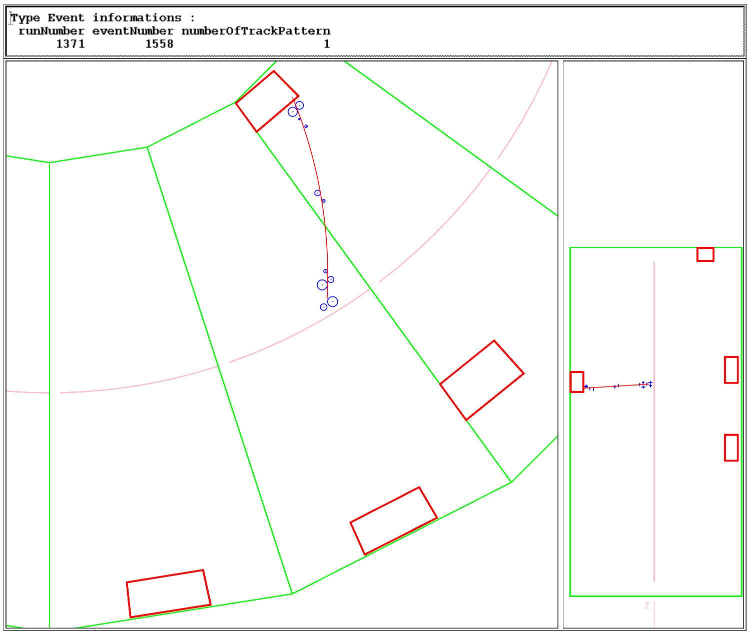

```
Type Event informations :
 runNumber eventNumber numberOfTrackPattern
      1371        1558                        1
```

Figure 3.7: A $e^-\gamma\gamma\gamma$ background event produced in a molybdenum foil (sector 16) and used for measurements of $^{208}$Tl internal contaminations of the $\beta\beta$ source foils (see Section 4.1.1).

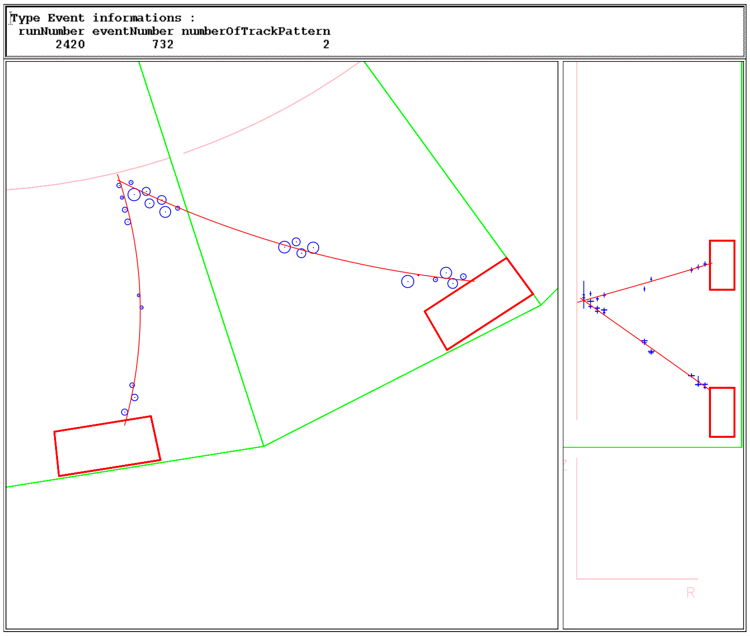

```
Type Event informations :
 runNumber eventNumber numberOfTrackPattern
      2420         732                        2
```

Figure 3.8: An $e^+e^-$ background event produced in a molybdenum foil (sector 15). Note the tracks of opposite curvature.

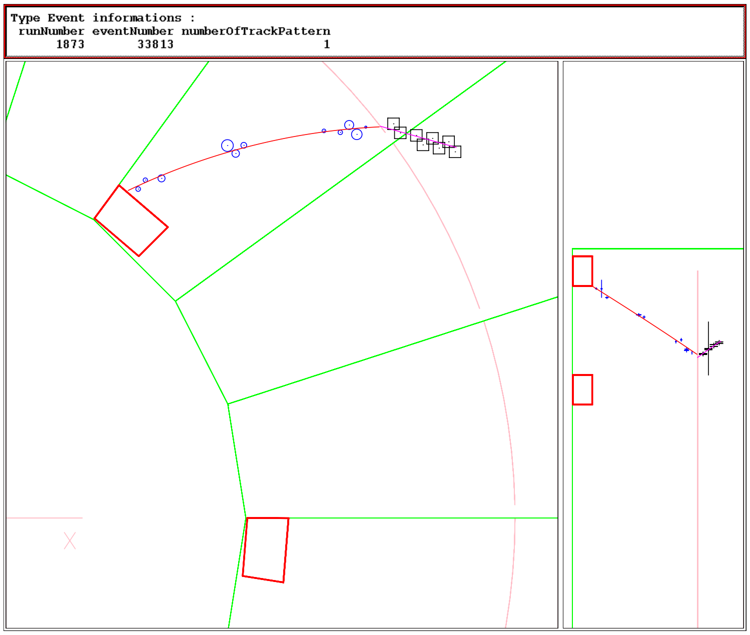

```
Type Event informations :
 runNumber eventNumber numberOfTrackPattern
      1873       33813                     1
```

Figure 3.9: Decay of some internal contamination producing a single electron event coming from a molybdenum source foil (sector 02) followed by a delayed alpha particle, which is the short straight track represented by open squares. Note the presence of one gamma-ray. This event from ($e^- \alpha\ N\gamma$) analysis channel is used to tag background from $^{214}$Bi decays.

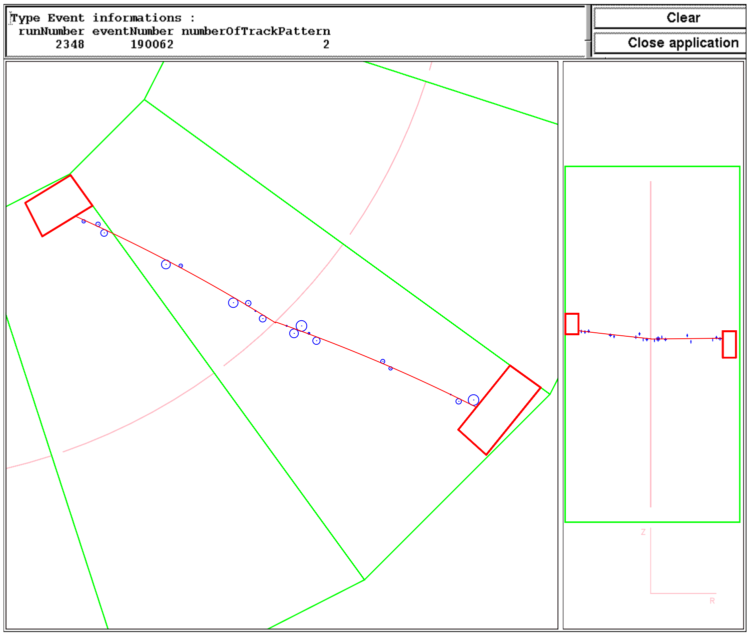

```
Type Event informations :
 runNumber eventNumber numberOfTrackPattern
      2348      190062                     2
```

Figure 3.10: Example of an external source of background: it is a view of high energy crossing electron, which is most likely produced by a $\gamma$-ray emitted after a neutron capture in the copper frame. This type of events is used to establish reconstruction formulae for transverse and longitudinal positions in the tracking detector. It can be distinguished from back-to-back source foil events by time-of-flight measurements (see Section 3.4).

## 3.3 Tracking detector performance

### 3.3.1 Final operating conditions of the tracking detector

Since February 2003, with the new gas mixture (He, Ar, ethyl alcohol and water), the mean operating voltage of the Geiger cells is 1620 V, the longitudinal propagation velocity is $\sim 5$ cm/$\mu$s corresponding to a full propagation time $< t_{LC} + t_{HC} > \sim 52$ $\mu$s, and 90% of Geiger cells have a longitudinal propagation efficiency greater than 95%. The single counting rate per cell is $\sim 0.2$ Hz.

There were eventually only 30 channels of the 6180 ($< 0.5\%$) with missing anode signals, of which there were four cells disconnected due to anode wires in contact with ground wires, eight cells due to interconnection problems, and 18 hot cells[1] ($\sim 0.3\%$). The number of Geiger cells with at least one missing cathode signal were 160 (2.6%), due again to interconnection problems.

### 3.3.2 Geiger TDC analysis

As discussed in Section 2.5 there are four variables associated with the Geiger TDCs. They are $tdc_{LC}$ and $tdc_{HC}$ for the two cathode ring times, $tdc_A$ for the anode time and $tdc_\alpha$ for the delayed time (see Eq. 2.6 to Eq. 2.9). The triggered Geiger cells are classified into different types according to the values of these four TDC signals. There are “in-time hits” coming from electron or positron tracks. Also “delayed hits” are delayed triggers of cells used to study $\alpha$-particle events. Finally there are “refired cells” which are active because of cross-talk (cells fired by a neighboring in-time cell) and “noisy cells”. A status is defined in each case for the real data and permits to make the distinction between in-time hits, delayed hits and refired or noisy cells. These different events are explained below in more detail.

- in-time hits:
  **status** = **1, 3, 5** or **7** depending on the longitudinal propagation (see below)
  The Geiger hit is in-time if:

  $$tdc_\alpha = 0 \text{ and } tdc_{min} \leq tdc_A \leq tdc_{max}$$

  or

  $$tdc_\alpha \neq 0 \text{ with } modulo(tdc_\alpha, 4096) \neq tdc_A \text{ and } tdc_{min} \leq tdc_A \leq tdc_{max}$$

  where $tdc_{min} = 220$ and $tdc_{max} = 307$ (these values were measured on $tdc_A$ spectrum). The second case corresponds to a false electronic retrigger for few known channels.
  Note that at mean, the actual value of $tdc_{min}$ is correct. But the high voltage is slightly different from layer to layer of Geiger cells. As a result some small quantity of useful Geiger hits in the layer 00 are loosing. Next improvement will be to use a different $tdc_{min}$ value according to the layer number [54].

  For hits in time, the definition of the status 1, 3, 5 or 7 depends on the cathode signals:

  - **status** = **1** if both high and low cathode signals are present ($tdc_{HC} \neq 0$ and $tdc_{LC} \neq 0$) ;

---

[1] self-discharging Geiger cell

- **status** = **3** if only low cathode signal is present ($tdc_{HC} = 0$ and $tdc_{LC} \neq 0$) ;
- **status** = **5** if only high cathode signal is present ($tdc_{HC} \neq 0$ and $tdc_{LC} = 0$) ;
- **status** = **7** if there is no cathode signal ($tdc_{HC} = 0$ and $tdc_{LC} = 0$).

The different times and status associated to the tracking detector are presented in Fig 3.11.

- delayed hits:
  **status = 10**
  The Geiger hit is a delayed hit (alpha) if:

  $$tdc_\alpha \neq 0 \text{ and } modulo(tdc_\alpha, 4096) = tdc_A$$

  Note that the status distinction using cathode signals (1, 3, 5 or 7) is always valid for delayed hits. Note also that $tdc_{\alpha max}$ corresponds to the fixed delay from the second trigger level, which is 710 $\mu$s since March 2003 (it was 770 $\mu$s before this date).

- refired or noisy cells:
  **status = 0**
  The Geiger hit is a noisy hit (self-discharged, refired) if:

  $$tdc_\alpha \neq 0 \text{ and } modulo(tdc_\alpha, 4096) \neq tdc_A$$

  $$\text{and } [tdc_A > tdc_{max} \text{ or } tdc_A < tdc_{min}]$$

  or

  $$tdc_\alpha = 0 \text{ and } [tdc_A > tdc_{max} \text{ or } tdc_A < tdc_{min}]$$

Note that in the simulation, it is not possible to distinguish between all these cases because one only have in-time hits (without condition applied to the value of $tdc_A$) and delayed hits.

## 3.3.3 Track reconstruction

### 3.3.3.1 Principle [49]

Geiger events are first tagged with one of the four previously defined criteria. The refired and noisy cells are rejected, with about one or two refired cells per event. The number of noisy cells is typically negligible. Then, two different pattern recognition and track fit procedures are carried out, one for in-time hits and the other for delayed hits.

For **in-time hits** the pattern recognition and tracking are carried out using a cellular automaton algorithm, which was previously used for NEMO 2 tracking [50]. The principle of this NEMO 3 algorithm is described in a note [51]. The NEMO 3 algorithm uses a set of consecutive segments which connect pairs of active cells in neighboring layers. A candidate track is defined and characterized by the number of segments (length of the track) and the sum of the angles between the segments. In NEMO 3, the longest track is favored and the track can not turn back to the foil (Geiger layers may be present in the track only in consecutive order). The curvature of the track is due to the magnetic field. Then one suppresses all segments used for the track and a new track search is begun with the other segments until there are not enough segments remaining to construct a track.

Concerning the track fitting procedure, to solve the left/right ambiguities in the transverse plane, each Geiger cell gives two possibilities at its left/right edge to form a segment during the search for a track. Once tracks are found, an iterative fit procedure finds track parameters from a helix.

Each reconstructed track is extrapolated to the source foil and a vertex position is calculated whose transverse and longitudinal coordinates are $R\phi$ and $Z$, with an origin $Z = 0$ at the half-height position of the source foils (see Section 3.3.6). The track is also projected onto an associated scintillator surface and the calculated coordinates of the scintillator are $R_S\phi_S$ and $Z_S$, where $R_S$ is the transverse distance between the detector's center and the entrance surface of the scintillator.

For **delayed hits** the treatment in the longitudinal plane is the same as that for in-time hits. The treatment in the transverse plane is slightly modified since there are only relative drift time measurements. Delayed hits can form a track only if the differences in anode times are shorter than 1.5 $\mu$s, which is approximately the maximum drift time in a Geiger cell. For each hit, the drift distance is computed from the $tdc_\alpha$ for the cell, assuming the delayed hit with the higher $tdc_\alpha$ value corresponds to a particle passing through the anode wire of the cell.

For both in time and delayed tracks, note that the coordinates of the reconstructed vertex are taken as zero if the track doesn't start from the foil (either there is no intersection between the track and the foil, or no Geiger cells in the two nearest layers to the foil are associated to the track).

#### 3.3.3.2 Association between tracks and energy deposited in the calorimeters

An electron or positron event needs track associated with a scintillator. This is accomplished if there is at least one hit in the two Geiger cell layers nearest to the scintillators which belongs to the track. Additionaly, geometrical cuts are applied which extrapolate the position of the track to the surface of the scintillator ($R_S\phi_S$ and $Z_S$) which has to be located less than 3 cm away from the edges of the scintillator.

### 3.3.4 Reconstruction of the particle position in the cell

Studies with a laser and a nine cell prototype of the tracking detector were carried out to establish formulae giving transverse ($r_\perp$) and longitudinal ($z$) positions in a cell from anode drift times and both cathode times [52]. These formulae have been improved with NEMO 3 [53], for initial gas mixture of helium and alcohol, using data taken with high energy crossing electrons ($>$ 4.5 MeV). These electrons were created by an intense Am-Be source producing fast neutrons with an activity of around $2.2 \times 10^5$ n/s. Fast neutrons are thermalized in the scintillators; then high energy $\gamma$-rays are created by the capture of the neutrons in the copper walls, producing one-crossing-electron events by the Compton effect. With high energy crossing electrons and with an energy deposited $>$ 3 MeV in the second scintillator, the multiple scattering is found to be negligible and the track is well defined.

The track resulting from the fit is assumed to be identical to the real track. Thus, the transverse and longitudinal reconstruction formulae are obtained by comparing the distance to the identified track with the drift anode time and the two cathode times.

Formulae were improved once again for 2003 data with new gas mixture of helium, argon, alcohol and water, using a method based on the knowledge of the scintillator block positions.

#### 3.3.4.1 Transverse position in the cell

For gas mixture of helium and alcohol, the transverse distance $r_\perp$ in mm was given using the anode time $t_A$ (as defined in Eq. 2.8) by the following relations [53]:

- $r_\perp = 0.025$ mm if $t_A = 0$ (corresponding to the radius of the anode wire, whose the diameter is 50 $\mu$m)
- $r_\perp = (0.598 + 0.0045 \times t_A)$ mm if $0 < t_A \leq 60$ ns
- $r_\perp = (-0.292 + 0.023 \times t_A)$ mm if $60 < t_A \leq 220$ ns
- $r_\perp = (0.22 \times t_A^{0.572})$ mm if $220 < t_A < 1480$ ns
- $r_\perp = 14.3$ mm if $t_A \geq 1480$ ns (corresponding to the radius of the cell, whose is 1.5 $\mu$s).

All these regions are presented in Fig. 3.12, which shows the transverse distance $r_\perp$ to the fitted track as a function of the anode time $t_A$ for this gas mixture. Near the wire (between 1 and 4.5 mm), the drift velocity corresponds to the saturation regime and is 2.3 cm/$\mu$s. Far from the anode wire, the drift speed is proportional to the electric field. Thus, for $220 < t_A < 1480$ ns, the electric field is proportional to $1/r$, which leads to a transverse distance proportional to $\sqrt{t_A}$.

Fig. 3.13 also give the transverse distance $r_\perp$ to the fitted track as a function of the anode time $t_A$, but showing the difference between the results obtained with helium plus alcohol gas mixture and those obtained after addition of argon and water [54].
This preliminary new analysis was done searching to use only one relation giving $r_\perp$ (in mm) for all $t_A$ values (in ns):

$$r_\perp = \frac{(6.759 \times t_A)}{t_A^{0.84} + 287.09} + 0.1877 \tag{3.1}$$

It can be shown from Fig. 3.13 that this calibration relation from Eq. 3.1 fits very well the data for anode times $t_A \gtrsim 60$ ns (and it also improves in the same time the $\beta\beta 2\nu$ angular distribution, as seen in Fig. 5.2 from Section 5.1). Nevertheless, for anode times $t_A \lesssim 60$ ns, improvements on the $r_{perp}$ versus $t_A$ fit will need the use of at least one other relation.

#### 3.3.4.2 Longitudinal position in the cell

For each Geiger hit, the longitudinal reconstruction $z$ depends on the cathode times (status 1, 3, 5 or 7 for the cell). According to the two measured cathode times $t_{LC}$ and $t_{HC}$, and using the origin of the $z$ axis fixed at the half-height of the cells, the longitudinal position $z$ is given, in mm, by [54]:

$$z = \frac{L_{eff}}{2} \frac{t_{HC} - t_{LC}}{t_{LC} + t_{HC}} \left[ 1 - 0.408\ 10^{-4} \frac{L_{eff}}{2} \left( 1 - \left| \frac{t_{HC} - t_{LC}}{t_{LC} + t_{HC}} \right| \right) \right] \tag{3.2}$$

where $L_{eff} = 2620$ mm is the effective length of the cell, which is lower than the full cell length of 2700 mm that includes the two rings (each is 30 mm long). This effective length is a consequence of the fact that cathode signals exceed their electronic threshold a few centimeters before the plasma reaches the cathode ring. The $L_{eff}$ value, which is given here for He, Ar, alcohol and water gas mixture, depends on the HV and gas mixture and was 2607 mm for helium and alcohol initial mixing [53].

The first order term corresponds to a constant propagation speed for the plasma. In this case, the longitudinal position is simply the propagation time of the plasma to the nearest ring, divided by the propagation velocity.

The second order term is a correction, which takes into account the reduced propagation velocity due to a decrease in the high voltage during the plasma propagation (this factor also depends on the HV and gas mixture and is given here for He, Ar, alcohol and water in the mixture)[2]. The correction has a maximum value of around 20 mm in two positions corresponding respectively to 25% and 75% of the cell length but is not the same for all cells. Thus improvements on the reconstruction program were needed for around 10% of the cells, by addition of new parameters in Eq. 3.2, which also improve the longitudinal resolution. Finally, parameters for each of the 6180 cells are stored in the database [54].

If one of the two cathode times is missing (**status 3** or **5**), the relation remains the same than for **status 1**, but only for the TDC with a non-zero value. The other cathode time is obtained using an average plasma propagation velocity. The $z$ position in the Geiger cell is then reconstructed using the same formula as above. The propagation velocity has to be calculated and stored in the database for each Geiger cell.

If both cathode times are missing (**status 7**), no reconstruction of the $z$ position of the Geiger cell hit is possible.

#### 3.3.4.3 Transverse and longitudinal resolution of the Geiger cells

The residual distribution in the transverse direction was obtained in a plane perpendicular to the wires by plotting the distance between the accepted track and the reconstructed position of the Geiger cell hit ($\Delta r$), using high energy crossing electrons [53]. The $\Delta r$ value can also be calculated using $\beta\beta$ events (see distribution in Fig. 3.14) [54]. The full-width at half maximum ($FWHM$) of this spectrum is used to compute the transverse resolution of the cells as $\sigma_{\perp} = FWHM/2.35$. For present gas mixture, the average value of this resolution is [54]:

$$\sigma_{\perp} = 0.6 \text{ mm}$$

In order to estimate the contribution of multiple scattering, a study of the transverse resolution was carried out as a function of the variable $\sqrt{L_{track}}/E$, where $L_{track}$ is the track length and $E$ is the initial energy of the electron in keV (see Fig. 3.15). The associated relation, which shows the resolution dependence with multiple scattering, is:

$$\sigma_{\perp} = \sqrt{\sigma_{int}^2 + k(\frac{\sqrt{L_{track}}}{E})^2}$$

where the intrinsic resolution is given by $\sigma_{int} = (0.37 \pm 0.02)$ mm and $k = (10.8 \pm 1.7)$ mm keV$^2$ is a constant [53].

The longitudinal resolution of the cells is obtained by the same method applied in the longitudinal plane. Fig. 3.16 shows the residual distribution in the longitudinal direction, obtained by plotting the distance between the accepted track and the reconstructed position of the Geiger cell hit ($\Delta z$), using $\beta\beta$ events and new gas mixture [54]. The corresponding average value is

$$\sigma_{//} = 0.3 \text{ cm}$$

---

[2] The correction factor was $0.505 \times 10^{-4}$ for initial gas mixture of helium and alcohol [53]

In case of one missing cathode in one cell's data, it is very important to take into account the presence of neighbour cells hit before. Using this, improvements were also obtained which can been shown on the residual distributions in the longitudinal direction (see Fig. 3.17). These distributions are obtained by plotting the distance between the accepted track and the reconstructed position of the Geiger cell hit ($\Delta z$), using $\beta\beta$ events [54]. Both the mean and RMS values are improved for the three cases (first, second or third fired cell).

Fig. 3.18 shows the influence of the dip angle $\theta$ on the longitudinal resolution (see Fig. 3.21 for definitions of dip and zenith angles). Here $\sigma_{//}$ is multiplied by a factor of 1.5 for an electron crossing the wire at an angle $\theta = 45^o$ compared to a track perpendicular to the wire. This increment is due to the longitudinal spread of the primary ionization electrons along the anode wire.

Fig. 3.19 shows the longitudinal resolution $\sigma_{//}$ as a function of the longitudinal position $z$ [54]. The associated relation is:

$$\sigma_{//} = \sigma_0 \sqrt{1 - (\frac{z}{L_{eff}/2})^2}$$

where $\sigma_0 \sim 1.1$ cm is the maximum resolution at the center of the detector; $L_{eff}$ is the effective length as defined above. This form is characteristic of the statistical fluctuations in the number of avalanches occuring during the longitudinal propagation.

### 3.3.5 Misidentification of electrons and positrons

There is a possible misidentification of electrons and positrons in tests with high energy ($\geq 3$ MeV) crossing electrons which are produced during neutron source studies. These crossing events are dominated ($> 99\%$) by electrons and are reconstructed as two half-sector electron-type events with successive negative curvature. The first half from an external scintillator to the source foil on one side of the foil, the second one from the source foil to an internal scintillator, both with a common vertex on the foil. Thus it is possible to check the probability of mistaking a positive curvature positron event against an electron event after the foil. The associated distribution of the rate of error as a function of the electron energy is presented in Fig. 3.20. The $e^+e^-$ misidentification is around 3% at 1 MeV using extrapolated results [53].

### 3.3.6 The vertex reconstruction

#### 3.3.6.1 Principle

The quality of vertex reconstruction has been analyzed by taking data with 60 $^{207}$Bi sources placed in the three positions (T for Top with $Z = 90$ cm, C for Center with $Z = 0$ cm, and B for Bottom with $Z = -90$ cm) on each sector inside the calibration tubes. The $R\phi$ and $Z$ positions of these sources (see Section 3.3.3) are known with an accuracy of 1 mm. $\phi$ is the polar angle (see Fig. 3.21), using cylindrical coordinates, with an origin at sector 0; $R = 155.5$ cm is the transverse distance between the detector's center and the source foils; for sector 00, the $R\phi$ value for the calibration source position is $(148.6 \pm 0.1)$ cm and there is a step of 18 degrees to obtain $R\phi$ for each subsequent sector.

Conversion electron events coming from these sources are selected, with energies of 482 keV or 976 keV. The distribution of the 60 reconstructed vertices are presented in Fig. 3.22. With this sample of data the differences between reconstructed and expected vertex positions can be estimated. The difference in the transverse plane is defined as $\Delta R\phi = R\phi_{\rm rec} - R\phi_{\rm exp}$ and in the longitudinal plane as $\Delta Z = Z_{\rm rec} - Z_{\rm exp}$.

For transverse reconstruction of the vertex, the average position shifts between reconstructed and expected vertices are the same for the three source positions (T, C and B). Here are given the values with initial gas mixture as published in Ref. [19]:

$$< \Delta R\phi >= 1.6 \text{ mm}$$

These $< \Delta R\phi >$ are compatible with the accuracy of the mechanical $R\phi$ positions of the calibration sources and calibration tubes.

The average differences in the longitudinal reconstruction for the three positions, which are given here are measured with the longitudinal calibration associated to the new gas mixing [54], as shown in Fig. 3.23:

$$< \Delta Z(T) >= -1.5 \pm 0.1 \text{ mm}$$

$$< \Delta Z(C) >= -1.4 \pm 0.1 \text{ mm}$$

$$< \Delta Z(B) >= -1.7 \pm 0.1 \text{ mm}$$

These average differences are closer to zero and present less asymmetry than those measured with initial mixing [19]. Note the maximum value of $< \Delta Z >$ is lower than the longitudinal vertex resolution. The longitudinal position of the vertex is independent of the angle.

### 3.3.6.2 Vertex resolution

The **transverse resolution** $\sigma_{R\phi}$ depends on the energy of the track. Using the two conversion electron energy values ($\sim$ 0.5 MeV and $\sim$ 1 MeV), it is possible to determine average values for these resolutions, as published in Ref. [19]:

$$\sigma_{R\phi}(0.5 \text{ MeV}) = 0.3 \text{ cm} \quad \text{and} \quad \sigma_{R\phi}(1 \text{ MeV}) = 0.2 \text{ cm}$$

The **longitudinal resolution** $\sigma_Z$ depends on both energy and position. The energy dependence was studied for new gas mixing, using 1 MeV electrons [54]. The same value of $\sigma_Z = 0.4$ cm was obtained for both T and B positions and $\sigma_Z = 0.5$ cm was obtained for the C position. For 0.5 MeV electrons, the longitudinal resolution is $\sigma_Z = 0.8$ cm on average for the T and B positions and 0.6 cm for the C position.

Another dependence on the dip angle $\theta$ (see Fig. 3.21) was studied only with initial gas mixing, as shown in Fig. 3.24. This dependence obeys the relation [53]:

$$\sigma_Z = \frac{\sigma'_0}{\cos\theta}$$

where, on average, $\sigma'_0 = (0.632 \pm 0.004)$ cm for the T position, $\sigma'_0 = (0.825 \pm 0.006)$ cm for the C position and $\sigma'_0 = (0.615 \pm 0.004)$ cm for the B position.

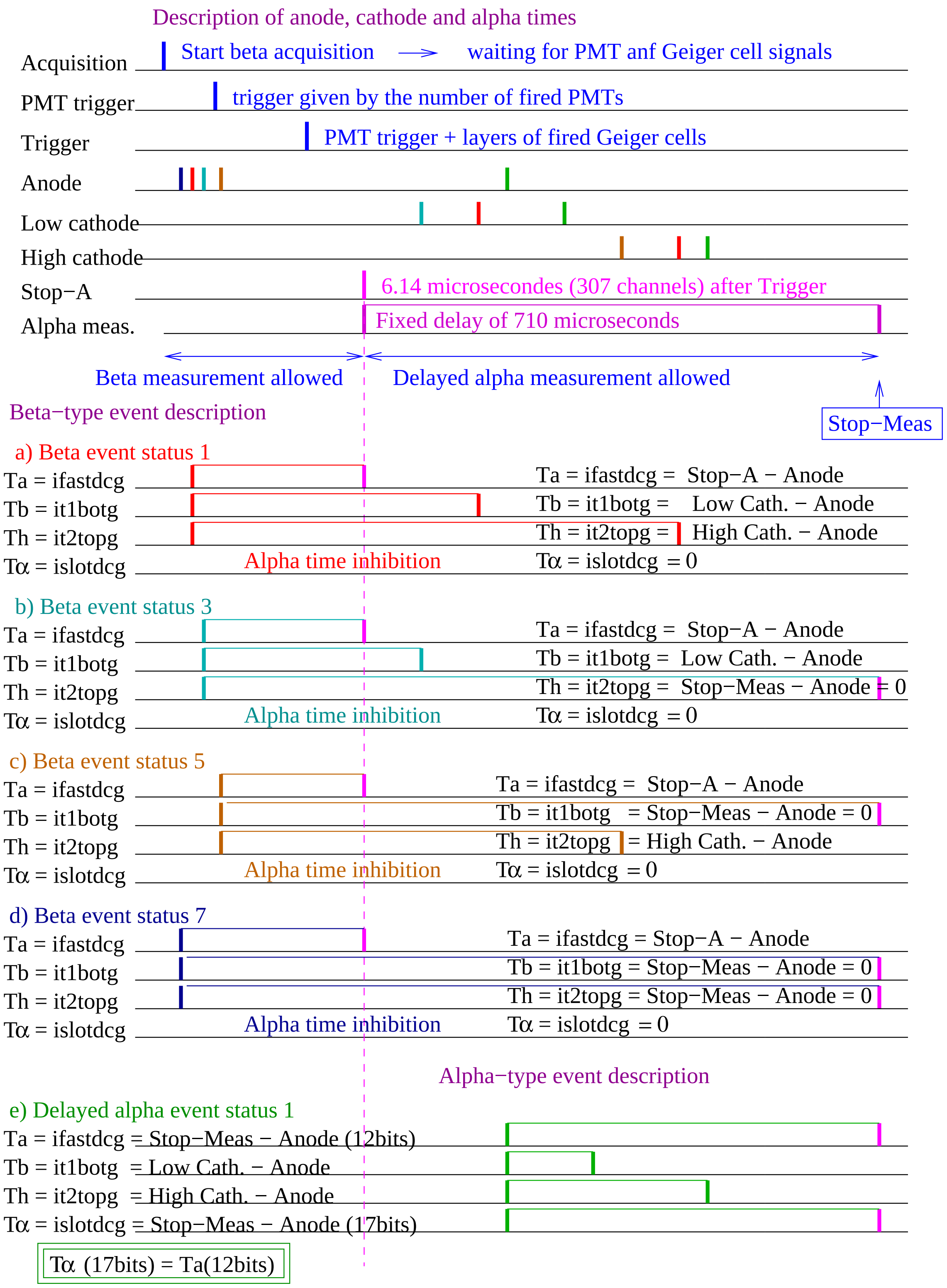

Figure 3.11 : Synopsis of different times associated to the tracking detector.

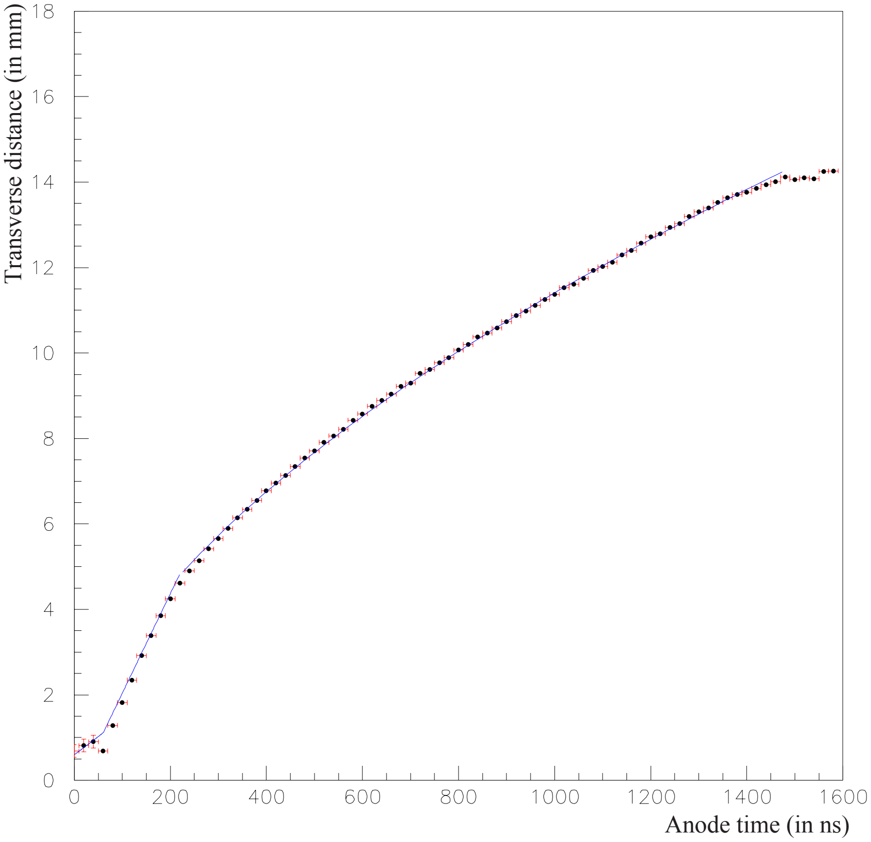

Figure 3.12: Transverse distance to a constructed track $r_\perp$ (in mm) as a function of anode time $t_A$ (in ns) obtained with high energy crossing events ($e_{cross} > 4.5$ MeV) [53].

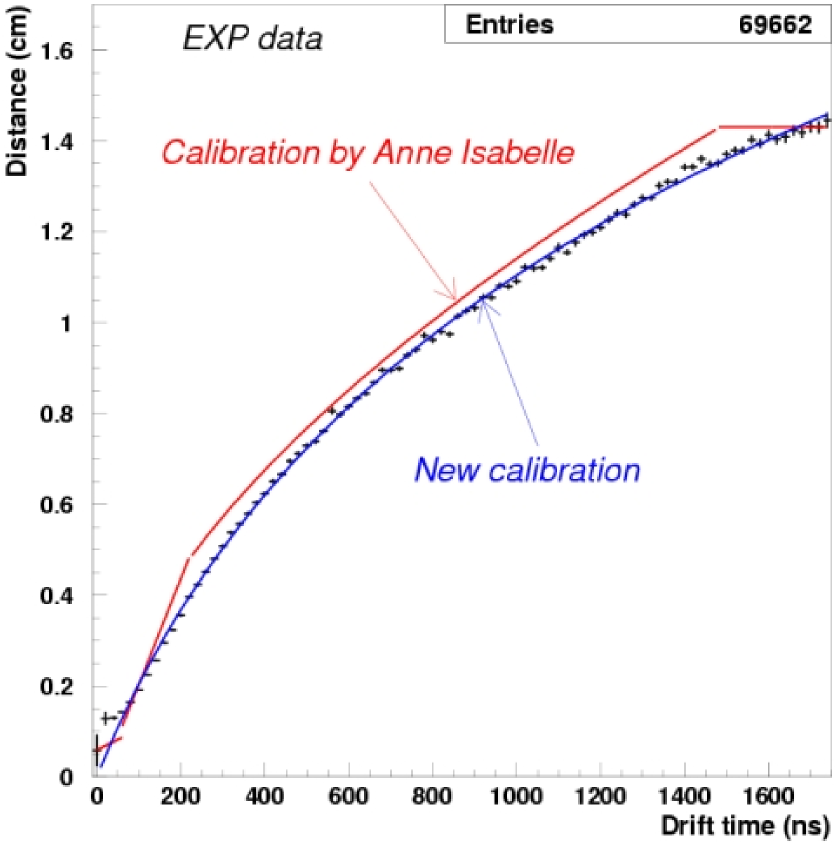

Figure 3.13 : Transverse distance to a constructed track $r_\perp$ (in mm) as a function of anode drift time $t_A$ (in ns), with a comparison between the calibration results from Fig. 3.12, which were obtained from data collection with initial gas mixing, and those obtained for data after February 2003, with addition of argon and water in the mixture [54].

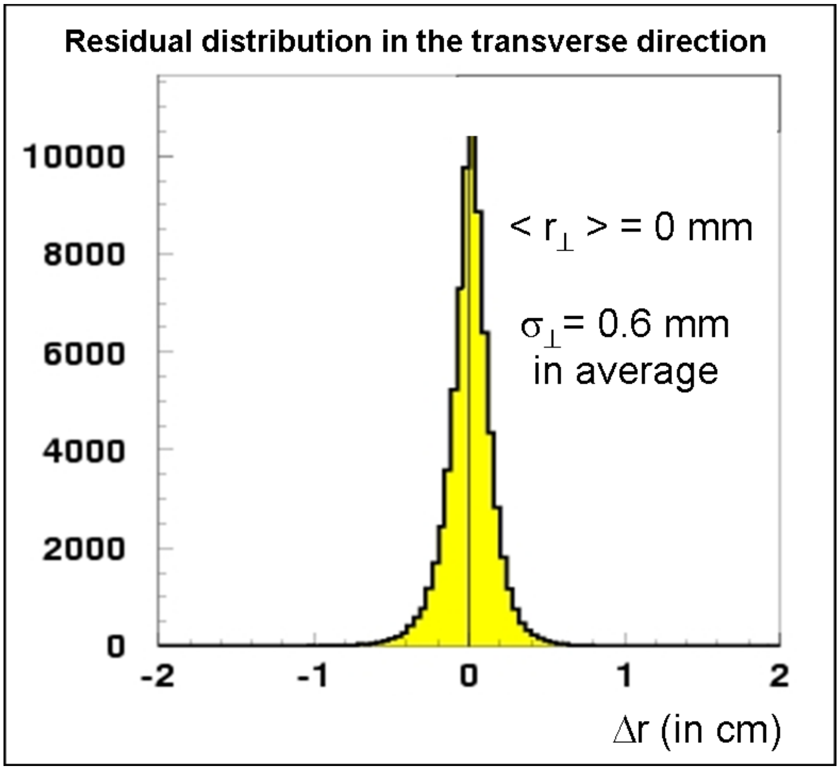

Figure 3.14: Residual distribution in the transverse direction obtained in a plane perpendicular to the wires by plotting the distance between the accepted track and the reconstructed position of the Geiger cell hit ($\Delta r$), using $\beta\beta$ events [54]. The associated resolution $\sigma_{\perp}$ as an average value of 0.6 mm.

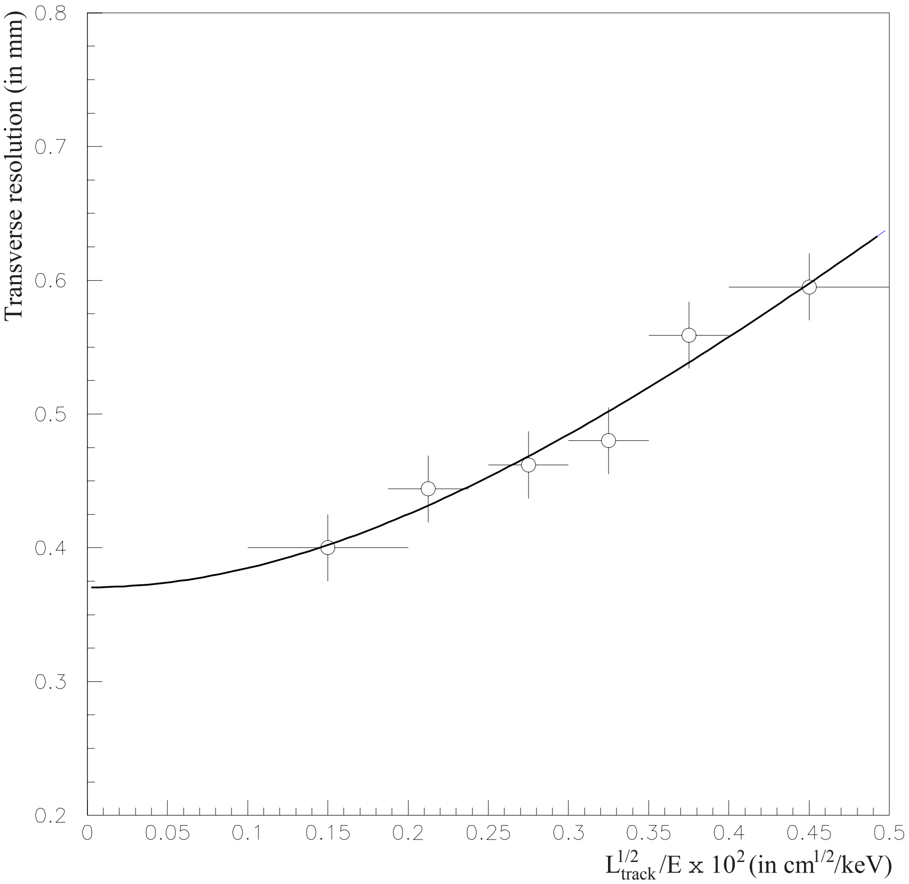

Figure 3.15: Distribution of transverse resolution per cell $\sigma_\perp$ (in cm) as a function of the variable $\sqrt{L_{track}}/E$ [53]. The associated curve is the result of the fit given by $\sigma_\perp = \sqrt{\sigma_{int}^2 + k\,(\sqrt{L_{track}}/E)^2}$.

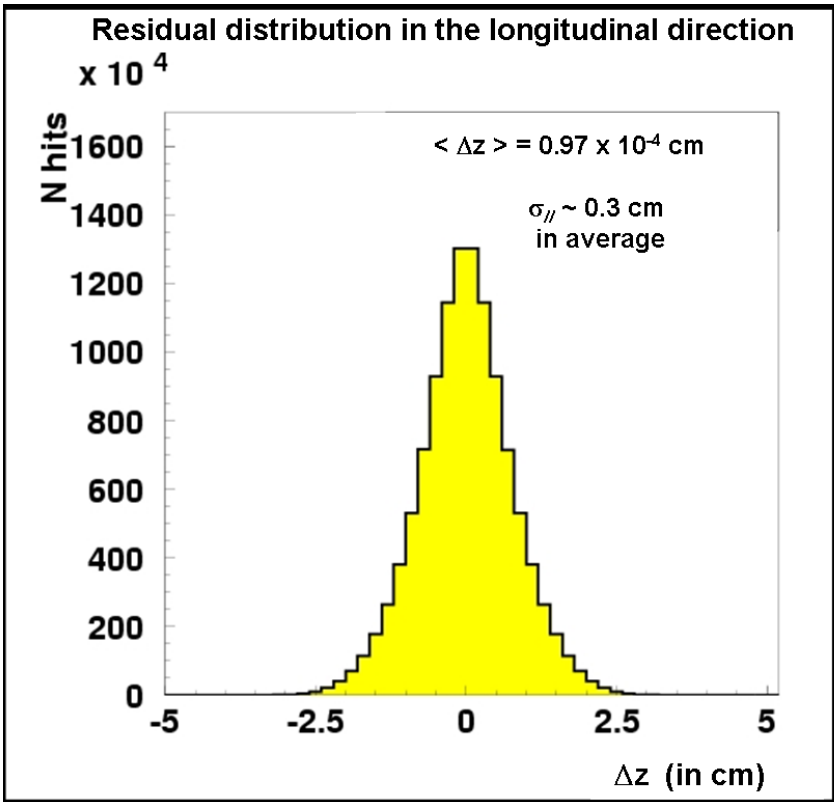

Figure 3.16 : Residual distribution in the longitudinal direction obtained by plotting the distance between the accepted track and the reconstructed position of the Geiger cell hit ($\Delta z$), using $\beta\beta$ events [54]. The associated resolution $\sigma_{//}$ as an average value of 0.3 cm.

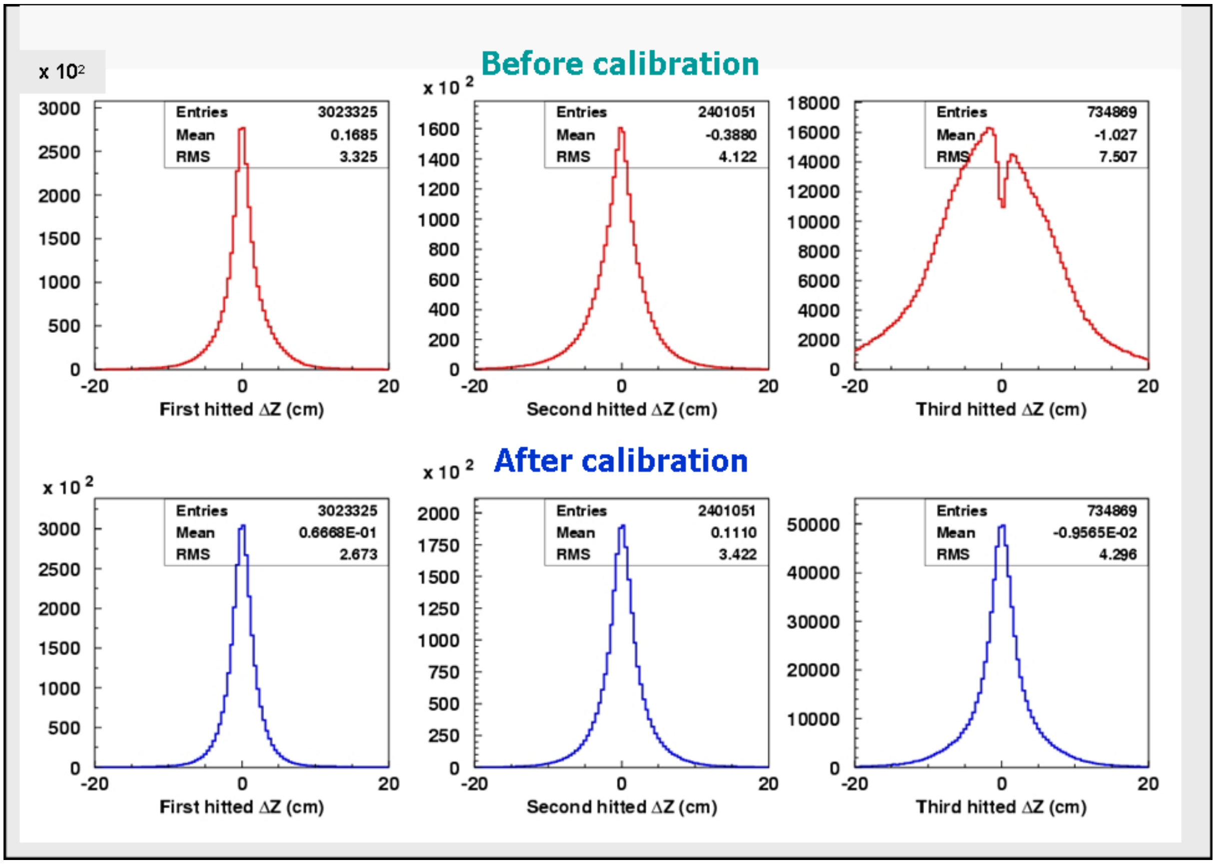

Figure 3.17: Distribution of $\Delta z$ (in cm) for one-missing cathod cells, before (top figures) and after (bottom figures) calibration consisting to take into account for each cell the presence of neighbour cells hitted before this cell. Three cases are used: if the cell was fired first, second or third. One clearly see that both the mean and RMS values are improved for the three cases.

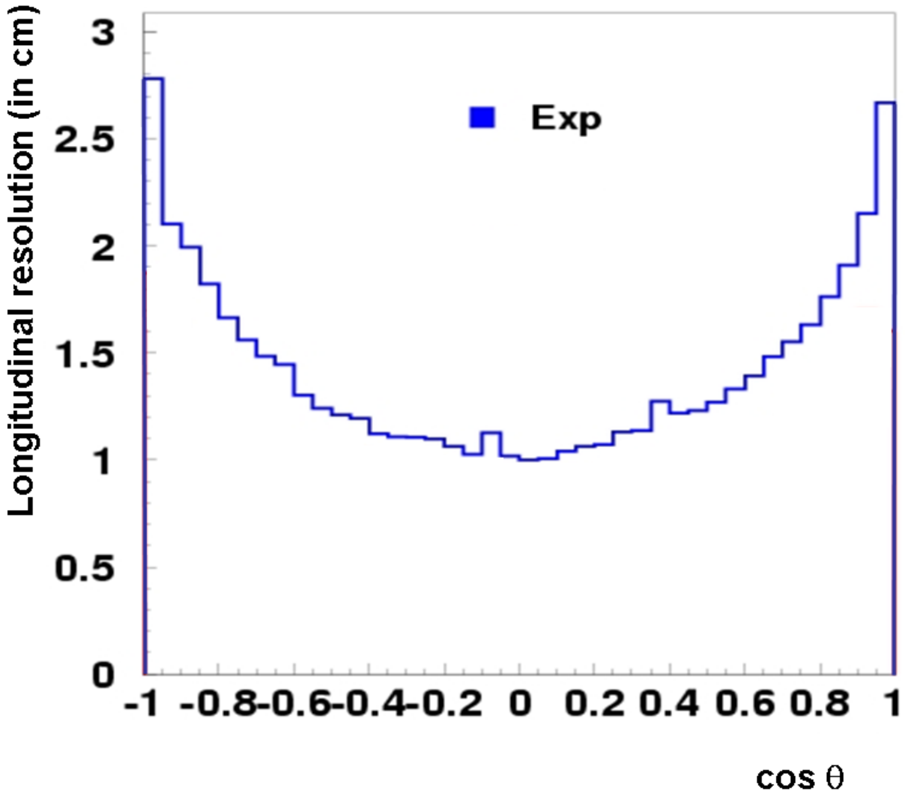

Figure 3.18: Distribution of longitudinal resolution in a cell $\sigma_{//}$ (in cm) as a function of $\cos\theta$, where $\theta$ is the dip angle [54].

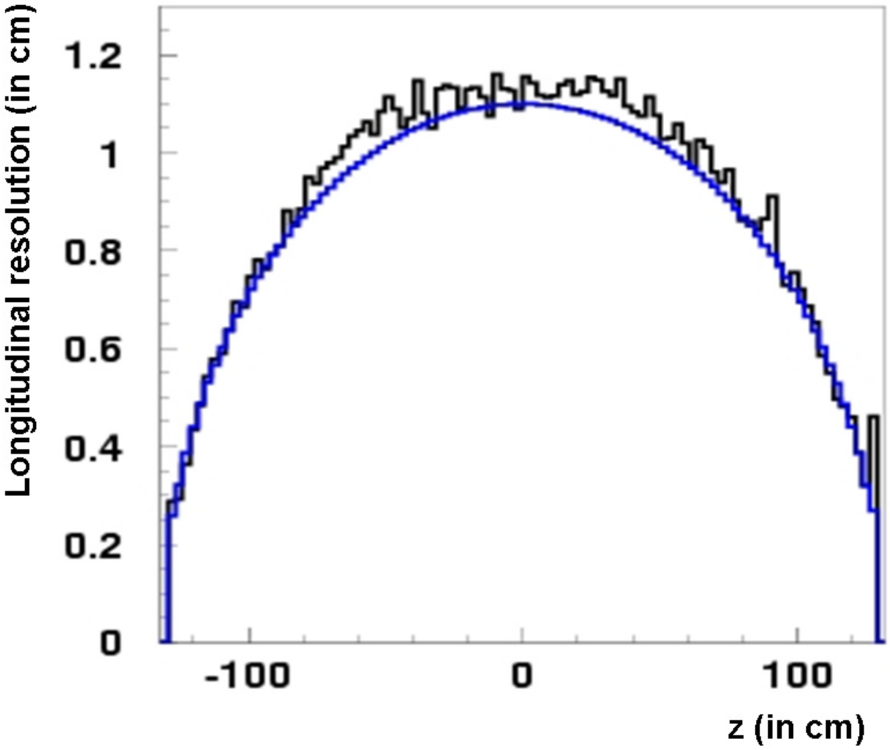

Figure 3.19: Distribution of the longitudinal resolution in a cell $\sigma_{//}$ (in cm) as a function of longitudinal position $z$ (in cm) [54]. The associated curve is the result of the fit given by $\sigma_{//} = \sigma_0 \sqrt{1 - (2z/L_{eff})^2}$.

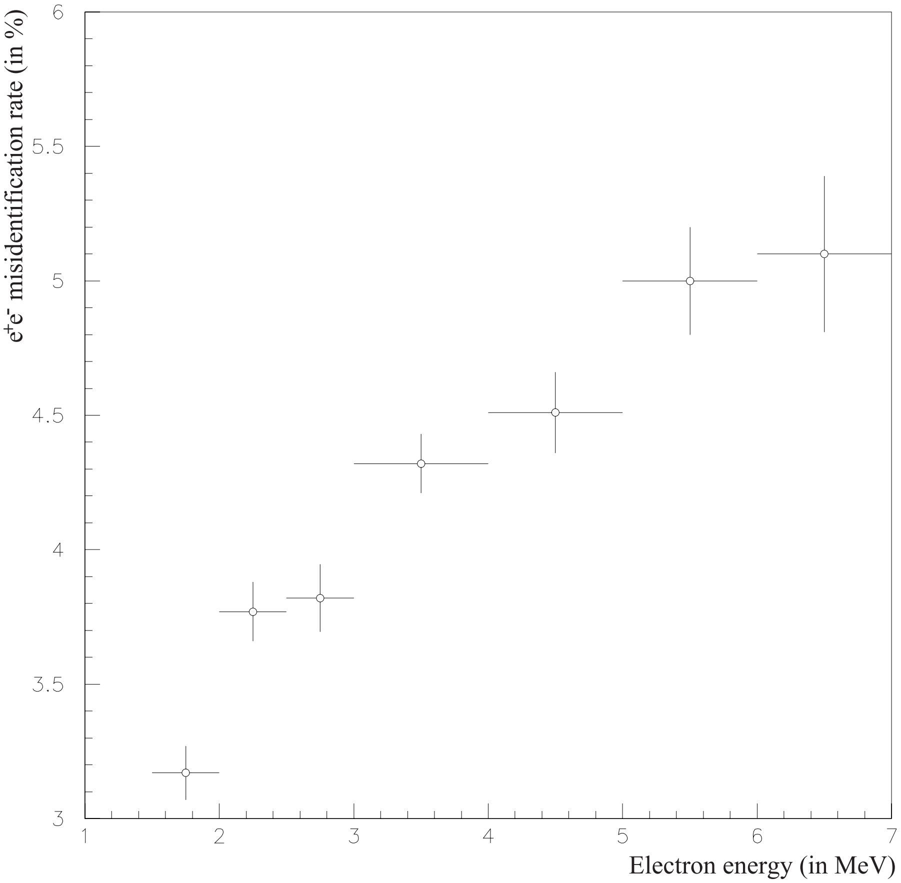

Figure 3.20 : Distribution of $e^+e^-$ misidentification rate as a function of electron energy [53].

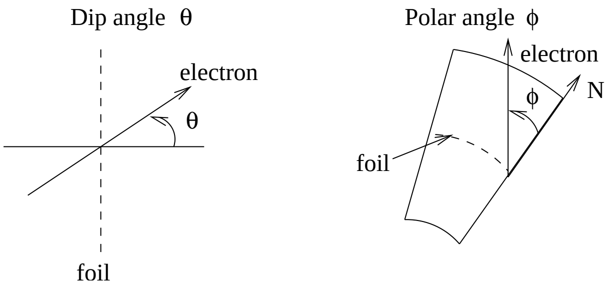

Figure 3.21 : Definitions for dip angle $\theta$ and polar angle $\phi$ for the tracking detector.

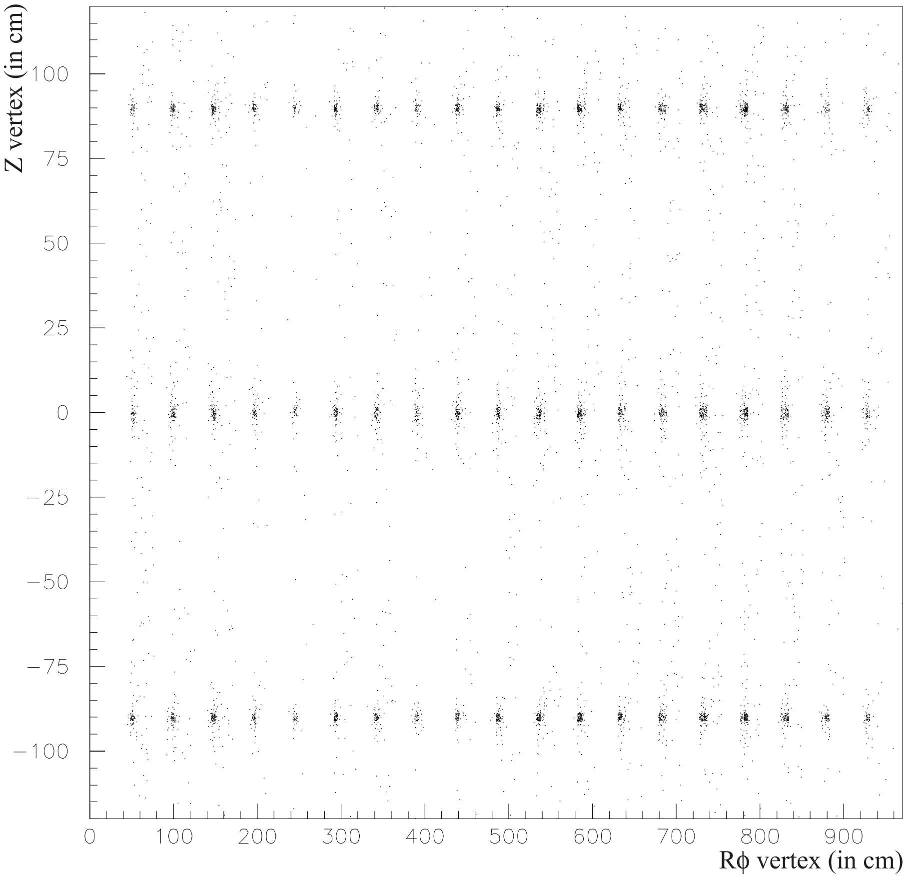

Figure 3.22: Distribution of reconstructed vertices for the 60 positions of the calibration $^{207}$Bi sources, in the one-electron channel [53].

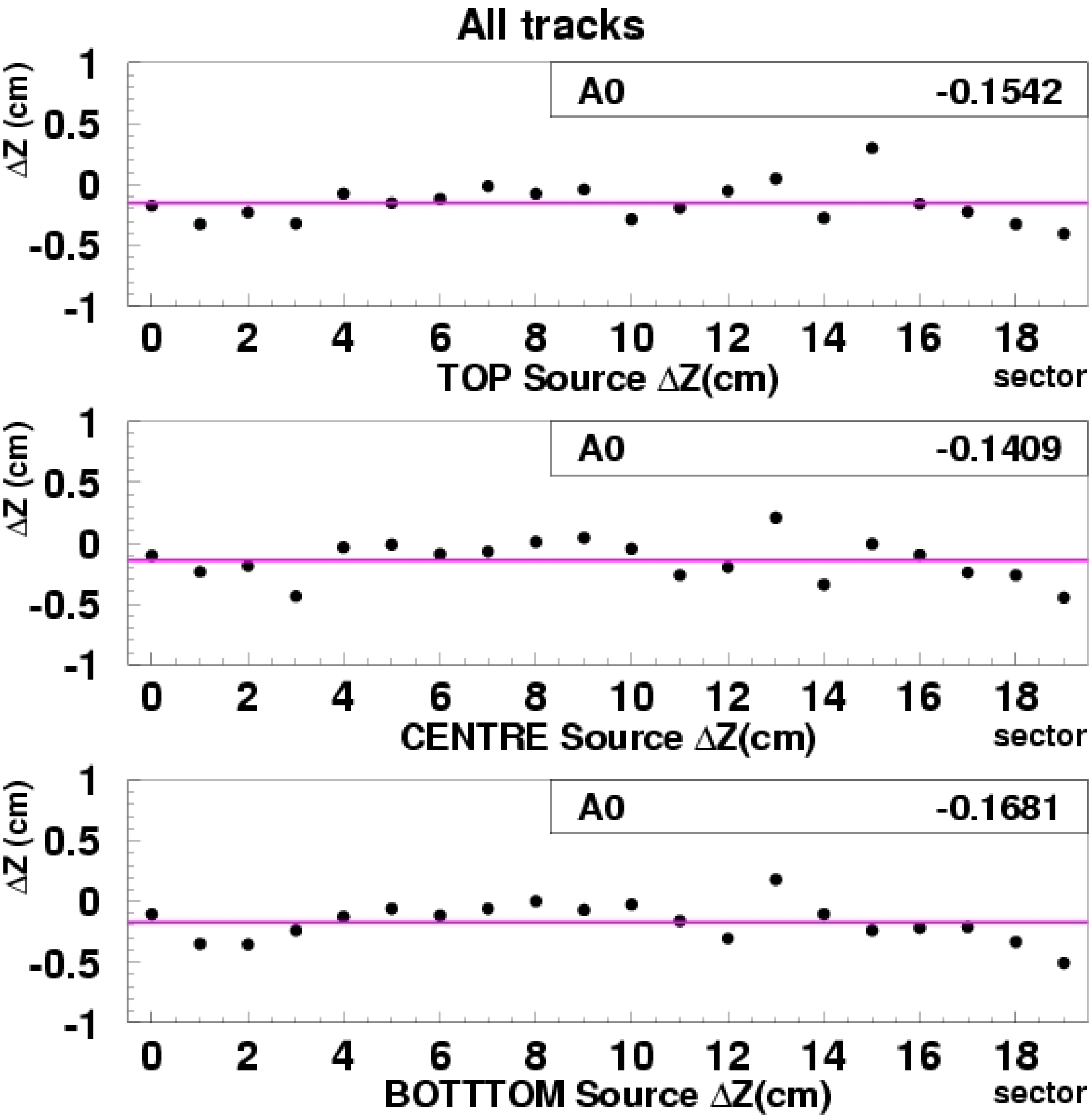

Figure 3.23: Average differences in the longitudinal reconstruction as a function of the sector number, for the three positions ($T$, $C$ and $B$) [54].

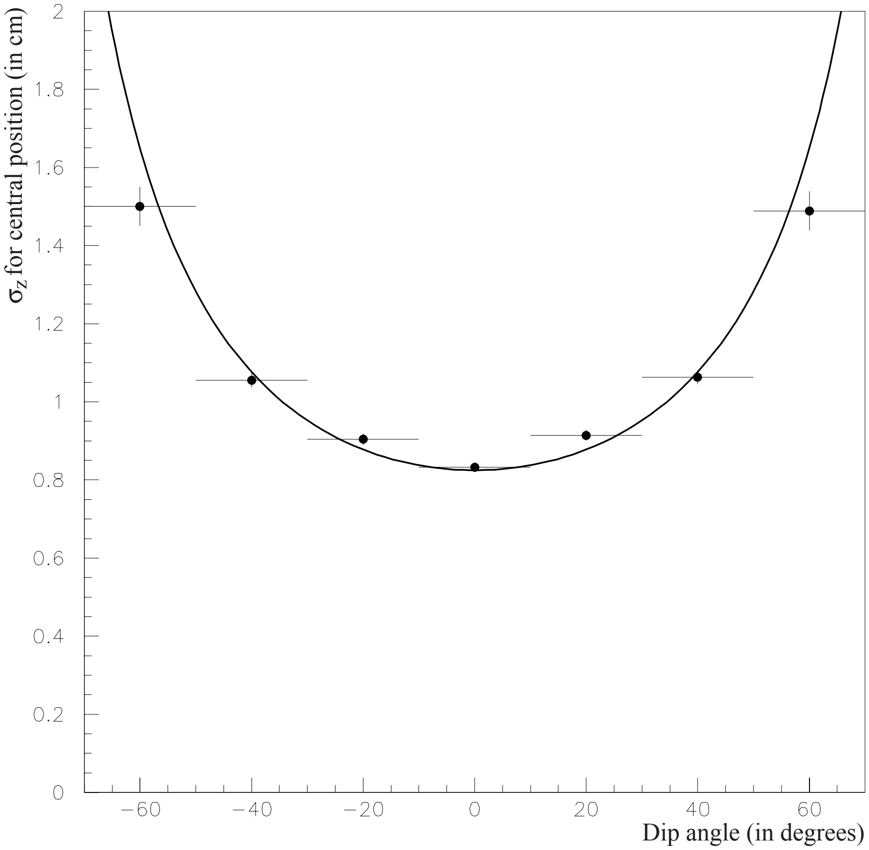

Figure 3.24: Distribution of the vertex longitudinal resolution $\sigma_Z$ (in cm) as a function of the dip angle $\theta$ (in degrees), with a $\sigma'_0/cos\theta$ adjustment (obtained with $^{207}$Bi sources located in the central position and initial gas mixture) [53].

#### 3.3.6.3 Study with two electrons events

The $\beta\beta$ analysis reconstructs events with two tracks coming from the same vertex. Thus, it is important to study the vertex resolution of the two electron channel in order to check the measured transverse and longitudinal dispersions. These dispersions, $\delta R\phi$ and $\delta Z$, are defined as the distance between the vertices associated with the two reconstructed tracks.

Using events coming from the 60 $^{207}$Bi sources with two simultaneous electrons (intensity of $\sim 2\%$), one builds $\delta R\phi$ and $\delta Z$ distributions, which produce the resolutions [57]:

$$\sigma(\delta R\phi) = 0.6 \text{ cm} \qquad \text{and} \qquad \sigma(\delta Z) = 1.0 \text{ cm}$$

Also $\sigma(\delta R\phi) = 0.1$ cm, if one constrains the two tracks to have a common vertex. These resolutions allow one to make a distinction between two strips in a source foil in a given sector, which is crucial for sectors composed of different sources.

## 3.4 Operating conditions of the calorimeter

### 3.4.1 Working performance of the calorimeter

The operating voltages of the PMTs are 1800 V for the 3" and 1350 V for the 5" PMTs. The single counting rate is $\sim 0.2$ Hz/PMT above a 48 mV threshold ($\sim 150$ keV). In total, 98% of the PMTs are functioning to design specifications. Changes in HV chain could allow recovering some of the 2% missing PMTs.

### 3.4.2 Energy resolution of the counters [55]

#### 3.4.2.1 Energy calibration results

As explained in Section 2.6, special calibration runs are used to obtain the three points on the energy versus ADC channel line. Two results of multi-gaussian fits (K, L, M electrons) to the peak positions in the $^{207}$Bi data (see Fig. 3.25), and one from the beta end-point energy from $^{90}$Sr data (see Fig. 3.26). Here only 482 and 976 keV energy peaks from $^{207}$Bi data are used, but the third peak, which has an energy value of 1682 keV, is also fitted to find "super-corrections" as explained later in this Section.

The calibration lines obtained from the two $^{207}$Bi peaks as well as the fit combining $^{207}$Bi and $^{90}$Sr results do not necessarily intersect the origin of the axes. This effect was previously observed with data obtained with an electron spectrometer and in other experiments. A typical example is given in Fig. 3.27.

It was first discovered with calibration data that the response of a counter depends upon the entrance point of the electron, with a weak dependence of 1 to 2% for counters equipped with 3" PMTs and a stronger dependence of up to 10% for those equipped with 5" PMTs. This effect has a non-negligible consequence on the energy resolution (FWHM), given by Eq. 3.3:

$$FWHM(E) = \sqrt{A \times E + B + C \times E^2} \tag{3.3}$$

as given earlier in Eq. 2.11 in Section 2.6.6.
Thus one had to correct this energy resolution for the seven different types of counters, L1 to L4 for petal scintillators and EE, EC and IN for wall scintillators.
A "super-correction" method was developed at IReS to get these impact point corrections for each individual counter with a given type of blocks (IN, L1, L2 and L3 with 3" PMTs, and EE, EC and L4 with 5" PMTs), dividing the front face surface of scintillators in 9 equal areas for 3" PMTs and 25 equal areas for 5" PMTs. An example is given in Fig. 3.28, which show gain variation for the 25 defined areas for external scintillator blocks.

Then, the 482, 976 and 1682 keV electron peaks are fitted again (with a correction for the mean energy loss), as shown in Table 3.8, to obtain the parameters $A$, $B$ and $C$ of the resolution function (from Eq. 3.3). These associated energy resolutions $\sigma(E)/E$ calculated using this "super-correction" method can be found both with parameters in Table 3.9. As an example of the "super-correction" effect is given in Fig. 3.29 the spectral fit of the 482, 976 and 1682 keV conversion electron peaks coming from $^{207}$Bi decays redone for one counter. "Super-corrections" are stored in the NEMO 3 database and used after track reconstruction in order to obtain the entrance point on the scintillator and to use it correct the energy values.

One can see that these resolutions depend primarily on the type of PMT associated with the scintillator which on average are 5.8% for the 5" PMTs and 7.0% for the 3" PMTs. It must be noted that energy resolutions can vary with time (see Fig. 3.30 and caption).

| Block type | 482 keV $e^-$ | 976 keV $e^-$ | 1682 keV $e^-$ |
|---|---|---|---|
| IN | 123.0 | 165.2 | 223.3 |
| EE | 96.7 | 133.9 | 188.6 |
| EC | 96.9 | 136.7 | 195.5 |
| L1 | 110.7 | 148.5 | 211.9 |
| L2 | 121.3 | 153.1 | 203.0 |
| L3 | 121.4 | 161.2 | 235.4 |
| L4 | 100.3 | 132.5 | 180.3 |

Table 3.8: Fitted resolutions at $^{207}$Bi conversion electron peak energies (FWHM) in keV.

| Block type | $A$ (MeV) | $B$ (MeV$^2$) | $C$ | $\sigma(E)/E$ (%) |
|---|---|---|---|---|
| IN | 0.0158 | 0.00611 | 0.00610 | $7.1 \pm 0.1$ |
| EE | 0.00801 | 0.00401 | 0.00640 | $5.8 \pm 0.1$ |
| EC | 0.00809 | 0.00379 | 0.00736 | $5.9 \pm 0.1$ |
| L1 | 0.00469 | 0.00758 | 0.104 | $6.4 \pm 0.2$ |
| L4 | 0.00779 | 0.00514 | 0.00504 | $5.7 \pm 0.2$ |

Table 3.9: Examples of parameters $A$, $B$ and $C$ from Eq. 3.3 and associated energy resolutions $\sigma(E)/E$ at 1 MeV, using "super-corrections" of entrance position on scintillators blocks. These preliminary results are obtained using only "good counters", which have no area failing the gain finding procedure. Concerning L2 and L3 blocks, the energy resolution values which are used for analysis are those given in Ref. [19] due to their higher precision.

### 3.4.3 Timing resolution of the counters

#### 3.4.3.1 Timing corrections

As explained in Section 2.6, the relative timing offset $\varepsilon^{(i)}$ for each counter $i$ is determined using different calibration sources, in order to provide the time alignment of the calorimeter.

The two-gamma events from $^{60}$Co sources are used for time alignment with $\gamma$-rays. The distribution of the arrival time difference in the counters before and after alignment is shown in Fig. 3.31. The distribution after alignment has a resulting RMS of $\sim$ 660 ps for gamma events.

The two-electron events from $^{207}$Bi sources are used for time alignment with electrons and to obtain the time resolution as a function of electron energy as shown in Fig. 3.32. This resolution is around 250 ps for 1 MeV electrons [56].

The energy dependence of the timing signal is adjusted by a four parameter formula, as shown in Eq. 2.14. The first method to find this dependence is to use a "complete" laser run. A second is to use the two-electron events from $^{207}$Bi sources. The results of this second method for the different types of scintillators are plotted in Fig. 3.33.

#### 3.4.3.2 The time-of-flight (TOF) selection criterion

To distinguish between one-crossing-electron events from external background and two-electron events from the source foil, the same TOF rejection criterion is applied that was used in the NEMO 2 experiment [11]. It is based on the comparison between the measured ($\Delta T_{meas}$) and the calculated ($\Delta T_{cal}$) time differences of the scintillator hits. A single electron crosses the detector in a time $(\Delta T_{cal})_{ext}$ and two electrons emitted from the source foil lead to a calculated TOF equal to $(\Delta T_{cal})_{int}$.

Fig. 3.34 represents $(\Delta T_{meas} - \Delta T_{cal})_{int}$ (for internal hypothesis) vs $(\Delta T_{meas} - \Delta T_{cal})_{ext}$ (for external hypothesis) for selected two track events (except TOF criterium) from $^{100}$Mo foils. The two-electron events coming from the source foil are centered around $(\Delta T_{meas} - \Delta T_{cal})_{int} \sim 0$ ns whereas the one-crossing-electron events have $(\Delta T_{meas} - \Delta T_{cal})_{int} \sim \pm 5$ ns for the internal background hypothesis. The calculated TOFs are based on the particle energy deposits in the scintillator counters. Thus, in the case of a through-going electron the calculation of $(\Delta T_{meas} - \Delta T_{cal})_{int}$ relies on a wrong estimate of the time (calculated from a hypothesis using the energy) of one of the tracks and results in a large (around 5 ns) positive or negative value for the TOF as it can be observed in Fig. 3.34, which shows well-separated bumps.

### 3.4.4 Counter stability

Using the survey system with laser light described in Section 2.6, the counter stability of the counters is checked daily. It permits to survey the gain stability of each ADC and TDC associated to the signals coming from the 1940 counters. Typical energy spectra obtained during the same laser run for a counter are shown respectively in Fig. 3.35 and 3.36: a laser light spectrum and the corresponding conversion electron spectrum, which come from $^{207}$Bi decays sources put in the associated reference counter. For each counter, the stability corrections are calculated using the absolute calibration obtained with sources as a reference and laser spectra. These corrections take into account any variation of the laser, which is monitored by reference PMTs. This variation measurement is determined by comparing the laser peak position and the 976 keV peak position from the $^{207}$Bi for the six reference counters (see Section 2.6.7).

It has been shown from the energy study [45] that for few PMTs, there is a drop of gain after the introduction of the calibration sources. It is explained by the usual low counting rate situation for the PMTs, which need an high counting rate (coming from sources) to reach stability. This effect is very well controlled and taken into account using laser runs carried each two hours during the energy calibration periods.

An example of a long term (one month) survey of the energy correction parameter ($e_{corr}$) for one counter is shown in Fig. 3.37. This stable behaviour with gain variations of around $\pm 1\%$ is consistent with 90% of the counters with 5" PMTs and 96% with 3" PMTs. Individuals attenuators will soon be changed to improve this stability for all the PMTs. These corrections are stored in the database and used with $\beta\beta$ runs to calculate particle energies. In case laser survey give different $e_{corr}$ values than the absolute calibrations for one PMT, a new correction called “retro-correction” is calculated and stored in the database [34].

A PMT status is defined for each of the NEMO 3 counters, after analysis of the calibration results coming from the database. If there is no problem, the PMT status is 1. All PMT quality flags, which are used for calorimeter data analysis, are summarized in Fig. 3.38 [34].

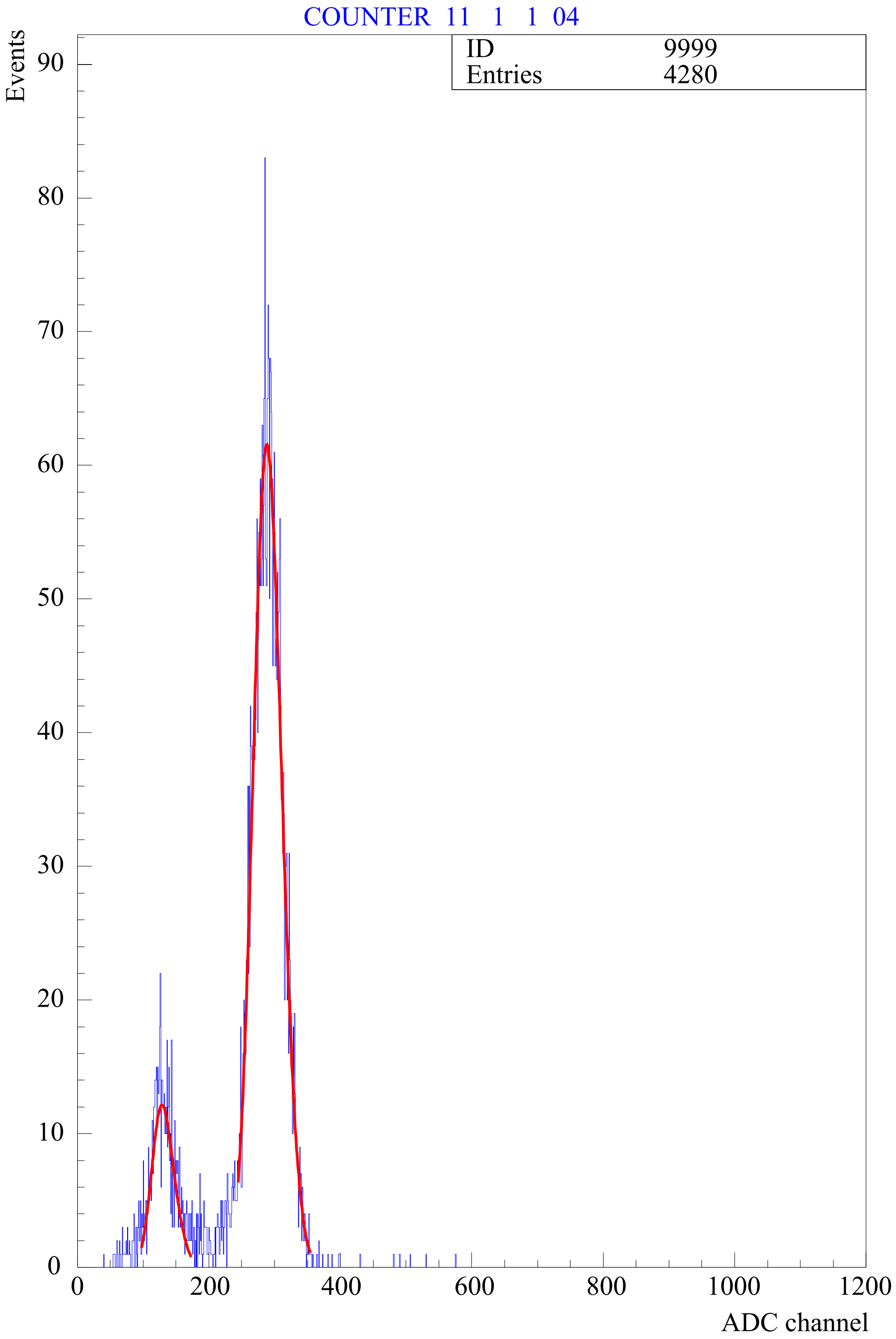

Figure 3.25: Spectral fit of the 482 keV and 976 keV conversion electron peaks coming from $^{207}$Bi decays for one counter ($\sim$ 3 keV/channel).

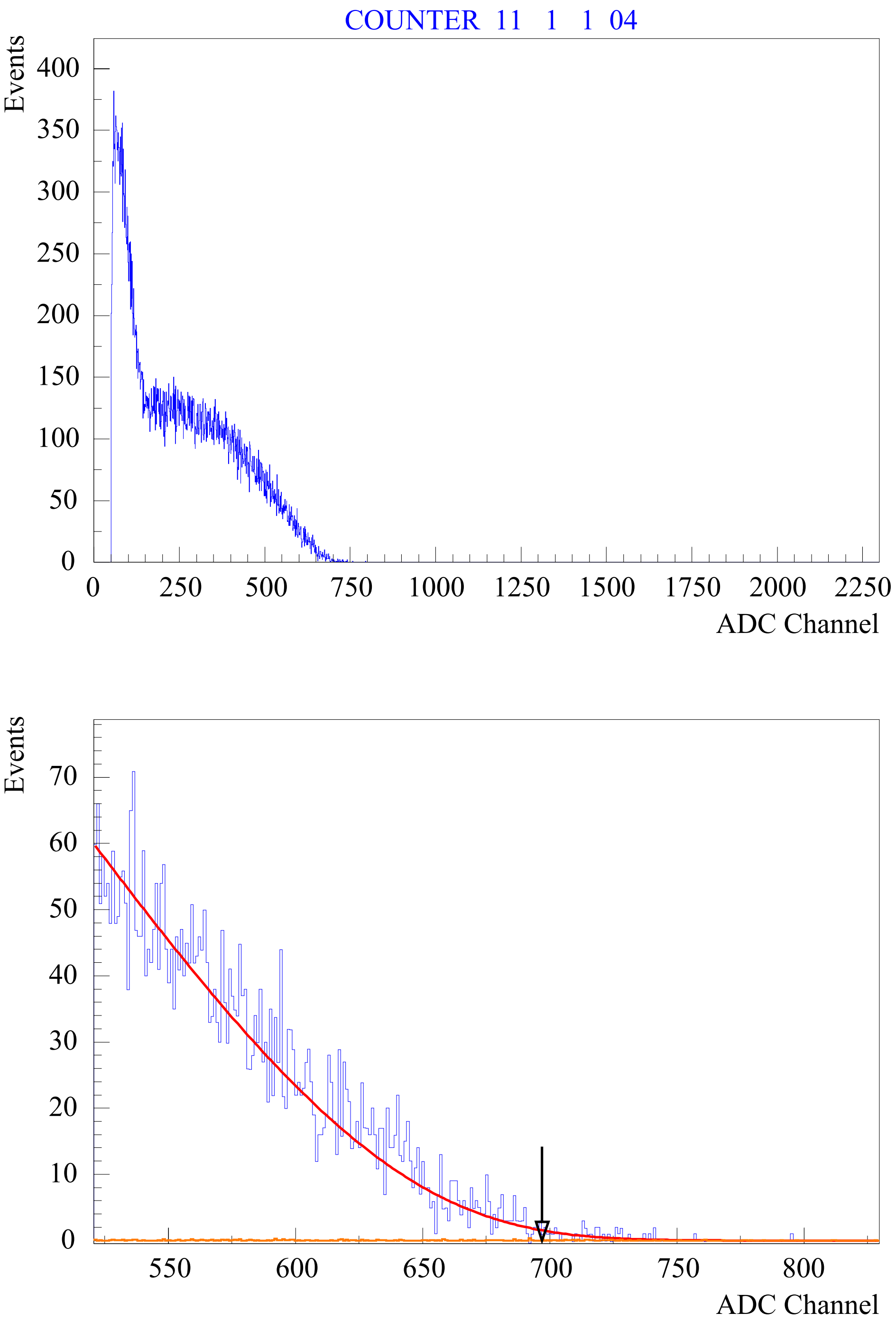

Figure 3.26: An example of beta-decay end-point adjustement (2.283 MeV) in the energy spectrum associated with $^{90}$Sr calibration sources ($\sim$ 3 keV/channel). The top of the figure shows the full spectrum and the bottom shows the fit to the high-energy tail of the spectrum, which is made with a function describing the shape of a single $\beta$ spectrum of $^{90}$Y, convolved with the energy resolution function $\sigma(E)$ and taking into account the mean energy loss of the electrons.

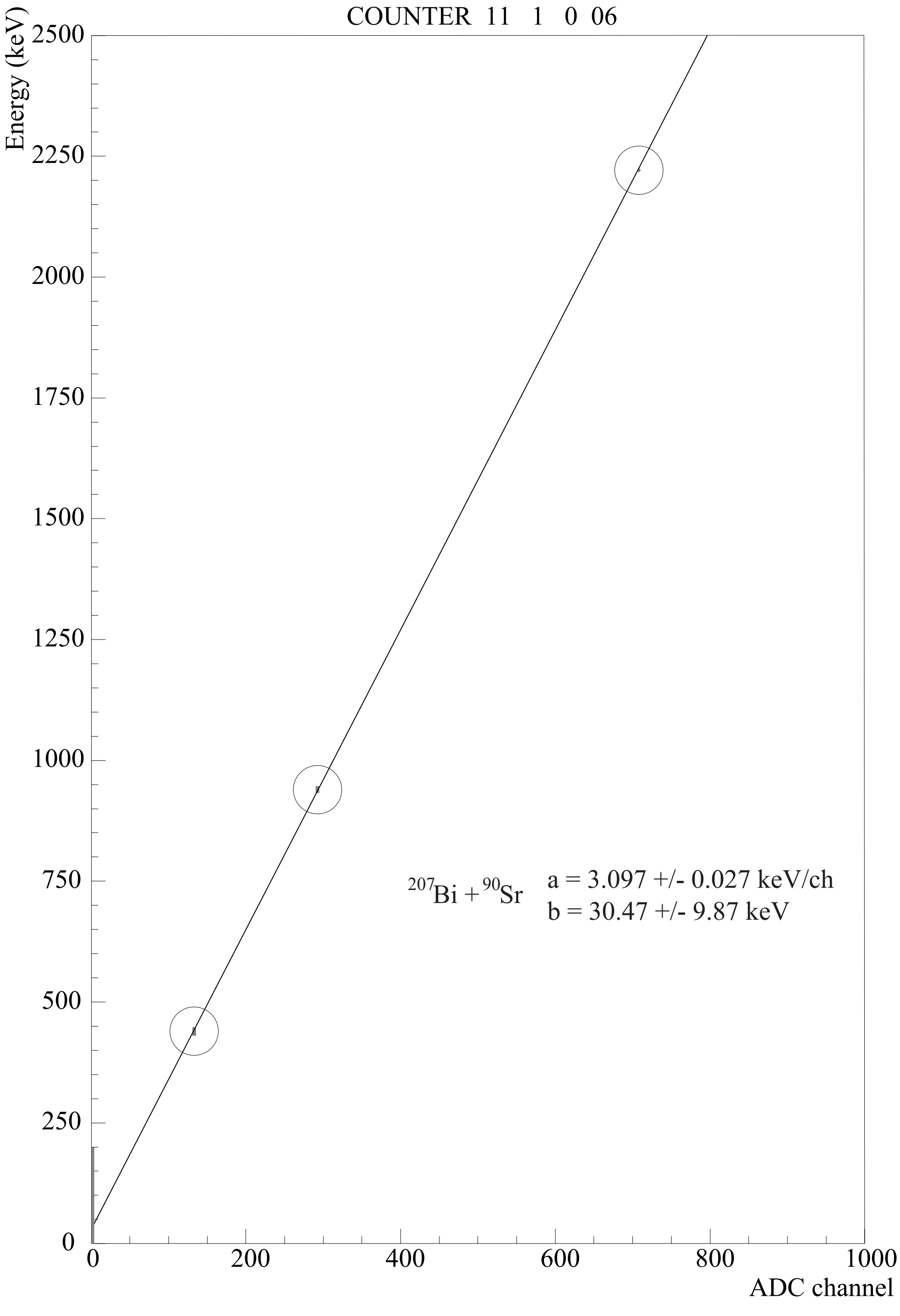

Figure 3.27: An example of the energy calibration using 3 points coming from $^{207}$Bi and $^{90}$Sr data. The calibration parameters ($a$ and $b$) of the energy-channel relation are obtained this way for each counter ($\sim$ 3 keV/channel).

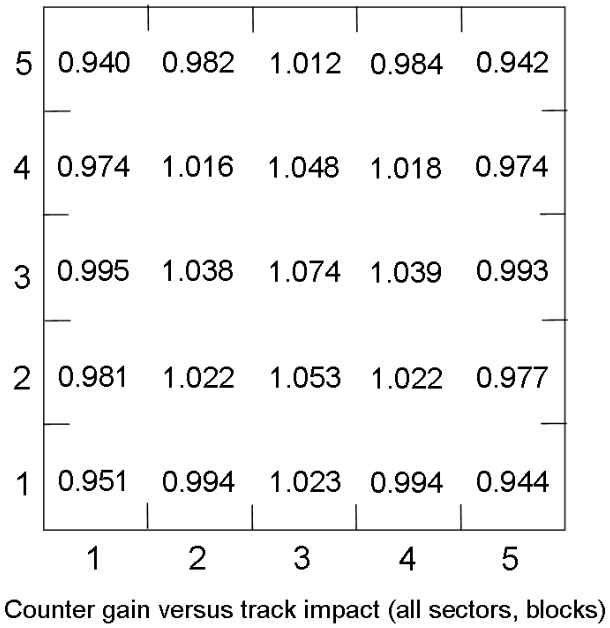

|  | 1 | 2 | 3 | 4 | 5 |
|---|---|---|---|---|---|
| 5 | 0.940 | 0.982 | 1.012 | 0.984 | 0.942 |
| 4 | 0.974 | 1.016 | 1.048 | 1.018 | 0.974 |
| 3 | 0.995 | 1.038 | 1.074 | 1.039 | 0.993 |
| 2 | 0.981 | 1.022 | 1.053 | 1.022 | 0.977 |
| 1 | 0.951 | 0.994 | 1.023 | 0.994 | 0.944 |

Counter gain versus track impact (all sectors, blocks)

Figure 3.28: Counter gains' variations for the 25 different areas for all EC external blocks. The indicated values correspond to the correction factors to apply compare to a gain of 1. Variations are from 0.940 (value in the (1,5) area) to 1.074 (value in the (3,3) area).

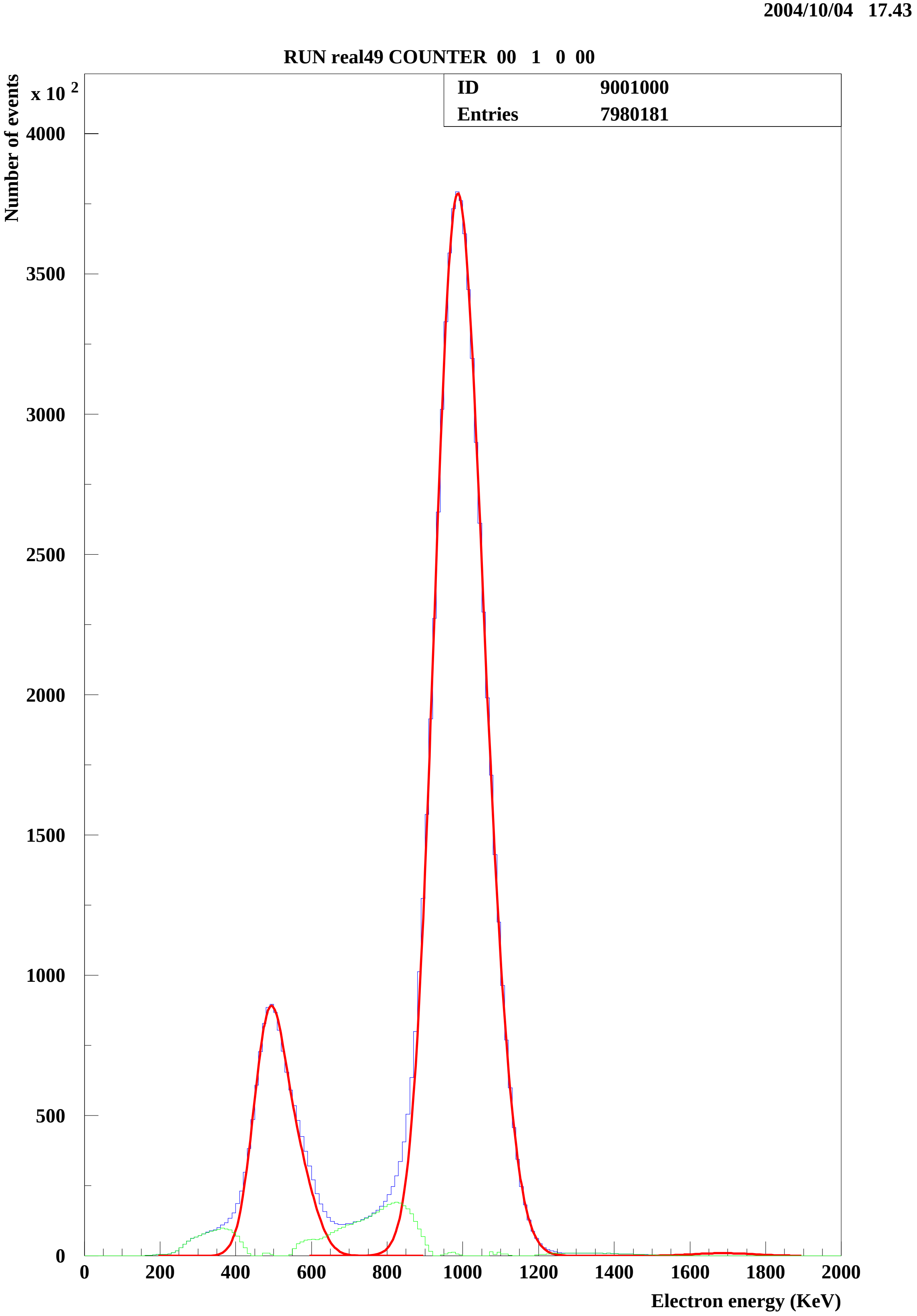

Figure 3.29: Spectral fit (in red) of the 482, 976 and 1682 keV conversion electrons coming from $^{207}$Bi decays for one counter (∼ 3 keV/channel) checked after the use of "super-corrections". In green are the subtracted background spectra.

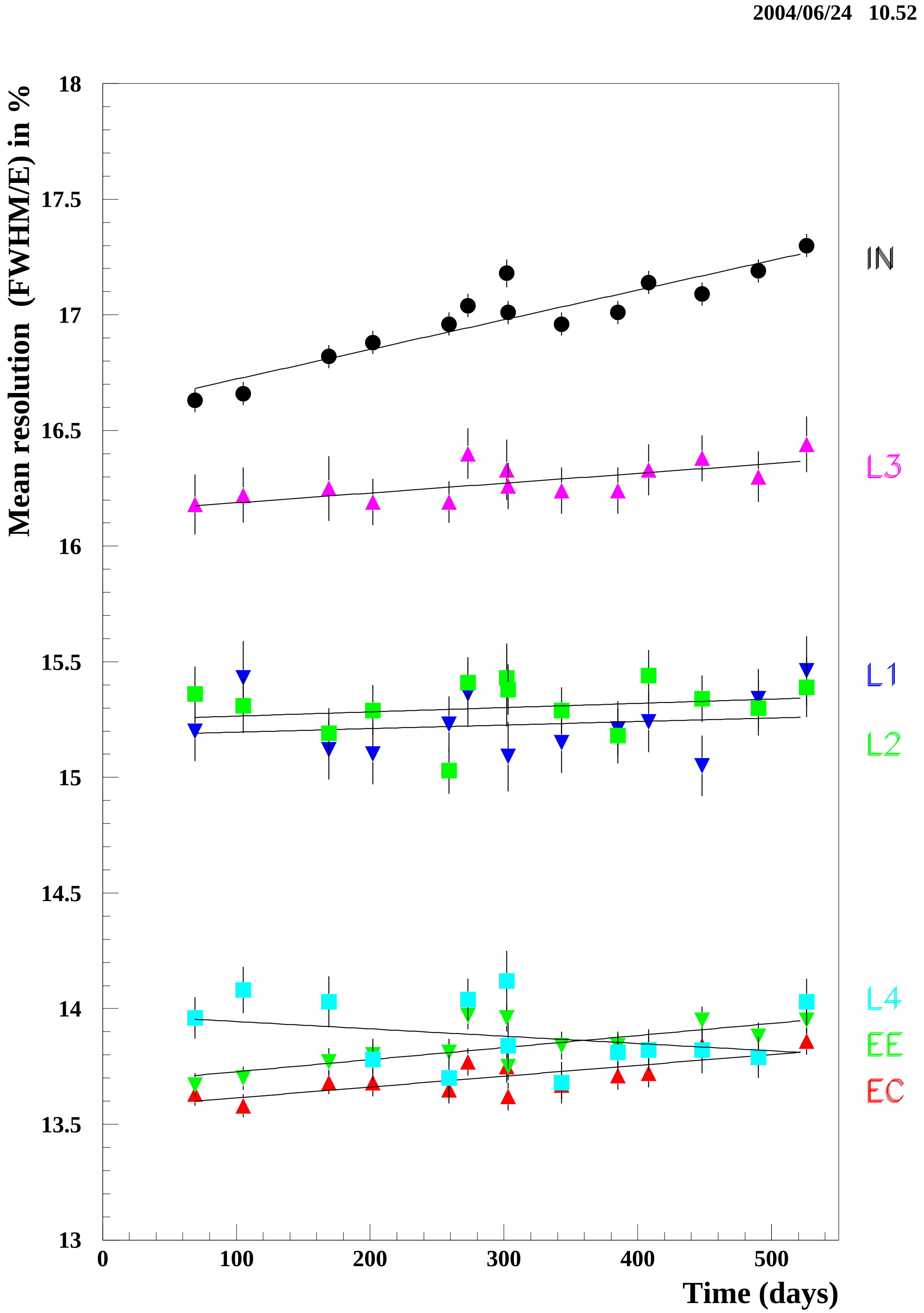

Figure 3.30: Energy resolutions (FWHM) in % as a function of time (in days) for the seven types of scintillator blocks. Except for IN blocks, which have a small increasing of their resolutions, all blocks have nearly stable resolutions values. This "aging" for IN blocks is not really understood seeing that scintillator production from Dubna, as glue, wrapping and mounting in CENBG are the same than for external EE and EC blocks, and concerning a possible PMT's aging, L1, L2 and L3 blocks are also connected to 3" PMTs and no change is visible on their resolution values.

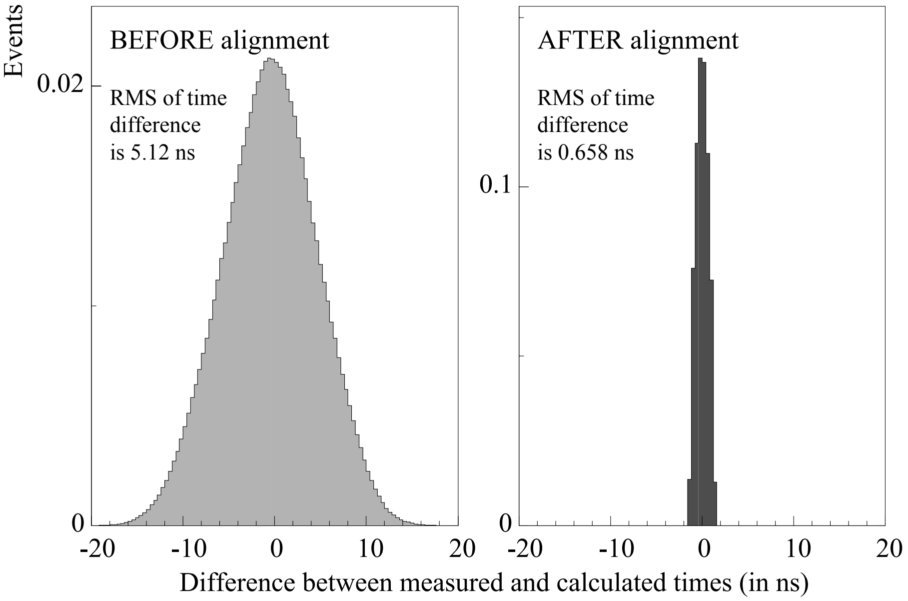

Figure 3.31 : Distribution of the arrival time difference in the counters before and after alignment with $^{60}$Co calibration sources. The distribution after alignment has an RMS of $\sim$ 660 ps (obtained with two-gamma events).

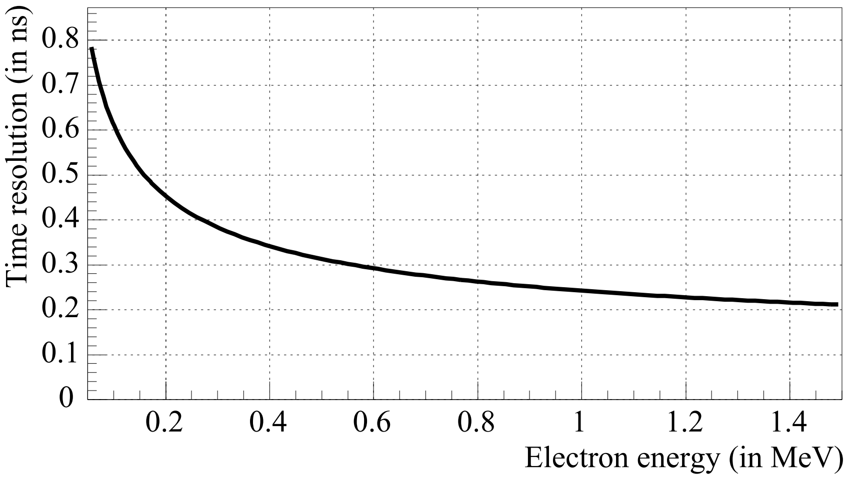

Figure 3.32 : Time resolution (in ns) as a function of the electron energy (in MeV), obtained with two-electron events.

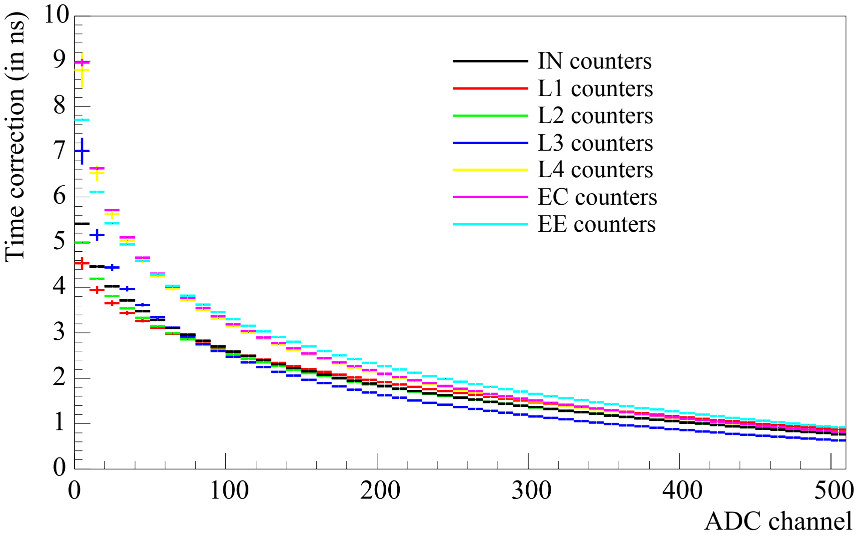

Figure 3.33: Time correction (in ns) as a function of the ADC channel for different types of counters (~ 3 keV/channel).

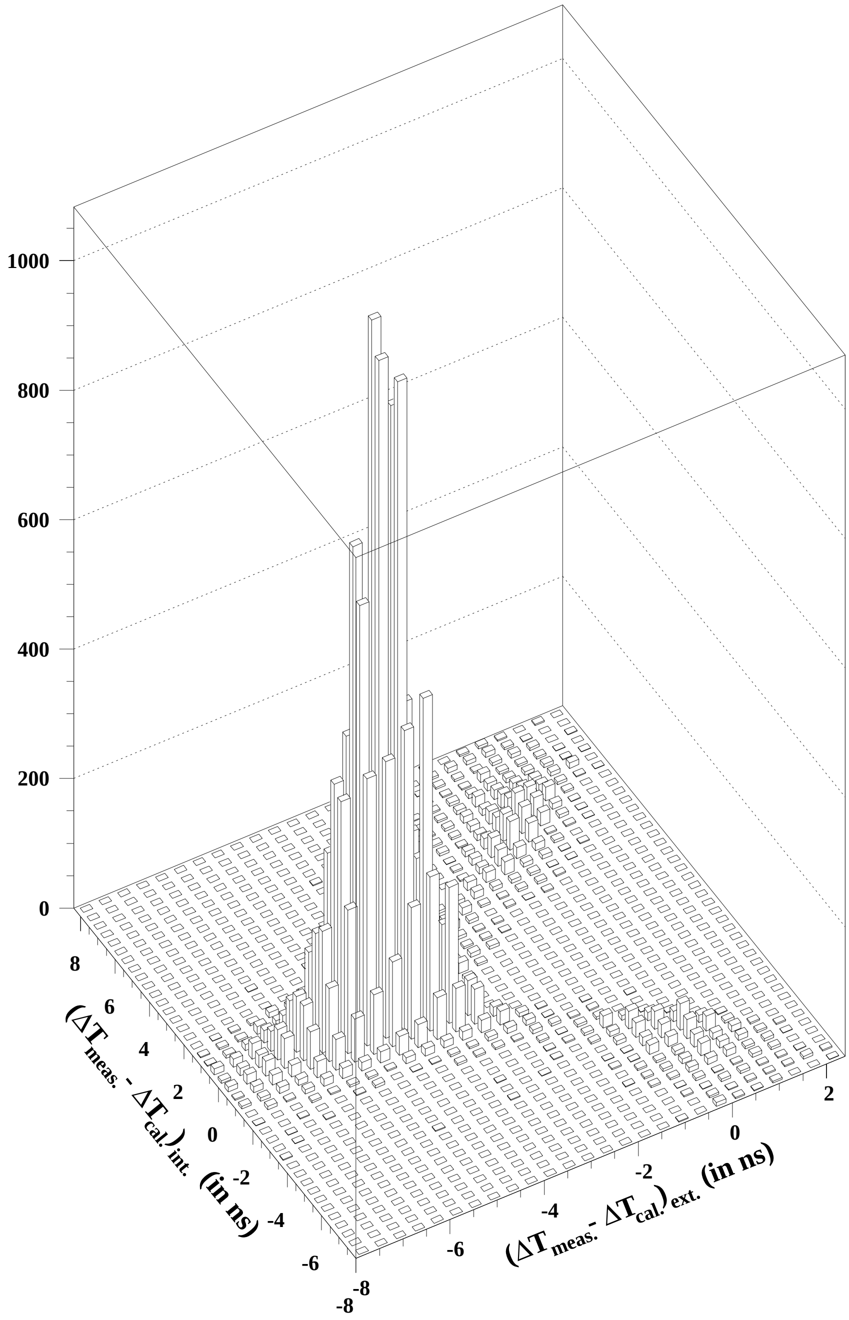

Figure 3.34 : $(\Delta T_{meas} - \Delta T_{cal})_{int}$ vs $(\Delta T_{meas} - \Delta T_{cal})_{ext}$ for two-track events from $^{100}$Mo source foils. The events located in the highest peak along the line $(\Delta T_{meas} - \Delta T_{cal})_{int} = 0$ ns (internal hypothesis) are produced in the source foils; those present in the two secondary bumps on the line $(\Delta T_{meas} - \Delta T_{cal})_{ext} \sim 0$ ns (external hypothesis) result from electrons crossing the detector. See text for more details.

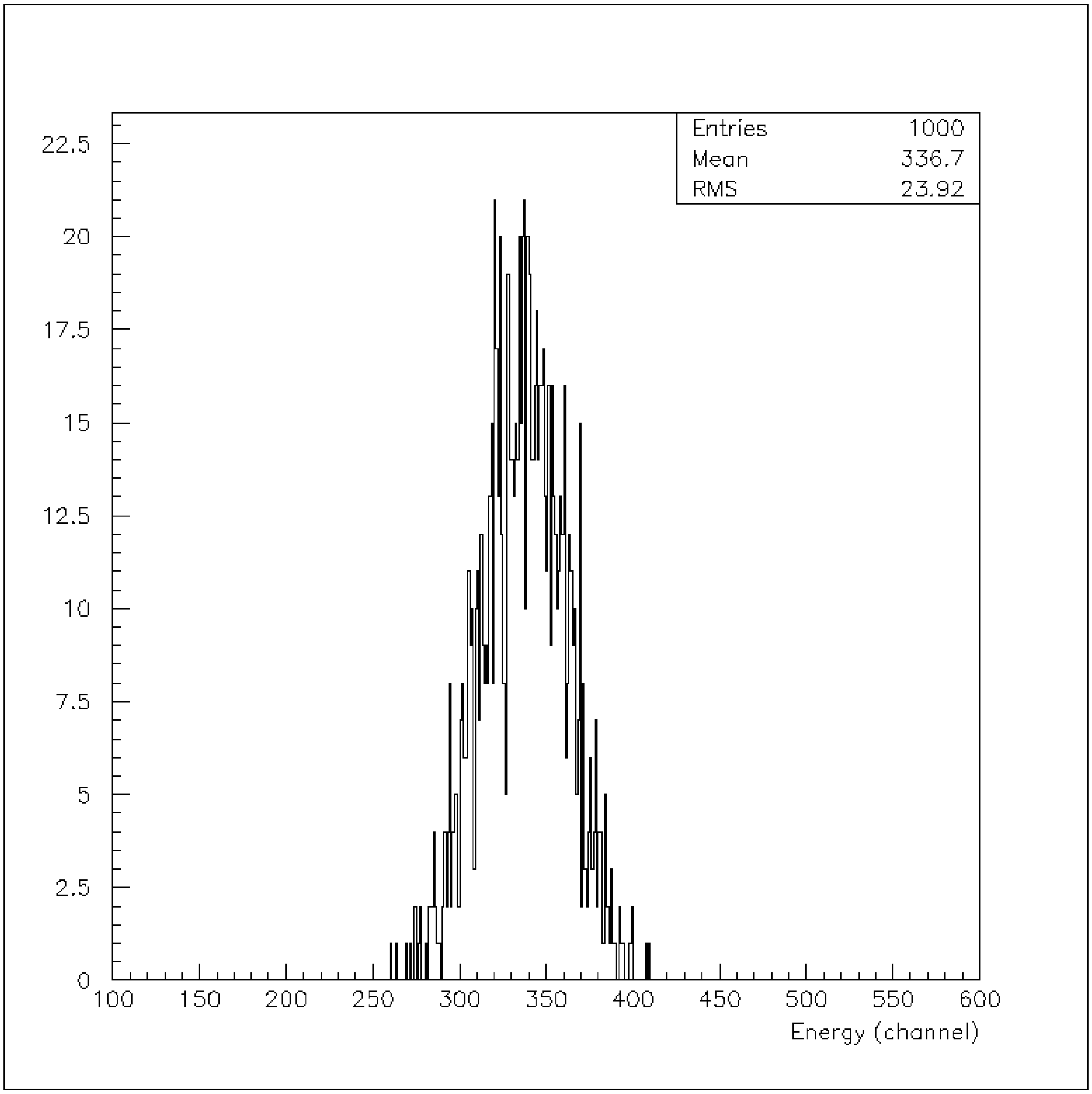

Figure 3.35: Typical laser spectrum for one counter.

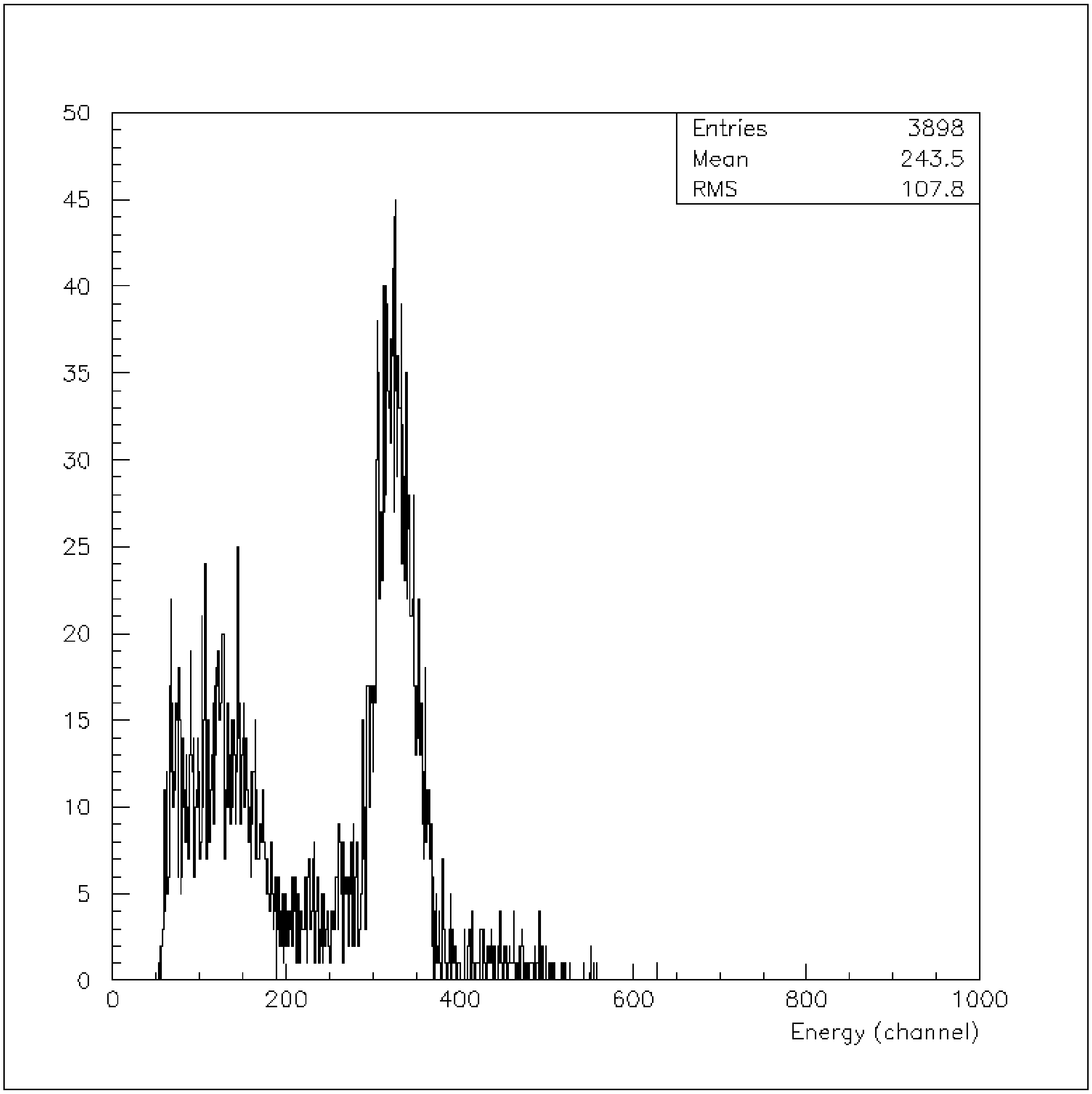

Figure 3.36 : Typical electron energy spectrum obtained during the same laser run for one counter. Electrons are coming from $^{207}$Bi decays sources put in the associated reference PMT.

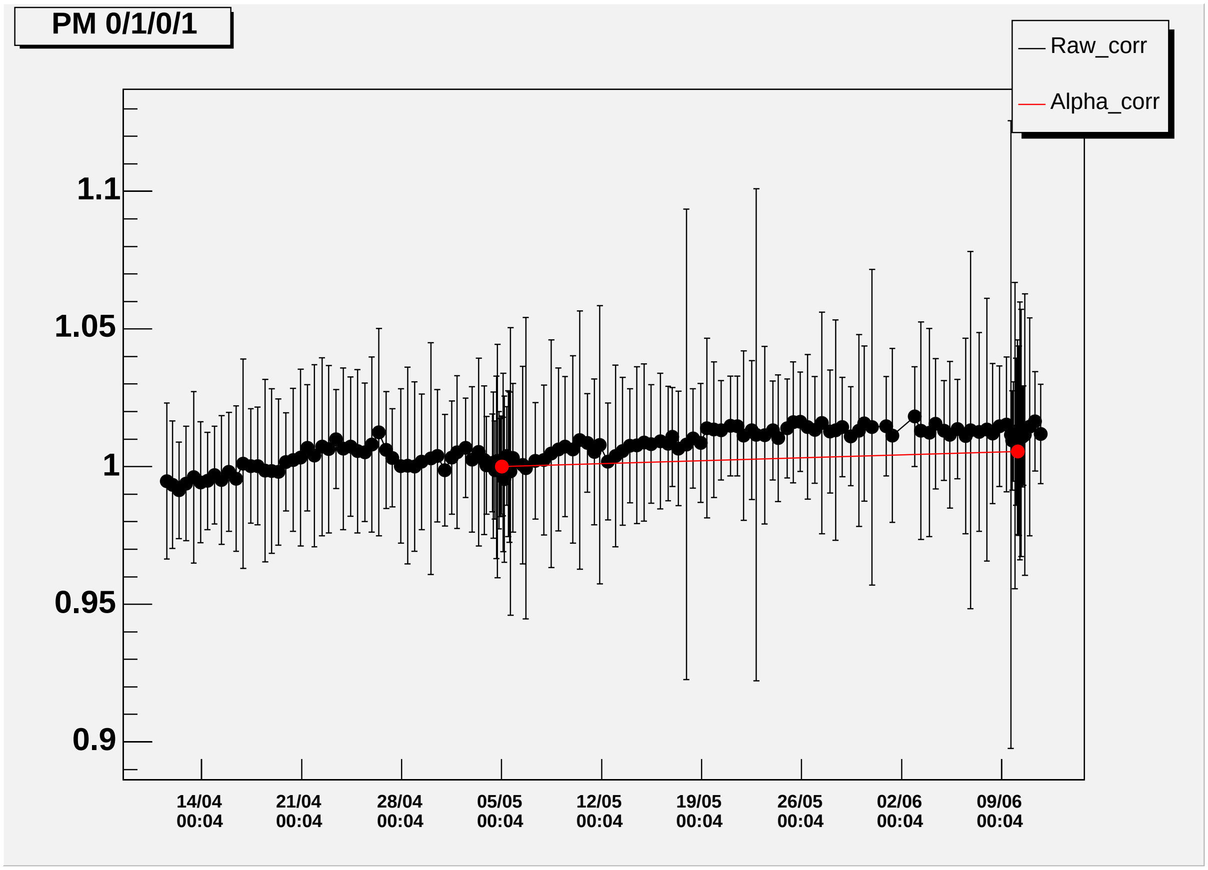

Figure 3.37 : Sample of the long term (three months) stability for the energy correction parameter $e_{corr}$. Black points correspond to the calculated laser corrections and the two red points are the value obtained from absolute calibrations with $^{207}$Bi sources [34].

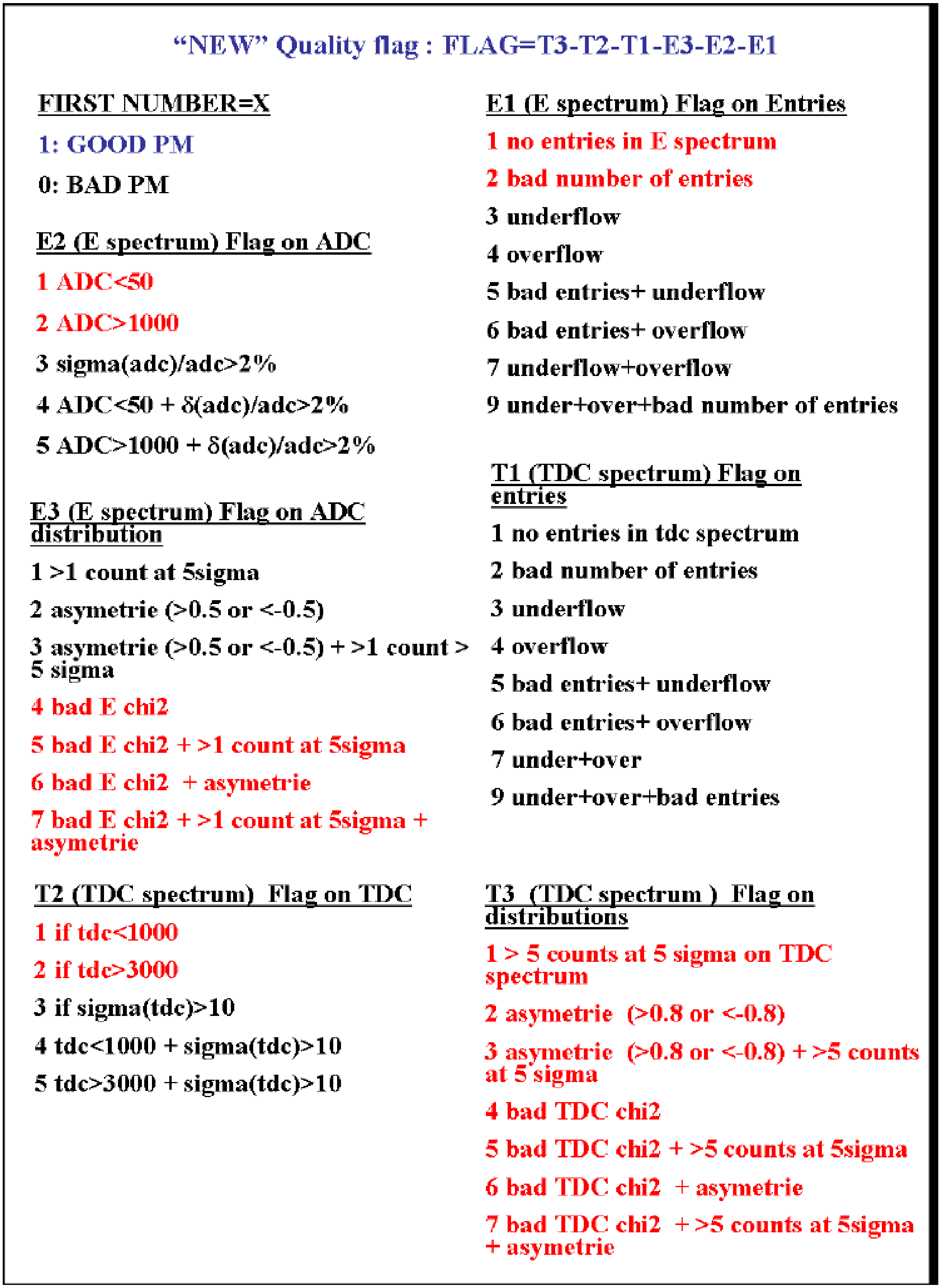

“NEW” Quality flag : FLAG=T3-T2-T1-E3-E2-E1

FIRST NUMBER=X

1: GOOD PM

0: BAD PM

E2 (E spectrum) Flag on ADC

1 ADC<50

2 ADC>1000

3 sigma(adc)/adc>2%

4 ADC<50 + $\delta$(adc)/adc>2%

5 ADC>1000 + $\delta$(adc)/adc>2%

E3 (E spectrum) Flag on ADC distribution

1 >1 count at 5sigma

2 asymetrie (>0.5 or <-0.5)

3 asymetrie (>0.5 or <-0.5) + >1 count > 5 sigma

4 bad E chi2

5 bad E chi2 + >1 count at 5sigma

6 bad E chi2 + asymetrie

7 bad E chi2 + >1 count at 5sigma + asymetrie

T2 (TDC spectrum) Flag on TDC

1 if tdc<1000

2 if tdc>3000

3 if sigma(tdc)>10

4 tdc<1000 + sigma(tdc)>10

5 tdc>3000 + sigma(tdc)>10

E1 (E spectrum) Flag on Entries

1 no entries in E spectrum

2 bad number of entries

3 underflow

4 overflow

5 bad entries+ underflow

6 bad entries+ overflow

7 underflow+overflow

9 under+over+bad number of entries

T1 (TDC spectrum) Flag on entries

1 no entries in tdc spectrum

2 bad number of entries

3 underflow

4 overflow

5 bad entries+ underflow

6 bad entries+ overflow

7 under+over

9 under+over+bad entries

T3 (TDC spectrum ) Flag on distributions

1 > 5 counts at 5 sigma on TDC spectrum

2 asymetrie (>0.8 or <-0.8)

3 asymetrie (>0.8 or <-0.8) + >5 counts at 5 sigma

4 bad TDC chi2

5 bad TDC chi2 + >5 counts at 5sigma

6 bad TDC chi2 + asymetrie

7 bad TDC chi2 + >5 counts at 5sigma + asymetrie

Figure 3.38 : Summary of the PMT flags used for calorimeter data analysis.

## 3.5 Run status

A run status code has also been developped concerning data collection since February 2003. The status, put in the NEMO 3 database, was defined to help comparing different analyses. If there is no problem, the run status is 1 and corresponds to a good run for $\beta\beta$ analysis. A bad run has a status 0. Other status values are given in Table 3.10, both with the associated problem which has been encountered. Four remarks have to be done:

- In case of status equal to 0, run has not to be used for $\beta\beta$ analysis.

- The code $10^5$ (ventillation OFF, high radon rate) is difficult to define. Thus it has been decided to add in the database for each run the real radon rate inside the detector measured with the NEMO 3 data from $(e^- \alpha\ N\gamma)$ channel.

- It is possible to use for analysis the runs, which have a status 10 or a status $10^2$, with the condition to switch off the same PMTs or Geiger cells in associated Monte-Carlo simulations.

- Run with code $10^6$ can be used if its analysis is carried out without the use of laser corrections.

| Run status | Type of problems |
|---:|---:|
| 0 | Bad run - Do not use for $\beta\beta$ analysis |
| **1** | **No problem - Good run for $\beta\beta$ analysis** |
| 2 | Good run, but trigger number is not 25 |
| 10 | Some PMTs' HV boards or PMT acquisition crates are OFF |
| $10^2$ | Some Geigers' HV boards or Geiger acquisition crates are OFF |
| $10^3$ | Less than 24 hours after calibration runs |
| $10^4$ | Less than 24 hours after general HV shutdown |
| $2 \times 10^4$ | Less than 24 hours after HV shutdown of one HV board |
| $10^5$ | Ventilation OFF - High radon rate |
| $10^6$ | No laser run for daily correction |
| $10^7$ | Less than 24 hours after acquisition crates' shutdown or electronics' shutdown |
| $10^8$ | Wrong HV value for some PMTs |
| $10^9$ | Jump of PMT HV for some HV boards due to a noisy PMT (jump of acquisition rate or acquisition time-out) |

Table 3.10: Run status associated with different types of calibration problems. Status 1 and 0 correspond respectively to good and bad runs for data analysis.

# Chapter 4

# The radon background

## 4.1 Background studies and effects on the $\beta\beta0\nu$ analysis for $^{100}$Mo

### 4.1.1 Summary of the background studies with the NEMO 3 detector

As explained in Section 1.3, a great advantage of the NEMO 3 detector is its ability to measure the different backgrounds by detecting electrons, positrons, $\gamma$-rays and delayed $\alpha$-particles in any combination with different multiplicities. Measurement values and results from this Section are those presented in Neutrino 2004 conference by the NEMO collaboration [57].

Concerning external backgrounds, contributions from $^{214}$Bi, $^{208}$Tl, neutrons and gammas have to be studied.

- Concerning external backgrounds from $^{214}$Bi and $^{208}$Tl, mainly originated from PMTs, analysis is performed in searching for $(e^-, \gamma)$ external events. Results are presented in Table 4.1 and show a good agreement with similar measurements from HPGe detectors (see Table 2.40 in Section 2.9 for comparison).

- For neutrons and high-energy $\gamma$-rays, analysis consists to search for $(e^-, e^-)$ events with an energy sum $E_1 + E_2 > 4$ MeV. Only two events have been found after one year of data collection (with $E_1 + E_2$ respectively equal to 4.253 MeV (26 March 2003) and 6.361 MeV (8 November 2003)). Another analysis with one-crossing electron events from Am-Be neutron source is presented in Section 3.1.2.

Concerning internal backgrounds, in addition to unavoidable background from $\beta\beta2\nu$-tail which depends on the half-life of the process, other background contributions to the $\beta\beta0\nu$ mode are $^{208}$Tl (located in the source foil) and $^{214}$Bi (on the foil surface or close to it in the gas) originated from the $^{222}$Rn decay chain.

- To estimate the $^{208}$Tl contamination in the source foils, events with one electron and two or three $\gamma$-rays are selected (see Fig. 3.7 in Section 3.2.2 for an example of event from $(e^-\gamma\gamma\gamma)$ channel). The TOF and high-energy cuts for electron and photon(s) are used to isolate $^{208}$Tl events from other backgrounds. The $^{208}$Tl activities in composite and metallic foils of $^{100}$Mo were found to be $115 \pm 13$ and $92 \pm 18$ $\mu$Bq/kg, respectively (90% C.L.). One can notice here that $^{208}$Tl internal contamination of $92 \pm 18$ $\mu$Bq/kg was also measured for $^{82}$Se source foils. These results are of the same order as the best limits or measurements obtained with HPGe detectors (see Table 2.38 in Section 2.2.6). The accuracy of these activities will be improved with additional data (results from Ref. [57] concern analysis of 260 days of data collection) and also after radon reduction (see next Sections).

- Estimation of the $^{214}$Bi internal contamination in the source foils is done using events initiated with one-electron track followed by one-alpha track made of delayed Geiger hits with a common vertex on the foil [63]. The associated analysis channel is called ($e^- \alpha\ N\gamma$) channel (with $N \geq 0$). It appeared that most of the $^{214}$Bi decays came from the decay of **radon** $^{222}$Rn inside the tracking chamber, which is due to a low level of diffusion inside the detector from the laboratory air, which has an activity level of $\sim$ 20 Bq/m$^3$ (as shown in Section 4.1.2).

  It has also been established that the radon penetrated in the detector by diffusion through the joint in RTV glue between sectors[64]. Fig. 4.1 presents this analysis, for ($e^- \alpha\ N\gamma$) events coming from $^{222}$Rn deposited on the source foil surface or in the tracking detector gas volume (supposing an uniform radon deposition on the wires). As a result of this analysis, around 200 counts per hour were measured. It has been shown that the radon which enters the detector is mainly deposited on the wires and leads to a total radon activity of $\sim$ 0.95 Bq (mean value between February 2003 and September 2004) in the gas volume of the tracking chamber, that means around 20-30 mBq/m$^3$.

  Note that the NEMO 3 trigger rate is also correlated to the radon level inside the detector. There are two contributions, the first one coming from radon present in the air inside the shields and producing decays by Compton effect in scintillators, the second one, which has a delay of around 2.6 days (see Section 4.2.4), coming from radon leaking into the gas volume of the tracking chamber, producing $\beta\gamma$ events from $^{214}$Pb and $^{214}$Bi decays. From mid-February 2003 to May 2004, the NEMO 3 trigger rate was between 6.9 Hz and 7.8 Hz.

In conclusion, at this analysis level, it was impossible to check specifications on the internal $^{214}$Bi contamination of the source foils ($<$ 300$\mu$Bq/kg for $^{100}$Mo) with the NEMO 3 detector because the dominant background is clearly the radon in the gas.

| Isotope | Activity (in Bq) from ($e^-$, $\gamma$) |
|---|---|
| $^{208}$Tl (PMTs) | $\sim$ 40 |
| $^{214}$Bi (PMTs) | 302 |
| $^{40}$K (PMTs) | $\sim$ 2040 |

Table 4.1: External background activity measurements obtained with ($e^-$, $\gamma$) external events' analysis. Note that $^{214}$Bi activity value is fixed at its result value from HPGe measurement.

### 4.1.2 Development of a high-sensitivity radon detector

#### 4.1.2.1 Principle of the radon detector

In order to measure the radon level in the NEMO 3 detector with an independant method, two identical high-sensitivity radon detectors, which are electrostatic collection units, were build by our Japanese collaborator with the same designed than those used for the SuperKamiokande experiment [58]. The principle of radon detection which is used in these detectors is the electrostatic collection of the positively charged daughter nuclei of $^{222}$Rn (for example, 90% of $^{218}$Po daughter

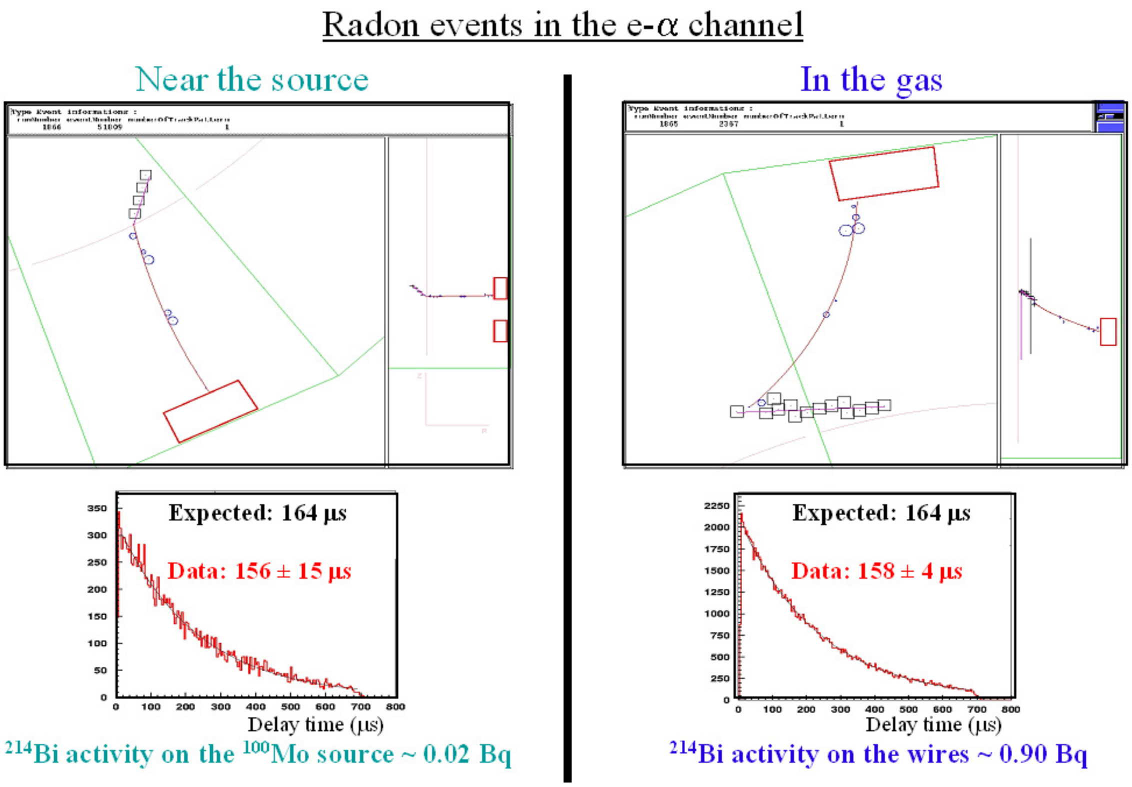

Figure 4.1: Study of events coming from radon decays using ($e^-\alpha\ N\gamma$) channel. Comparison is done between events near the source foils (left part) and events in the gas, which correspond to a $^{214}$Bi activity on the cells' wires (right part). Measurement of decay periods for these events, which is nearly 164 $\mu$s, ensure the correspondance with $^{214}$Bi decays. As a result of this analysis, the radon which enters the detector by diffusion is mainly deposited on the wires and leads to an activity of $\sim$ 0.9 Bq in the gas volume of the tracking chamber, that means around 20-30 mBq/m$^3$.

atoms tend to become positively charged). Thus the radon detector collects these daughter nuclei in the gas using an electrostatic field. Energy measurement of the alpha ray is carried out with a PIN photodiode.

Fig. 4.2 shows a schematic view of the radon detector. It consists of a cylindrical stainless steel vessel, a PIN photodiode, a high-voltage divider and amplifier circuit, and a feed through. A negative high-voltage of $-1500$ V is supplied to the p-layer of the photodiode. The vessel is grounded. Then, an electric field is produced in the vessel. The daughter nuclei which ionized positively are collected on the surface of the photodiode, then the energy of alpha decays are measured.

The dimensions of the stainless steel vessel are 50 cm in diameter and 35 cm in height. The volume is 68.7 l. In order to achieve a low background level, the inside of the vessel is electropolished. The PIN photodiode, which is a Hamamatsu Photonics S3204-06-SP with passivation finish, is electrically isolated from the vessel with an acrylic plate and a ceramic feed through.

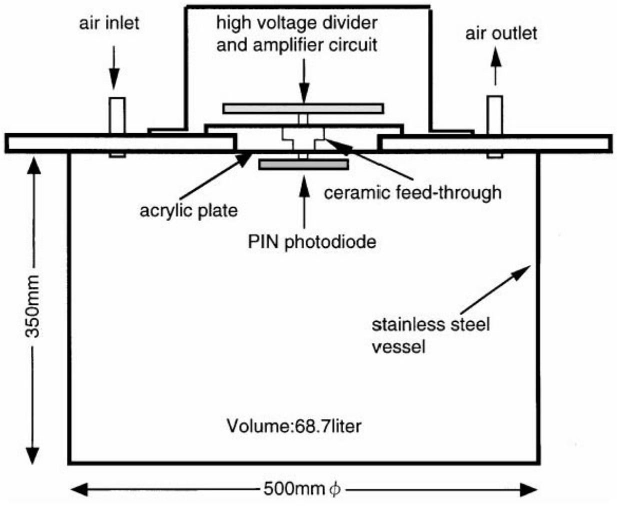

Figure 4.2: A schematic view of the high-sensitivity radon detector.

The glass cover plate is removed to measure the energy of $\alpha$-particles. The detection area, sensitive thickness, and capacity are 16 mm × 16 mm, 500 $\mu$m, and 80 pF, respectively. A typical energy spectrum in LSM air is shown in Fig. 4.4. In order to measure radon activity, only the $^{214}$Po peak ($E_\alpha = 7.7$ MeV) is used because that energy region has fewer noise events, no other alpha peak overlapped, and it has a higher energy collection efficiency than $^{218}$Po. This is due to the fact that some of the $^{218}$Po ions are collected on the PIN photodiode surface, so $^{214}$Po daughter ions have an higher probability to be detected.

Concerning the two radon detectors, one is called "NEMO" and the second is called "Ge", because the first one was used mainly for measurements of radon inside NEMO 3 (at the gas input or output) and the second one was used in a first period in the HPGe detectors' room [65]. The "NEMO" radon detector had some hardware problems but its functioning is good since July 2004. Absolute calibration is not realized for this detector. There is just an estimation of the calibration from SuperKamiokande measurements.
The "Ge" radon detector has a good functioning (except a gain drift since October 2004). Since end of June 2004, peak measurements are realized every three hours, which is enough for decay constants' measurements and for the number of measured counts. From calibration of this detector, 1250 counts in 3 h corresponds to 10 Bq/m$^3$.
There are difference between calibrations of the two detectors for the same level of radon

$$\frac{NEMO}{Ge} \sim 1.4 \tag{4.1}$$

which produce some difficulties to compare measurements from the two detectors. Thus results presented in this report are given when all associated measurements has been realized with the same radon detector.

Figure 4.3 : Picture of one radon detector.

#### 4.1.2.2 Measurements of the radon present in the air laboratory

In the LSM, air in the laboratory renewed two times per hour with fresh air from the tunnel ventilation system. Thus the radon activity in the laboratory air is due to both the radon activity in fresh air and the radon outgasing in the laboratory [65].

This radon rate is extremely variable, depending on the period of the day and of the week, and it is strongly correlated to the tunnel ventilation. Measurements realized between May and July 2004 using the two radon detectors showed the radon activity in the laboratory was $\sim 18$ Bq/m$^3$ in average, that means around 7 Bq/m$^3$ higher than the radon activity in fresh air, which was $\sim 11$ Bq/m$^3$ in average.

#### 4.1.2.3 Measurements of the radon present in the gas coming from the NEMO 3 detector

In a mixture gas of helium with 4% of ethyl alcohol, the energy collection efficiencies of the radon detectors are divided by a factor 10 for $^{218}$Po and a factor 3 for $^{214}$Po respectively compare to measurements in pure helium. This is an another reason for using only $^{214}$Po peak ($E_\alpha$ = 7.7 MeV) to measure radon activity. Addition of argon and water in the NEMO 3 gas mixture did not change these efficiencies.

One of the radon detectors was used for measurements at the NEMO 3 detector's gas inlet and outlet in 2002 and 2003. No significant level of radon was found at the exit of the gas system, before the NEMO 3 detector gas input (around 2 counts/day, which is the background level). Nevertheless, around 15-20 counts/day were found at the gas exit of the detector, correspond-

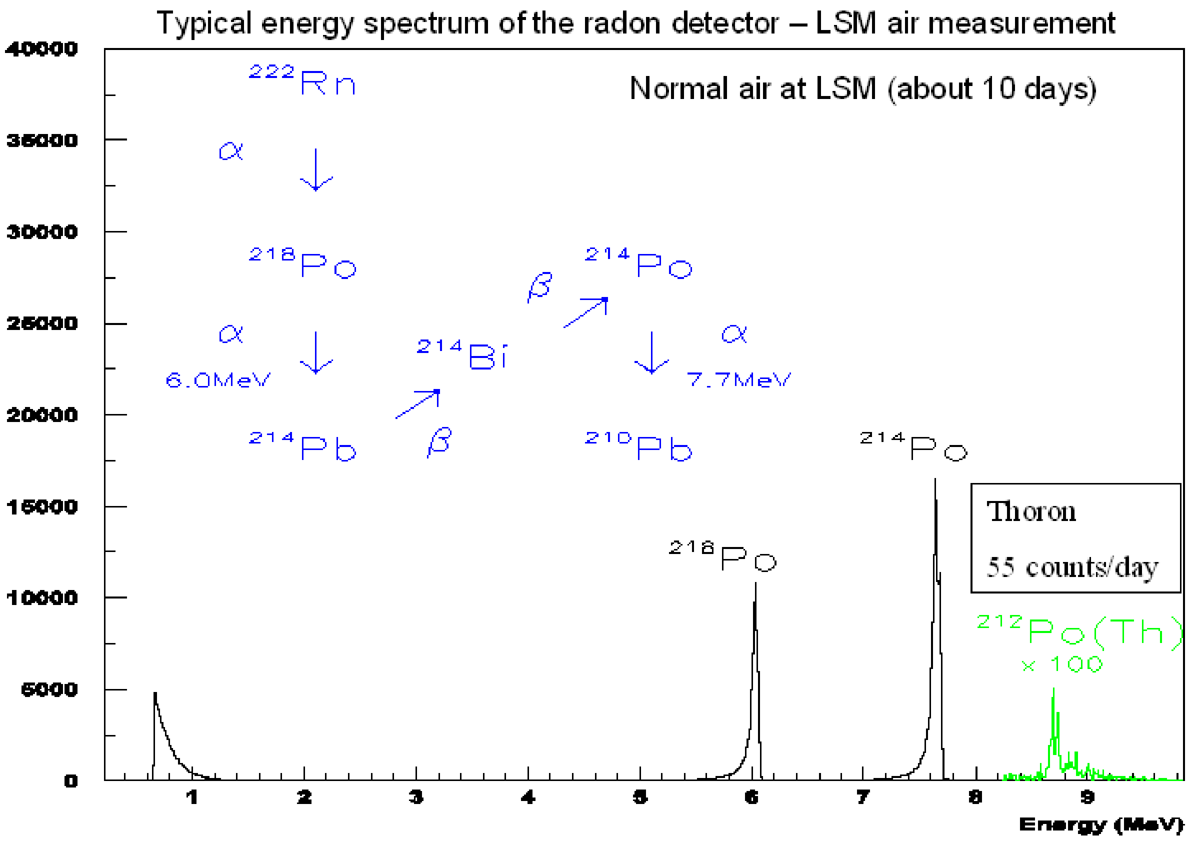

Figure 4.4 : Typical energy spectrum for alpha particles from radon and thoron daughter products measured for normal air at LSM during 10 days using one of the radon detectors. Alpha peaks of 6.6 and 7 MeV corresponding respectively to $^{218}$Po and $^{214}$Po decays from radon are clearly seen in this figure. For comparison, amplitude of the alpha peak associated $^{212}$Po decays from thoron is multiplied by a factor of 100.

ing to a radon activity inside NEMO 3 of 20 mBq/m$^3$, which confirmed the need of a radon purification facility.

### 4.1.3 Effects of the backgrounds on the $\beta\beta0\nu$ window

#### 4.1.3.1 Two-electron events' selection

Using energy and time calibrations presented in Section 3.4, associated to track reconstruction as defined in Section 3.3.3, the criteria used to define a two-electron event are finally:

- Two tracks, each with curvature associated with negative charge
- Two fired PMT, each with energy greater than 200 keV
- Geometrical association between the fired PMT and the reconstructred track
- Common vertex for the two tracks, for both $\Delta R\phi$ and $\Delta Z$

- TOF corresponding to the internal hypothesis to ensure external event rejection
- No other isolated PMT to reject presence of $\gamma$-ray
- No delayed track or delayed hit near the two-electron vertex, for $^{214}$Bi rejection.

With these defined criteria the number of real two-electron events is one each 2.5 minutes.

#### 4.1.3.2 Backgrounds in the $\beta\beta0\nu$ energy window

Using background studies as explained in Section 4.1.1, the number of expected events in the $\beta\beta0\nu$ energy window, between 2.8 and 3.2 MeV for $^{100}$Mo and $^{82}$Se, is summarized below for each type of backgrounds.

- Concerning external $^{214}$Bi and $^{208}$Tl, the expected number of $\beta\beta0\nu$-like events is negligible, $\lesssim 10^{-3}$ counts.kg$^{-1}$.yr$^{-1}$ in the [2.8 - 3.2] MeV window.
- External backgrounds from neutrons and high-energy $\gamma$-rays are also negligible, producing $\lesssim 0.05$ counts.kg$^{-1}$.yr$^{-1}$ in the [2.8 - 3.2] MeV window (see also Section 3.1.2).
- Impurities from $^{208}$Tl inside the $^{100}$Mo source foils give an expected number of $\beta\beta0\nu$-like events of $\sim 0.1$ counts.kg$^{-1}$.yr$^{-1}$ in the $\beta\beta0\nu$ energy window.
- The expected level of background due to the tail of the $\beta\beta2\nu$ spectrum in the [2.8 - 3.2] MeV window is $\sim 0.3$ counts.kg$^{-1}$.yr$^{-1}$ .
- Finally, concerning the dominant background which is the radon present inside the tracking chamber of the NEMO 3 detector, remember that two measurements were performed, the first one with the dedicated radon detector using gas at the outlet of the NEMO 3 detector, and the second one using NEMO 3 analysis of the ($e^- \alpha\ N\gamma$) channel (with $N \geq 0$). Both measurements are in agreement and gave a typical value for the $^{222}$Rn activity of $\sim 20-30$ mBq/m$^3$ inside NEMO 3, but it has been demonstrated that analysis of ($e^- \alpha\ N\gamma$) channel is the most sensitive method to measure the radon activity inside the NEMO 3 detector. This value corresponds to an expected level of background of $\sim 1$ count.kg$^{-1}$.yr$^{-1}$ in the $\beta\beta0\nu$ energy window. That means the radon is clearly the dominant background, with a factor $\sim 10$ too high to reach the expected $\beta\beta0\nu$ sensitivity. To reduce this radon level, the NEMO collaboration decided to build a radon-free air installation.

Finally, in the energy window [2.8 ; 3.2] MeV, the expected background was $7.0 \pm 1.7$ after 265 days of data collection and 8 events have been observed for $^{100}$Mo [57]. Thus the data are in agreement with the radon simulation.

## 4.2 Radon purification facility for NEMO 3

As explained above, it is needed to remove the radon inside the detector by at least a factor 10. Analysis have shown that radon enters the detector by diffusion through the joint in RTV glue between sectors and is coming from the air of the laboratory, which contains radon at a level of $\sim$ 20 Bq/m$^3$. The diffusion through RTV already produces a radon reduction by a factor $\sim 500 - 750$ as the level of radon measured in the gas of the detector is $20 - 30$ mBq/m$^3$. The chosen solution to avoid this radon contamination inside the detector is to install an airtight tent which fully encloses the NEMO 3 detector with an internal atmosphere purified in radon at a level one hundred times lower than the air of the laboratory. To obtain this free-radon air, a radon-reduction system is needed. The choice has been made to build a radon trapping facility using charcoal providing a continuous flow of air with a level of radon less than 0.2 Bq/m$^3$. In this purpose it has been studied the type of trapping for radon and the feasibility of a full scale radon purification factory, based on the system developped for the SuperKamiokande experiment [59].

### 4.2.1 The airtight tent

In the begining of 2003, the NEMO collaboration decided to build an airtight tent to fully enclose the whole detector and electronics in order to allow the entrance of only the free-radon air from the facility, as well to isolate the detector from laboratory's air.

Before the installation, the laboratory ground was covered with low radioactivity Epoxy paint.

The tent has a metallic structure in steel covered with ten facets. The first floor of the tent is composed of aluminium and plexiglas windows. The second floor is covered with double sheets of polyethylene, 200 $\mu$m thick, which allow the pumping between the two sheets. The roof is made of iron plates with eight outlets which contain filters and 200 mm of active charcoal each to avoid air-back (see Fig. 4.5).

### 4.2.2 Influence of helium in PMTs

Helium migrates into the PMTs through their glass, affecting their performances. Moreover, the radon purification facility and especially the airtight tent have increased helium concentration in PMTs[1]. Thus, a study has been realized [60] to check what helium concentration was tolerable for five years of data collection.

Using for helium pressure in air $5.2 \times 10^{-6}$ P$_{atm}$ and in the worst case scenario, a NEMO 3 PMT exposure to helium of $5 \times 10^{-4}$ P$_{atm}$ during five years of data collection correspond to the same behavior than a PMT exposure during 22 hours in pure He. Other experiments studies [61] showed helium takes 30-50 days to migrate through the glass. The method chosen by the collaboration to check the influence of helium was to put a PMT in pure helium for 22 h and to monitor its response for a few months to see possible variations of quantum efficiency, gain, afterpulsing and energy resolution. All these tests were realized by UCL collaborators [60].

The PMT used for this study is a NEMO 3-like 5" one with scintillator, at HV = 1450 V. Signals from a $^{60}$Co radioactive source were obtained via NIM/CAMAC based DAQ. Afterpulses were studied with a digital oscilloscope and found to be 3-4% due to accidentals (see an example in Fig. 4.6).

---

[1] The increasing factor was at most ten before the opening of the tent's doors and it is now a factor three in average

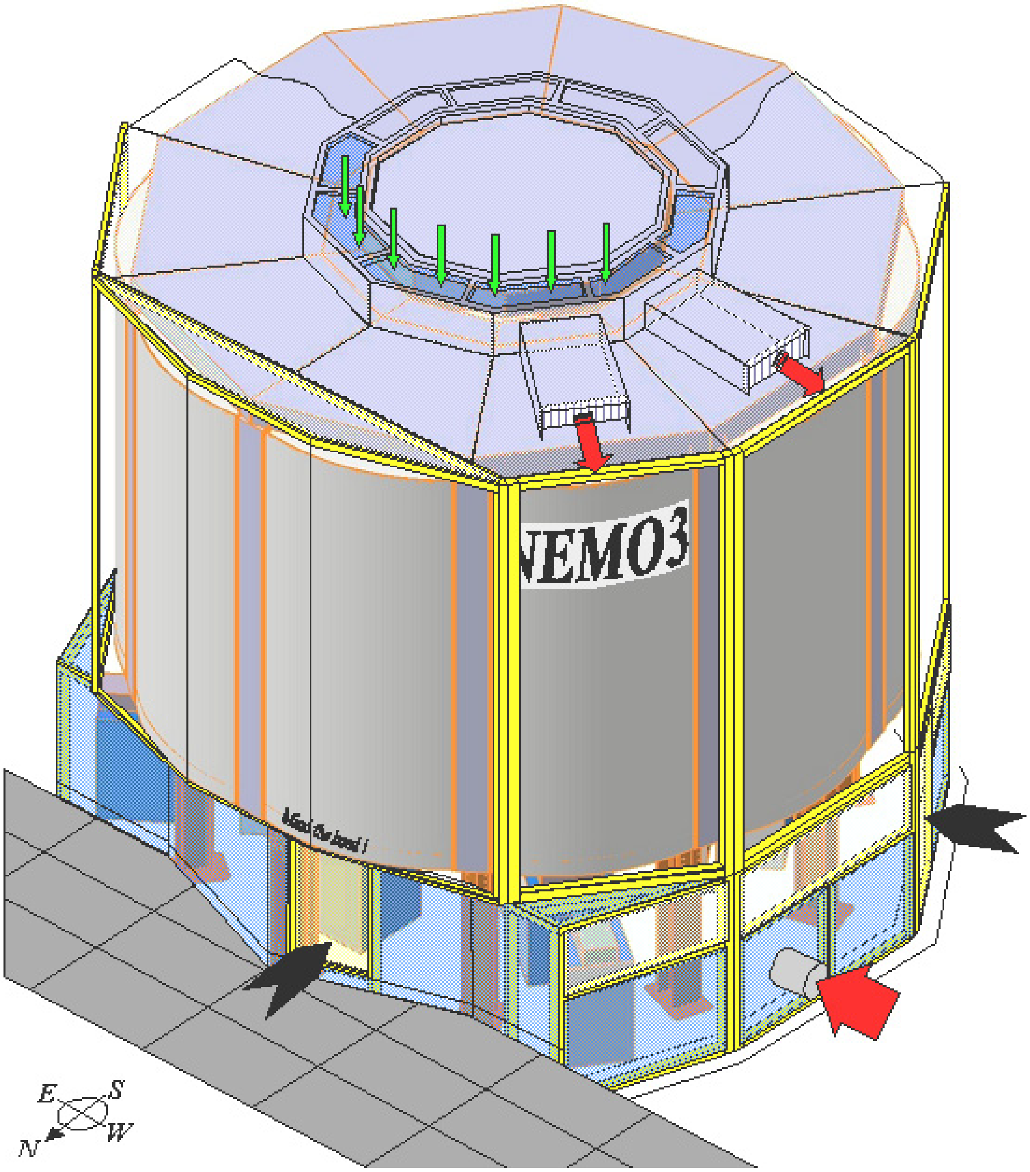

Figure 4.5: A schematic view of the airtight tent surrounding the NEMO 3 detector. Note that the lower part of the tent, which enclosed the electronics, is now removed to avoid radon degassing from electronics. Also the radon-free air is sent inside the tent by the iron roof and finally the outlets are now closed.

The 5" PMT was put in immersion in pure helium the 5 August 2003, removed after 22 hours and monitored since. For this report, the last measurement used was done in November 2004, that means 416 days after immersion.

An example of afterpulse signal 216 days after immersion is given in Fig 4.7. After 465 days, the afterpulsing rate is stabilized at 80-85%, as it can be shown in Fig. 4.8, which presents evolution of afterpulses' rate as a function of time.

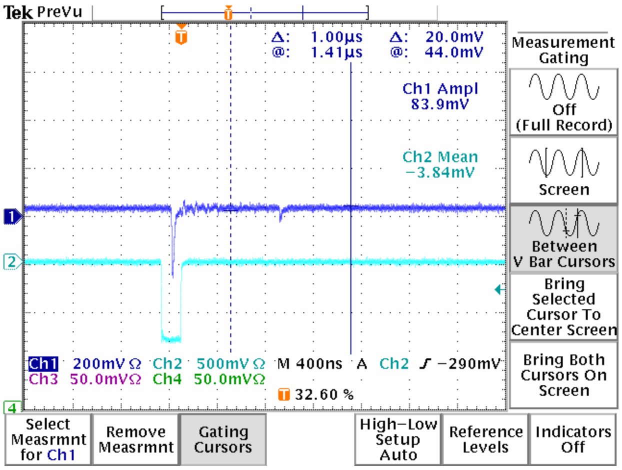

Figure 4.6: Example of afterpulse signal as measured with digital oscilloscope.

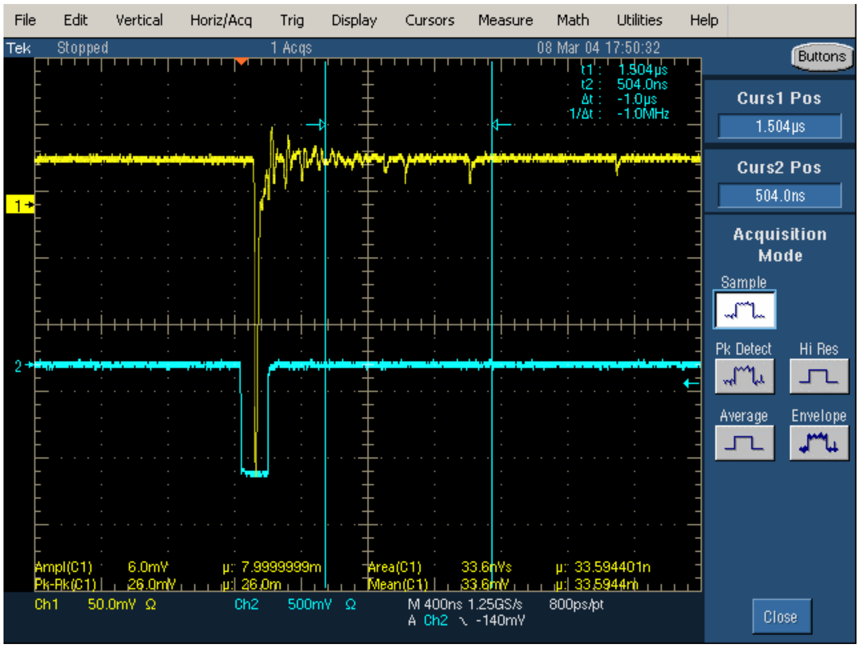

Figure 4.7: Afterpulses 216 days after immersion.

In conclusion of these measurements during 465 days after immersion during 22 hours in pure helium, there is no significant effect on $^{60}$Co spectra (see Fig. 4.9) obtained after discriminator's threshold correction, which allows to check 1% (absolute) resolution effects from Helium.
Thus there is no significant change in more than one year of monitoring. There is no apparent change in gain nor in $QEtimesCE$ (for both 165 and 70 ns integrating windows).
Afterpulses' spectrum looks like widened pedestal and there are in average four afterpulses per signal, with amplitude around 20-40 keV, which may cause higher single trigger rates.

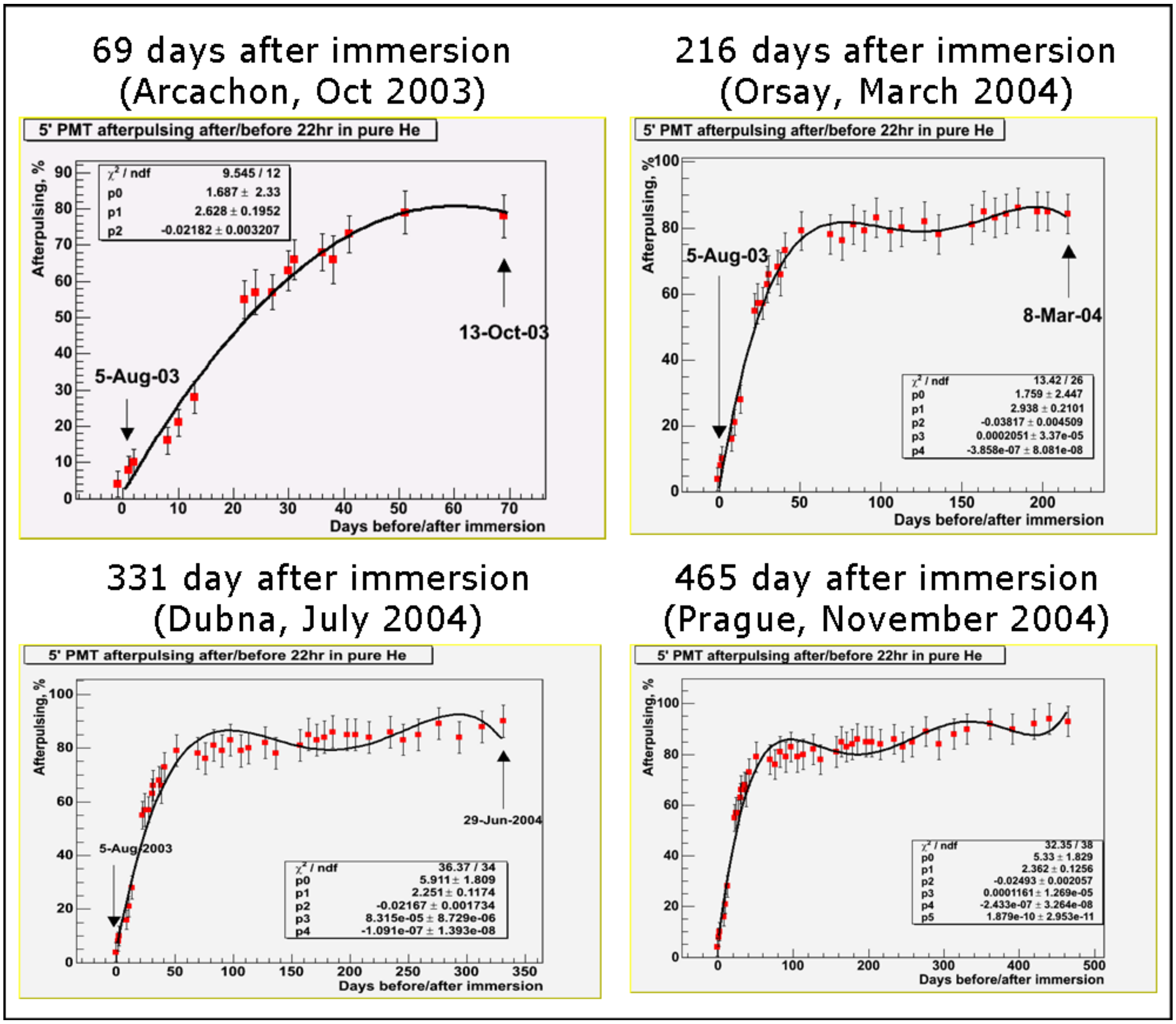
69 days after immersion (Arcachon, Oct 2003)

216 days after immersion (Orsay, March 2004)

331 day after immersion (Dubna, July 2004)

465 day after immersion (Prague, November 2004)

Figure 4.8 : Evolution of the afterpulsing rate: results are given for respectively 69, 216, 331 and 465 days after immersion. There is a stabilization at ∼ 90%.

The next tests to do are to repeat this test in a mixture containing 70% of air and 30% of He with a new 5" PMT and to check afterpulsing in LSM for comparison with laboratory results. First tests with a 3" Hamamatsu PMT in November 2004 showed afterpulsing rate at around 40% before immersion in helium. Thus a new 3" Hamamatsu PMT is needed to check this afterpulsing rate and conclude if it is connected to a bad PMT or due to a normal behavior for this type of 3" PMTs.

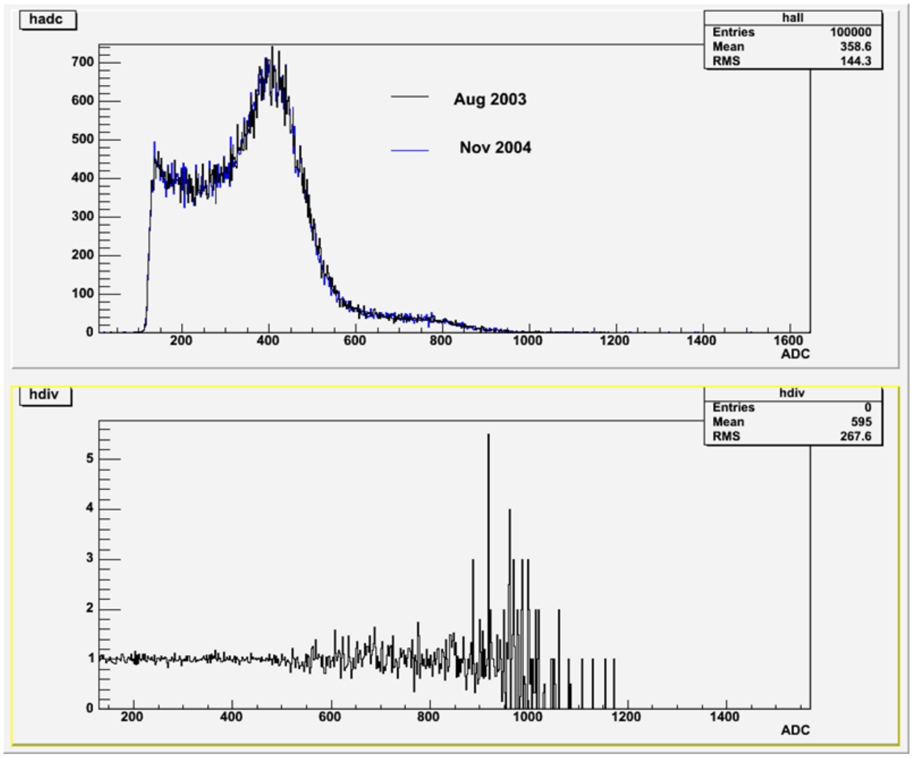

Figure 4.9 : Comparison between $^{60}$Co spectra before immersion and after 465 days. The agreement is always very good.

## 4.2.3 The radon trapping facility [66]

### 4.2.3.1 Principle of radon trapping

Radon trapping is basically done as for other atoms or molecules by using a charcoal trapping (see Fig. 4.10).

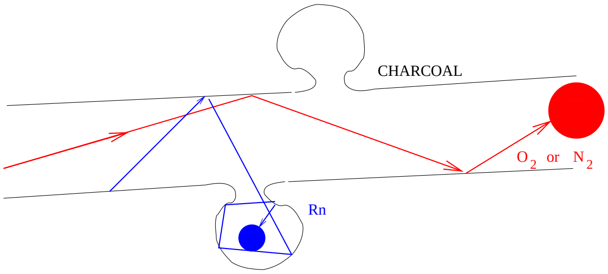

Figure 4.10 : Principle of radon trapping using charcoal.

Many parameters are involved in the action of charcoal but the one currently under control is the charcoal temperature inside the gas flow. In order to characterize each charcoal and to choose the most efficient a test bench developed at Neuchâtel University [62] was performed (see Fig. 4.11). It used a gas flow of nitrogen with flux and temperatures controls, for which the concentration of radon was done by a calibrated radium source of low activity (to avoid saturation effects). A sample of charcoal was placed as a trap in the flux and the level of radon was measured at the exit of the trap. After stabilization, the charcoal was removed and placed on a germanium detector in order to measure the trapped radon activity, which gave the radon trapping factor for each charcoal sample. Measurements were done for various temperatures of the charcoal. The $K$-factor, in $m^3/kg$, is the adsorption coefficient of activated charcoal and is defined as the ratio of the activity of radon trapped in the charcoal (in Bq/kg) over the activity of radon in the gas flow (in $Bq/m^3$). Higher is the $K$-factor, better is the charcoal capability for radon trapping.

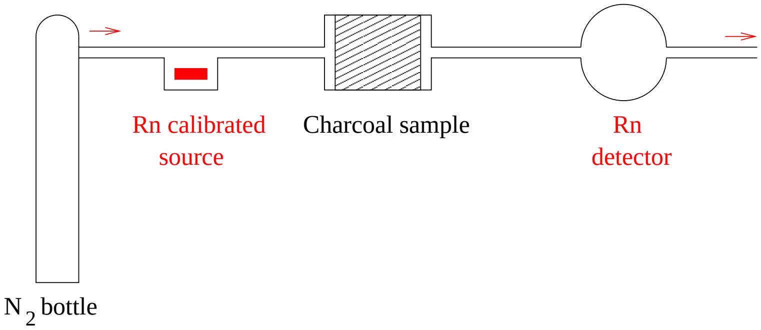

Figure 4.11 : Principle of the method used to measure the $K$-factor.

#### 4.2.3.2 Study of the $K$-factor with temperature

The $K$-factor depends on charcoal type, temperature and pressure. Measurements of various types of charcoal have been realized to find the best one. Table 4.2 gives the results for two different types of charcoal for various temperatures between room temperature and commercial low temperatures. For the temperature choice, one have to note that it is very expansive to decrease the temperature below -55$^o$C because it needs a new technology with a different coolant.

| Gaz temperature and charcoal conditions | $K$-factor ($m^3.kg^{-1}$) | $\sigma_K$ ($m^3.kg^{-1}$) |
|---|---|---|
| $Pl$ + 20$^o$C $N_2$ gas | 4.25 | 0.41 |
| $Pl$ + 0$^o$C $N_2$ gas | 12.1 | 3.6 |
| $Za$ + 20$^o$C $N_2$ gas | 3.01 | 0.69 |
| $Za$ + 0$^o$C $N_2$ gas | 7.89 | 0.90 |
| $Za$ + -40$^o$C $N_2$ gas | 65.36 | 9.70 |
| $Za$ + -50$^o$C $N_2$ gas | 110.54 | 16.58 |
| $Za$ + -60$^o$C $N_2$ gas | 302.27 | 43.76 |

Table 4.2 : Variation of the $K$-factor with temperature for two charcoal samples (where $Pl$ is “Dr Pleisch” charcoal and $Za$ is “Zander France - NC35” charcoal).

#### 4.2.3.3 Measurements of various types of charcoal

The reduction of radon concentration obeys a law in $\exp(-\tau_R/\tau_{decay})$, where $\tau_{decay}$ is the radon lifetime equal to 132 hours and $\tau_R$ is the radon retention time in charcoal, which is related to the $K$-factor by the formula:

$$\tau_R = \frac{K \times M}{F}$$

where $\tau_R$ is in hour and $K$ in $m^3/kg$. Here $M$ is the charcoal mass in kg and $F$ is the gas flux in $m^3/h$. For a reduction of radon activity by a factor 100, an order of magnitude higher than the factor 10 required for NEMO 3 the retention time must be 26 days (radon period is 3.8 days and a factor 100 corresponds to 7 periods)[2]. Various charcoal types were compared at a temperature of -40$^o$C with $N_2$ gas. Results of these measurements are given in Table 4.3.

| Charcoal type | $K$-factor ($m^3.kg^{-1}$) | $\sigma_K$ ($m^3.kg^{-1}$) |
|---|---|---|
| Czech SC44 21278 grinded 0.5-2 mm | 46.47 | 6.15 |
| Czech Silcarbon C46 grinded 0.5-2 mm | 95.20 | 11.85 |
| Czech Chemviron F30470 grinded 0.5-2 mm | 103.66 | 12.95 |
| Dr Pleish (new sample) | 60.70 | 12.77 |
| Czech Silcarbon K847 (new sample) | 66.32 | 13.55 |
| Sil 40 grinded 0.5-2 mm (new sample) | 52.91 | 11.05 |
| Czech Silcarbon K48 grinded 0.5-2 mm (sample number 283) | 141.31 | 25.62 |
| Czech Silcarbon K48 grinded 0.5-2 mm (sample number 403) | 134.72 | 28.51 |

Table 4.3: Comparison between several types of charcoal at -40$^o$C with $N_2$ gas.

The radon trapping properties clearly depend on the charcoal choice. Among the various tested charcoal the Czech Silcarbon K48 was the best one. Two measurements were performed with two different samples of K48 charcoal (see the two last lines in Table 4.3) and similar results were obtained demonstrating the good stability of this product. With an operating temperature of -50$^o$C for the K48 charcoal and a maximal variation of ±5$^o$C, the expected $K$-factor is approximately 250, which is sufficient to obtain a one hundred radon attenuation factor.

#### 4.2.3.4 Measurement of radon degassing of molecular sieves and zeolite

Using a radon trapping at freezing temperature, it is necessary to remove water present in the gas flow at a level below the dew point. To reach -50$^o$C for the ultimate temperature of the charcoal, the dew point of air must be at -70$^o$C (20 degrees lower). This value is technically possible using industrial trapping with molecular sieves, which unfortunately are zeolite type. Thus the residual radioactivity of these products can make them inappropriate for the NEMO 3 experiment, if their degassing itself is increasing the level of radon in the gas flow by more than a few 10%. A test bench was used to measure this parameter for various molecular sieves obtained

---

[2] Note that the chosen reduction factor of 100 was one order of magnitude higher that the requested one but it was a safer choice than to build a facility with a reduction factor of only 10

from industrial dryer setups. The gas flow was pure nitrogen and the measurements were done after twenty hours of flushing. Note that it was much easier to measure the thoron activity ($^{220}$Rn, with a half-life of 55 seconds) than the radon one ($^{222}$Rn, with a half-life of 3.8 days).

These measurements have shown that radon lines were negligible ($< 2$ Bq/m$^3$ before and after flushing) but thoron were not ($100 \pm 5$ Bq/m$^3$ before flushing and $30 \pm 2$ after). Nevertheless, due to its short half-life, the thoron is not a damaging contributor to the NEMO 3 backgrounds. Thus it is appropriate to use these types of sieves for the radon purification system.

#### 4.2.3.5 Conclusions for the radon trapping facility

As a result of these measurements, the choice was made to use -50$^o$C as the charcoal temperature, with a maximal variation of $\pm 5^o$C. With one ton of Silcarbon K48 charcoal operating in this temperature range (-55 to -45$^o$C) and a gas flow of 150 m$^3$/h, an expected attenuation factor of 100 could be reached on the radon level of the air at the radon trapping facility exit. Moreover the contribution of molecular sieves in the dryer is not damaging to the radon level for this facility specifications. Finally the responsability of this facility realization was given to the ATEKO company in Czech Republic.

The final specifications of the radon trapping facility are:

- Compressor from Atlas-Copco GA22 scew type - 194 Nm$^3$/h at 25$^o$C and 950 mbars - 10 bars - 28 kW at maximum value
- Filtration with oil separator (0.03 $\mu$m) and dust separator (0.1 $\mu$m)
- Air dryer from ZanderKen - 150 m$^3$/h - with a dew point at -70$^o$C for 8.5 bars - 30$^o$C at maximum value
- Cooling unit from Bitzer - 10 kW - Output air temperature at -50$^o$C - 17.6 m$^3$/h at 8.5 bars
- Two adsorption columns, with internal diameter of 600 mm and 3 m high - insulator Aeroflex KKS with a temperature range [$-200^o$C, $+175^o$C]
- Charcoal: activated carbon K48 from Silcarbon Aktivkohle - 2 × 500 kg

The input and output air have a temperature of around 25 and 20$^o$C respectively.

### 4.2.4 Installation of the radon trapping facility in the LSM

#### 4.2.4.1 Installation of the airtight tent

The installation of the airtight tent took place in the LSM between September 2003 and April 2004. After installation of the fire detection system, the tent was ready (see Fig. 4.12) in May. After only few hours with door closed, a very significant increase of the trigger rate was shown, probably due to internal radon degassing. There was also an increasing of the temperature which was dangerous for the electronics.

Thus, eight independent cooling systems were installed inside the tent. The doors were definitely closed only mid-July, after cooling improvements and flushing with fresh air instead of the laboratory air (there is a difference of around 7 Bq/m$^3$ between their radon activities).

Figure 4.12: Picture of the airtight tent surrounding the NEMO 3 detector after its final installation in the LSM. As shown in this picture, the lower part of the tent which surrounded the electronics is now removed.

#### 4.2.4.2 First measurements after airtight tent installation

Using the two radon detectors, measurements were carried out. Remember that due to the different calibrations for "NEMO" and "Ge" radon detectors (see Eq. 4.1), it is not really obvious to compare radon measurements inside and outside the airthight tent using these two detectors.

Radon activity measurements inside the closed tent with fresh air gave a value of $\sim 16$ Bq/m$^3$ using radon detectors [65].

Using NEMO 3 analysis of the $(e^- \alpha \; N\gamma)$ channel (with $N \geq 0$) [63], the total radon activity inside NEMO 3 showed a small increasing after the airtight tent was closed, which was probably due to an internal radon degassing inside the tent. The NEMO 3 trigger rate also increased of around 0.3-0.4 Hz. The maximal value of total radon activity inside NEMO 3 was obtained in the beginning of August 2004, with a value of around 1.2 Bq.

### 4.2.4.3 Installation of the radon trapping system

The principle of the radon trapping facility is shown in Fig. 4.13. The installation was tested in Czech Republic by NEMO collaborators from Prague and then transported to the LSM for the final installation in September 2004. A picture of the facility in the LSM is shown in Fig. 4.14.

The functioning of the radon trapping facility began October $4^{th}$ 2004. After first tests, it was decided to use only one charcoal tank (AC1), with an air flux of 150 $m^3/h$ and a temperature of -57$^o$C [66].

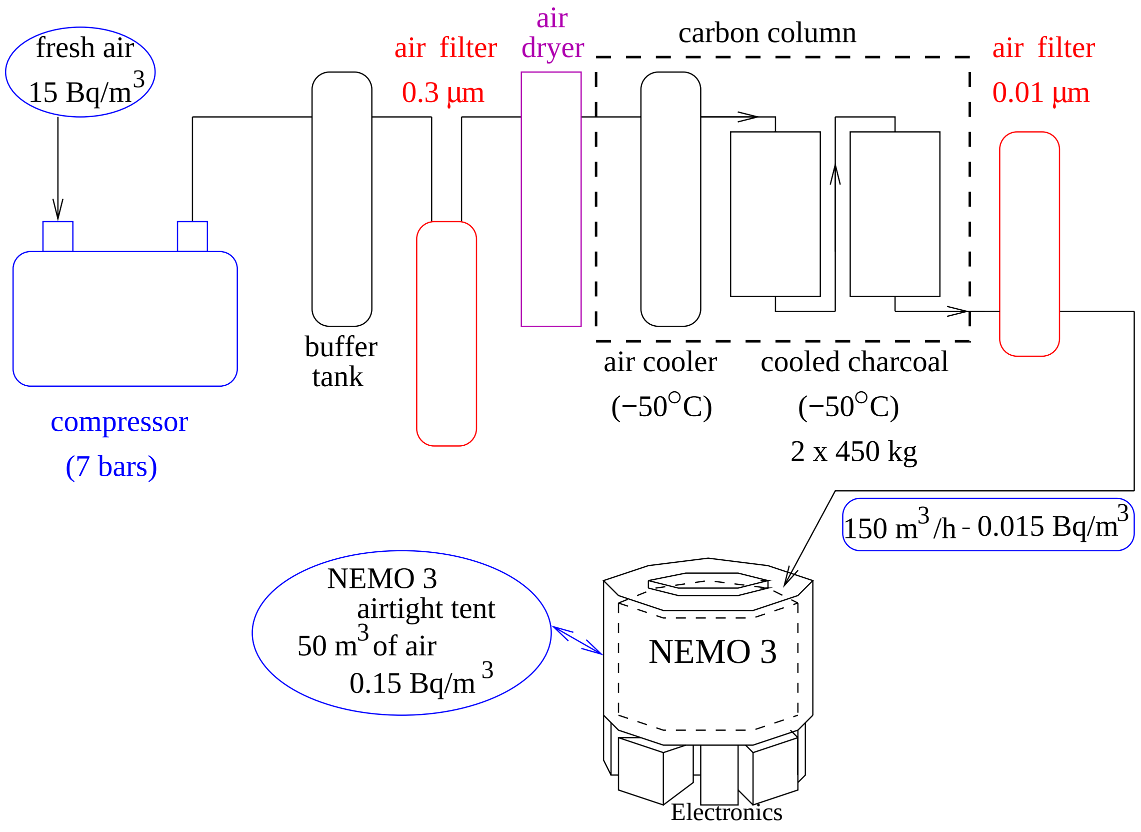

Figure 4.13: Principle of the radon trapping facility. As indicated on this figure, the radon-free air is now sent only to the upper part of the tent (from the top to the bottom) because there is a plastic separation between the lower acquisition and electronics' part and the upper detector's part (plastic sheets are put above electronics racks), to avoid radon degassing from the electronics.

Figure 4.14: Picture of the radon trapping facility in the LSM.

#### 4.2.4.4 Measurements after radon facility installation

After starting the radon trapping facility, radon-free air was measured during few hours at the exit of the system with radon detector. With a 15 Bq/m$^3$ radon activity at the entrance of the facility, value at the output was found to be $\sim$ 10 mBq/m$^3$ measured with the radon detectors. Thus the expected performances of the radon trapping facility have been completely reached with only one tank [67].

Using NEMO 3 analysis of the ($e^- \alpha\ N\gamma$) channel (with $N \geq 0$), four different periods have been analysed since the starting of the radon trapping facility, to check the evolution of the radon activity inside NEMO 3 [63]. In the same time, radon activity was measured inside the airtight tent for comparison, using radon detector [65].

In the beginning of October 2004, after that air flowing through charcoal has been sent inside the airtight tent surrounding the NEMO 3 detector, the radon value measured inside this tent passed from $\sim$ 16 Bq/m$^3$ to $\sim$ 5 Bq/m$^3$. The corresponding value of total radon activity, which was 0.95 Bq in average for the period mid-February to end of September 2004, became $\sim$ 0.35 Bq inside the detector. The NEMO 3 trigger rate decreased to around 6.25 Hz.

At the end of October 2004, a plastic sheet was put above the electronics to separate the lower part below the NEMO 3 detector from the detector itself, to avoid electronics degassing. In the same time, it was decided to put radon-free air input at the top of the tent and its output at the bottom of the top (but above the plastic part). The radon value measured inside the airtight tent (upper part) and the corresponding value of total radon activity inside NEMO 3 became respectively $\sim 1.2$ Bq/m$^3$ and $\sim 0.2$ Bq.

The third period, in the beginning of November 2004, was after the opening of the airtight tent doors, which was needed to avoid a too big increasing of the temperature dangerous for the electronics. Note it was not a problem for the radon inside NEMO 3 due to the separation between the lower part of the tent (with the doors) and the upper part surrounding the detector. Thus no increasing was observed, since the measured total radon activity inside NEMO 3 was always $\sim 0.2$ Bq, and the validity of the separation was demonstrated. In the same time the ventilation of the electronics racks has been oriented toward outside (it was before oriented towards the detector).

Mid-November 2004, a new campaign to fill the holes in the plastic separation was carried out to improve the tightness and the radon activity inside the airtight tent decreased from more than a factor two (measured value of 0.4 Bq/m$^3$ with radon detector). Finally, Fig. 4.15 shows the evolution of the total radon activity in NEMO 3 during the fourth period. Measurements were done between the 15 December 2004 and the 18 January 2005, using analysis of the ($e^- \alpha\ N\gamma$) channel (with $N \geq 0$) [63]. The associated total radon activity inside the detector, which seemed to have reached an asymptotic value, is $\sim 0.15$ Bq compare to $\sim 0.95$ Bq in average before using radon-free air, that means a reduction factor around 6-7.

Measurements done during nearly the same period with the radon detector are presented in Fig. 4.16 and correspond to a radon activity inside the airtight tent of 0.3 Bq/m$^3$ [65].

The associated NEMO 3 trigger rate is $\sim 5.7$ Hz since this period.

The evolution time of the radon activity $\tau_{in}$ is given by:

$$\frac{1}{\tau_{in}} = \frac{1}{\tau_d} + \frac{\phi_{in}}{V}$$

where $\tau_d = 476595$ s is the radon decay time (mean life), $\phi_{in} \sim 0.24$ m$^3$/h is the gas flux into the NEMO 3 detector and $V = 28$ m$^3$ is the fiducial volume of the detector.

Thus the expected value of $\tau_{in}$ equals 223250 s = 2.58 days. Using the analysis corresponding to the total radon activity showed in Fig. 4.15, the measured evolution time is $\tau_{meas} = 215000 \pm 6000$ s $= 2.49 \pm 0.07$ days, which is in very good agreement with the expected value [63].

Fig. 4.17 presents evolution of the radon activity measured inside the airtight tent with one radon detector during 1.5 months. First measurements correspond to an activity of 0.3 Bq/m$^3$ and the last ones to 0.1 Bq/m$^3$ after searching on new leaks inside the separation plastic film. One can see some increasing of the radon rate which respectively correspond to the calibration sources' introduction and removing, which needs opening the top shields, an electronical shut-down, and also some problems with the plastic sheet and the facility compressor. This figure shows the decreasing of the radon activity after each trouble, which ensure the quality of the radon purification facility. Best radon values for these last weeks of February 2005 correspond to an activity of 0.1 Bq/m$^3$, that means a gain of a factor $\sim 100$ compare to measurements with fresh air from the ventilation tunnel sent inside the airtight tent.

In March 2005, there were no measurements inside the tent because the radon detectors were used for measurements at the exit of the radon facility, which was under tests (from 10 to 26 of March).
The level of radon activity has been measured at the exit of the radon trapping facility at -57 and -50$^o$C and the obtained values of $\sim 10$ mBq/m$^3$ were for both at the background level. After

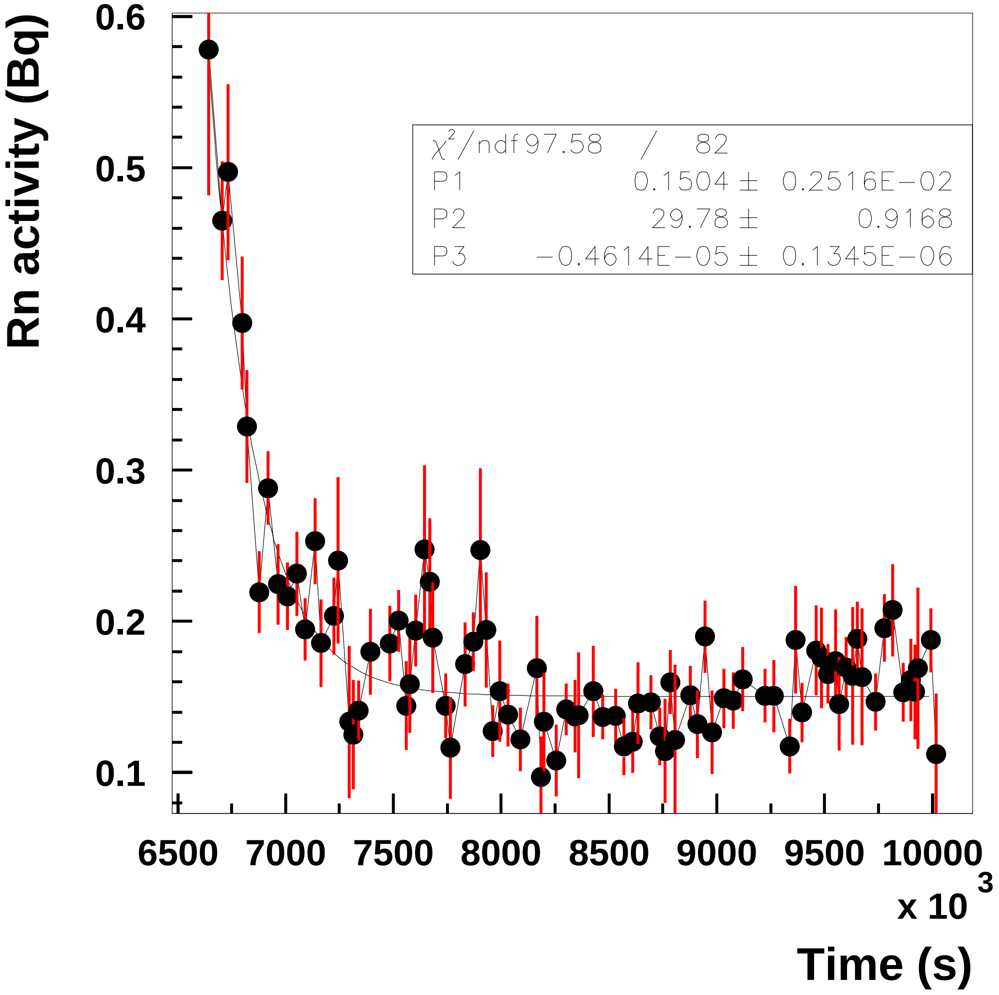

Figure 4.15: Evolution of the total radon activity in NEMO 3 during the fourth period. Measurements were done between the 15 December 2004 and the 18 January 2005, using analysis of the ($e^-\alpha\ N\gamma$) channel (with $N \geq 0$) [63]. The associated total radon activity inside the detector seemed to have reached an asymptotic value of ∼ 0.15 Bq. Measurements done during nearly the same period with the radon detector are presented in Fig. 4.16 and correspond to a radon activity inside the airtight tent of 0.3 Bq/m$^3$ [65].

some tests consisting to switch off cooling during few hours, no influence was observed. After switch off during three days and the use of the other charcoal tank, there has been an increasing of the radon activity.

Finally, it was decided to start again the facility with the first tank, at -50$^o$C (in order to test the functioning of the facility at this temperature value) with an air flux of 150 m$^3$/h [68]. There were some residuals of radon inside the facility's charcoal tank. As a consequence, purified air

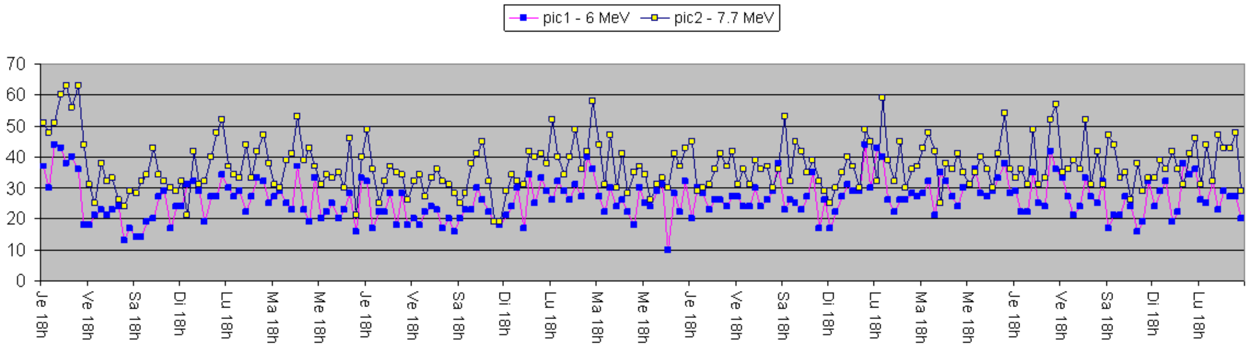

Figure 4.16 : Evolution of the radon activity inside the airtight tent measured with one radon detector the 16 December 2004 and the 11 January 2005, which is nearly the same period than for Fig. 4.15. These measurements correspond to a radon activity inside the airtight tent of 0.3 Bq/m$^3$ [65].

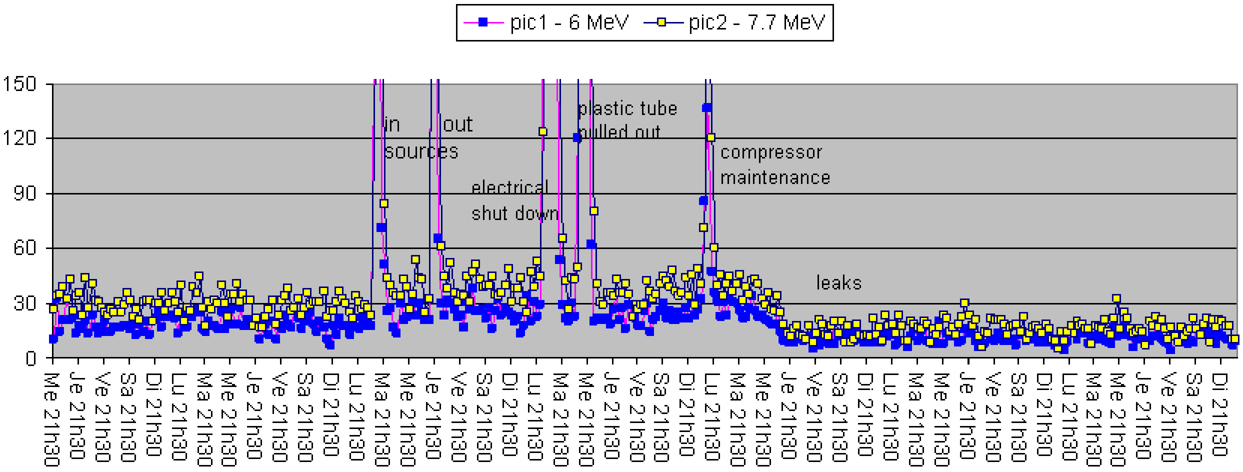

Figure 4.17 : Evolution of the radon activity measured inside the airtight tent with radon detector between the 12 January and the 28 February 2005. One measurement is realized every three hours. First measurements correspond to an activity of 0.3 Bq/m$^3$ and the last ones to 0.1 Bq/m$^3$ after searching on new leaks inside the separation plastic film. One can see some increasing of the radon date due to known activities or problems, but also the decreasing of the radon activity after each trouble, which ensure the quality of the radon purification facility.

was not completely free of radon and the radon activity measured inside the airtight tent was around 0.3 Bq/m$^3$ in the beginning of April. It will take around two months to retrieve the best values of radon activity at 0.1 Bq/m$^3$.

### 4.2.5 Preliminary conclusions about the radon trapping facility

It seems there is a residual radon activity inside the NEMO 3 detector. Assuming an emanation from one of the detector components, upper limit of this residual contamination can be calculated.

Supposing an emanation from the aluminised Mylar wrapped in front of the scintillators, which correspond to a total surface of $\sim$ 100 $m^2$ with a thickness of 12 $\mu$m, the associated weight is around 1 kg. The inner volume of the NEMO 3 detector is 28 $m^3$ and the upper limit obtained from HPGe measurements was $A(^{226}\text{Ra}) \equiv A(^{214}\text{Bi}) < 35$ mBq/kg. Assuming that each radon nucleus escapes the Mylar foil (50% towards Nemo and 50% the other side towards the scintillators), the associated radon activity is less than 0.6 mBq/$m^3$, which is much more less than the searched activity.

Supposing an emanation from the stainless steel wires of the tracking detector, new HPGe measurements have been realized one year after the first measurements to check the $^{226}$Ra activity in these wires, in order to understand this residual radon value inside the NEMO 3 detector. Only upper limits were obtained once again, corresponding to a total activity of 1.20 mBq ($A(^{226}\text{Ra}) \equiv A(^{214}\text{Bi}) < 0.70$ mBq/kg for 1.7 kg of wires) which is very good agreement with the upper limit of 1 mBq as put in Table 2.43 from Section 2.9. Assuming that each radon nucleus escapes the wires, the associated radon activity is less than 0.05 mBq/$m^3$, which is also less than the searched activity.

Supposing an emanation from the isotopes source foils and using $^{214}$Bi contaminations as measured with HPGe detectors and presented in Table 2.38 from Section 2.9, the radon upper limit (or value) is $A(^{226}\text{Ra}) \equiv A(^{214}\text{Bi}) < 7$ mBq. Assuming that each radon nucleus escapes the source foils, the associated radon activity is less than 0.25 mBq/$m^3$, which is also much more less than the searched activity.

In conclusion, none of these values can explain the residual radon activity inside the detector and more studies have to be realized.

Fig. 4.18 was used to calculate the air volume between the NEMO 3 detector and the iron shield, including the central tower volume, in order to improve the radon simulation inside the tent. The calculation gives $V_{air} = 44$ $m^3$ ($\pm$10%).

The radon trapping facility is in operation since October 2004 and allows a reduction of the radon level around the detector at a value of $\sim$ 100 mBq/$m^3$. With this system, the radon activity inside the NEMO 3 detector has been reduced to $\lesssim$ 5 mBq/$m^3$. Improvements are already planed, as the use of a second plastic sheet between the detector and electronics to avoid leaks. Also since mid-April 2005, the gas flux inside the tracking detector has been increased to $\sim$ 450 l/h, which provides a new decreasing of the radon activity inside the detector. Thus the radon reduction factor has now reached the expected value of ten, which provides a negligible radon contribution to the backgrounds in the $\beta\beta0\nu$ energy window.

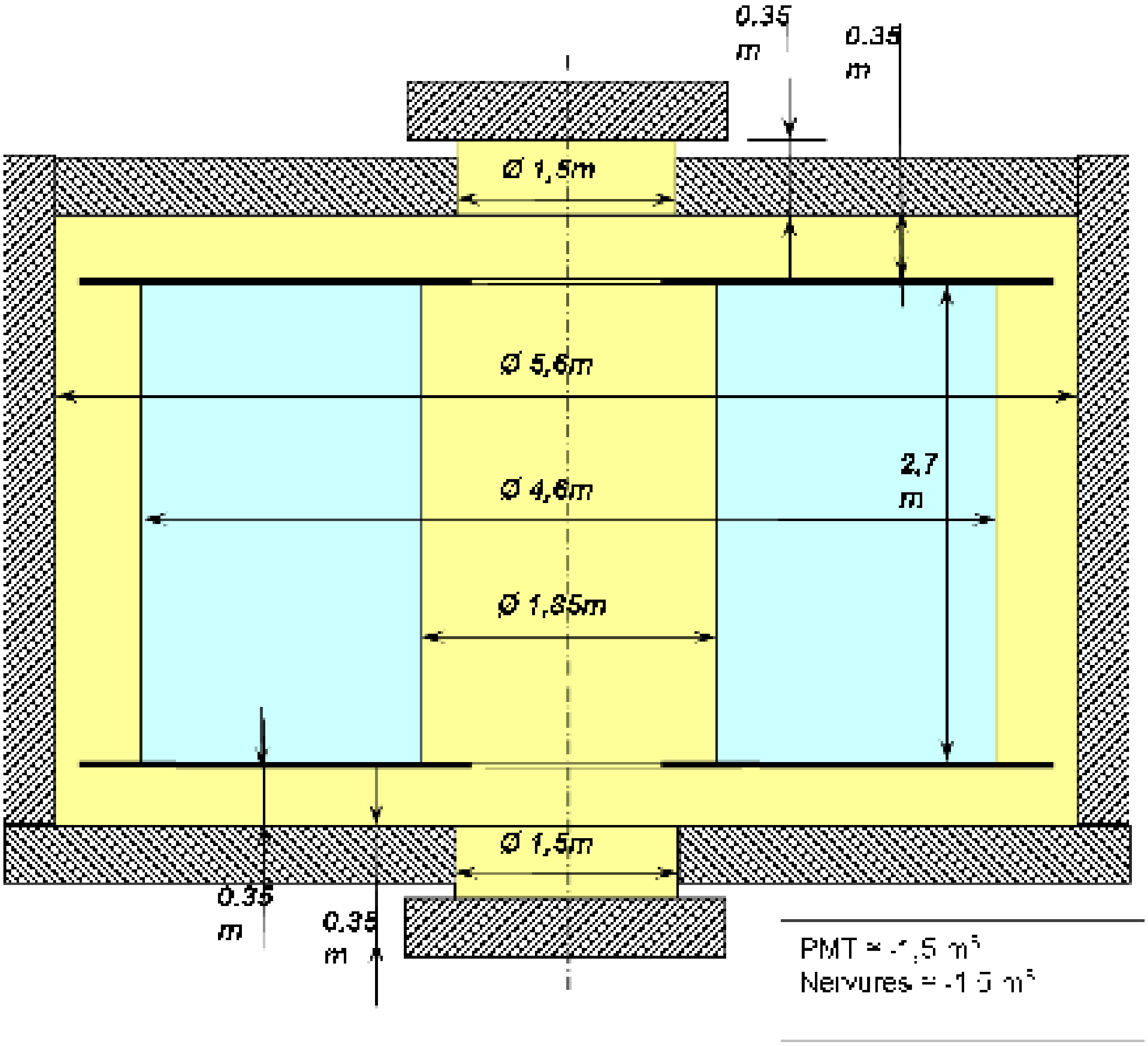

Figure 4.18 : Scheme of the NEMO 3 detector and iron shield, used to calculate the air volume inside the airtight tent.

# Chapter 5

# Conclusions and prospects

## 5.1 Status of the NEMO 3 performance and results

The NEMO 3 experiment is based on the direct detection of the two electrons emitted from double beta decay isotopes, with the detector and the source of the double beta decay being independent. This allows the collaboration to study seven $\beta\beta$ isotopes simultaneously. The isotopes which are distributed among 20 sectors are $^{100}$Mo, $^{82}$Se, $^{130}$Te, $^{116}$Cd, $^{150}$Nd, $^{96}$Zr and $^{48}$Ca. A calorimeter made of large blocks of scintillators coupled to very low radioactivity PMTs permits one to measure the energies of electrons, positrons, gamma-rays and also their time-of-flight, which are used to reject events from external backgrounds. In addition of a tracking volume with delayed tracking electronics for identification of alpha particles coming from $^{214}$Bi decay, a 25 Gauss magnetic field allows three-dimensional track reconstruction of charged particles. Thus the NEMO 3 detector is able to identify electrons, positrons, $\gamma$-rays and $\alpha$-particles and to detect multi-particle events in the energy domain of natural radioactivity. Using registered events in the $e^-N\gamma$ ($N \geq 0$), $e^-\gamma\gamma$, $e^-\gamma\gamma\gamma$ and $e^-\alpha N\gamma$ ($N \geq 0$) channels for backgrounds studies, the NEMO 3 detector is able to characterize and measure its own background, which can be subtracted from the two-electron signal.

The main objective of the NEMO 3 experiment is to search for neutrinoless double beta decay. To avoid the high energy region of natural radioactivity the $\beta\beta0\nu$ isotopes are selected for their high $Q_{\beta\beta}$ value. Every attempt has been made to minimize internal backgrounds in the $\beta\beta0\nu$ sources by purification of the enriched samples as well to suppress external backgrounds using shields and by carefully selecting all the detector materials. The tail of the $\beta\beta2\nu$ decay distribution troublesomely overlaps the $\beta\beta0\nu$ distribution as a function of the energy resolution. It is the unavoidable background for neutrinoless double beta decay studies.

The NEMO 3 detector has been running in the Fréjus Underground Laboratory in nearly optimal conditions since mid-February 2003. Fig. 5.1 and Fig. 5.2 reflect the performance of the detector. The first shows the distribution of the summed two electron energies of $\beta\beta2\nu$ events measured for the molybdenum sources (background substracted). The data sample corresponds to 389 days of data for the runs since mid-February 2003. The number of events is $\sim 219,000$, with a signal-to-background ratio of 40:1. The second figure presents the experimental angular distribution for the two emitted electrons in molybdenum sources. The same data for the summed energy and angular distribution are shown with the $\beta\beta2\nu$ Monte-Carlo calculation. The high statistics of the data will allow for detailed checks of the models used for the Monte-Carlo calculation. This angular distribution is obtained using the ability of the NEMO 3 detector to reconstruct the two electron tracks, thus to measure the angle between them. Fig. 5.3, which present analysis results from the one-electron channel for the strips 6 and 7 of sector 05, also reflect the performance of the detector. Using this channel analysis with the NEMO 3 data allows measuring pure $\beta$-emitter $^{90}$Sr internal contamination of $\sim 30$ mBq inside the $^{48}$Ca source disks, which was not detected by HPGe detectors, and thus subtracting it from the two-electron signal.

A radon trapping facility using charcoal has been designed to reduce the radon level in the fresh air coming inside the laboratory. The free-radon air is then sent inside an airtight tent which fully encloses the NEMO 3 detector. This system is in operation since October 2004 and allows a reduction of the radon level around the detector at a value of $\sim 0.1$ Bq/m$^3$. With new improvements since April 2005, the radon activity inside the detector has been reduced to $\lesssim 3$ mBq/m$^3$, which is very near the required level of 2 mBq/m$^3$ needed to have negligible background from radon.

## 5.2 Advantages and limitations of the NEMO 3 detector

The NEMO 3 detector has been running in the LSM in nearly optimal conditions since mid-February 2003 and data analyses have shown that the performance of the detector are as expected. Concerning the tracking detector, the transverse and longitudinal resolutions associated with two-electron events are respectively 0.6 cm and 1.0 cm. The energy resolutions (FWHM) at 1 MeV for the calorimeter are 14% and 17% for counters associated respectively with 3" and 5" PMTs. 99.5% of the drift cells are on and 98% of the PMTs are functioning to design specifications (changes in HV chain could allow recovering some of them). After two years of functioning, there is no sign of wire chamber or calorimeter aging. The first NEMO 3 results have shown the background reductions at the expected levels, for both internal and external backgrounds. The main result from this data collection is that all the sources of backgrounds are well identified and understood. Taking into account all the different background contributions and after the radon suppression, the sensitivity after 5 years of data taking will be for the period respectively $T_{1/2}^{2\nu} > 2 \times 10^{24}$ yr for $^{100}$Mo and $T_{1/2}^{2\nu} > 8 \times 10^{23}$ yr for $^{82}$Se. The corresponding sensitivity on the effective neutrino mass should be $\langle m_\nu \rangle < 0.3 - 0.5$ eV for $^{100}$Mo and $\langle m_\nu \rangle < 0.62 - 1.72$ eV for $^{82}$Se [57].

As a summary, the collaboration has shown with the NEMO 3 detector:

- its ability to identify and understand all the sources of backgrounds associated with a tracko-calo detector,
- its capability to build a very low-background detector,
- the quality of the technical choices, since the expected performances of the tracking detector, the calorimeter and the trigger have been successfully achieved,
- its capability of using both physical and chemical methods to purify $\beta\beta$ isotopes, removing $^{214}$Bi and $^{208}$Tl contaminants,
- its ability to remove radon from air, building an airtight tent to enclose the detector coupled to a radon trapping facility,
- the detector's ability to measure both external and internal contaminations of the source foils,

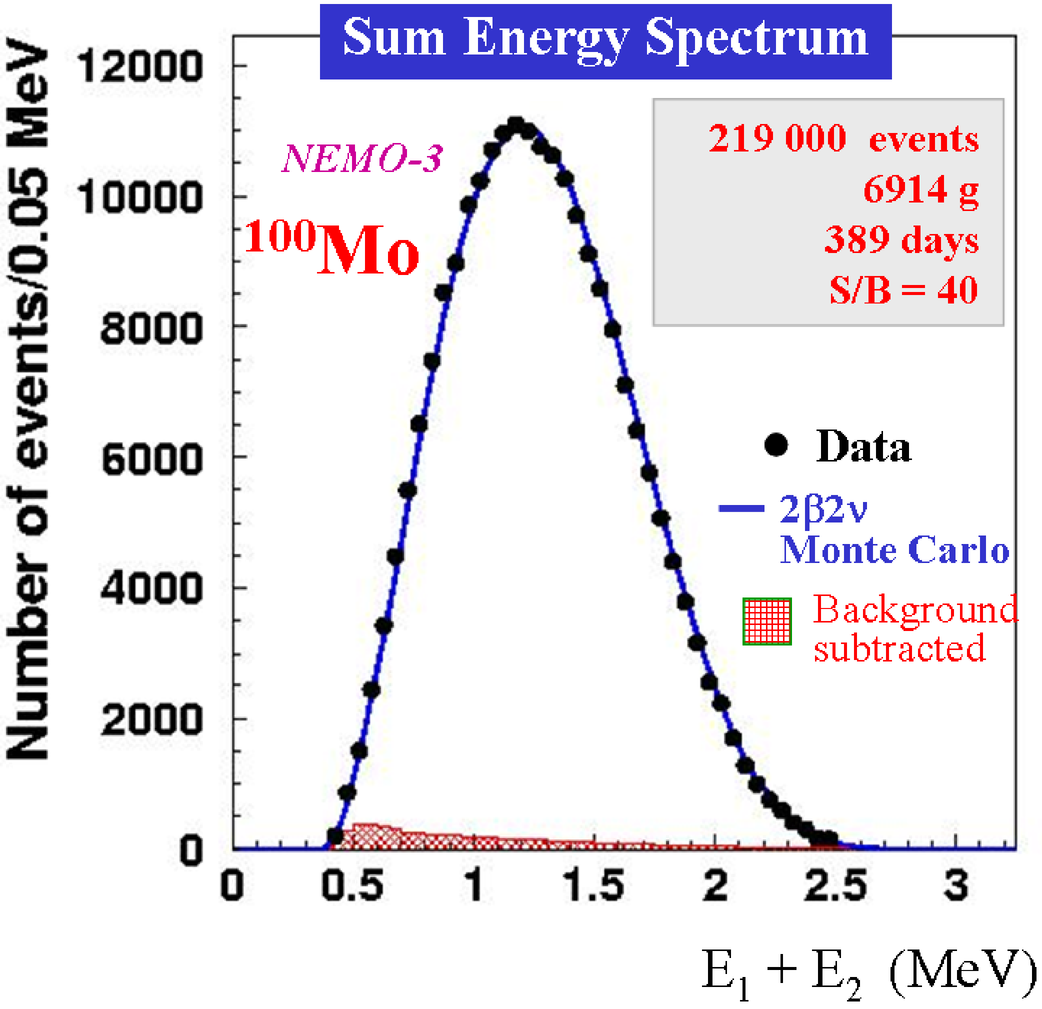

Figure 5.1: Distribution of the experimental total energy sum measured with molybdenum sources. Solid line corresponds to the expected $\beta\beta2\nu$ spectra from simulations and shaded histogram is the Monte-Carlo computed background subtracted. It corresponds to 389 days of data collection in stable conditions, since mid-February 2003. The number of events is $\sim 219,000$, with a signal-to-background ratio of 40 to 1.

- its capability to control the external backgrounds from natural radioactivity, neutrons and muons,
- its expertise to develop ultra low background HPGe detectors as well as radon detectors which are sensitive to a 1 mBq/m$^3$ radon activity.

The NEMO collaboration in association with new UK, US, Russian and Japanese groups began in December 2003 to study the feasibility of a NEMO 3 technique extrapolation to a detector with a mass of at least 100 kg to reach a sensitivity of around 50 meV on the effective neutrino mass for the transitions towards the fundamental or excited states.

The SuperNEMO detector will use the NEMO 3 technical choices: a thin source between two

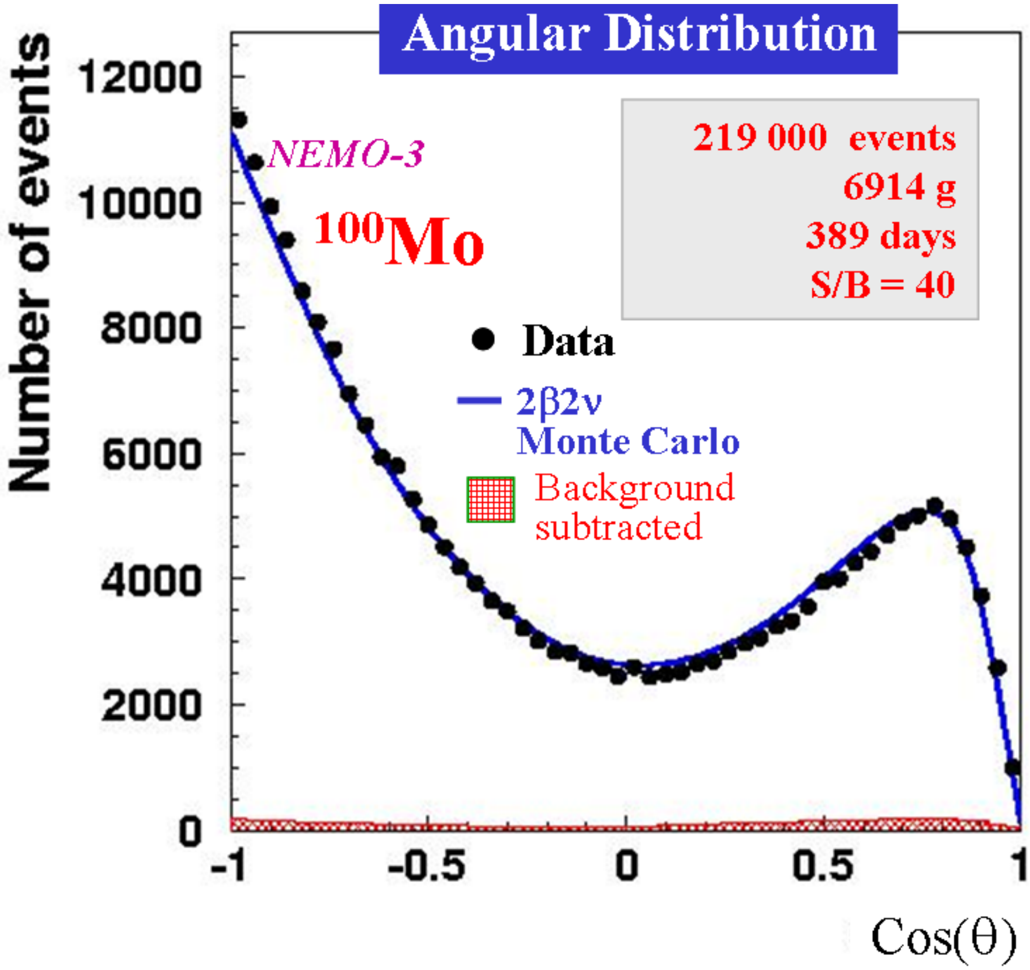

Figure 5.2: Experimental angular distribution for molybdenum sources. Solid line corresponds to the expected $\beta\beta2\nu$ angular distribution from simulations and shaded histogram is the Monte-Carlo computed background subtracted. The distribution corresponds to the data in Fig. 5.1.

tracking volumes surrounded by a calorimeter. The main points to improve compare to the NEMO 3 detector performances are the energy resolution and the $\beta\beta0\nu$ detection efficiency. The thickness and radiopurity of the source foils have also to be decreased and thus new measurements techniques have to be found. Finally concerning the backgrounds which are well identified and understood with the NEMO 3 detector, their rejections have to be improved.
R&D proposals for a design study for the SuperNEMO detector have been approved by both the Scientific Council of IN2P3 [6] (France, in March 2005) and PPARC Scientific Council (UK, in July 2005).

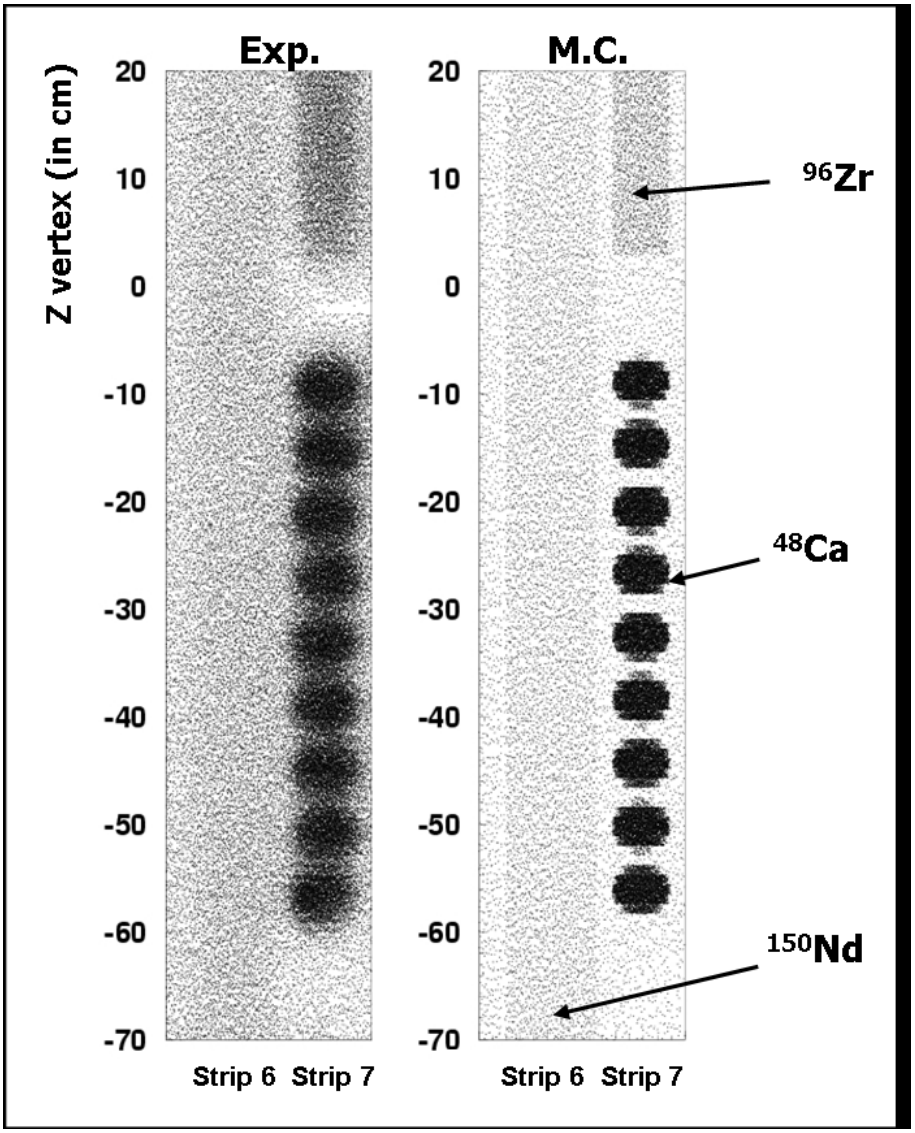

Figure 5.3 : Results from one-electron channel analysis for both experimental and simulated data, which show good agreement between both. Here are presented lower part of the strips 6 and 7 of sector 05, for longitudinal vertices $Z$ between -70 and 20 cm, which correspond to $^{150}$Nd, $^{96}$Zr and $^{48}$Ca source strips. One clearly see greater activity in this one-electron channel for the nine disks of calcium than for others strips, which is representative of pure beta emitter $^{90}$Sr internal contamination of $\sim$ 2 Bq/kg inside this $\beta\beta$ isotope. This measurement allows subtracting this background contamination from the associated two-electron signal.

# Bibliography

[1] B. Pontecorvo, *Zh. Eksp. Teor. Fiz.* **33** (1957) 549 and *ibid.* **34** (1958) 247; Z. Maki, M. Nakagawa, S. Sakata, *Prog. Theor. Phys.* **28** (1962) 870

[2] R. Mohapatra et al., *Theory of neutrinos*, **Review of American Physical Society** (2004)

[3] C. Aalseth et al., *Neutrinoless double beta decay and direct searches for neutrino mass*, **Review of American Physical Society** (2004)

[4] J. Schechter and J. Valle, *Phys. Rev* **D25** (1982) 2951

[5] W. H. Furry, *Phys. Rev.* **56** (1939) 1184

[6] F. Piquemal for the NEMO collaboration, *Presentation to IN2P3 scientific council*, 21 March 2005

[7] A. S. Barabash, *Czech. J. Phys.* **52** (2002) 567

[8] G. Audi and A.H. Wapstra, *Nucl. Phys.* **A 595** (1995) 409

[9] F. Boehm and P. Vogel, *Physics of massive neutrinos*, Cambridge University Press, second edition (1992)

[10] D. Dassié et al., NEMO collaboration, *Nucl. Instr. and Meth.* **A309** (1991) 465

[11] R. Arnold et al., NEMO collaboration, *Nucl. Instr. and Meth.* **A 354** (1995) 338

[12] NEMO collaboration, *NEMO3 Proposal*, **LAL 94-29** (1994)

[13] D. Dassié et al., NEMO collaboration, *Phys. Rev.* **D51** (1995) 2090

[14] R. Arnold et al., NEMO collaboration, *Z. Phys.* **C 72** (1996) 239

[15] R. Arnold et al., NEMO collaboration, *Nucl. Phys.* **A 636** (1998) 209

[16] R. Arnold et al., NEMO collaboration, *Nucl. Phys.* **A 658** (1999) 299

[17] *Table of Isotopes*, 8th edition, R.B. Firestone, V.S. Shirley Editor (1996)

[18] *WWW Table of Radioactive Isotopes*, **http://ie.lbl.gov/toi/nucSearch.asp**

[19] R. Arnold et al., NEMO collaboration, *Nucl. Instr. and Meth.* **A 536** (2005) 79

[20] T. Bernatowicz et al., *Phys. Rev. Lett.* **69** (1992) 2341

[21] N.Takaoka, Y. Motomura, K.Nagao, *Phys. Rev.* **C 47** (1996) 1557

[22] R. Arnold et al., NEMO collaboration, *Nucl. Instr. and Meth.* **A474** (2001) 93

[23] J. Busto et al., *Nucl. Instr. and Meth.* **A492** (2002) 35

[24] C. Augier, D. Lalanne and G. Szklarz, several contributions to NEMO collaboration meetings (1994/95/96/97)

[25] J.A. Kadyk, *Nucl. Instr. and Meth.* **A 300** (1991) 436-479

[26] F. Sauli, *Nucl. Instr. and Meth.* **A 515** (2003) 358

[27] L. Malter, *Phys. Rev.* **50**, (1936) 48

[28] P. Bernaudin et al., *NEMO 3 Calorimeter Electronics*, contributed paper to the 2000 IEEE NSS-MICC Conference, Lyon, France, 15-20 octobre 2000, **LAL/RT 00-13** (2000)

[29] F. Mauger, *The NEMO 3 Trigger Documentation*, note LPC Caen, july 2001

[30] Y. Perrin et al., *CASCADE: Tool kit for the construction of distributed real time data acquisition systems*, Conference Records of RT 93, Vancouver (1993)

[31] Y. Chitov, *The NEMO DB, a database for the NEMO 3 experiment*, note

[32] R. Arnold, *The energy calibration of NEMO 3*, note

[33] Ch. Marquet, several contributions to NEMO collaboration meetings (1998/99 and 2000/01/02)

[34] G. Lutter, contribution to NEMO collaboration meeting, Orsay, 10-12 March 2004 and Caen, 5-7 April 2005

[35] H. Ohsumi et al., NEMO collaboration, *Nucl. Instr. and Meth.* **A482** (2002) 832

[36] Ch. Marquet et al., NEMO collaboration, *Nucl. Instr. and Meth.* **A457**(2001) 487

[37] G. Szklarz, several contributions to NEMO collaboration meetings (2003/04)

[38] F. Hubert and Ph. Hubert, several contributions to NEMO collaboration meetings (from 1995 to 2000)

[39] J. Busto et al., *Nucl. Phys. Proc. Suppl.* **28A**(1992) 425

[40] M. Garcia-Talavera et al., *Journal of Radiation and Isotopes*, **54** (2001) 769

[41] R. Arnold and V.I. Tretyak, *The NEMO 3 simulation program: current status*, **CRN 97-01** (1997)

[42] *GEANT - Detector description and simulation tool*, CERN Program Library Long Writeup W5013, CERN (1994)

[43] *EUCLID 3*, version 1.1F, Matra Datavision (1994)

[44] C. Zeitnitz and T.A. Gabriel, *Nucl. Instr. and Meth.* **A349** (1994) 106

[45] C. Jollet, PhD Thesis, **CENBG 02-24** (2002)

[46] G. Lutter, contribution to NEMO collaboration meeting, Caen, 5-7 April 2005

[47] L. Simard, contribution to NEMO collaboration meeting, Caen, 5-7 April 2005

[48] F. Mauger, *Estimation of trigger efficiency*, NEMO internal note

[49] Y. Chitov, K. Errahmane, X. Sarazin, L. Simard, NEMO internal note, May 2001

[50] I. Kisel et al., NEMO collaboration, *Nucl. Instr. and Meth.* **A387** (1997) 433

[51] X. Sarazin, *Algorithme de l'Automate Cellulaire*, NEMO internal note

[52] K. Errahmane, PhD Thesis, **LAL 01-20** (2001)

[53] A.I. Etienvre, PhD Thesis, **LAL 03-13** (2003)

[54] V. Tretyak, contributions to NEMO collaboration meeting, Orsay, 26-28 May 2003, Dubna, 8-10 July 2004, and Prague, 24-26 November 2004

[55] R. Arnold, contribution to NEMO collaboration meeting, Prague, 24-26 November 2004

[56] V. Kovalenko, contribution to NEMO collaboration meeting, Chambéry, 9-11 July 2002

[57] X. Sarazin, talk presented at Neutrino 2004 conference *Nucl. Physics (Proc. Suppl,)* **B143** (2004) 221-224; R. Arnold et al., NEMO collaboration, in preparation for *Phys. Lett.* (2005)

[58] Y. Takeuchia et al, *Nucl. Instr. and Meth.* **A421** (1999) 334

[59] Y. Takeuchia et al, Super-Kamiokande collaboration, *Phys. Lett.* **B452** (1999) 418-424

[60] R. Saakyan, contributions to NEMO collaboration meeting, Orsay, 10-12 March 2004, Dubna, 8-10 July 2004 and Prague, 24-26 November 2004

[61] Ph. Bourgeois, M. Karolak and G. Vasseur, *Performance of the photomultiplier tubes used in the DIRC of BABAR: effect of a magnetic field and helium*, **dapnia-99-03** internal note (1999)

[62] J. Busto et al, Institut de Physique, Université de Neuchâtel, NEIPH/CORP/04/02, internal note (2004)

[63] L. Simard, contributions to NEMO collaboration meeting, Orsay, 10-12 March 2004, Dubna, 8-10 July 2004, Prague, 24-26 November 2004, and Caen, 5-7 April 2005

[64] C. Longuemare, F. Mauger and L. Simard *Variation of the radon activity in the laboratory and in the NEMO 3 detector, in the case of a ventilation*, NEMO internal note, April 2003

[65] G.Szklarz and Ph. Hubert, contributions to NEMO collaboration meeting, Dubna, 8-10 July 2004, Prague, 24-26 November 2004, and Caen, 5-7 April 2005

[66] D. Lalanne, contributions to NEMO collaboration meeting, Dubna, 8-10 July 2004, Prague, 24-26 November 2004, and Caen, 5-7 April 2005

[67] L. Vála, contribution to NEMO collaboration meeting, 24-26 November 2004

[68] I. Stekl, contribution to NEMO collaboration meeting, Caen, 5-7 April 2005